



UNIVERSIDAD DE CONCEPCIÓN
FACULTAD DE CIENCIAS FÍSICAS Y MATEMÁTICAS
DEPARTAMENTO DE FÍSICA

**STUDY OF THE LINEAR AND NONLINEAR REGIMES
IN AN UNMAGNETIZED ELECTRON-ION PLASMA**

A dissertation presented to Universidad de Concepción in partial fulfillment of the requirements for the degree of Master in Sciences majoring in Physics

By: Hugo Alexis Carril Pardo

Advisor: Dr. Jaime Andrés Araneda Sepúlveda

Co-advisor: Dr. Roberto Elías Navarro Maldonado

30 of august, 2020

Concepción, Chile

Se autoriza la reproducción total o parcial con fines académicos, por cualquier medio o procedimiento, incluyendo la cita bibliográfica del documento.



Contents

1	Introduction	1
1.1	Hypotheses of the work	13
1.1.1	Damped perturbations	13
1.1.2	Nonlinear perturbations - isothermal case	14
1.1.3	Nonlinear perturbations - temperature variation	14
1.2	Objectives	15
1.2.1	General objectives	15
1.2.2	Specific objectives	15
1.3	Methodology	16
1.3.1	Simulations	16
1.3.2	Linear dispersion relation	17
1.3.3	Scope and limitations	18
1.4	Organization of the work	19
1	Introducción	20
1.1	Hipótesis del trabajo	33
1.1.1	Perturbaciones amortiguadas	33
1.1.2	Perturbaciones no-lineales - caso isotérmico	34

1.1.3	Perturbaciones no-lineales - variación de temperatura	34
1.2	Objetivos	35
1.2.1	Objetivos generales	35
1.2.2	Objetivos específicos	35
1.3	Metodología	36
1.3.1	Simulaciones	36
1.3.2	Relación de dispersión lineal	38
1.3.3	Alcance y limitaciones	38
1.4	Organización del trabajo	39
2	Plasma physics kinetic theory and electrostatic waves	41
2.1	Vlasov equation and system of equations	41
2.1.1	Properties of the Vlasov-Poisson system	43
2.2	Linear approach to the Vlasov-Poisson system of equations	44
2.2.1	Linear dispersion relation	45
2.2.2	Linear modes in an electron-ion plasma	47
2.3	Nonlinear phenomena	51
2.3.1	Nonlinear Landau damping	51
2.3.2	BGK states and electron holes	52
2.3.3	Electron hole interaction with heavy ions	55
2.3.4	Ion acoustic solitons	56
3	Basis of the numerical integration and numerical implementation	58
3.1	Normalizations and species scales	58
3.2	Integration of the Vlasov-Poisson system	61
3.2.1	Integration of the electric field	61

3.2.2	Integration of the Vlasov equation	62
3.3	Resolution of the linear dispersion relation	69
3.4	Nonlinear curve fit	70
4	Single wave excitation - Damped perturbations in a Maxwellian electron-ion plasma	71
4.1	Electric field energy and spectra	72
4.2	Behavior in velocity domain	75
4.3	Contribution of each species to the damped oscillations	81
4.4	Summary and discussion	86
5	Single wave excitation - Nonlinear evolution of a Maxwellian electron-ion plasma	90
5.1	Low frequency dynamics in the case of immobile ions	91
5.1.1	Electric field spectra	91
5.1.2	Electrons density and phase space	91
5.2	Comparison between mobile ions and immobile ions for the nonlinear regime	95
5.2.1	Electric field spectrum	95
5.2.2	Frequency filtered electrons density	96
5.2.3	Electrons distribution function	98
5.2.4	Effects on the high velocity range	99
5.3	Low frequency dynamics due to mobile heavy ions	101
5.3.1	Electric field spectrum	102
5.3.2	Low frequency component of the electrostatic potential	102
5.3.3	Evolution of the electrons density	105

5.3.4	Evolution of the heavy ions density	107
5.4	Electron and ion nonlinear structures	110
5.4.1	Local correlations	111
5.4.2	Particle distribution functions	112
5.5	Variation of the amplitude of the initial perturbation ε_e	122
5.5.1	Effects on the amplitude of the ions density	123
5.5.2	Determination of the threshold amplitude ε_e for the localiza- tions in ions density	124
5.6	Summary and discussion	125
6	Single wave excitation - Variation of the initial temperature ratio for nonlinear perturbation in a Maxwellian electron-ion plasma	129
6.1	Electric field spectra	129
6.2	Nonlinear structures propagating in position space	135
6.2.1	Frequency filtered electrostatic potential	135
6.2.2	Particle densities	136
6.3	Phase space structures	145
6.3.1	Electrons distribution	145
6.3.2	Ions distribution	150
6.4	Summary and discussion	164
7	Conclusions	169
7	Conclusiones	176
	Appendices	184

A	Linear dispersion relation calculation	185
A.1	Linear dispersion relation from (2.2.6) to (2.2.8)	185
A.2	Linear dispersion relation from (2.2.8) to (2.2.10)	186
B	Dictionary	190
B.1	Abbreviations	190



List of Figures

1.1	Particle trajectories variations from the equilibrium trajectory, $x_{eq,i}(t) = x_{0,i} + v_{0,i}t$, for a light particle, m_1 , and a heavy particle, m_2 , driven by a LW and a lower amplitude IAW. The particle m_2 does not deviate significantly from its equilibrium trajectory (a). At larger times (b), deviations are not negligible.	2
1.2	Evolution of the excited mode of the electric field, $ E(m = 1) $ for different initial perturbation amplitudes (a) $\varepsilon_e = 1.0 \times 10^{-1}$, (b) $\varepsilon_e = 1.0 \times 10^{-2}$, (c) $\varepsilon_e = 8.0 \times 10^{-3}$ and (d) $\varepsilon_e = 3.0 \times 10^{-3}$, for mobile and immobile ions, with $T_i/T_e = 1.0$. Plots from Xu <i>et al.</i> [27].	6
1.1	Variaciones de trayectorias de partículas respecto del equilibrio, $x_{eq,i}(t) = x_{0,i} + v_{0,i}t$, para una partícula ligera, m_1 , y una partícula pesada, m_2 , impulsadas por una LW y una IAW de baja amplitud. La partícula m_2 no se desvía significativamente con respecto de su trayectoria de equilibrio (a). A tiempos más largos (b), las desviaciones no son despreciables.	21

1.2	Evolución del modo excitado del campo eléctrico $ E(m = 1) $ para diferentes amplitudes de perturbación (a) $\varepsilon_e = 1.0 \times 10^{-1}$, (b) $\varepsilon_e = 1.0 \times 10^{-2}$, (c) $\varepsilon_e = 8.0 \times 10^{-3}$ y (d) $\varepsilon_e = 3.0 \times 10^{-3}$, para iones móviles e inmóviles, con $T_i/T_e = 1.0$. Gráficos cortesía de Xu <i>et al.</i> [27].	26
2.1	Least damped modes that solve the linear dispersion relation of an electrostatic unmagnetized plasma with Maxwellian electrons and ions (2.2.10). Mass ratio $m_i/m_e = 1836.153$ and several temperature ratios. Frequency (a) and damping rate (b) of the Langmuir mode, and frequency (c) and damping rate (d) of the IA mode. The Langmuir branch remains the same for the tested T_i/T_e ratios.	48
2.2	Roots of the linear dispersion relation (2.2.10) corresponding to low frequency higher order modes. Frequency and damping rates for $T_i/T_e = 5.0$ [(a) and (b)], $T_i/T_e = 1.0$ [(c) and (d)] and $T_i/T_e = 0.025$ [(e) and (f)]. Mass ratio $m_i/m_e = 1836.153$. The seven least damped higher order modes are shown for each temperature ratio.	50
2.3	Evolution of the amplitude of the excited mode of the electric field, $m = 1$ in an electron plasma (immobile ions), for linear case, $\varepsilon_e = 1.0 \times 10^{-4}$, the slightly nonlinear damped, $\varepsilon_e = 8.0 \times 10^{-3}$, and the nonlinear case, $\varepsilon_e = 4.0 \times 10^{-2}$, being ε_e the amplitude of the initial perturbation.	51
2.4	Evolution of the electrons distribution function f_e around the resonance zone for nonlinear Landau damping, considering immobile ions.	52

2.5	Schematic distribution function $f_e(E) = f_e(x, v)$ (2.3.1). The solution is centered in the trapping zone, in the range $-\sqrt{v_0^2 + 2\phi} < v < \sqrt{2\phi}$, where ϕ is the normalized electrostatic potential. Figure from Schamel, 1986 [28].	53
2.6	Scheme of the (a) electrostatic potential of amplitude ψ around an electron hole and (b) of the electron phase space with contours of constant energy E , depicting trapped electrons (gray region) and untrapped electrons (white region). Position is measured in electron Debye lengths, λ_{De} , velocity in IA speed, c_S and potential measured in energy per charge, T_e/e . Figure from Zhou and Hutchinson, 2017 [67].	54
2.7	Ion acoustic solitons approaching. The figure depicts the ions density n_i (black dashed line) and the electrostatic potential ϕ (blue solid line). Position is measured in electron Debye lengths, λ_{De} , ions density in the equilibrium density, n_∞ , and potential measured in T_e/e . Figure from Zhou and Hutchinson, 2018 [43].	56
4.1	Evolution of the amplitude of the first mode of the electric field $ \bar{E}_1 $ for (a) $\varepsilon_e = 1.0 \times 10^{-3}$ and (b) $\varepsilon_e = 8.0 \times 10^{-3}$, with and without mobile ions. The damping rates of the observed modes are shown for the LW (red-dashed line) and the IAW (blue-dashed line).	73
4.2	Electric field spectra $ \bar{E}_{k,\omega} $ of $\varepsilon_e = 1.0 \times 10^{-3}$ simulations for (a) high frequency early-range and (b) low frequency later-range. Roots of the linear dispersion relation are shown for comparison.	74

4.3	Electric field spectra $ \bar{E}_{k,\omega} $ of $\varepsilon_e = 8.0 \times 10^{-3}$ simulations for (a) high frequency early-range, (b) high frequency later-range and (c) low frequency later-range (right panel). Roots of the linear dispersion relation are shown for comparison.	75
4.4	Evolution of the variation position-averaged ions distribution function, $\langle \delta \bar{f}_i \rangle_{\bar{x}}$. As references, the phase velocity of the IAW (white dotted line) and the initial resonant velocity (white dashed line) are shown, for $\varepsilon_e = 8.0 \times 10^{-3}$	76
4.5	Details of (a) the initial stage and (b) transition to long-term range of the variations of the position-averaged ions distribution function, $\langle \delta \bar{f}_i \rangle_{\bar{x}}$, for $\varepsilon_e = 8.0 \times 10^{-3}$. The same velocities are plotted.	77
4.6	Sections of the variations of the position-averaged particle distribution function of electrons, $\langle \delta \bar{f}_e \rangle_{\bar{x}}$ [(a), (b) and (c)], and ions, $\langle \delta \bar{f}_i \rangle_{\bar{x}}$ [(d), (e) and (f)], for $\varepsilon_e = 8.0 \times 10^{-3}$. The initial resonant velocity (black dashed-line) and $\bar{v}_{\phi,IA}$ (black dotted-line) are shown.	78
4.7	Variations of the ions density $\delta \bar{n}_i$ during the initial evolution of the plasma. Perturbative amplitude $\varepsilon_e = 8.0 \times 10^{-3}$	79
4.8	Evolution of the variation position-averaged particles distribution function, $\langle \delta \bar{f}_e \rangle_{\bar{x}}$. As references, the phase velocity of the IAW (white dotted line) and one resonant velocity (white dashed line) are shown, for $\varepsilon_e = 8.0 \times 10^{-3}$	80
4.9	Evolution of the position averaged amplitudes $\langle \delta \bar{n}_j^2 \rangle_{\bar{x}}$ of the particle densities for $\varepsilon_e = 1.0 \times 10^{-3}$	82
4.10	Evolution of the position averaged amplitudes $\langle \delta \bar{n}_j^2 \rangle_{\bar{x}}$ of the particle densities for $\varepsilon_e = 8.0 \times 10^{-3}$	82

4.11	Early evolution of the correlations $\langle C [\langle \delta \bar{f}_{e,i} \rangle_{\bar{x}} \langle \delta \bar{f}_{e,m} \rangle_{\bar{x}}] \rangle_{\bar{v}_r}$ over the range $v_r = [0.0, 1.5]$ for $\varepsilon_e = 1.0 \times 10^{-3}$ and 8.0×10^{-3}	83
4.12	Evolution of the correlations $\langle C [\langle \delta \bar{f}_{e,i} \rangle_{\bar{x}} \langle \delta \bar{f}_{e,m} \rangle_{\bar{x}}] \rangle_{\bar{v}_r}$ over the range $v_r = [2.0, 4.0]$ for $\varepsilon_e = 1.0 \times 10^{-3}$ and 8.0×10^{-3}	84
4.13	Spectra of the (a) electric field, $ \bar{E}_{k,\omega} $, (b) electrons density, $ \bar{n}_{e,k,\omega} $, and (c) ions density, $ \bar{n}_{i,k,\omega} $, from the range $0 \leq t\omega_{pe} \leq 200$ for $\varepsilon_e = 1.0 \times 10^{-3}$	85
4.14	Spectra of (a) the electric field, $ \bar{E}_{k,\omega} $, (b) electrons density, $ \bar{n}_{e,k,\omega} $, and (c) ions density, $ \bar{n}_{i,k,\omega} $, from the range $200 \leq t\omega_{pe} \leq 1700$ for $\varepsilon_e = 1.0 \times 10^{-3}$	86
4.15	Spectra of (a) the electric field, $ \bar{E}_{k,\omega} $, (b) electrons density, $ \bar{n}_{e,k,\omega} $, and (c) ions density, $ \bar{n}_{i,k,\omega} $, from the range $0 \leq t\omega_{pe} \leq 200$ for $\varepsilon_e = 8.0 \times 10^{-3}$	87
4.16	Spectra of (a) the electric field, $ \bar{E}_{k,\omega} $, (b) electrons density, $ \bar{n}_{e,k,\omega} $, and (c) ions density, $ \bar{n}_{i,k,\omega} $, from the range $200 \leq t\omega_{pe} \leq 1700$ for $\varepsilon_e = 8.0 \times 10^{-3}$	88
5.1	Spectra of the electric field $ \bar{E}_{k,\omega} $ for $\varepsilon_e = 4.0 \times 10^{-2}$ for the case of immobile ions. Three time intervals are shown.	92
5.2	Evolution of the variation of (a) electrons density, filtered in frequency, $\delta \bar{n}_{e,\text{fil}}$, and its spatial Fourier transform (b) for $\varepsilon_e = 4.0 \times 10^{-2}$, for immobile ions.	93

5.3	Evolution of the variations of the electrons distribution function, $\delta\bar{f}_e$, in the low velocity range with immobile ions for perturbative amplitude $\varepsilon_e = 4.0 \times 10^{-2}$. The velocity of the structures found in Fig.5.2 are shown (black dashed line).	94
5.4	Evolution of the electric field energy \bar{E}_E for the nonlinear case, $\varepsilon_e = 4.0 \times 10^{-2}$	95
5.5	Spectra of the electric field $ \bar{E}_{k,\omega} $ for $\varepsilon_e = 4.0 \times 10^{-2}$ for the case of mobile ions. Three time intervals are shown. Roots of the linear dispersion relation (2.2.10) are shown, corresponding to the IA mode (solid white line) and the least damped higher order mode (dashed white line).	96
5.6	Evolution of the variation of (a) electrons density, filtered in frequency, $\delta\bar{n}_{e,fl}$, and its spatial Fourier transform (b) for $\varepsilon_e = 4.0 \times 10^{-2}$, for mobile ions.	97
5.7	Evolution of the variations of the electrons distribution function, $\delta\bar{f}_e$, in the low velocity range with mobile ions for perturbative amplitude $\varepsilon_e = 4.0 \times 10^{-2}$. The velocity of the structures is shown for each instant (black dashed line).	98
5.8	Velocity averaged correlations between the position averaged variations in the electrons distributions of the case with mobile ions, $\langle\delta\bar{f}_{e,m}\rangle_x$, and immobile ions, $\langle\delta\bar{f}_{e,i}\rangle_x$, $\langle C [\langle\delta\bar{f}_{e,m}\rangle_x, \langle\delta\bar{f}_{e,i}\rangle_x] \rangle_v$. Correlations are averaged over the velocity range $2.0 \leq \bar{v} \leq 5.0$	99

5.9	Sections of the position averaged correlations between the variations of the electrons distributions of the case with mobile ions, $\delta\bar{f}_{e,m}$, and immobile ions, $\delta\bar{f}_{e,i}$, $\langle C[\delta\bar{f}_{e,i}, \delta\bar{f}_{e,m}] \rangle_x$. Perturbative amplitude is $\varepsilon_e = 4.0 \times 10^{-2}$	100
5.10	Phase space of the variations of the electrons distribution function for the case of immobile ions [(a) through (d)] and mobile ions [(e) through (h)], for the trapping region related to the Langmuir mode. Perturbative amplitude is $\varepsilon_e = 4.0 \times 10^{-2}$	101
5.11	Evolution of the variation of (a) the electrostatic potential, filtered in frequency, $\bar{\Phi}_{\text{fil}}$, and its spatial Fourier transform (b) for $\varepsilon_e = 4.0 \times 10^{-2}$, for mobile ions. Time interval corresponding to the localization of the solitary structure in the potential.	103
5.12	Evolution of the variation of (a) the electrostatic potential, filtered in frequency, $\bar{\Phi}_{\text{fil}}$, and its spatial Fourier transform (b) for $\varepsilon_e = 4.0 \times 10^{-2}$, for mobile ions. The time interval considers the initial formation of the solitary structures and further propagation.	104
5.13	Evolution of the variation of (a) the electrons density filtered in frequency, $\delta\bar{n}_{e,\text{fil}}$, and its spatial Fourier transform (b) for $\varepsilon_e = 4.0 \times 10^{-2}$, for mobile ions. The time interval considers the initial formation of the electron cavities.	106
5.14	Spectra of the electrons density $ \delta\bar{n}_{e,k,\omega} $ for $\varepsilon_e = 4.0 \times 10^{-2}$ for the case of mobile ions. Three time intervals are shown. Roots of the linear dispersion relation (2.2.10) are shown, corresponding to the IA mode (solid white line) and the least damped higher order mode (dashed white line).	107

5.15	Evolution of the variation of (a) ions density, $\delta\bar{n}_i$, and its spatial Fourier transform (b) for $\varepsilon_e = 4.0 \times 10^{-2}$. The time interval considers the localization of compressive pulses.	108
5.16	Evolution of the variation of (a) ions density, $\delta\bar{n}_i$, and its spatial Fourier transform (b) for $\varepsilon_e = 4.0 \times 10^{-2}$. The time interval considers the formation of the ion compressive pulses and further propagation.	109
5.17	Spectra of the ions density $ \delta\bar{n}_{i,k,\omega} $ for $\varepsilon_e = 4.0 \times 10^{-2}$ for the case of mobile ions. Three time intervals are shown. Roots of the linear dispersion relation (2.2.10) are shown, corresponding to the IA mode (solid white line) and the least damped higher order mode (dashed white line).	110
5.18	Evolution of $C[\delta\bar{n}_i, \delta\bar{n}_{e,\text{fil}}]$ and the transition to the localization of perturbations in position space. The localization time τ_{loc} is indicated (red dashed line) for $\varepsilon_e = 4.0 \times 10^{-2}$	111
5.19	Phase space portraits of electrons $\delta\bar{f}_e$ [(a) through (d)] and ions $\delta\bar{f}_i$ [(e) through (h)] for $\varepsilon_e = 4.0 \times 10^{-2}$, before the localization of the structures in both densities. Velocity $\bar{v}_{\phi,IA}$ (black dotted line) is indicated.	113
5.20	Evolution of the variations of the position averaged distribution function of ions, $\langle\delta\bar{f}_i\rangle_{\bar{x}}$, around $\bar{v} = \bar{v}_{\phi,IA}$ for $\varepsilon_e = 4.0 \times 10^{-2}$	114
5.21	Evolution of the variations of the position averaged distribution function of electrons, $\langle\delta\bar{f}_e\rangle_{\bar{x}}$, around $\bar{v} = \bar{v}_{\phi,IA}$ for $\varepsilon_e = 4.0 \times 10^{-2}$	115

5.22	Phase space portraits of electrons $\delta\bar{f}_e$ [(a) through (d)] and ions $\delta\bar{f}_i$ [(e) through (h)] for $\varepsilon_e = 4.0 \times 10^{-2}$, during the propagation of the electron cavities and the ion compressive pulses. Velocity $\bar{v}_{\phi,IA}$ (black dotted line) and the electron hole velocity \bar{v}_H (black dashed line) are indicated.	116
5.23	Variations of the low frequency component of the electrons density, $\delta\bar{n}_{e,\text{fil}}$ (black), and ions density, $\delta\bar{n}_i$ (red), for the instants shown in Fig.5.22, considering positive and negative velocities of the distribution functions.	117
5.24	Phase space portraits of electrons $\delta\bar{f}_e$ [(a) through (d)] and ions $\delta\bar{f}_i$ [(e) through (h)] for $\varepsilon_e = 4.0 \times 10^{-2}$, during the propagation of the electron cavities and the ion compressive pulses. Velocity $\bar{v}_{\phi,IA}$ (black dotted line) and the electron hole velocity \bar{v}_H (black dashed line) are indicated.	119
5.25	Variations of the low frequency component of the electrons density, $\delta\bar{n}_{e,\text{fil}}$ (black), and ions density, $\delta\bar{n}_i$ (red), for the instants shown in Fig.5.24, considering only positively propagating structures.	120
5.26	Details of the variations of electrons distribution $\delta\bar{f}_e$ [(a) through (d)], and ions distribution $\delta\bar{f}_i$ [(e) through (h)]. Velocity range $\bar{v}_{\phi,IA} \leq \bar{v} \leq \bar{v}_H$ during the process of acceleration of the primary electron hole. Velocity $\bar{v}_{\phi,IA}$ (black dotted line) and the electron hole velocity \bar{v}_H (black dashed line) are indicated.	121
5.27	Evolution of the position averaged squared amplitude of the ions density, $\langle\delta\bar{n}_i^2\rangle_x$, for different ε_e . The time of localization τ_{loc} (black crosses) is indicated.	123

5.28	Simulation data and curve fit of π_{loc} for the range $1.66 \times 10^{-2} \leq \varepsilon_e \leq 5.0 \times 10^{-2}$. The red dotted lines correspond to the confidence bands of the curve fit, with a 0.85 confidence for the fit.	124
6.1	Evolution of the electric field spectra, $ \bar{E}_{k,\omega} $, for $\bar{T}_i = 1.0$ [(a) through (c)], 0.2 [(d) through (f)] and 0.025 [(g) through (i)], for three time intervals (rows). Perturbative amplitude $\varepsilon_e = 4.0 \times 10^{-2}$. The respective IA mode (solid white line) and higher order linear modes (dashed white line) from the linear dispersion relation are shown. For $\bar{T}_i < 1.0$, the higher order modes show the boundaries of the excited region. . .	130
6.2	Evolution of the electric field spectra, $ \bar{E}_{k,\omega} $, for temperature ratios $\bar{T}_i = 5.0$ [(a) through (c)], 1.8 [(d) through (f)] and 1.0 [(g) through (i)]. The respective IA mode (solid white line) and the least damped higher order linear modes (dashed white line) from the linear dispersion relation are shown. Perturbative amplitude $\varepsilon_e = 4.0 \times 10^{-2}$	132
6.3	Comparison of the electric field spectra, $ \bar{E}_{k,\omega} $, between the case of immobile ions [(a), (c) and (e)] and the case of mobile ions with initial temperature ratio $\bar{T}_i = 5.0$ [(b), (d) and (f)]. Perturbative amplitude $\varepsilon_e = 4.0 \times 10^{-2}$	133

6.4	Comparison of the electric field spectra, $ \bar{E}_{k,\omega} $, between the case of immobile ions [(a), (c) and (e)] and the case of mobile ions with initial temperature ratio $\bar{T}_i = 5.0$ [(b), (d) and (f)]. Three long term time intervals are considered. The respective IA mode (solid white line) and the least damped higher order linear mode (dashed white line) from the linear dispersion relation are shown. Perturbative amplitude $\varepsilon_e = 4.0 \times 10^{-2}$	134
6.5	Evolution of the frequency filtered electrostatic potential, $\bar{\Phi}_{\text{fil}}$, for temperature ratios (a) $\bar{T}_i = 1.0$, (b) 0.2 and (c) 0.025. Perturbative amplitude $\varepsilon_e = 4.0 \times 10^{-2}$	136
6.6	Evolution of the frequency filtered electrostatic potential, $\bar{\Phi}_{\text{fil}}$, for temperature ratios (a) $\bar{T}_i = 5.0$, (b) 1.8 and (c) 1.0. Perturbative amplitude $\varepsilon_e = 4.0 \times 10^{-2}$	137
6.7	Evolution of variations of the ions density, $\delta\bar{n}_i$, for temperature ratios (a) $\bar{T}_i = 1.0$, (b) 0.1 and (c) 0.025. Perturbative amplitude $\varepsilon_e = 4.0 \times 10^{-2}$	138
6.8	Evolution of variations of the ions density, $\delta\bar{n}_i$, for temperature ratios (a) $\bar{T}_i = 5.0$, (b) 1.8 and (c) 1.0. Perturbative amplitude $\varepsilon_e = 4.0 \times 10^{-2}$	139
6.9	Evolution of variations of the electrons density filtered in frequency, $\delta\bar{n}_{e,\text{fil}}$, for temperature ratios (a) $\bar{T}_i = 1.0$, (b) 0.1 and (c) 0.025. Perturbative amplitude $\varepsilon_e = 4.0 \times 10^{-2}$	140
6.10	Evolution of variations of the electrons density filtered in frequency, $\delta\bar{n}_{e,\text{fil}}$, for temperature ratios (a) $\bar{T}_i = 5.0$, (b) 1.8 and (c) 1.0. Perturbative amplitude $\varepsilon_e = 4.0 \times 10^{-2}$	141

6.11	Evolution of variations of the ions density, $\delta\bar{n}_i$, for temperature ratio $\bar{T}_i = 0.025$. Perturbative amplitude $\varepsilon_e = 4.0 \times 10^{-2}$. Long term time interval.	142
6.12	Evolution of variations of the electrons density filtered in frequency, $\delta\bar{n}_{e,\text{fil}}$, for temperature ratio $\bar{T}_i = 0.025$. Perturbative amplitude $\varepsilon_e = 4.0 \times 10^{-2}$. Long term time interval.	142
6.13	Evolution of variations of the ions density, $\delta\bar{n}_i$, for temperature ratio $\bar{T}_i = 5.0$. Perturbative amplitude $\varepsilon_e = 4.0 \times 10^{-2}$. Long term time interval.	143
6.14	Evolution of variations of the electrons density filtered in frequency, $\delta\bar{n}_{e,\text{fil}}$, for temperature ratio $\bar{T}_i = 5.0$. Perturbative amplitude $\varepsilon_e = 4.0 \times 10^{-2}$. Long term time interval.	143
6.15	Evolution of the amplitude of the position averaged squared variations of the ions density $\langle\delta\bar{n}_i^2\rangle_{\bar{x}}$ for temperature ratios from $\bar{T}_i = 0.025$ to $\bar{T}_i = 5.0$. Perturbative amplitude $\varepsilon_e = 4.0 \times 10^{-2}$	144
6.16	Initial evolution of the variations of the ions density $\delta\bar{n}_i$ for all the tested temperature ratios. Perturbative amplitude $\varepsilon_e = 4.0 \times 10^{-2}$. . .	145
6.17	Evolution of variations of the electrons distribution function, $\delta\bar{f}_e$, for temperature ratios $\bar{T}_i = 1.0$ [(a), (d), (g) and (j)], $\bar{T}_i = 0.2$ [(b), (e), (h) and (k)] and $\bar{T}_i = 0.025$ [(c), (f), (i) and (l)], at four instants. The respective IA speed (black dotted line) and the speed of the trapping region (black dashed line) are shown. Perturbative amplitude $\varepsilon_e = 4.0 \times 10^{-2}$	146

6.18	Early instants of the evolution of variations of the electrons distribution function, $\delta\bar{f}_e$, for temperature ratios $\bar{T}_i = 1.0$ [(a), (d), (g) and (j)], $\bar{T}_i = 0.2$ [(b), (e), (h) and (k)] and $\bar{T}_i = 0.025$ [(c), (f), (i) and (l)], at four instants. The respective IA speed (black dotted line) is shown. Perturbative amplitude $\varepsilon_e = 4.0 \times 10^{-2}$	147
6.19	Evolution of variations of the electrons distribution function, $\delta\bar{f}_e$, for temperature ratios $\bar{T}_i = 5.0$ [(a), (d), (g) and (j)], $\bar{T}_i = 1.8$ [(b), (e), (h) and (k)] and $\bar{T}_i = 1.0$ [(c), (f), (i) and (l)], at four instants. The respective IA speed (black dotted line) and the speed of the trapping region (black dashed line) are shown. Perturbative amplitude $\varepsilon_e = 4.0 \times 10^{-2}$	149
6.20	Comparison of the variations of the electrons distribution function, $\delta\bar{f}_e$, between the cases of immobile ions [(a) through (d)] and temperature ratio $\bar{T}_i = 5.0$ [(e) through (h)]. Perturbative amplitude $\varepsilon_e = 4.0 \times 10^{-2}$	150
6.21	Half of the equilibrium distribution function of the ions distribution, $\bar{f}_{0,i}$, for different temperature ratios \bar{T}_i . The respective speed $\bar{v}_{\phi,IA}$ is shown (dashed line of the respective color).	151
6.22	Sections of the position averaged variations of the ions distribution function $\langle\delta\bar{f}_i\rangle_{\bar{x}}$ (upper row) and of the ions kinetic energy distribution $\langle\delta\bar{w}_i\rangle_{\bar{x}}$ (lower row) for temperature ratios $\bar{T}_i = 1.0$ [(a) and (b)], 0.2 [(c) and (d)] and 0.025 [(e) and (f)], during the beginning of the simulation. The respective IA speeds are shown. Perturbative amplitude $\varepsilon_e = 4.0 \times 10^{-2}$	152

6.23	Sections of the position averaged variations of the ions distribution function $\langle \delta \bar{f}_i \rangle_{\bar{x}}$ (upper row) and of the ions kinetic energy distribution $\langle \delta \bar{w}_i \rangle_{\bar{x}}$ (lower row) for temperature ratios $\bar{T}_i = 5.0$ [(a) and (b)], 1.8 [(c) and (d)] and 1.0 [(e) and (f)]. The respective IA speeds (black dotted line) are shown. Perturbative amplitude $\varepsilon_e = 4.0 \times 10^{-2}$	153
6.24	Sections of the position averaged variations of the ions distribution function $\langle \delta \bar{f}_i \rangle_{\bar{x}}$ (upper row) and of the ions kinetic energy distribution $\langle \delta \bar{w}_i \rangle_{\bar{x}}$ (lower row) for temperature ratios $\bar{T}_i = 1.0$ [(a) and (b)], 0.2 [(c) and (d)] and 0.025 [(e) and (f)]. The respective IA speeds are shown. Perturbative amplitude $\varepsilon_e = 4.0 \times 10^{-2}$	155
6.25	Sections of the position averaged variations of the ions distribution function $\langle \delta \bar{f}_i \rangle_{\bar{x}}$ (upper row) and of the ions kinetic energy distribution $\langle \delta \bar{w}_i \rangle_{\bar{x}}$ (lower row) for temperature ratios $\bar{T}_i = 1.0$ [(a) and (b)], 0.2 [(c) and (d)] and 0.025 [(e) and (f)]. The respective IA speeds are shown. Perturbative amplitude $\varepsilon_e = 4.0 \times 10^{-2}$	156
6.26	Phase space plots of the variations of the ions distribution, $\delta \bar{f}_i$ and their corresponding variations in particle density, $\delta \bar{n}_i$, for $\bar{T}_i = 5.0$ [(a) through (d)], 1.0 [(e) through (h)] and 0.025 [(i) through (l)], for three instants during the damping of $\delta \bar{n}_i$ with $\bar{T}_i = 5.0$. Perturbative amplitude $\varepsilon_e = 4.0 \times 10^{-2}$. Mass ratio is $\bar{m}_i = 1836.153$	158

- 6.27 Evolution of variations of the ions distribution function, $\delta \bar{f}_i$, for temperature ratios $\bar{T}_i = 1.0$ [(a), (d), (g) and (j)], $\bar{T}_i = 0.2$ [(b), (e), (h) and (k)] and $\bar{T}_i = 0.025$ [(c), (f), (i) and (l)], at four instants. The respective IA speed (black dotted line) and the speed of the trapping region (black dashed line) are shown. Perturbative amplitude $\varepsilon_e = 4.0 \times 10^{-2}$. Mass ratio is $\bar{m}_i = 1836.153$ 160
- 6.28 Evolution of variations of the ions distribution function, $\delta \bar{f}_i$, and of the electrons distribution function, $\delta \bar{f}_e$, for temperature ratio $\bar{T}_i = 0.025$ during the formation of secondary holes from the primary hole. The respective IA speed (black dotted line) is shown. Perturbative amplitude $\varepsilon_e = 4.0 \times 10^{-2}$. Mass ratio is $\bar{m}_i = 1836.153$ 161
- 6.29 Evolution of variations of the ions distribution function, $\delta \bar{f}_i$, and of the electrons distribution function, $\delta \bar{f}_e$, for temperature ratio $\bar{T}_i = 0.025$ during the formation of the primary electron hole. The respective IA speed (black dotted line) is shown. Perturbative amplitude $\varepsilon_e = 4.0 \times 10^{-2}$. Mass ratio is $\bar{m}_i = 1836.153$ 162
- 6.30 Evolution of variations of the ions distribution function, $\delta \bar{f}_i$, for temperature ratios $\bar{T}_i = 5.0$ [(a), (d), (g) and (j)], $\bar{T}_i = 1.8$ [(b), (e), (h) and (k)] and $\bar{T}_i = 1.0$ [(c), (f), (i) and (l)], at four instants. The respective IA speed (black dotted line) and the speed of the trapping region (black dashed line) are shown. Perturbative amplitude $\varepsilon_e = 4.0 \times 10^{-2}$. 164

ACKNOWLEDGEMENTS

Quiero agradecer a las personas que permitieron que este trabajo pudiera realizarse y llevarse a término. Por un lado, quiero agradecer a mi familia, que estuvo apoyándome, en especial a mis padres que trabajaron ardua y esforzadamente para que pudiera realizar no sólo esta tesis sino que también para que pudiera llegar a esta instancia de mi vida, y por enseñarme la importancia de estudiar.

Agradezco a mis tutores en esta etapa final de mis estudios. Al profesor Jaime Araneda, por sus ideas, su experiencia, la agudeza de sus análisis y su comprensión. Al profesor Roberto Navarro, en quien ha sido un gran ser humano y un ejemplo a seguir.

De consideración especial, quiero agradecer a mis amigos, que han sido un apoyo vital en varios aspectos y también han sido un gran cable a tierra, especialmente durante el magíster.

Agradezco a los funcionarios de la Universidad de Concepción por su inmensa disposición y paciencia, particularmente durante estos tiempos de pandemia y al final esta etapa.

Agradezco al Ministerio de Educación de Chile por financiar las becas de Excelencia Académica, Bicentenario y Gratuidad que recibí, al señor Gonzalo Pincheira, quien financió gran parte de mis estudios en mi primera carrera, y a la Universidad

de Concepción por la beca de Articulación pregrado-postgrado. Esto le permitió a mi familia y a mí librarnos de preocupaciones económicas a causa de mis estudios. Así mismo, agradezco a quienes lograron poner en la mesa el problema educacional en este país. Es cierto que no está resuelto, pero esos pequeños avances han permitido a más personas, entre quienes me incluyo, poder acceder a la educación superior y continuar sus estudios sin que el financiamiento sea un obstáculo.

También quiero agradecer a Alexandra Elbakyan, por su loable contribución a hacer el conocimiento más accesible al mundo.

Finalmente, agradezco a ANID, Chile, por la Beca Nacional de Magíster 2018 Nro. 22182152 del presente autor, el proyecto FONDECYT Nro. 1180947 de Roberto Navarro Maldonado, Nro. 116170 de Jaime Araneda Sepúlveda, y CONICYT-PAI Nro. 9170095 de Roberto Navarro Maldonado.



Abstract

In order to study how the dynamics of an unmagnetized Maxwellian electron plasma is modified by the presence of mobile positive heavy ions, the present work aims to study the regimes of damped and nonlinear perturbations in a driftless Maxwellian electron-ion plasma, considering a mass ratio $m_i/m_e = 1836.153$ and charge ratio $q_i/|q_e| = 1.0$, specifically in the range of low frequencies ($\omega_r \leq 0.2\omega_{pe}$) and velocities in the order of the ion acoustic phase velocity $v_{\phi,IA}$ for the excited wavenumber, primarily for the temperature ratio $T_i/T_e = 1.0$. Also, the response of the plasma is studied for different temperature ratios T_i/T_e above and below $T_i/T_e = 1.0$. The whole study is accomplished through numerical simulations of the Vlasov-Poisson system of equations using spectral interpolation in position and velocity, and symplectic integration in the time dependency. It is expected that in the case of damped perturbations both Langmuir and ion acoustic waves propagate relatively independent from each other and exhibit opposite behaviors in the velocity range of interest, whereas in the nonlinear case, electrostatic solitary waves are expected to arise due to the presence of heavy mobile ions related to electron trapping and ion acoustic solitons. It is expected that dynamics related to the ions is accentuated with lower ratios T_i/T_e .

Resumen

Para estudiar cómo se modifica la dinámica de un plasma Maxwelliano de electrones no magnetizado con la presencia de iones positivos pesados, el presente trabajo tiene por objetivo estudiar los regímenes amortiguado y no lineal de perturbaciones en un plasma Maxwelliano electrón-ión sin deriva relativa considerando una razón de masa $m_i/m_e = 1836.153$ y razón de carga $q_i/|q_e| = 1.0$, específicamente en el rango de bajas frecuencias ($\omega_r \leq 0.2\omega_{pe}$) y velocidades del orden de la velocidad de fase de ondas ión acústicas $v_{\phi,IA}$ para el número de onda excitado, principalmente para la razón de temperatura $T_i/T_e = 1.0$. También se estudia la respuesta del plasma para diferentes razones de temperatura T_i/T_e por encima y por debajo de $T_i/T_e = 1.0$. Todo el estudio se realiza por medio de simulaciones numéricas del sistema de ecuaciones de Vlasov-Poisson usando interpolación espectral en posición y velocidad, e integración simplética en la dependencia temporal. Se espera que en el caso de perturbaciones amortiguadas se espera que las ondas de Langmuir e ión-acústicas se propaguen relativamente independientes una de la otra y que exhiban un comportamiento opuesto en el rango de velocidades de interés, mientras que en caso no lineal, se espera que surjan ondas electrostáticas solitarias debido a la presencia de iones móviles, asociadas a atrapamiento de electrones y solitones ión-acústicos. Se espera que la dinámica asociada a los iones se acentúe con razones T_i/T_e más bajas.

1 Introduction

In the investigation of plasma waves approximations are made depending on the masses of the composing species, the spatial, time, and velocity scales of the phenomena of interest. While in some cases the lightest species are moved only, the addition of a mobile heavy species to the plasma might yield a more realistic model. It has been demonstrated that the presence of positively charged, Maxwellian-distributed, heavy mobile ions (protons) modifies evolution of an unmagnetized, collisionless, plasma during linear Landau damping of Langmuir waves in initially isothermal Maxwellian electron collisionless plasmas, exploring particle densities and field energy, but without exploring velocity dependency was not discussed. In the nonlinear regime of the same plasma, the amplitude of the excited mode indicates that the effects of mobile ions are reduced. However, this fact does not discard any dynamics related to the ions scales. Therefore, the present work addresses the issue of how the presence of mobile heavy positively charged ions modifies the dynamics of an unmagnetized electron Maxwellian plasma in the range of the ions scales for both damped and nonlinear perturbations, and to characterize the phenomena arisen by the introduction of such heavy species.

From the equations of motion of any particle j of the plasma, the time scale of

its dynamics is estimated as $\tau_j \sim m_j$, where m_j is the mass of a particle of the species j . Therefore, the motion of heavier species occurs on a longer time scale. The existence of different time scales can be observed in Fig.1.1, where the trajectories of two particles of mass $m_1 = m_e$ and $m_2 = 1836m_e$, with m_e the electron mass, are shown. Both are simultaneously subjected to the force due to a Langmuir wave (LW), of short time scale, and a lower amplitude ion acoustic wave (IAW), of large time scale, with the same wavenumber. The light particle is resonant with the Langmuir wave and the heavy particle is resonant with the IAW. Figure 1.1(a) shows that the motion of the heavy particle can be neglected during a short range of time and the low frequency forcing remains negligible.

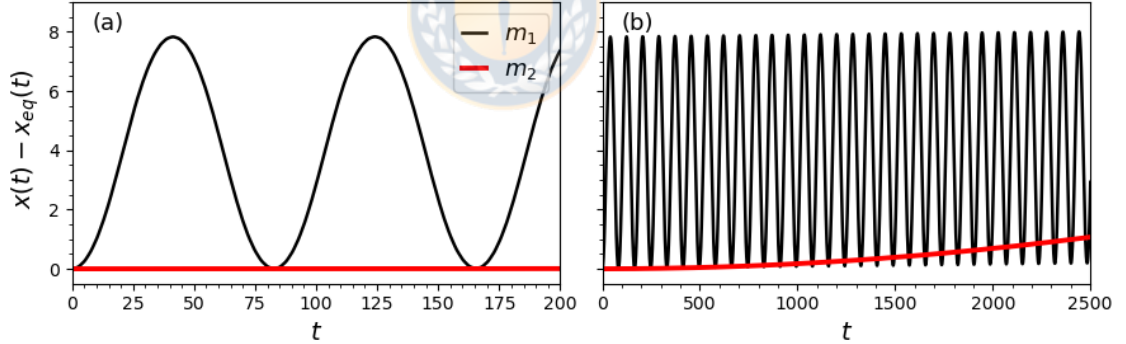


Figure 1.1: Particle trajectories variations from the equilibrium trajectory, $x_{eq,i}(t) = x_{0,i} + v_{0,i}t$, for a light particle, m_1 , and a heavy particle, m_2 , driven by a LW and a lower amplitude IAW. The particle m_2 does not deviate significantly from its equilibrium trajectory (a). At larger times (b), deviations are not negligible.

The approximation of immobile heavy species considers light particles as mobile and the remaining species are assumed to be infinitely heavy and static, as in the case of a typical electron and ion plasma. Ions can be uniformly or non-uniformly distributed. Plenty of studies use this approximation with uniform ions, address-

ing phenomena whose frequency and velocity ranges are such that heavy species do not contribute to the evolution of the plasma, achieving good agreement with experiments and observations: works as fundamental as those concerning the collisionless linear and nonlinear Landau damping of LWs in electron plasmas [1–7], assume immobile ions, with experimental works confirming the predicted behavior [8]. In critical phenomena in plasma physics [9], it has been demonstrated that the presence of mobile ions does not affect the critical behavior of the Landau damping of Langmuir waves [10]. Other works considering immobile ions focus on the propagation of nonlinear phase space states such as BGK waves, analytical solutions of the Vlasov-Poisson system, consisting of quasi-stationary electrostatic structures involving particle trapping [11], such as electron holes [12], or the broadband electrostatic noise in terrestrial and planetary magnetospheres, in which the plasma is modeled by hot and cold electron cores, and an electron beam, in order to excite nonlinear electron acoustic modes[13].

However, certain phenomena may take place in longer time scales and the dynamics of heavy species is not negligible, as shown in Fig.1.1(b). In such cases, the heaviest species dynamics must be included in the system of equations, as their presence might modify the observed dynamics, yielding a more complete description of the actual phenomenon or introduce additional phenomena, unnoticed on short time scales. In the context of laser experiments, for example, in testing nuclear fusion configurations such as inertial confinement fusion plasmas, in which laser light is directed to a target inside a cavity to ignite it [14]. The process involves a stimulated Brillouin scattering instability in which an incoming electromagnetic wave, produced by a laser, decays into an IAW and a backscattered electromagnetic wave [15]. Such

a process is undesirable in inertial confinement fusion as a fraction of the radiation sent to the target is reflected. Several mechanisms related to the IAW component have been proposed to reduce this instability, in order to reduce reflection and increase absorption of electromagnetic waves, such as the excitation of ion trapping [16], ion distribution heating [17], ion Landau damping [18], the addition of multiple ion species to enhance ion Landau damping [19], and saturation through two-ion parametric decays [20].

In astrophysical plasmas, *in situ* measurements of electric fields and spectra made by Freja satellite and SCIFER sounding rocket in the terrestrial auroral region indicate that the modulation of Langmuir wave packets observed therein, corresponding to narrow band emissions, is explained by scattering of whistler and lower hybrid modes, related to proton dynamics; these waves must be included to account for low frequency signals found in the modulation process [21]. *In situ* measurements in the parallel auroral acceleration region made by FAST satellite in 1997 indicate the presence of frequency peaks around 300[Hz], corresponding to the range of the hydrogen ion acoustic frequency, would modulate the amplitude of electron acoustic wave packets [22].

Low frequency waves are also found directly in solar wind plasmas, related to the so called type III solar sources, discovered in 1950, which correspond to radioemissions proceeding from solar bursts, that would indicate the presence of nonthermal electron beams in the solar wind itself, as well as in the solar system, providing information of conditions of the background medium, and of acceleration and transport of electrons [23]. Spectral observations from Galileo spacecraft in 1990 indicate the ex-

istence of three strong peaks, two of high frequencies close to 24[kHz], corresponding to Langmuir waves, and one of low frequency around 400[Hz], identified as IAWs [24].

The generating mechanism of type III radioemissions has been discussed by Cairns [25], led by discrepancies between observations and theoretical works. Two possible mechanisms have been considered, the nonlinear resonant wave-wave coupling Langmuir electrostatic decay, consisting of the decay of a primary LW into a secondary LW and a IAW, and scattering of thermal ions, in which individual ions and their screening electron cloud responses are out of phase due to their mass difference, producing the scattering of incoming LWs [26]. It is argued that in order for the scattering to occur, the collective ion response must be inhibited. Such inhibition takes place if the time scale of this response is short compared to that of the scattering, and if the time scale of the scattering is much larger than the time scale of the slowest process and lasts several cycles [25]. According to measurements, the energy levels required for the scattering are not possible, and in regions with electric field energy density to plasma thermal energy ratio $W \lesssim 10^{-5}$, Langmuir decay is expected to be related to type III radioemissions; the scattering of thermal ions would be relevant only in regions with $W \lesssim 10^{-3}$.

Electron oscillations have been studied in the presence of mobile heavy positive ions through kinetic simulations in unmagnetized plasmas. Xu *et al.* [27] studied the linear regime of Landau damping in a collisionless Maxwellian electron and ion plasma, by exciting the first mode only. In this work, it is found that ions ($m_i/m_e = 1836$), initially isothermal species $T_i/T_e = 1.0$ with $q_i/|q_e| = 1.0$, notoriously affect the linear damping, observed in the amplitude of the excited mode

($|E(m = 1)|$) in Fig.1.2. For initial amplitudes of perturbation of the electrons distribution (ε_e) in the damped regime [Figs.1.2 (c) and (d)], the usual linear Landau damping (compared to the case of immobile ions) occurs up to $t \simeq 100$, when slow damped oscillations become dominant and an important deviation from the case with immobile ions is observed.

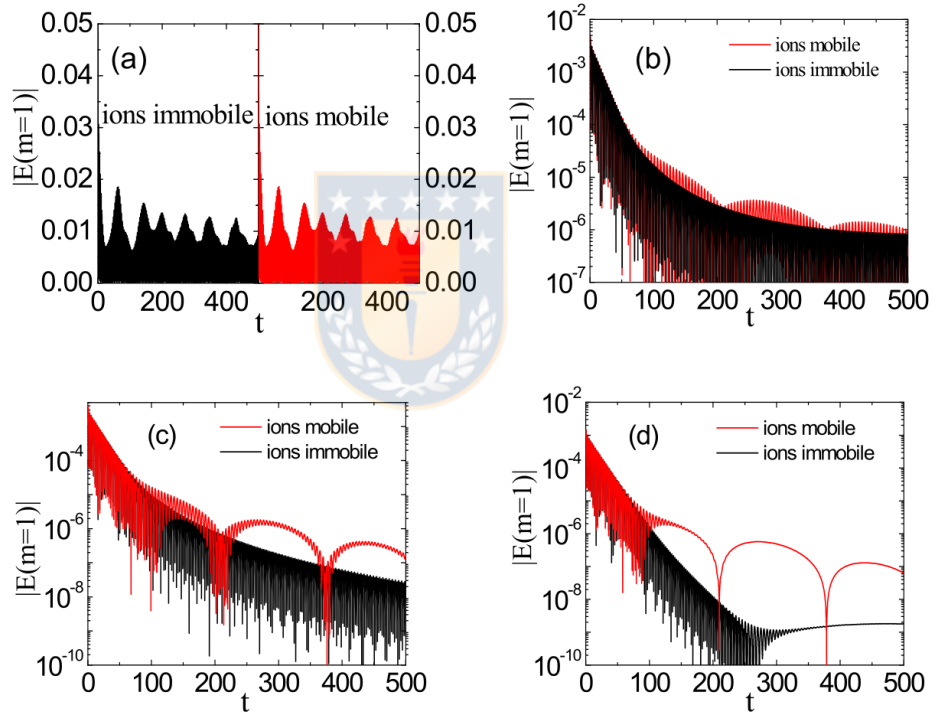


Figure 1.2: Evolution of the excited mode of the electric field, $|E(m = 1)|$ for different initial perturbation amplitudes (a) $\varepsilon_e = 1.0 \times 10^{-1}$, (b) $\varepsilon_e = 1.0 \times 10^{-2}$, (c) $\varepsilon_e = 8.0 \times 10^{-3}$ and (d) $\varepsilon_e = 3.0 \times 10^{-3}$, for mobile and immobile ions, with $T_i/T_e = 1.0$. Plots from Xu *et al.* [27].

Two kind of waves are identified: a LW, with frequency and damping rate estimated through linear Vlasov-Poisson dispersion relation, and an IAW, with frequency

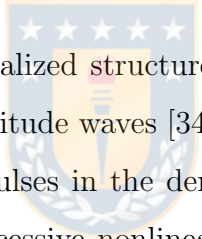
estimated with the fluid approximation and damping rate estimated through linear Vlasov-Poisson dispersion relation. As the frequency of $|E(m = 1)|$ changes, variations of the electrons density, δn_e , become of the same order compared to those of the ions density, δn_i , and exhibit the same dependency in position and time domain with low frequency oscillations for $t > 100$, indicating that electrons ultimately follow the motion of the ions. However, details of the velocity dependency about the resonance zones involved in the propagation of those waves, and how each species of the plasma contributes to their development are not studied in Xu *et al.* work.

At perturbative amplitudes well above the critical amplitude to excite nonlinear Landau damping of LWs [see Fig.1.2 (a)], fast oscillations are dominant and ion dynamics is not distinguishable through the evolution $|E(m = 1)|$. Although in Ref.[27] it is stated that ion perturbations may occur, they would be negligible in comparison with those of the electrons, and no further discussion is provided.

Nonlinear, long-lasting, coherent structures in position space and phase space have been observed in the presence of mobile heavy positive ions in unmagnetized collisionless Maxwellian electron and ion plasmas, such as ion holes, solitons, as well as ion interactions with electrons structures of the same nature, such as electron holes.

An ion hole consists of ions trapped around a local minimum of electrostatic potential [12, 28], repelling electrons around it. In this case, electrons are Boltzmann distributed, meaning that they respond so rapidly that they develop instantaneous equilibrium configurations, and it is required for them to be hot enough to pro-

duce pressure to sustain the depopulation of ions at the center of the structure [29]. They have been measured with high resolution in the Earth's auroral region by FAST spacecraft, propagating with velocity consistent with the IA mode [30], and also found in Vlasov-Poisson simulations of unmagnetized Maxwellian electron and ion beam plasmas initially exciting a slow electron hole, after the growth of several smaller electron holes, considering a low mass ratio ($m_i/m_e = 4$) [31]. Other configurations that yield an ion hole are setting this state directly at the initial instant in the ions distribution in simulations [32], ion-ion two-stream instability [33], and generally unstable configurations involving streaming populations of ions [29].



Solitons are defined as localized structures propagating without loss or dispersion, evolving from large amplitude waves [34], and are observed in the electrostatic potential or as compressive pulses in the density of the species driving the propagation, which result from successive nonlinear coupling between the excited waves limited by the dispersion of waves whose phase of velocity importantly differs from that of the fundamental wave [35]. Ion acoustic solitons (IASs) are considered. These structures are observed in the ions density involving IAWs [36]. Based on the fluid model, they are found to propagate at velocities v_S in the range $1 < v_S/c_S \lesssim 1.6$ [35], where c_S is the ion acoustic speed in the fluid model. Kinetic features have been further included in the model, such as ion and electron Landau damping, and electron trapping [37]. Simulation studies using hybrid models (kinetic ions, Boltzmann electrons) and fully kinetic models, show that IASs might not always retain their characteristics unaltered: unstable IASs might break into several IAWs [38], or grow in amplitude for large initial perturbations [39]. Properties such as the velocity of propagation can be modified by electron trapping. Further differences are noted

for velocities of propagation larger than c_S [40]. This implies that solitons interact and even couple to electron holes, as reported in several studies [41–45], propagating with velocities in the range indicated above. However, a certain perturbation in the ions density is required for solitons to arise and couple [43]. Other works involving electron hole-ion soliton coupling still label the soliton component as IASs although it propagates with velocity $v_S = 4.06c_S$, out of the predicted range [46].

Hutchinson and Zhou developed a theory for the propagation of accelerating electron holes considering interaction with heavy ionic species from a kinematic approach, focusing on momentum exchange [47, 48]. In this case, ions interact with the hole by exchanging momentum through reflection if the trapping potential is intense enough, and passing through it in the opposite case, tending to accumulate ions in the region of lower electron density. Through simulations with nonzero drift, mass ratio $m_i/m_e = 1836$ and a temperature ratio $T_i/T_e = 2.5 \times 10^{-2}$, the authors observe the same coupling between electron holes and ion solitons discussed by Saeki and Rasmussen [44] and Saeki and Genma [45]. They also show that holes rapidly react to changes in the distribution of the ions. For faster electron holes, the degree of interaction with ions is relatively smaller and can be neglected [48].

Works involving Maxwellian electron and ion plasmas with a relative drift, $m_i/m_e = 1836$ and $T_i/T_e = 0.1$, have shown that slow electron holes interact with the distribution of the ions, tending to produce localized perturbations in the latter, as in the context of subcritical plasma turbulence, where it has been shown that the excitation of an electron hole in conditions of linear stability may lead to the excitation of nonlinear electron holes due to the dependency of the initial perturbation [46,

49]. The excited electron hole is observed to accelerate to velocities faster than c_s as IAWs are excited in the ions density, attributed to IASs. It is shown that faster holes in this velocity range propagate stably [49], and it is indicated that the hole allows for bunching of ions within the trapping region, as discussed by Hutchinson and Zhou [47].

Considering the same system with a low mass ratio, $m_i/m_e = 4$, a relative drift and initially isothermal species, but addressing the mechanism of excitation of current driven IAWs in collisionless plasmas, Lesur *et al.* [31] excite nonlinear modes related to phase space structures which involve momentum and energy exchange. The development of slow primary electron holes eventually leads to the generation of secondary, smaller holes, yielding phase space turbulence with an ensemble of structures, as the primary one leaves a trail of negative density as it is accelerated. The electron holes are reported to grow more easily when there is more overlap between both species distributions.

For higher mass ratio, $m_i/m_e = 29500$, drifting, and initially isothermal species, Eliasson and Shukla [50] studied the interaction of electron holes with the plasma through Vlasov-Poisson simulations of a Maxwellian electron-oxygen ion plasma by initializing electrons with a static Schamel hole. The positive potential developed by the hole expels low energy ions, producing a cavity in the ions density, and therefore a negative potential which eventually repels the hole away, with the ion cavity remaining static.

The temperature ratio between species is an important parameter in plasma

physics. In the linear approximation, the damping rate and propagation of IAWs in Maxwellian electron and ion plasmas depend directly on T_i/T_e . The IAWs are favored by cold ions, as the damping rate tends to zero [51], due to the lack of resonant ions available for wave-particle interaction. On the contrary, as this ratio tends to the unity, the wave is heavily damped for any wavenumber, because there are more ions available for such interaction. In the work of Norgren *et al.* [52], the linear dispersion relation is used to characterize linear instabilities in a Maxwellian electron and ion plasma with an electron beam, in the context of electrostatic solitary waves in the magnetosphere. They show that for higher T_i/T_e the condition of marginal instability is displaced to larger beam speed because a larger population of ions is available at lower velocities, damping waves due to resonant interaction.

Measurements in space plasmas indicate that the temperature ratio varies depending on the observed region. On the magnetotail, measurements made by Cluster spacecraft on slow electron holes, capable of interaction with surrounding ions, are explained with plasmas composed by species with relative drift whose temperature ratio is in the range $0.89 \leq T_i/T_e \leq 1.78$ [53]. In zones related to the solar wind, temperature varies in a wide range, $0.1 \leq T_i/T_e \leq 2.0$ [23] and it has been found that nonlinear IAWs generated by streaming electron-ion plasmas tend to be observed with higher amplitudes for lower ratios [54].

The use of a high temperature ratio can modify the coupling between IASs and electron holes. Zhou *et al.* reported that the coupling is disrupted for high temperature ratios, $T_i/T_e > 1$, as more ions are available in the resonance zone, hence ion Landau damping becomes stronger and the soliton decays, yielding a free electron

hole [43]. In the investigation of electrostatic instabilities, in the context of broadband and narrowband electrostatic noise signals obtained by the Geotail spacecraft, Omura *et al.* [55] studied simulations of bi-stream instability, using an ion core with an electron beam with mass ratio $m_i/m_e = 100$, finding that hot ions yield electrostatic solitary waves, whereas for cold ions lead the electrostatic potential to decay into several IAWs.

In the light of this exposition, the same configuration in the work of Xu *et al.* is used in this work to study further effects of mobile, heavy, positively charged ions in an unmagnetized, collisionless, Maxwellian electron and ion plasma without relative drift, for the cases of damped and nonlinear perturbations. For the former, it is proposed to study the velocity dependency of both species around the resonance zones with an emphasis on lower velocities, around the phase velocity of the excited IAW, $v_{\phi,IA}$, and how each of the composing species is affected by the propagation of both waves.

In the nonlinear case, although several of the previously described works involve relative drift between the electron and ion distributions, it is interesting to determine whether the energy injected by a large amplitude initial monochromatic perturbation in the plasma allows for the development of nonlinear dynamics in the distribution of the ions. If such nonlinear behavior does occur, it is proposed to study the structures and waves that might develop, their interaction with the electrons distribution, the effect of the observed waves on each of the resonant regions in velocity space, and how microscopic and macroscopic quantities, other than the electric field energy, are affected by their motion.

Due to the relevance of the temperature ratio in the dynamics in an electron and ion plasma in the nonlinear regime, it is of interest to determine the response of the plasma as the temperature ratio T_i/T_e is varied with respect to the isothermal case, as waves related to collective response of ions are reported to be affected by this ratio.

1.1 Hypotheses of the work

According to the previously discussed topics and the proposed work, the following hypotheses are considered. All of them are applied on collisionless, unmagnetized, driftless plasmas composed by Maxwellian electrons and heavy ions with mass ratio $m_i/m_e = 1836.153$ and charge ratio $q_i/|q_e| = 1.0$.

1.1.1 Damped perturbations

For the case of amplitudes lower than the critical amplitude for exciting nonlinear Landau damping of Langmuir waves (ε_C), **(i)** a resonance zone is expected to be found around $v_{\phi,IA}$ for the excited k in the distribution function of each species. In such a resonance region, **(ii)** both electrons and ions should exhibit opposite behavior in velocity space, as predicted by the linear theory. **(iii)** The waves found by Xu *et al.* [27], are expected to develop independently and the resonance zone of one wave is not likely to affect the resonance zone of the other.

1.1.2 Nonlinear perturbations - isothermal case

Concerning the case perturbations above ε_C , **(i)** there should be low frequency signals due to the presence of ions detectable on other macroscopical quantities, of lower amplitudes due to the large inertia. **(ii)** It is expected that ions develop nonlinear behavior, specifically solitary electrostatic waves involving electron holes and IASs, rather than ion holes, since the system does not involve streaming. **(iii)** The observation of IASs implies that the low frequency dynamics is related to waves coinciding with the IA branch. **(iv)** As perturbations in the ions density exhibit lower levels, a threshold amplitude larger than the threshold for nonlinear Landau damping is expected.



1.1.3 Nonlinear perturbations - temperature variation

For the case of amplitudes larger than ε_C and a variation of the initial temperature ratio T_i/T_e , **(i)** the hypothesized nonlinear regime of the variations of the ions density for the isothermal case should become intensified if T_i/T_e is reduced, and as a consequence **(ii)** the tendency of the waves on the IA mode to be less damped with lower T_i/T_e from the linear theory should still hold in this regime, and waves coinciding with that branch should become more intense. **(iii)** For higher T_i/T_e , it is expected that electrostatic solitary waves involving electron holes propagate, and that ion structures become decoupled from the holes or not to couple to them at all.

1.2 Objectives

1.2.1 General objectives

The general objectives of this work, applied to the addressed plasmas, are **(i)** to determine the dynamic effects of the presence of mobile, heavy positively charged ions on each of the species composing the plasma and to determine whether the modes found by Xu *et al.* [27] develop independently from each other, in the case of damped perturbations. **(ii)** For the case of nonlinear perturbations, to characterize the low frequency response of both the ions and electrons distribution, to determine the threshold amplitude for the low frequency dynamics, and **(iii)** to determine the effects of initializing the plasma with different temperature ratios.

1.2.2 Specific objectives

Specific objectives common to all three cases are to estimate the roots of the linear dispersion relation and to compare them with the respective electric field spectra, to follow the position averaged distribution functions around the speed $v_{\phi,IA}$ estimated through the linear dispersion relation and to establish a comparison with the case of immobile ions for the same perturbative amplitudes. For the cases of damped perturbations and nonlinear perturbations with $T_i/T_e = 1.0$, other specific objectives are to use perturbative amplitudes that lead to the same qualitative behavior found by Xu *et al.*, to estimate correlations in the electrons distribution functions with the respective case of immobile ions. A common specific objective related to the nonlinear cases is to follow the distribution functions around possible characteristic nonlinear structures. To estimate the threshold in the isothermal case, several per-

turbative amplitudes ε_e are tested, whereas in the case of the variation of the initial temperature, temperature ratios T_i/T_e both above and below $T_i/T_e = 1.0$ are tested.

1.3 Methodology

1.3.1 Simulations

In order to carry out this work, a simulation study is performed, considering the kinetic theory, modeling both mobile species through the Vlasov-Poisson system of equations. For this purpose, a code that solves the system of equations through symplectic integration is used. Such a code is written in Julia programming language version 1.3.1, and is part of a library called `Vlasova.jl`, developed by J. A. Gidi, in the Physics Department of Universidad de Concepción. Julia is an MIT license open source, high level syntax language developed for high performance, appropriate for the simulations required for this work. The computationally expensive simulations required for this work are performed on a server with 504Gb RAM, processor Intel Xeon CPU E5-2699 v4 of 44 cores, 2 threads per core and Linux 4.19.0-6-amd64 kernel.

Simulation parameters and domain

The simulations consider one dimensional plasmas only, both in the linear ($\varepsilon_e = 1.0 \times 10^{-3}$ and 8.0×10^{-3}) and nonlinear ($\varepsilon_e = 4.0 \times 10^{-2}$) regime of perturbations. The equilibrium state of the plasma is initially perturbed with a monochromatic wave ($k = 0.4\lambda_{De}^{-1}$). The plasma is allowed to evolve up to 3000 electron plasma periods, in order to allow for the development of quasi-stationary dynamics. In the nonlinear case, several runs are made with lower ε_e ($\varepsilon_e > 1.66 \times 10^{-2}$). In order to

observe nonlinear dynamics, simulations require up to 5000 electron plasma periods.

The velocity domain for both species is $[-8v_{Tj}, 8v_{Tj}]$, where v_{Tj} is the initial thermal velocity of the species j , and the domain is large enough to retain the important physics of the problem, and for the distributions to be nearly zero at the boundaries of the domain. For simulations lasting 3000 electron plasma periods, $N_v = 8192$ nodes are used ($\varepsilon_e \leq 2.0 \times 10^{-2}$), which are increased to $N_v = 16384$ for simulations lasting up to 5100 electron plasma cycles ($2.0 \times 10^{-2} < \varepsilon_e \leq 1.72 \times 10^{-2}$), and to $N_v = 32768$ for up to 6000 electron plasma cycles ($1.72 \times 10^{-2} < \varepsilon_e \leq 1.66 \times 10^{-2}$). The number of nodes is duplicated because the fine structure in velocity space reaches the simulation grid in the electrons distribution for long term simulations with $N_v = 8192$. The same observation applies for $N_v = 16384$. It is noted that the use of $N_v = 16384$ in simulations lasting 3000 electron plasma periods does not change the results significantly, as test runs show.

The position domain is common for both species, $[0, L_x]$ with $L_x = 5\pi\lambda_{De}$ and considers periodic boundary conditions with the same number of nodes for all simulations, $N_x = 512$. Test simulations indicate that a higher number, $N_x = 1024$, retains the same features as with the half.

1.3.2 Linear dispersion relation

The determination of roots of the linear dispersion relation is also performed by a main code run on Julia language which solves the dispersion relation through the Muller method. The latter is written in Python and was developed by R. E. Navarro, in the Physics Department of Universidad de Concepción. These codes are run on a

Dell notebook model Inspiron 14 7472 with 8 Gb RAM, processor Intel Core i5-8250U CPU and Linux 4.14.175-1 Manjaro kernel.

1.3.3 Scope and limitations

The work is focused in one dimensional collisionless, non-drifting, unmagnetized, Maxwellian electron and ion plasmas with fixed mass and charge ratios, and with electrostatic perturbations. Although the configuration of Maxwellian species without drift is basic, it is widely used in theoretical plasma physics and to model plasmas in laboratory as well as in space environment. Hence, it is expected to contribute to the spectrum of phenomena related to this distribution.

The work focuses on the development of nonlinear structures in position and phase space through the evolution of the distribution function f_j from each species, allowing for the occurrence of fully kinetic phenomena, for a wide range of perturbation amplitudes, from the linear damped regime to large nonlinear amplitudes. Other nonlinear structures are observed through the evolution of the particle density with their respective spectra compared to the linear dispersion relation, and the averaged particle distribution functions around resonance zones.

Concerning the position domain, it is noted that due to its extension, the propagating modes cannot develop wavelengths larger than $L_x = 15.7080\lambda_{De}$, limiting the observed phenomena to sizes from the order of the electron Debye length to ten electron Debye lengths, which, although restricted, still allows for the development of short wavelength collective phase space structures such as electron holes.

For the analysis, the electrons density and the electrostatic potential are filtered in frequency. As Fourier transforms are used to apply the frequency filter and as the signals are not periodic in the time dependency, Gibbs phenomenon occurs in the initial instants of the filtered quantities remaining inaccessible up to a hundred of electron plasma cycles. Therefore, the evolution of these quantities is inferred from other quantities which are accessible at those instants, such as the position averaged distribution functions and the ions density.

1.4 Organization of the work

The present work is organized as follows. In Chapter 2, kinetic theory is thoroughly described and the linear dispersion relation for waves is found. Also, a description of nonlinear structures is given. In Chapter 3, the methods for the numerical integration of the Vlasov-Poisson equations are shown. In Chapter 4 the case of monochromatic perturbation with low enough amplitude to yield damped waves is studied considering the perturbation of the distribution of the ions. The excited modes are identified in the electric field spectrum and in the distribution functions, the resonance zone related to the slow mode is studied and compared with the case of immobile ions. In Chapter 5, the nonlinear case is studied, finding the formation and propagation of slow electron holes and solitary ion waves, which couple and lead to the formation of secondary structures at larger times. Chapter 6 studies the same problem for different temperature ratios, finding changes in the observed structures in the ions distribution, the excited waves, but retaining the propagation of slow electron holes. Finally, Chapter 7 summarizes the previous results and provides the conclusions of this work.

1 Introducción

En la investigación de ondas de plasma se hacen aproximaciones según las masas de las especies que lo componen, y las escalas espacial, temporal y de velocidades de los fenómenos de interés. Mientras que en algunos casos sólo se mueven las especies más livianas, la adición de una especie pesada móvil en el plasma corresponde a un modelo más realista. Se ha demostrado que la presencia de iones móviles pesados (protones), con carga positiva y con distribución Maxwelliana, modifica la evolución del plasma no colisional y no magnetizado durante el amortiguamiento lineal de Landau de ondas de Langmuir en plasmas Maxwellianos de electrones inicialmente isotérmicos, explorando la densidad de partículas y la energía del campo eléctrico, pero sin explorar la dependencia de velocidad. En el régimen no-lineal del mismo plasma, la amplitud del modo excitado indica que los efectos de iones móviles se reducen. Sin embargo, esto no descarta alguna dinámica relacionada con las escalas de los iones. Por lo tanto, el presente trabajo aborda cómo la presencia de iones pesados, móviles con carga positiva modifican la dinámica de un plasma Maxwelliano de electrones en el rango de las escalas de iones para los regímenes lineal y no-lineal de perturbaciones, y caracterizar los fenómenos que surgen por la introducción de tal especie.

De las ecuaciones de movimiento de una partícula j cualquiera del plasma, la escala de tiempo de su dinámica se estima como $\tau_j \sim m_j$, donde m_j es la masa de la partícula de la partícula. Por lo tanto, el movimiento de las especies más pesadas ocurre en una escala de tiempo más larga. La existencia de escalas de tiempo se puede observar en Fig.1.1, donde se muestran las trayectorias de dos partículas de masa $m_1 = m_e$ y $m_2 = 1836m_e$, con m_e la masa del electrón. Ambas están simultáneamente sometidas a una fuerza debido a una onda de Langmuir (LW), de corta escala de tiempo, y una onda ión acústica (IAW) de baja amplitud, de escala de tiempo más larga, con el mismo número de onda. La partícula ligera es resonante con la onda de Langmuir y la partícula pesada lo es con la IAW. La Fig.1.1(a) muestra que el movimiento de una partícula pesada puede despreciarse durante un corto intervalo de tiempo y el forzamiento de baja frecuencia es despreciable.

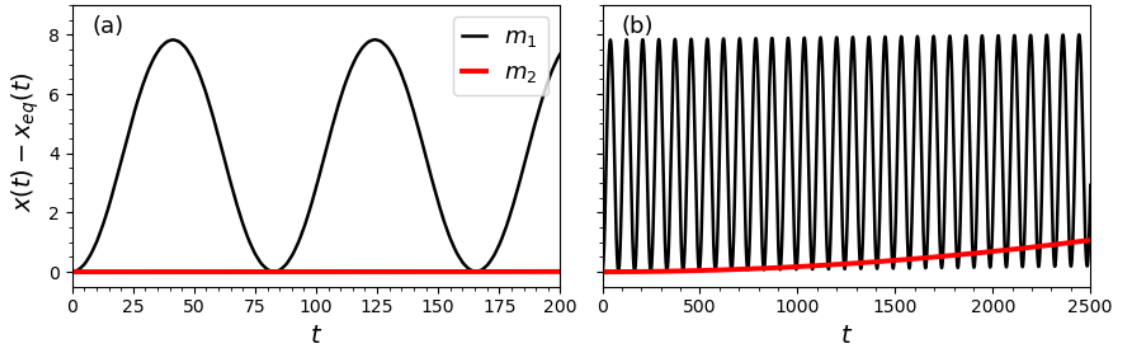


Figure 1.1: Variaciones de trayectorias de partículas respecto del equilibrio, $x_{eq,i}(t) = x_{0,i} + v_{0,i}t$, para una partícula ligera, m_1 , y una partícula pesada, m_2 , impulsadas por una LW y una IAW de baja amplitud. La partícula m_2 no se desvía significativamente con respecto de su trayectoria de equilibrio (a). A tiempos más largos (b), las desviaciones no son despreciables.

La aproximación de especies pesadas móviles consideran partículas livianas como

móviles y las especies restantes son supuestas infinitamente pesadas y estáticas, como el caso típico de un plasma de electrones y iones. Muchos estudios usan esta aproximación con iones uniformes, abordando fenómenos cuya frecuencia y rangos de velocidad son tales que las especies pesadas no contribuyen a la evolución del plasma, coincidiendo con experimentos y observaciones: trabajos tan fundamentales como aquellos referentes al amortiguamiento no colisional lineal y no-lineal de Landau de LWs en plasmas de electrones [1–7], suponen iones inmóviles, con trabajos experimentales confirmando el comportamiento predicho [8]. En fenómenos críticos en física de plasmas [9], se ha mostrado que la presencia de iones móviles no afecta al comportamiento crítico del amortiguamiento de Landau de LWs [10]. Otros trabajos que consideran iones inmóviles se enfocan en la propagación de estados de espacio fase no-lineales tales como ondas BGK, soluciones analíticas del sistema de Vlasov-Poisson, que consisten en estructuras cuasi-estacionarias, electrostáticas que involucran atrapamiento de partículas [11], tales como agujeros de electrones (electron holes) [12], o el ruido electrostático de banda ancha en magnetósferas terrestres y planetarias, en las que el plasma es modelado como núcleos calientes y fríos de electrones y un haz de electrones, con el fin de excitar modos electrón acústicos [13].

Sin embargo, ciertos fenómenos pueden tener lugar en escalas de tiempo más largas y la dinámica de las especies pesadas no es despreciable, como se muestra en Fig.1.1(b). En tales casos, la dinámica de las especies pesadas debe incluirse en el sistema de ecuaciones, ya que su presencia puede modificar la dinámica observada, resultando en una descripción más completa del fenómeno o introduciendo fenómenos adicionales, inadvertidos en escalas de tiempo cortas. En el contexto de experimentos láser, por ejemplo, en configuraciones de fusión nuclear como el confinamiento

inercial de plasmas de fusión, en que una luz láser es dirigida hacia un objetivo dentro de una cavidad para encenderlo [14]. El proceso involucra una inestabilidad de scattering estimulado de Brillouin, en que una onda electromagnética incidente, producida por un láser, decae en una IAW y en una onda electromagnética en la dirección opuesta a la incidente [15]. Tal proceso es indeseable en confinamiento inercial, ya que una fracción de la radiación enviada al objetivo se refleja. Se han propuesto distintos mecanismos relacionados a la componente IAW para reducir esta inestabilidad, con el fin de reducir la reflexión y aumentar la absorción de ondas electromagnéticas, tales como la excitación de atrapamiento de iones [16], calentamiento en la distribución de iones [17], amortiguamiento de Landau por iones [18], adición de múltiples especies iónicas para potenciar el amortiguamiento de Landau por iones [19], y saturación a través de decaimientos paraméticos iónicos [20].

En plasmas astrofísicos, mediciones *in situ* de campos eléctricos y espectros realizados por el satélite Freja y el cohete sonda SCIFER en la región auroral terrestre indican que la modulación de paquetes de LWs observados allí, correspondientes a emisiones de banda corta, se explican por *scattering* de modos *whistler* y *lower hybrid*, relacionados con la dinámica de protones; estas ondas se incluyen para dar cuenta en señales de baja frecuencia encontradas en procesos de modulación [21]. Mediciones *in situ* en la región de aceleración paralela auroral hechas por el satélite FAST en 1997 indican la presencia de *peaks* de frecuencia alrededor de 300[Hz], correspondientes al rango de la frecuencia hidrógeno-ión acústica, modularían la amplitud de paquetes de onda electrón acústicas [22].

También se encuentran directamente ondas de baja frecuencia en plasmas del

viento solar, relacionadas a las llamadas fuentes solares tipo III, descubiertas en 1950, que corresponden a radioemisiones provenientes del viento solar mismo, así como en el sistema solar, proporcionando información sobre las condiciones del medio de fondo, y de la aceleración y transporte de electrones [23]. Observaciones espectrales de la sonda Galileo de 1990 indican la existencia de tres *peaks* intensos, dos de alta frecuencia cercanos a 24[kHz], correspondientes a ondas de Langmuir, y uno de baja frecuencia alrededor de 400[Hz], identificados como IAWs [24].

El mecanismo de generación de radioemisiones tipo III ha sido discutido por Cairns [25], llevado por discrepancias entre observaciones y trabajos teóricos. Se han considerado dos mecanismos, el acoplamiento no-lineal, resonante onda-onda conocido como decaimiento electrostático de Langmuir, consistente en el decaimiento de una LW primaria en una IAW y *scattering* por iones térmicos, en el que iones individuales y la respuesta de su nube de electrones apantallante están fuera de fase debido a la diferencia de masas, produciendo *scattering* de LWs entrantes [26]. Se argumenta que para que el *scattering* ocurra, la respuesta colectiva de los iones debe inhibirse. Tal inhibición tiene lugar si la escala de tiempo de esta respuesta es corta comparada con la del *scattering* y si la escala de tiempo del *scattering* es mucho más larga que la escala de tiempo del proceso más lento y culmina varios ciclos después [25]. De acuerdo a mediciones, los niveles de energía requeridos para el *scattering* no pueden ocurrir, y en regiones con razón de densidad de energía de campo eléctrico y energía térmica de plasma $W \lesssim 10^{-5}$, se espera que ocurra decaimiento de Langmuir relacionado con radioemisiones tipo III; el *scattering* por iones térmicos sería relevante sólo en regiones con $W \lesssim 10^{-3}$.

Se han estudiado oscilaciones de electrones en la presencia de iones pesados móviles con carga positiva a través de simulaciones cinéticas. Xu *et al.* estudiaron el régimen lineal del amortiguamiento de Landau en un plasma no colisional, no magnetizado, de electrones y iones Maxwellianos, excitando sólo el primer modo. En este trabajo, se encuentra que iones ($m_i/m_e = 1836$), con especies inicialmente isotérmicas $T_i/T_e = 1.0$ con $q_i/|q_e| = 1.0$, notoriamente afectan el amortiguamiento lineal, observado en la amplitud del modo excitado ($|E(m = 1)|$) en Fig.1.2. Para amplitudes de perturbación en la distribución de electrones (ε_e) en el régimen amortiguado [Figs.1.2 (c) and (d)], ocurre el amortiguamiento de Landau usual (comparado con el caso de iones inmóviles) hasta $t \simeq 100$, cuando oscilaciones amortiguadas lentas comienzan a dominar y se observa una importante desviación respecto del caso con iones inmóviles.

Se identifican dos tipos de ondas: una LW, con frecuencia y amortiguamientos estimados con la relación de dispersión lineal del sistema de Vlasov-Poisson, y una IAW, con frecuencia estimada con la aproximación fluida y amortiguamiento estimado por medio de la relación de dispersión lineal del sistema de Vlasov-Poisson. Mientras la frecuencia de $|E(m = 1)|$ cambia, las variaciones de la densidad de electrones, δn_e , se reducen al mismo orden que las de la densidad de iones, δn_i , y exhiben la misma dependencia en los dominios de posición y tiempo con oscilaciones de baja frecuencia para $t > 100$, indicando que los electrones terminan por seguir el movimiento de los iones. Sin embargo, en el trabajo de Xu *et al.* no se estudian detalles de la dependencia de velocidades alrededor de las zonas de resonancia involucradas en la propagación de estas ondas, ni cómo cada especie del plasma contribuye a su desarrollo.

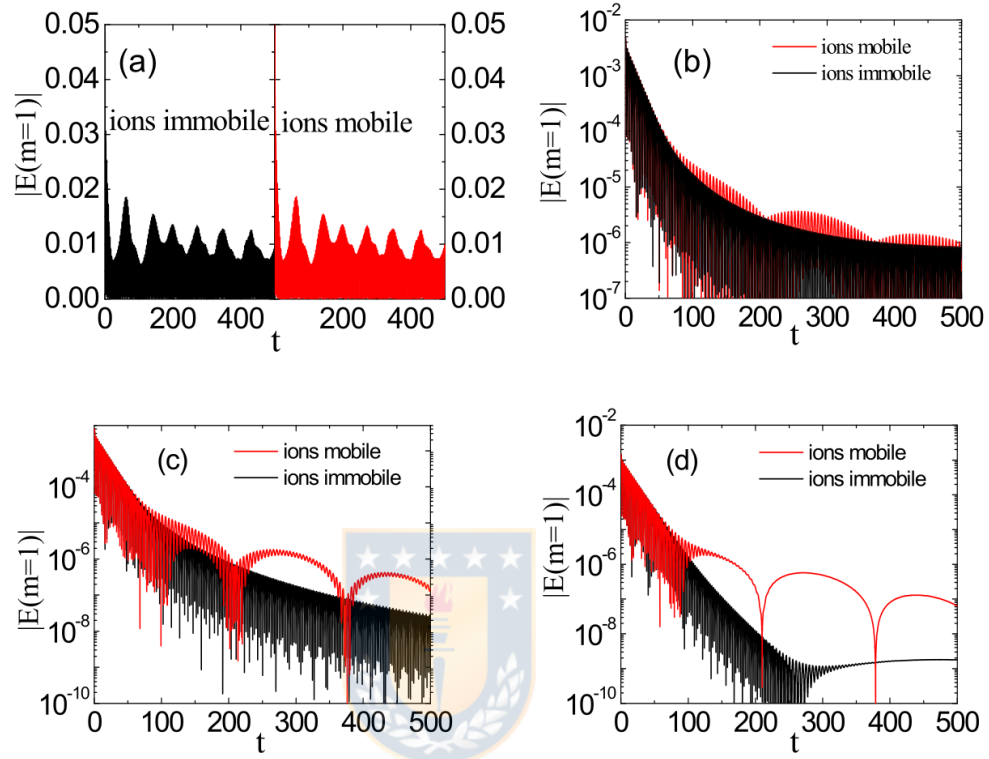


Figure 1.2: Evolución del modo excitado del campo eléctrico $|E(m = 1)|$ para diferentes amplitudes de perturbación (a) $\varepsilon_e = 1.0 \times 10^{-1}$, (b) $\varepsilon_e = 1.0 \times 10^{-2}$, (c) $\varepsilon_e = 8.0 \times 10^{-3}$ y (d) $\varepsilon_e = 3.0 \times 10^{-3}$, para iones móviles e inmóviles, con $T_i/T_e = 1.0$. Gráficos cortesía de Xu *et al.* [27].

Con amplitudes de perturbación por encima de la amplitud crítica para excitar el amortiguamiento no-lineal de LWs [see Fig.1.2 (a)], dominan oscilaciones rápidas y la dinámica de los iones no puede distinguirse a través de la evolución de $|E(m = 1)|$. Aunque en Ref.[27] se afirma que pueden ocurrir perturbaciones iónicas, serían despreciables en comparación con aquellas de los electrones, sin más discusión al respecto.

Se han observado estructuras coherentes de larga duración en el espacio de posiciones y en el espacio de fases en la presencia de iones móviles con carga positiva en plasmas no colisionales y no magnetizados de electrones y iones Maxwellianos, como agujeros de iones (*ion holes*), así como interacciones de iones con estructuras de la misma naturaleza, tales como *electron holes*.

Un *ion hole* consiste en iones atrapados alrededor de un mínimo local de potencial electrostático [12, 28], repeliendo electrones a su alrededor. En este caso, los electrones tiene una distribución de Boltzmann, es decir, responden tan rápidamente que desarrollan configuraciones de equilibrio instantáneo, y se requiere que sean lo suficientemente calientes como para producir presión para sostener la despoblación de iones en el centro de la estructura [29]. Se han medido con alta resolución en la región auroral terrestre, por medio de la sonda FAST, propagándose con velocidades consistentes con el modo IA [30], y también se han encontrado en simulaciones de Vlasov-Poisson de plasmas no magnetizados de electrones y haz de iones Maxwellianos excitando inicialmente el *electron hole*, después del crecimiento de varios *electron holes* pequeños, considerando una razón de masas baja ($m_i/m_e = 4$) [31]. Otras configuraciones que producen un *ion hole* son colocar este estado directamente en el instante inicial en la distribución de iones en simulaciones [32], inestabilidad de dos corrientes ión-ión [33], y en general, configuraciones inestables que involucran corrientes contra-propagantes de iones [29].

Los solitones se definen como estructuras localizadas que se propagan sin pérdida o dispersión, evolucionando desde ondas de gran amplitud [34], y se observan en el potencial electrostático o como pulsos compresivos en la densidad de la especie

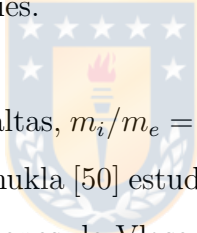
que sustenta su propagación, que resulta de acoplamiento no-lineal sucesivo entre las ondas excitadas limitadas por la dispersión de ondas cuya velocidad de fase difiere importantemente de la de la onda fundamental [35]. Se consideran solitones ión acústicos (IASs). Estas estructuras se observan en la densidad de los iones, involucrando IAWs [36]. Basado en el modelo fluido, se encuentra que se propagan con velocidades v_S en el rango $1 < v_S/c_S \lesssim 1.6$ [35], donde c_S es la velocidad de onda ión acústica del modelo fluido. Se han incluido elementos cinéticos en su modelación, tales como amortiguamiento de Landau por iones y electrones, y atrapamiento de electrones [37]. Estudios de simulación usando modelos híbridos (iones cinéticos y electrones con distribución de Boltzmann) y modelos puramente cinéticos, muestran que los IASs no siempre podrían reneter sus propiedades inalteradas: IASs inestables podrían generar varias IAWs [38], o crecer en amplitud para grandes perturbaciones iniciales [39]. Propiedades como la velocidad de propagación pueden modificarse con atrapamiento de electrones. Pueden notarse más diferencias para velocidades de propagación mayores a c_S [40]. Esto implica que los solitones interactúan e incluso pueden acoplarse a *electron holes*, como se ha reportado en varios estudios [41–45], propagándose con velocidades en el rango indicado. Sin embargo, se requiere una cierta perturbación en la densidad de los iones para que puedan excitarse solitones y acoplarse [43]. Otros trabajos que involucran acoplamiento *electron hole-soliton* ión aún identifican al solitón como IASs, aunque se propaguen con velocidades $v_S = 4.06c_S$, fuera del rango predicho [46].

Hutchinson y Zhou han desarrollado una teoría para la propagación de *electron holes* acelerados considerando interacción con especies iónicas pesadas usando un enfoque cinemático, enfocándose en el intercambio de momentum [47, 48]. En este

caso, los iones interactúan con el *hole* intercambiando momentum a través de reflexión si el potencial de atrapamiento es lo suficientemente intenso, y pasando a través de él en el caso opuesto, tendiendo a acumular iones en la región de menor densidad electrónica. Por medio de simulaciones de plasmas no colisionales, no magnetizados y electrostáticos con deriva relativa no nulo entre especies, razón de masas $m_i/m_e = 1836$ y una razón de temperatura $T_i/T_e = 2.5 \times 10^{-2}$, los autores observan el mismo acoplamiento entre *electron holes* y solitones de iones discutidos por Saeki y Rasmussen [44] y Saeki y Genma [45]. Ellos también muestran que los *holes* rápidamente reacciones ante cambios en la distribución de iones. Para *electron holes* más rápidos, el grado de interacción con los iones es relativamente pequeño y puede despreciarse [48].

Trabajos que incluyen plasmas no colisionales, no magnetizados de electrones y iones con deriva relativa, $m_i/m_e = 1836$ y $T_i/T_e = 0.1$, han mostrado que *electron holes* lentos interactúan con la distribución de iones, tendiendo a producir perturbaciones localizadas en la última, como en el contexto de turbulencia subcrítica en plasmas, donde se ha mostrado que la excitación de un *electron hole* en condiciones de estabilidad linear puede llevar a la excitación de *electron holes* debido a la dependencia de la perturbación inicial [46, 49]. Se observa que el *electron hole* excitado acelera a velocidades más rápidas que c_S debido a que se excitan IAWs en la densidad de iones, atribuidas a IASs. Se muestra que los *holes* más rápidos en este rango de velocidades se propagan establemente [49], y se indica que el *hole* permite acumulación de iones en el interior de la región de atrapamiento, como discuten Hutchinson y Zhou [47].

Considerando el mismo sistema con una razón de masas baja, $m_i/m_e = 4$, un *drift* relativo inicial y especies inicialmente isotérmicas pero abordando el mecanismo de excitación de IAWs por medio de corriente in plasmas sin colisiones, Lesur *et al.* [31] excitan modos no-lineales relacionados con estructuras del espacio de fase que involucran intercambio de momentum y energía. El desarrollo de *electron holes* primarios eventualmente conduce a la generación de *holes* de menor tamaño, resultando en turbulencia en el espacio de fase con un conjunto de estructuras a medida que el *hole* primario deja un rastro de densidad negativa y es acelerado. Se reporta que los *electron holes* crecen más fácilmente cuando hay un solapamiento entre las distribuciones de ambas especies.



Para razones de masa más altas, $m_i/m_e = 29500$, especies inicialmente isotérmicas con drift relativo, Eliasson y Shukla [50] estudiaron la interacción de *electron holes* con el plasma a través de simulaciones de Vlasov-Poisson de un plasma con electrones-iones de oxígeno Maxwellianos inicializando los electrones con un *hole* estático de Schamel. El potencial positivo desarrollado por el *hole* repele iones de baja energía, produciendo una cavidad en la densidad de iones, y por lo tanto un potencial negativo que eventualmente repele al *hole*, quedando estática la cavidad de iones.

La razón de temperatura entre especies es un parámetro importante en física de plasmas. En la aproximación lineal, la tasa de amortiguamiento y la propagación de IAWs en plasmas con electrones e iones Maxwellianos dependen directamente de T_i/T_e . Las IAWs son favorecidas con iones fríos, dado que la tasa de amortiguamiento tiende a cero [51], debido a que hay una menor cantidad de iones resonantes disponibles para interacción onda-partícula. Por otro lado, cuando esta razón

tiende a la unidad, la onda es fuertemente amortiguada para cualquier número de onda, porque hay más iones disponibles para tal interacción. En el trabajo de Norgren *et al.* [52], la relación de dispersión lineal es usada para caracterizar inestabilidades lineales en un electrones y iones con un haz de electrons, todos Maxwellianos, en el contexto de ondas solitarias electrostáticas en la magnetósfera. Se muestra que para T_i/T_e más altos, la condición de inestabilidad marginal se desplaza a velocidades de haz más grandes, porque hay una población de iones más grande a velocidades más bajas, amortiguando ondas por interacción resonante.

Mediciones en plasmas espaciales indican que la razón de temperatura var'ia dependiendo de la región observada. En la magnetocola, mediciones realizadas sobre *electron holes* lentos, por la sonda Cluster, capaz de interactuar con iones de alrededor, se explican con plasmas compuestos por especies con drift relativo cuya razón de temperatura está en el rango $0.89 \leq T_i/T_e \leq 1.78$ [53]. En zonas relacionadas con el viento solar, la temperatura var'ia en un amplio rango, $0.1 \leq T_i/T_e \leq 2.0$ [23] y se ha encontrado que IAWs no-lineales generadas por plasmas con corrientes de electrones y iones tienden a observarse con mayor amplitud con razones de temperatura más bajas [54].

El uso de una razón de temperatura alta puede modificar el acoplamiento entre IASs y *electron holes*. Zhou *et al.* reportaron que el acoplamiento se rompe con razones de temperatura alta, $T_i/T_e > 1$, ya que hau más iones en la zona de resonancia, por lo que el amortiguamiento de Landau por iones se vuelve más fuerte y el solitón decae, obteniéntose un *electron hole* libre [43]. En la investigación de inestabilidades electrostáticas, en el contexto de señales del ruido electrostático de banda ancha

y corta obtenidas por la sonda Geotail, Omura *et al.* [55] estudiaron simulaciones de inestabilidad de dos corrientes (*bi-stream instability*), usando un núcleo de iones con un haz de electrones con razón de masa $m_i/m_e = 100$, encontrando que iones calientes producen ondas solitarias electrostáticas, mientras que iones fríos llevan al potencial electrostático a decaer en varias IAWs.

A la luz de esta exposición, en este trabajo se utiliza la misma configuración usada en el trabajo de Xu *et al.* para estudiar más efectos de iones móviles pesados con carga positiva en plasmas no magnetizados y no colisionales compuestos por electrones y iones Maxwellianos sin deriva relativa, para los casos de perturbaciones amortiguadas y no-lineales. For el primero, se propone estudiar la dependencia de velocidad del ambas especies alrededor de las zonas de resonancia con énfasis en las velocidades bajas, alrededor de la velocidad de fase de las IAWs excitadas, $v_{\phi,IA}$, y cómo cada una de las especies que componen el plasma es afectada por la propagación de ambas ondas.

En el caso no-lineal, aunque muchos de los trabajos previamente descritos involucran deriva relativa entre las distribuciones de electrones y iones, es interesante determinar si la energía inyectada por una perturbación inicial de gran amplitud en el plasma permite el desarrollo de dinámica no-lineal en la distribución de los iones. Si tal comportamiento no-lineal ocurre, se propone estudiar las estructuras y ondas que pudieran desarrollarse, su interacción con la distribución de los electrones, el efecto de las ondas observadas en las regiones resonantes en el espacio de velocidades, y cómo cantidades microscópicas y macroscópicas, además de la energía del campo eléctrico, resultan afectadas por su movimiento.

Debido a la relevancia de la razón de temperatura en la dinámica de un plasma de electrones y iones en el régimen no-lineal, es de interés determinar la respuesta del plasma a medida que se varía la razón de temperatura T_i/T_e con respecto al caso isotérmico, debido a que las ondas relacionadas con la respuesta colectiva de los iones es afectadas por esta razón.

1.1 Hipótesis del trabajo

De acuerdo a los temas previamente discutidos y el trabajo propuesto, se consideran las siguientes hipótesis. Todas ellas se aplican a plasmas no colisionales, no magnetizados, sin deriva relativa y compuestos por electrones y iones Maxwellianos con razón de masa $m_i/m_e = 1836.153$ y razón de carga $q_i/|q_e| = 1.0$.

1.1.1 Perturbaciones amortiguadas

Para el caso de amplitudes inferiores a la amplitud crítica requerida para excitar el amortiguamiento no-lineal de Landau de LWs ($\varepsilon_{e,C}$) [56], **(i)** se espera encontrar una zona de resonancia alrededor de $v_{\phi,IA}$ para el número de onda excitado en la función de distribución de cada especie. En tal región de resonancia, **(ii)** ambas especies deberían exhibir un comportamiento opuesto en el espacio de velocidades, según se estima con la teoría lineal. **(iii)** Se espera que Las ondas encontradas por Xu *et al.* [27] se desarrollen de forma independiente y que la zona de resonancia de una onda es poco probable que afecte la zona de resonancia de la otra.

1.1.2 Perturbaciones no-lineales - caso isotérmico

Con respecto al caso de perturbaciones por sobre $\varepsilon_{e,C}$, **(i)** debiera hacer señales de baja frecuencia debido a la presencia de los iones, detectables en otras cantidades macroscópicas, de amplitudes más bajas debido a su mayor inercia. **(ii)** Se espera que los iones desarrollen un comportamiento no-lineal, específicamente ondas solitarias electrostáticas que involucren *electron holes* y IASs, en lugar de *ion holes*, debido a que el sistema no involucra corrientes. **(iii)** La observación de IAAs implica que la dinámica de baja frecuencia está relacionada con ondas que coinciden con la rama IA. **(iv)** Dado que las perturbaciones en la densidad de iones tiene niveles más bajos, se espera que esta dinámica requiera un umbral de perturbación más alto que en el caso del amortiguamiento no-lineal de Landau.

1.1.3 Perturbaciones no-lineales - variación de temperatura

Para el caso de amplitudes de perturbación mayores que ε_C y una variación de la razón de temperatura inicial T_i/T_e , **(i)** el régimen no-lineal hipotetizado en las variaciones de la densidad de iones en el caso isotérmico debería intensificarse si se reduce T_i/T_e , y como consecuencia **(ii)** la tendencia de las ondas en el modo IA de ser menos amortiguada con T_i/T_e más pequeño de la teoría lineal debería mantenerse en este régimen, y las ondas que coinciden con esa rama deberían intensificarse. **(iii)** Para T_i/T_e más altos, se espera que se propaguen ondas solitarias electrostáticas que involucren *electron holes*, y que las estructuras relacionadas con los iones se desacoplen de ellos o que no haya acoplamiento en lo absoluto.

1.2 Objetivos

1.2.1 Objetivos generales

Los objetivos generales de este trabajo, aplicados al plasma objetivo del estudio, son **(i)** determinar los efectos dinámicos de la presencia de iones móviles pesados con carga positiva en cada una de las especies que componen el plasma y determinar si los modos encontrados por Xu *et al.* [27] se desarrollan uno independiente del otro, el caso de perturbaciones amortiguadas. **(ii)** Para el caso de perturbaciones no-lineales, se busca caracterizar la respuesta de baja frecuencia de ambas especies, determinar la amplitud de perturbación umbral para la dinámica de baja frecuencia y **(iii)** determinar los efectos de inicializar el plasma con diferentes razones de temperatura.

1.2.2 Objetivos específicos

Son objetivos específicos comunes para los tres casos estimar las raíces de la relación de dispersión lineal y compararlas con los espectros del campo eléctrico respectivos, seguir las funciones de distribución promediadas en posiciones alrededor de la velocidad $v_{\phi,IA}$ estimada por medio de la relación de dispersión lineal y establecer una comparación con el caso de iones inmóviles con la misma amplitud de perturbación. Objetivos específicos para los casos de perturbaciones amortiguadas y no-lineales inicialmente isotérmicas $T_i/T_e = 1.0$ son usar amplitudes de perturbación que conduzcan cualitativamente al mismo comportamiento encontrado por Xu *et al.*, estimar correlaciones en las funciones de distribución de los electrones con caso respectivo de iones inmóviles. Un objetivo específico común a los casos no-lineales es seguir las funciones de distribución alrededor de posibles estructuras no-lineales car-

acterísticas. Con el fin de estimar la amplitud umbral en caso isotérmico, se prueban varias amplitudes de perturbación ε_e are tested, mientras que en el caso de variación de tempertura inicial, se prueban razones de temperatura T_i/T_e por encima y por debajo de $T_i/T_e = 1.0$.

1.3 Metodología

1.3.1 Simulaciones

Para llevar a cabo este trabajo, se realiza un estudio de simulaciones considerando teoría cinética, modelando ambas especies móviles a través del sistema de ecuaciones de Vlasov-Poisson. Para este propósito, se usa un código que resuelve el sistema de ecuaciones a través de integración simpléctica. Tal código está escrito en lenguaje de programación Julia versión 1.3.1, y es parte de una librería llamada `Vlasova.jl`, desarrollada por J. A. Gidi, en el Departamento de Física de la Universidad de Concepción. Julia es un lenguaje con licencia de código abierta MIT y sintaxis de alto nivel, desarrollado para alto rendimiento, apropiado para las simulaciones que se requieren en este trabajo. Las simulaciones, computacionalmente demandantes requeridas para este trabajo se realizan en un servidor con 504 Gb de RAM, procesador Intel Xeon CPU E5-2699 v4 de 44 núcleos, 2 hilos por núcleo y kernel Linux 4.19.0-6-amd64.

Parámetros de la simulación y dominios

Las simulaciones consideran plasmas unidimensionales, tanto para el régimen lineal ($\varepsilon_e = 1.0 \times 10^{-3}$ y 8.0×10^{-3}) como no-lineal de perturbaciones ($\varepsilon_e = 4.0 \times 10^{-2}$). El estado de equilibrio del plasma es inicialmente perturbado con una onda

monocromática ($k = 0.4\lambda_{De}^{-1}$). Se permite que el plasma evolucione hasta 3000 ciclos de oscilación de plasma de electrones, con el fin de permitir el desarrollo de dinámica cuasi-estacionaria. En el caso no-lineal, se realizan varias simulaciones con amplitudes ε_e más bajas ($\varepsilon_e > 1.66 \times 10^{-2}$). Con el fin de observar la dinámica no-lineal, las simulaciones requieren hasta 6000 ciclos de oscilación de plasma de electrones.

El dominio de velocidades para ambas especies es $[-8v_{Tj}, 8v_{Tj}]$, donde v_{Tj} es la velocidad térmica inicial de la especie j , y el dominio es lo suficientemente largo como para retener la física importante del problema, y para que las distribuciones sean aproximadamente cero en el borde del dominio. Para simulaciones que duren 3000 ciclos de oscilación de plasma de electrones, se usan $N_v = 8192$ nodos ($\varepsilon_e \leq 2.0 \times 10^{-2}$), los que son incrementados a $N_v = 16384$ para simulaciones que duren hasta 5100 ciclos de oscilación de plasma de electrones ($2.0 \times 10^{-2} < \varepsilon_e \leq 1.72 \times 10^{-2}$), y a $N_v = 32768$ para hasta 6000 ciclos de oscilación de plasma de electrones ($1.72 \times 10^{-2} < \varepsilon_e \leq 1.66 \times 10^{-2}$). El número de nodos es duplicado porque la estructura fina en el espacio de velocidades alcanza la grilla de la simulación en la distribución de electrones para simulaciones de larga duración con $N_v = 8192$. La misma observación se hace para $N_v = 16384$. Se hace notar que el uso de $N_v = 16384$ en simulaciones que duren 3000 ciclos de oscilación de plasma de electrones no cambia significativamente los resultados, según simulaciones de prueba.

El dominio de posiciones es común a ambas especies, $[0, L_x]$ con $L_x = 5\pi\lambda_{De}$ y considera condiciones de borde periódicas con el mismo número de nodos para todas las simulaciones, $N_x = 512$. Simulaciones de prueba indican que un número mayor, $N_x = 1024$, tiene las mismas características que con la mitad.

1.3.2 Relación de dispersión lineal

La determinación de las raíces de la relación de dispersión lineal también se lleva a cabo con un código principal realizado en lenguaje Julia, que resuelve la relación de dispersión por medio del método de Muller. Este último está escrito en lenguaje Python y fue desarrollado por R. E. Navarro, en el Departamento de Física de la Universidad de Concepción. Estos códigos se hacen correr en un computador portátil Dell modelo Inspiron 14 7472 con 8 Gb de RAM, procesador Intel Core i5-8250U CPU y kernel Linux 4.14.175-1 Manjaro.

1.3.3 Alcance y limitaciones

Este trabajo está enfocado en plasmas no colisionales, sin deriva, no magnetizados compuestos por electrones e iones Maxwellianos con razón de masa y carga fijas, y con perturbaciones electrostáticas. Aunque la configuración de especies Maxwellianas sin deriva es básica, es ampliamente utilizada en física teórica de plasmas y para modelar plasmas de laboratorio así como en plasmas en ambientes espaciales. Por lo tanto, se espera contribuir al espectro de fenómenos relacionados a esta distribución.

Este trabajo se enfoca en el desarrollo de estructura no-lineales en el espacio posiciones y de fase a través de la evolución de la función de distribución f_j de cada especie, permitiendo que ocurran fenómenos completamente cinéticos, para un amplio rango de amplitudes perturbación, desde el régimen lineal amortiguado, hasta grandes amplitudes no-lineales. Se observan otras estructuras no-lineales en la evolución de la densidad de partículas y sus espectros respectivos comparados con la relación de dispersión lineal, y en las funciones de distribución promediadas alrede-

dor de las zonas de resonancia.

Con respecto al dominio de posiciones, se debe notar que debido a su extensión, los modos que se propagan no pueden desarrollar longitudes de onda mayores que $L_x = 15.708\lambda_{De}$, limitando los fenómenos que pueden observarse a tamaños en el orden de una a una decena de longitudes de Debye, las que, aunque restringidas, aún permiten el desarrollo de estructuras colectivas en el espacio de fases de corta longitud de onda, tales como *electron holes*.

Para el análisis, la densidad de electrones y el potencial electrostático se filtran en frecuencia. Dado que se usan transformadas de Fourier para filtrar en frecuencias y como la señal no es periódica en la dependencia temporal, ocurre fenómeno de Gibbs en los instantes iniciales, siendo inaccesibles hasta unos cientos de ciclos de oscilación de plasma de electrones. Por lo tanto, la evolución de estas cantidades se infiere de otras cantidades que sí son accesibles a esos instantes, como las distribuciones promediadas en posición y la densidad de iones.

1.4 Organización del trabajo

El presente trabajo se organiza como sigue. En el Capítulo 2, se describe completamente la teoría cinética y se encuentra una relación de dispersión de ondas. También, se da una descripción de estructuras no-lineales en el marco de la teoría de Vlasov. En el capítulo 3, se muestran los métodos numéricos de integración de las ecuaciones de Vlasov-Poisson. En el Capítulo 4 se estudia el caso de perturbación monocromática con baja amplitud para obtener ondas amortiguadas. Se identifican los modos excitados en el espectro del campo eléctrico y en la función de distribución, se estudia la

zona de resonancia relacionada con el modo lento y se compara con el caso de iones inmóviles. En el Capítulo 5, se estudia el caso no-lineal, encontrando la formación y propagación de *electron holes* lentos y ondas solitarias de iones, las que se acoplan y conduce a la formación de estructuras secundarias a tiempos largos. El Capítulo 6 estudia el mismo problema del caso anterior para diferentes razones de temperatura, encontrando cambios in las estructuras observadas en la distribución de los iones, las ondas excitadas, pero reteniendo la propagación de *electron holes* lentos. Finalmente, el Capítulo 7 resume los resultados anteriores y provee las conclusiones de este trabajo.



2 Plasma physics kinetic theory and electrostatic waves

In this chapter, the theoretical framework of the thesis is exposed. First, the Vlasov-Poisson system, used to model the electrostatic collisionless plasmas addressed in this work, is stated, followed by a discussion of the involved approximations and properties of the system of equations. Then, the Vlasov-Poisson system is linearized to first order to derive the linear dispersion relation for a Maxwellian electron-ion plasma, allowing to find and describe the modes involved in the addressed problem. Finally, nonlinear phenomena related to slow the dynamics of electrostatic electron-ion plasmas are discussed, such as slow electron holes and ion acoustic solitons.

2.1 Vlasov equation and system of equations

Plasmas are physical systems composed of particles mainly interacting through Lorentz force and collisions. The number of these particles in a plasma is in the order of the Avogadro number. Solving the individual dynamics of each particle is quickly demanding in most numerical situations. A statistical approach that retains the main features of the system is then desired. The kinetic theory fulfills this requirement, by dealing with a scalar density for each species composing the plasma, called the

particle distribution function, instead of individual particles.

The kinetic theory models a non-relativistic, unmagnetized, electrostatic, collisionless plasma through the Vlasov equation (2.1.1), the Gauss law (2.1.2) and the Faraday-Lenz law (2.1.3),

$$\left[\frac{\partial}{\partial t} + \mathbf{v} \cdot \nabla + \frac{q_j}{m_j} \mathbf{E} \cdot \nabla_v \right] f_j(\mathbf{r}, \mathbf{v}, t) = 0, \quad (2.1.1)$$

$$\nabla \cdot \mathbf{E}(\mathbf{r}, t) = \frac{\rho(\mathbf{r}, t)}{\epsilon_0}, \quad (2.1.2)$$

$$\nabla \times \mathbf{E} = \mathbf{0} \quad (2.1.3)$$

where f_j is the distribution function of the species j , depending on position \mathbf{r} , velocity \mathbf{v} and time t , q_j and m_j are the charge and mass per particle of the species j and ρ is the charge density, obtained from the distribution functions f_j as

$$\rho = \sum_j q_j \int f_j d^3v. \quad (2.1.4)$$

The Faraday-Lenz law (2.1.3) implies that the electric field can be written in terms of a scalar electrostatic potential Φ as $-\nabla\Phi = \mathbf{E}$. This system of equations is referred to as the Vlasov-Poisson system. Throughout this work, the Vlasov-Poisson system is used to model the plasmas.

In this plasma, magnetic field is not induced. Although the field \mathbf{E} usually depends on time, equation (2.1.3) prohibits the induction of time variations in a magnetic field. The electrostatic approximation also implies that the induced electric field is due solely to variations in the charge density [57]. Ampere-Maxwell law is

then reduced to $\mathbf{J} = -\epsilon_0 \partial \mathbf{E} / \partial t$, meaning that currents in the plasma are longitudinal with respect to \mathbf{E} and no transverse currents responsible of magnetic inductions exists. This condition relaxes the first restriction in the sense that magnetic induction may occur but its effect is negligible in comparison with the dynamics related to the electric field alone [57].

Generally, a plasma may exhibit collisions or short range interparticle interactions. In such a case, f_j is governed by the Boltzmann equation [35]. For the plasmas addressed in this work, Boltzmann equation is

$$\left[\frac{\partial}{\partial t} + \mathbf{v} \cdot \nabla + \frac{q_j}{m_j} \mathbf{E} \cdot \nabla_v \right] f_j(\mathbf{r}, \mathbf{v}, t) = \left. \frac{df_j}{dt} \right|_C, \quad (2.1.5)$$

where the right side is the term of collisions, which is proportional to the frequency ν_c at which binary interparticle collisions would occur. Anatoly Vlasov [58] demonstrated that, in certain plasmas, the collision term is negligible compared to the characteristic frequency of electron oscillations, the electron plasma frequency ω_{pe} , concluding that the collision term may be neglected. Most plasmas can be considered as collisionless. In this condition, equation the Boltzmann equation (2.1.5) is the Vlasov equation (2.1.1).

2.1.1 Properties of the Vlasov-Poisson system

The Vlasov equation has conserved quantities. The most important one is the distribution function f_j for each species when evaluated along their characteristic curves,

which correspond to particle trajectories. In an electrostatic plasma

$$\frac{d\mathbf{r}}{dt} = \mathbf{v}, \quad \frac{d\mathbf{v}}{dt} = \frac{q_j}{m_j} \mathbf{E}.$$

Accordingly, equation (2.1.1) is reduced to $df_j/dt = 0$. Thus, by following the trajectory of each particle composing the plasma at all times, the distribution function remains unchanged [59]. As a consequence, the number of particles remains constant in any volume of phase space of the plasma [35]. Generally, any analytic function of f_j is conserved [60], such as the entropy of the plasma. In conjunction with the electrostatic equations, the total energy of the plasma E_T , given by

$$E_T = \frac{1}{2} \sum_j m_j \int \int v^2 f_j d^3r d^3v + \frac{1}{2} \int \epsilon_0 |\mathbf{E}|^2 d^3r,$$

where the first term is the total particle kinetic energy and the second term is the electric field energy, is found to be a conserved quantity by evaluating the second moment of the Vlasov equation, implying that the energy of the plasma is constantly transferred between particles and the electric field.

Due to its collisionless character, the evolution of a system modeled by the Vlasov equation is reversible [57].

2.2 Linear approach to the Vlasov-Poisson system of equations

The Vlasov-Poisson system is solved through first order perturbative theory. Within this framework, equilibrium quantities are perturbed. For any quantity G , with its

equilibrium state G_0 , the perturbation G_1 verifies $G = G_0 + G_1$ and $|G_1| \ll |G_0|$. To first order, equations (2.1.4), (2.1.1) and (2.1.2) are reduced to

$$\left[\frac{\partial}{\partial t} + \mathbf{v} \cdot \nabla \right] f_{1,j} = - \frac{q_j}{m_j} \mathbf{E}_1 \cdot \nabla_v f_{0,j}, \quad (2.2.1)$$

$$\nabla \cdot \mathbf{E}_1 = \frac{\rho_1}{\epsilon_0}, \quad (2.2.2)$$

$$\nabla \times \mathbf{E}_1 = \mathbf{0}, \quad (2.2.3)$$

$$\rho_1 = \sum_j q_j \int f_{1,j} d^3v, \quad (2.2.4)$$

where (2.2.3) implies that $-\nabla\Phi_1 = \mathbf{E}_1$. The system considers initial conditions and periodic boundary conditions. The equilibrium state is assumed to be quasi-neutral, meaning that $\rho_0 = 0$. By further assuming that $\Phi_0 = 0$ at the boundaries, the equilibrium state has $\mathbf{E}_0(\mathbf{r}) = \mathbf{0}$.

2.2.1 Linear dispersion relation

The above system of equations can be solved through the characteristic curves method, according to Ref.[60], by considering that the initial perturbation is adiabatically turned on, that is, perturbations are zero at $t \rightarrow -\infty$ [59] and remain small at the instant of interest t . The perturbative distribution function is then

$$f_{1,j}(\mathbf{r}, \mathbf{v}, t) = - \frac{q_j}{m_j} \int_{-\infty}^t \mathbf{E}_1(\mathbf{r}, t') \cdot \nabla_v f_{0,j}(\mathbf{r}, \mathbf{v}) dt'. \quad (2.2.5)$$

A Fourier transform in space and Laplace transform in time can be used on this solution, since the problem considers initial conditions and periodic boundary con-

ditions,

$$f_{1,j,\mathbf{k},\omega} = -\frac{q_j}{m_j} \int_{-\infty}^t \exp [i (\mathbf{k} \cdot [\mathbf{r}'(t') - \mathbf{r}] - \omega[t' - t])] \mathbf{E}_{1,\mathbf{k},\omega} \cdot \nabla_v f_{0,j}(\mathbf{r}, \mathbf{v}) dt'. \quad (2.2.6)$$

The conditions for the unperturbed trajectories at $t' = t$ are $\mathbf{r}'(t) = \mathbf{r}$ and $\mathbf{v}'(t) = \mathbf{v}$ yielding straight lines, $\mathbf{r}'(t') = \mathbf{v}(t' - t) + \mathbf{r}$, $\mathbf{v}'(t') = \mathbf{v}$. The use of a Fourier-Laplace transform implies that ω and \mathbf{k} are constant in time. The variable ω can be expanded as $\omega = \omega_r + i\gamma$, where ω_r is the frequency of oscillation of the wave and γ is its damping or growth rate. Furthermore, quantities exhibit a dependency $a(\mathbf{r}, t) = a_{\mathbf{k}} \exp [i(\mathbf{k} \cdot \mathbf{r} - \omega t)]$, being $a_{\mathbf{k}}$ the amplitude of a . By replacing these results into the charge density, then into the Gauss law (2.2.2), and considering the electrostatic potential through $\mathbf{E}_{1,\mathbf{k},\omega} = -i\mathbf{k}\Phi_{1,\mathbf{k},\omega}$, the system of equations is reduced to the form

$$\varepsilon_{\mathbf{k},\omega} \Phi_{1,\mathbf{k},\omega} = 0, \quad (2.2.7)$$

where $\varepsilon_{\mathbf{k},\omega}$ is the dielectric function of the plasma, given by (details are given in Appendix A.1)

$$\varepsilon_{\mathbf{k},\omega} = 1 + \sum_j \frac{q_j^2}{\epsilon_0 m_j k^2} \int \frac{\mathbf{k} \cdot \nabla_v f_{0,j}}{\omega - \mathbf{k} \cdot \mathbf{v}} d^3v. \quad (2.2.8)$$

The dispersion relation is obtained by setting $\varepsilon_{\mathbf{k},\omega} = 0$, as non-trivial solutions for $\mathbf{E}_{1,\mathbf{k},\omega}$ are required. It is noted that $\varepsilon_{\mathbf{k},\omega}$ has no singularities, as $\gamma \neq 0$.

As the configuration studied in this work is the same as the used by Xu *et al.*

[27], a Maxwellian distribution is chosen as equilibrium configuration,

$$f_{0,j}(\mathbf{v}) = \frac{n_{0,j}}{[\sqrt{2\pi}v_{Tj}]^3} \exp\left[-\frac{v^2}{2v_{Tj}^2}\right], \quad (2.2.9)$$

with $v_{Tj} = \sqrt{k_B T_j / m_j}$ the initial particle thermal speed for each species, k_B is the Boltzmann constant and T_j the initial temperature of the species j . Without loss of generality, the axes of the system are aligned with \mathbf{k} . The integral in (2.2.8) is then reduced to one dimension and it can be written in terms of the plasma dispersion function $Z(\zeta_j)$ [61], where $\zeta_j = \omega / \sqrt{2} k v_{Tj}$, is the resonance parameter (details are given in Appendix A.2).

$$1 + \sum_j \frac{\omega_{pj}^2}{v_{Tj}^2 k^2} [1 + \zeta_j Z(\zeta_j)] = 0, \quad (2.2.10)$$

where $\omega_{pj} = \sqrt{q_j^2 n_{0,j} / \epsilon_0 m_j}$ is the plasma frequency of species j . This dispersion relation provides an infinite number of modes that may take in a plasma with equilibrium particle distributions of the form (2.2.9).

2.2.2 Linear modes in an electron-ion plasma

An electron-ion Maxwellian plasma with zero relative drift is considered throughout this work. In such a plasma, two modes can be analytically calculated through approximations of the $Z(\zeta_j)$ function, based on the location of the resonance zone with respect to the thermal speed of both species.

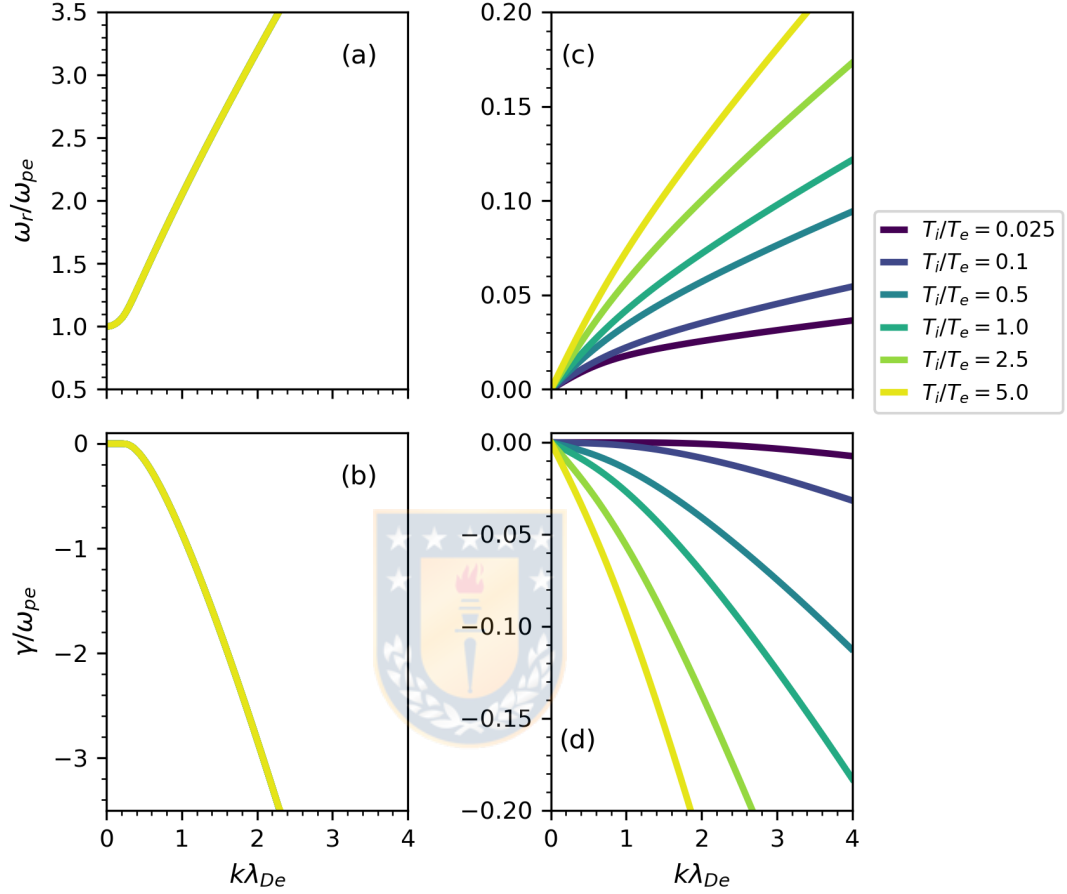


Figure 2.1: Least damped modes that solve the linear dispersion relation of an electrostatic unmagnetized plasma with Maxwellian electrons and ions (2.2.10). Mass ratio $m_i/m_e = 1836.153$ and several temperature ratios. Frequency (a) and damping rate (b) of the Langmuir mode, and frequency (c) and damping rate (d) of the IA mode. The Langmuir branch remains the same for the tested T_i/T_e ratios.

Langmuir and ion acoustic modes

Roots of the dispersion relation are shown in Figs.2.1 and 2.2 for $m_i = 1836.153m_e$, zero drift and temperature ratios $T_i/T_e = 2.5 \times 10^{-2}$, 1.0×10^{-2} , 5.0×10^{-1} , 1.0, 2.5 and 5.0. The least damped modes are shown in Fig.2.1. The Langmuir mode is shown

in Figs.2.1(a) and (b). It is related to electron dynamics and remains unaltered for the tested temperature ratios. As its phase speed is higher than the ion thermal range, it remains unaffected by details of the ions distribution. It is weakly damped for $k < 0.4\lambda_{De}^{-1}$ and it becomes heavily damped for shorter wavelengths, lasting a few oscillation cycles before its amplitude is zero. The IA mode is shown in Figs.2.1(c) and (d) and is related to the heavy ions dynamics, exhibiting an increase in frequency at larger T_i/T_e , implying a faster propagation for fixed k , but with an increasing damping. The mode is least damped for lower temperature ratios, remaining nearly zero for $k \lesssim 2\lambda_{De}^{-1}$. It is noted that this mode has nearly constant phase speed for long wavelengths, $k < 0.5\lambda_{De}^{-1}$.

Acoustic-like modes

The linear dispersion relation (2.2.10) also predicts infinite modes of higher order whose damping ratio is larger than that of the IA mode and the Langmuir mode. If the wave phase speed is in the order of the electron thermal speed or larger (not shown), they are termed electron-acoustic waves [62] and are due to electrons dynamic. For Maxwellian plasmas, they were predicted to be heavily damped to be observed in experiments and numerical simulations [63, 64].

There are also slower acoustic-like modes whose phase speed is in the order of the IA speed, and their dynamics involves the ions distribution. Low frequency acoustic-like branches are shown in Fig.2.2 for mass ratio $m_i/m_e = 1836.153$ and three temperature ratios, $T_i/T_e = 5.0$ [Figs.2.2(a) and (b)], $T_i/T_e = 1.0$ [Figs.2.2(c) and (d)] and $T_i/T_e = 2.5 \times 10^{-2}$ [Figs.2.2(e) and (f)]. The seven least damped higher order low frequency modes are shown. It is observed that they have larger frequencies

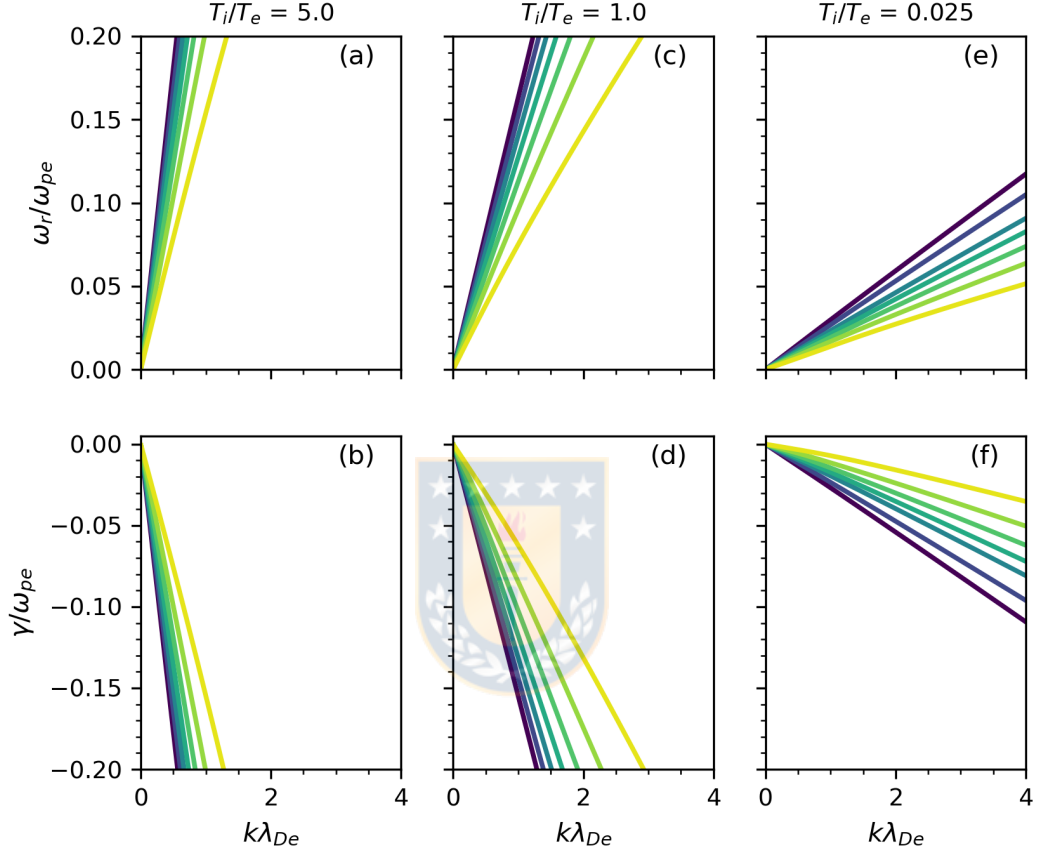


Figure 2.2: Roots of the linear dispersion relation (2.2.10) corresponding to low frequency higher order modes. Frequency and damping rates for $T_i/T_e = 5.0$ [(a) and (b)], $T_i/T_e = 1.0$ [(c) and (d)] and $T_i/T_e = 0.025$ [(e) and (f)]. Mass ratio $m_i/m_e = 1836.153$. The seven least damped higher order modes are shown for each temperature ratio.

than the IA mode, and therefore larger phase speed but also larger damping rates. These features are accentuated at high temperature ratio, as observed in Fig.2.2.

2.3 Nonlinear phenomena

2.3.1 Nonlinear Landau damping

The linear analysis ceases to be valid at perturbations of finite amplitude. Experimental [8] and theoretical works focused both on the short time evolution [4] and the asymptotic regime [2], show that γ varies in time for finite amplitudes. A large amplitude perturbation yields a stage of nonlinear damping, which deviates from the exponential decay (see $\varepsilon_e = 8.0 \times 10^{-3}$ in Fig. 2.3). If the amplitude is further increased (see $\varepsilon_e = 4.0 \times 10^{-2}$ in Fig. 2.3), damping occurs but it is arrested and the excited mode amplitude begins to grow till it saturates, oscillating irregularly in time, as seen in Fig. 2.3.

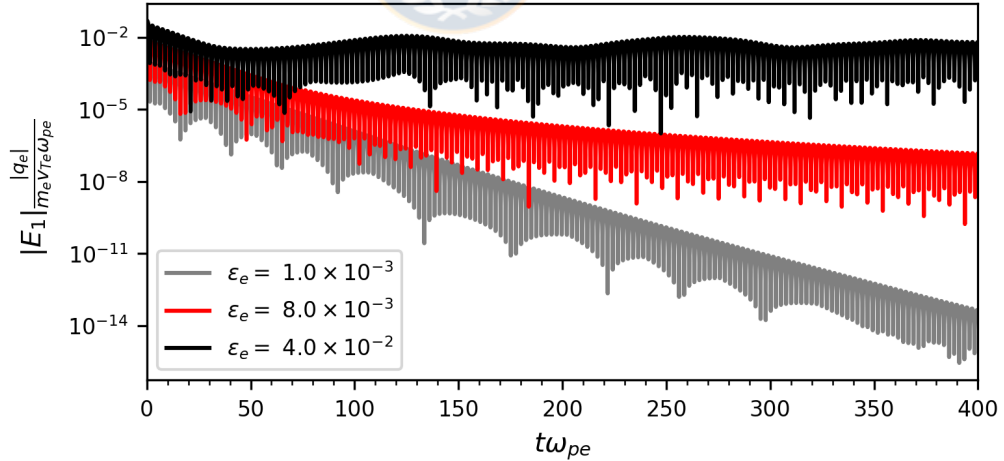


Figure 2.3: Evolution of the amplitude of the excited mode of the electric field, $m = 1$ in an electron plasma (immobile ions), for linear case, $\varepsilon_e = 1.0 \times 10^{-4}$, the slightly nonlinear damped, $\varepsilon_e = 8.0 \times 10^{-3}$, and the nonlinear case, $\varepsilon_e = 4.0 \times 10^{-2}$, being ε_e the amplitude of the initial perturbation.

At further instants, particles are trapped by the self-consistent potential, that is, a population of particles whose velocity is close to the phase velocity of the propagating wave oscillates irregularly about it, developing a BGK state as shown in Fig. 2.4.

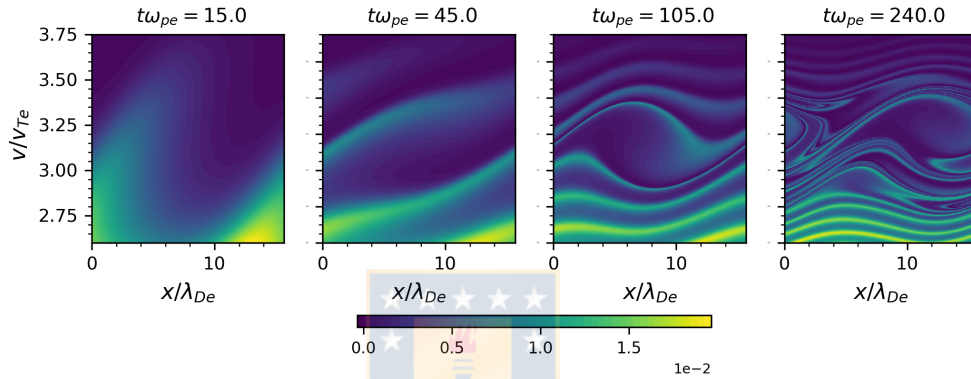


Figure 2.4: Evolution of the electrons distribution function f_e around the resonance zone for nonlinear Landau damping, considering immobile ions.

2.3.2 BGK states and electron holes

Nonlinear exact quasi-stationary solutions for the Vlasov-Poisson system were first found by Bernstein, Greene and Kruskal (BGK) [11] in 1957, by addressing the problem of trapped particles in an electrostatic plasma. These states are labeled as BGK.

Further works [46, 65, 66] obtain the same states through an improved method, ruling out singular solutions. Those works consider as a solution for a Maxwellian electron plasma exhibiting trapping, the distribution function f_e as a function of the

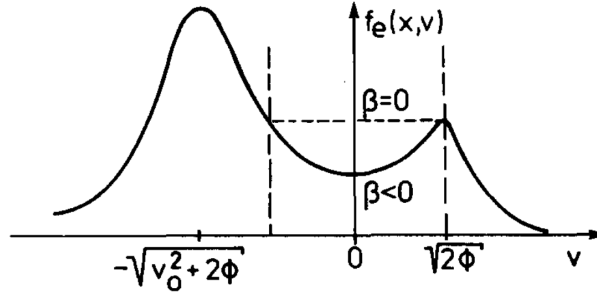


Figure 2.5: Schematic distribution function $f_e(E) = f_e(x, v)$ (2.3.1). The solution is centered in the trapping zone, in the range $-\sqrt{v_0^2 + 2\phi} < v < \sqrt{2\phi}$, where ϕ is the normalized electrostatic potential. Figure from Schamel, 1986 [28].

total electron energy $E = m_e v^2/2 + q_e \Phi$ given by [65]

$$f_e(E) = \frac{1 + k_0^2 \Psi/2}{\sqrt{2\pi}} \begin{cases} \exp \left[-\frac{1}{2} \frac{\sigma \left(\sqrt{2E} - [v_D - v_0] \right)^2}{v_{Te}^2} \right], & E > 0, \\ \exp \left[-\frac{1}{2} \frac{(v_D - v_0)^2}{v_{Te}^2} \right] \exp[-\beta E], & E < 0, \end{cases} \quad (2.3.1)$$

where k_0 provides the length of the trapping structure, Ψ is the perturbation amplitude, v_D is a possible drift of the equilibrium distribution, v_0 is the speed of the trapping structure, $\sigma = \text{sgn}(v)$, and β is a parameter that controls the degree of trapping, being $\beta < 0$ if there are trapped particles. The condition $E > 0$ means untrapped electrons, whereas $E < 0$ means trapped electrons. A schematic profile of the distribution is shown in Fig.2.5.

These states are characterized as quasi-stationary of electrostatic nature that persist longer times without undergoing Landau damping, and are inherently related to particle trapping [11, 12].

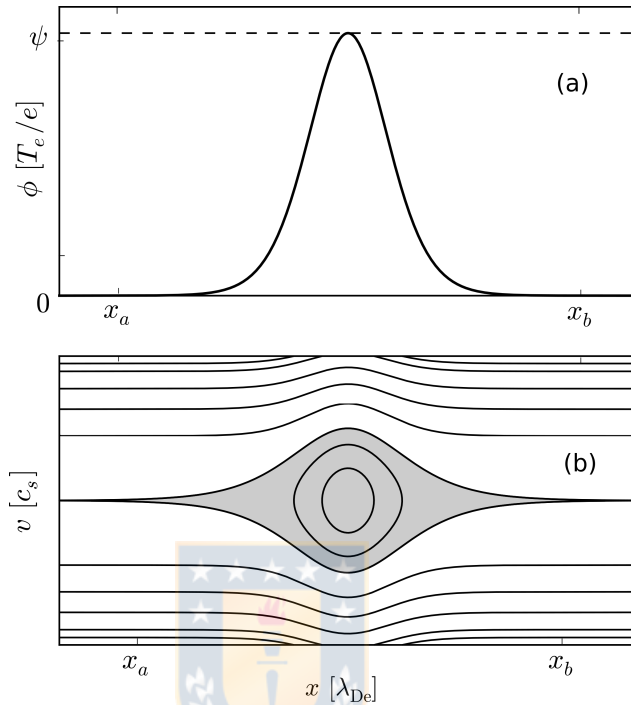


Figure 2.6: Scheme of the (a) electrostatic potential of amplitude ψ around an electron hole and (b) of the electron phase space with contours of constant energy E , depicting trapped electrons (gray region) and untrapped electrons (white region). Position is measured in electron Debye lengths, λ_{De} , velocity in IA speed, c_S and potential measured in energy per charge, T_e/e . Figure from Zhou and Hutchinson, 2017 [67].

Typical BGK states are particle holes, observed in phase space of one or several species as vortices moving with velocity v_0 , and exhibit a deficit of particle density within that region, surrounded by a particle excess, which is related to shielding [48]. Figure 2.6 shows the electrostatic potential and the phase space around a region of trapping of an electron distribution. Two regions can be distinguished in such a structure: **(i)** one for untrapped particles [white region in Fig.2.6(b)], corresponding to nearly free streaming particles, and one for trapped particles [gray

region in Fig.2.6(b)], corresponding to particles moving back and forth within the potential region.

2.3.3 Electron hole interaction with heavy ions

Electron holes can propagate in electron-ion plasmas. If their speed of propagation is in the order of the ion thermal speed, electron holes interact with heavy ions [48]. Hutchinson and Zhou developed a momentum theory for electron holes, by assuming that the transit time of ions through the hole is shorter than the time scale of the hole acceleration [47]. Their theory considers that ions interact with electron holes through four ways: by **(i)** transit through the trapping region, **(ii)** accumulation of ions within the trapping region due to transit, **(iii)** reflection and **(iv)** growth of the trapping potential.

In the frame of the hole, ions transiting through it change their incident velocities due to the acceleration of the hole, leading to an accumulation of ions within the region of trapping. In an inertial frame, this difference is [47]

$$v'_2 - v'_1 = \frac{dv'_0}{dt} \int_{x_1}^{x_2} \left[\frac{1}{v} - \frac{2}{v_1 + v_2} \right] dx, \quad (2.3.2)$$

where primed velocities are measured in an inertial frame, unprimed velocities are measured in the hole frame, the indices 1 and 2 indicate entrance and exit of the hole, respectively, v'_0 is the hole velocity and $v = \sqrt{v_1^2 - q_i \Phi(x)/m_i}$ is the ion velocity. These ions have kinetic energy larger than the electrostatic energy. In the opposite case, ions are reflected from the potential. Acceleration is not needed for reflection to occur. The growth in the depth of the trapping potential also affects the flow of

ions, as seen from the energy equation in the frame of the hole,

$$v_2 - v_1 = \frac{q_i}{m_i v_1^2} \int_{x_1}^{x_2} \frac{v_1}{v} \frac{d\Phi}{dt} dx, \quad (2.3.3)$$

and lead to further accumulation of ions within the hole [47].

2.3.4 Ion acoustic solitons

Solitons are nonlinear structures that propagate without dispersion, retaining their properties unaltered. They were predicted in 1967 by Washimi and Tanuti [36] from fluid plasma equations. These structures propagate with speed v_s such that $1 < v_s/c_S \lesssim 1.6$, where c_S is the IA speed. Solitons can be observed as a compressive pulse in the particle density as shown in Fig.2.7. If the charge of the species is positive, the soliton yields a positive potential.

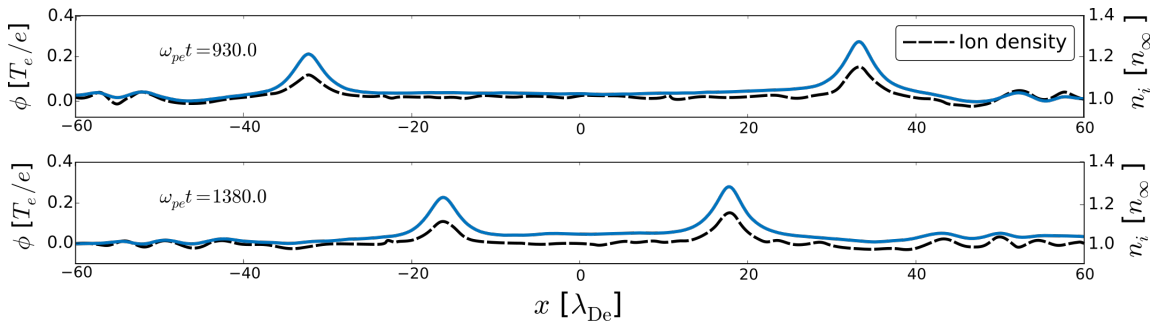


Figure 2.7: Ion acoustic solitons approaching. The figure depicts the ions density n_i (black dashed line) and the electrostatic potential ϕ (blue solid line). Position is measured in electron Debye lengths, λ_{De} , ions density in the equilibrium density, n_∞ , and potential measured in T_e/e . Figure from Zhou and Hutchinson, 2018 [43].

The mechanism behind these structures involves a nonlinear resonant wave coupling between waves allowed by the dispersion relation. In the case of IASs, the

dispersion relation is that of the IAWs [59], shown in Fig.2.1(c), approximated to small k , where the phase speed is nearly constant. The strength of the coupling depends on the relative phase speed between the waves, being maximum when they propagate at the same speed [35]. As the phase speed of IAWs changes for larger k , further waves are not excited and the soliton is established.

Ion solitons have been theoretically predicted and observed to couple to slow electron holes and to propagate jointly in position space [41–45], considering a kinetic approach. In this structure, slow electrons are trapped around the potential of the soliton. This interaction can be modified by the temperature of the ions distribution T_i/T_e as shown by Zhou and Hutchinson [43] in an electron-ion plasma. At larger T_i/T_e , kinetic effects enter in the dynamics and the IA mode behind the IASs becomes heavily damped, as there is a larger number of resonant ions. The structure is then decoupled and the electron hole propagates alone.

3 Basis of the numerical integration and numerical implementation

The present chapter is devoted to the description of the used normalization, and to considerations on position, velocity and time scales. Also, both the theoretical and the numerical implementation behind the integration of the Poisson equation, and of the symplectic integration used to solve the Vlasov equation are described.

3.1 Normalizations and species scales

The simulation is performed for the one dimensional case. In order to proceed, the variables and functions are nondimensionalized as follows.

- Time t , time step Δt and frequencies ω are normalized with respect to electron plasma frequency ω_{pe} , $\bar{t} \equiv \omega_{pe} t$, $\Delta \bar{t} \equiv \omega_{pe} \Delta t$, $\bar{\omega} \equiv \omega / \omega_{pe}$.
- Position \mathbf{r} , lengths L and wavevectors \mathbf{k} are normalized with respect to the electron Debye length λ_{De} , $\bar{\mathbf{r}} \equiv \mathbf{r} / \lambda_{De}$, $\bar{L}_{x,y,z} \equiv L_{x,y,z} / \lambda_{De}$, $\bar{\mathbf{k}} \equiv \mathbf{k} \lambda_{De}$.
- Velocities are normalized with respect to the electron thermal velocity v_{Te} , $\bar{\mathbf{v}} \equiv \mathbf{v} / v_{Te}$. It is also needed to normalize velocities with respect to their own thermal velocity, $\bar{\mathbf{v}}_j \equiv \mathbf{v} / v_{Tj}$, to describe the species j . Other thermal

velocities are $\bar{v}_{Tj} \equiv v_{Tj}/v_{Te}$. The associated wavevector in velocity space is normalized as $\bar{\boldsymbol{\mu}}_j \equiv \boldsymbol{\mu}v_{Tj}$.

- Electric charges are normalized with respect to the module of the electron charge $|q_e|$, as $\bar{q}_j \equiv q_j/|q_e|$.
- Electric field is normalized as $\bar{\mathbf{E}} \equiv \mathbf{E}(|q_e|/m_e\omega_{pe}v_{Te})$, the charge density is normalized as $\bar{\rho} = \rho(|q_e|\lambda_{De}/m_e\omega_{pe}v_{Te}\epsilon_0)$, and the electrostatic potential is normalized as $\bar{\Phi} \equiv \Phi(|q_e|/m_e\omega_{pe}v_{Te}\lambda_{De})$.
- The species masses and densities are normalized with respect to the electron mass, m_e , as $\bar{m}_j = m_j/m_e$, and to the total electron particle density n_e as $\bar{n}_j \equiv n_j/n_e$.
- The distribution function is normalized considering that the system is one-dimensional, $\bar{f}_j \equiv v_{Te}f_j/n_e$. As in the case of the velocity, the distribution is also normalized with respect the thermal velocity of its own species, $\tilde{f}_j \equiv v_{Tj}f_j/n_e$.

The numerical solution of the system involves solving two species, different scales arise.

- The integration considers the same time scale for all species because all the species affect each other through changes in the electric field at all times. The use of different scales would lead to problems in solving common quantities, such as the electric field and the charge density. For instance, in between two successive instants in the scale of the heaviest species of the plasma, there are several instants in the scale of the lightest species. Therefore, the contribution of each species would be unbalanced.

- The integration considers the same position scale for all species, by a similar argument. When calculating the charge density and the electric field in a certain space region, there will not be a contribution of all species at the same points of the grid, leading to problems in estimating these quantities.
- The integration considers individual velocity scales for each species. In the case of an electron-ion plasma with mass ratio $m_i/m_e = 1836$, for instance, most of the dynamics of electrons occurs in a range of $[-8, 8]v_{Te}$, whereas that of ions, occurs in a range of $[-0.17, 0.17]v_{Te}$. If the same scale is used, the grid would contain several nodes for solving electrons dynamics, but it would have considerably less for solving ions dynamics. The use of individual velocity scales allows solving both species with the same number of nodes just by re-scaling the velocity dependency with the respective thermal velocity to the electrons velocity scale. Also, there are no common quantities defined in velocity space.

Regarding the previous considerations about species scales, the system of equations to numerically solve is the following

$$\left[\frac{\partial}{\partial t} + \bar{v}_{Tj} \bar{v}_j \frac{\partial}{\partial \bar{x}} + \frac{\bar{q}_j}{\bar{m}_j \bar{v}_{Tj}} \bar{E} \frac{\partial}{\partial \bar{v}_j} \right] \tilde{f}_j = 0, \quad (3.1.1)$$

$$-\frac{\partial \bar{\Phi}}{\partial \bar{x}} = \bar{E}, \quad (3.1.2)$$

$$-\frac{\partial^2 \bar{\Phi}}{\partial \bar{x}^2} = \sum_j \bar{q}_j \int_{-\infty}^{\infty} \tilde{f}_j d\bar{v}_j. \quad (3.1.3)$$

The coefficients $\bar{v}_{Tj} = \sqrt{T_j/\bar{m}_j}$ and $\bar{q}_j/\bar{m}_j \bar{v}_{Tj} = \bar{q}_j/\sqrt{\bar{m}_j T_j}$ in the Vlasov equation allow to perform the integration on the velocity space of each species and then to re-scale it to the electrons velocity scale.

3.2 Integration of the Vlasov-Poisson system

3.2.1 Integration of the electric field

The electric field in this scheme is calculated through equations (3.1.2) and (3.1.3), which require the distribution functions \tilde{f}_j . These equations can be solved through Fourier transform. Let $\tilde{f}_{j,\bar{k}} \equiv \mathcal{F}_{\bar{k}} [\tilde{f}_j]$ and $\bar{\Phi}_{\bar{k}} \equiv \mathcal{F}_{\bar{k}} [\bar{\Phi}]$ the Fourier transforms in position space of the distribution function and the electrostatic potential, respectively. Hence, the Fourier transform of (3.1.3) yields

$$\bar{k}^2 \bar{\Phi}_{\bar{k}} = \sum_j \bar{q}_j \int_{-\infty}^{\infty} \tilde{f}_{j,\bar{k}} d\bar{v}_j.$$

The electric field is then determined through the Fourier transform of equation (3.1.2), $-i\bar{k}\bar{\Phi}_{\bar{k}} = \bar{E}_{\bar{k}}$, from which the electric field is obtained as

$$\bar{E} [\tilde{f}_j] = \mathcal{F}_{\bar{x}}^{-1} \left[-\frac{i}{\bar{k}} \sum_j \bar{q}_j \int_{-\infty}^{\infty} \tilde{f}_{j,\bar{k}}(\bar{v}_j, \bar{t}) d\bar{v}_j \right].$$

The quasi-neutrality condition is implemented by setting $\bar{E}_{\bar{k}=0} = 0$, meaning that the mean electric field is zero in the plasma at all times.

Numerical implementation

The calculation is numerically performed in the integrator through the Fast Fourier Transform of the West (FFTW) algorithm. The use of periodic boundary conditions in position space makes suitable the use of the Fourier transform. The electric field is then obtained through the inverse FFTW. Let be N_v the number of nodes of the

velocity grid on which the distribution function is defined. The electric field at each time step is then calculated as

$$\bar{E} = \text{IFFT}_{\bar{x}} \left[-\frac{i}{\bar{k}} \sum_j \bar{q}_j \Delta \bar{v}_j \sum_{n=1}^{N_v} \text{FFT}_{\bar{k}} \left[\tilde{f}_j \right] \right],$$

where the integral over the velocity space has been discretized into a summatory from 1 to N_v , and $\Delta \bar{v}_j = \Delta v / v_{Tj}$ is the resolution of the velocity grid of the species j .

3.2.2 Integration of the Vlasov equation

Symplectic operators and integrators

Symplectic operators are related to Hamiltonian systems, that is, physical systems consisting of whether discrete particles or continuum media, whose dynamics can be represented through a Hamiltonian function and evolve according to Hamilton equations [68, 69]. A symplectic operator is a linear operator which acts on the phase space coordinates of a Hamiltonian system or quantities depending on those coordinates that constitutes a canonical transformation [70] and verifies Liouville's theorem, conserving volumes in phase space [71], preserving details of the phase space of the system.

Symplectic integrators are numerical integration schemes constructed with symplectic operators. In defining numerical integrators, an approximate Hamiltonian \tilde{H} arises, related to a flow map that evolves the system in a similar way than the exact Hamiltonian H does [72]. The relation between the exact Hamiltonian and its

approximation is obtained through a series expansion [73],

$$\tilde{H} = H + \Delta t^n H_n + \mathcal{O}(\Delta t^{n+1}),$$

where n is the order of the integrator. The expansion means that \tilde{H} is close to the original Hamiltonian except for variations of the n -th order in the time step Δt . Therefore, in a conservative Hamiltonian system, \tilde{H} exhibit variations about H , ensuring bounded variations in the Hamiltonian and the total energy, in cases when the total energy is equivalent to its Hamiltonian. Therefore, the main features of a symplectic integrator are the preservation of details of phase space of the system, remaining close to its actual dynamics, and the conservation of the total energy in a conservative system, being adequate for long term simulations.

Other methods, such as the Runge-Kutta family of integrators, have been reported to be unstable for long time dynamics, introducing numerical dissipation and changing the evolution of the system [74, 75]. These methods are not based on dynamical equations, and hence they conserve neither the phase space structure nor the energy of the system.

Symplectic integration of the Vlasov equation

The Vlasov equation can be regarded as the evolution of the distribution function of the species j given the Hamiltonian operator $\mathbb{H} = \mathbb{T} + \mathbb{V}$,

$$\mathbb{H}f_j = \frac{\partial f_j}{\partial t}, \tag{3.2.1}$$

where the non-commuting operators \mathbb{T} and \mathbb{V} are defined as

$$\mathbb{T} \equiv -\mathbf{v} \cdot \nabla, \quad \mathbb{V} \equiv -\frac{q_j}{m_j} \mathbf{E} \cdot \nabla_v.$$

Thus, the Vlasov equation is related to the conservative Hamiltonian \mathbb{H} , and the use of symplectic integration to estimate the evolution of the distribution function f_j is justified. Given a time interval Δt and all the quantities at the instant t , the distribution function at $t + \Delta t$ is straightforwardly integrated.

$$f_j(\mathbf{r}, \mathbf{v}, t + \Delta t) = \exp[\Delta t (\mathbb{T} + \mathbb{V})] f_j(\mathbf{r}, \mathbf{v}, t), \quad (3.2.2)$$

This solution is valid as long as the operators \mathbb{T} and \mathbb{V} do not explicitly depend on time. It is noted that although \mathbf{E} does vary in time, it is formally a function of f_j , hence, it does not explicitly depend on t . Therefore, if the time interval of interest is divided into M partitions whose width is Δt , then the general solution of the Vlasov equation for the species j is given by [74]

$$f_j(\mathbf{r}, \mathbf{v}, t) = [\exp(\Delta t [\mathbb{T} + \mathbb{V}])]^M f_j(\mathbf{r}, \mathbf{v}, 0),$$

where the operator \mathbb{V} is updated before each application. An approximation is made to estimate the exponential. In the construction of symplectic integrator methods, it has been demonstrated that the exponential operator in (3.2.2) can be expanded as [76]

$$\exp[\Delta t (\mathbb{T} + \mathbb{V})] = \prod_{j=1}^n \exp[\Delta t \tau_j \mathbb{T}] \exp[\Delta t \nu_j \mathbb{V}] + \mathcal{O}(\Delta t^{r+1}), \quad (3.2.3)$$

where n is the number of operator pairs, r is the order of the integrator, and τ_j and ν_j are real positive coefficients. These conditions ensure that in solving the system the physics always evolves covariantly with time. Negative coefficients would imply that the system evolves backward in time [77], which produces nonphysical results in non time-invariant systems. Each of the exponential operators is symplectic since each of them comes from a canonical transformation.

In the solution (3.2.3) the operators \mathbb{T} and \mathbb{V} are applied separately on the initial condition while truncating the operator up to terms of order Δt^r . Each operator acts on independent variables of f_j , therefore, each dependency is independently solved. Such a solution is based on the Strang splitting scheme [78], which, although it uses a time advance operator based on finite differences (Lax-Wendroff operators), it splits the differential equation in the same way.

The order r of the integrator is determined by comparing the obtained solution with the Baker-Campbell-Hausdorff expansion of the exact exponential [74], and choosing the coefficients τ_j and ν_j such that terms up to order Δt^r vanish. Along with conditions of decomposition, the coefficients are then determined for the integrator. In some cases there might be several choices of coefficients, in which case, they are determined through a minimization process for the coefficient proportional to Δt^{r+1} .

Advections and the used integrator

In analogy with the solution (3.2.2), solving each of the exponentials in (3.2.3) implies solving equations

$$\left[\frac{\partial}{\partial t} + \tau_l \mathbf{v} \cdot \nabla \right] f_j = 0, \quad (3.2.4)$$

$$\left[\frac{\partial}{\partial t} + \nu_l \frac{q_j}{m_j} \mathbf{E} \cdot \nabla_v \right] f_j = 0, \quad (3.2.5)$$

which are advection equations related to the \mathbb{T} operator [eq. (3.2.4)], and to the \mathbb{V} operator [eq. 3.2.5]. In this sense, the problem of integrating the Vlasov equation has been reduced to solve advections of the distribution function f_j on each of its dependencies. For the one dimensional problem with the normalized variables, the above set of equations to solve is then

$$\left[\frac{\partial}{\partial \bar{t}} + (\tau_l \bar{v}_{Tj}) \bar{v}_j \frac{\partial}{\partial \bar{x}} \right] \tilde{f}_j = 0, \quad (3.2.6)$$

$$\left[\frac{\partial}{\partial \bar{t}} + \left(\frac{\nu_l \bar{q}_j}{\bar{m}_j \bar{v}_{Tj}} \right) \bar{E} \frac{\partial}{\partial \bar{v}_j} \right] \tilde{f}_j = 0, \quad (3.2.7)$$

where the electric field \bar{E} must be calculated before each advection (3.2.7) is performed. In this work, these equations are solved through Fourier transforms, that is, each advection is Fourier transformed on the variable of integration, and then it is inverse transformed. Thus, the advection equations to solve are

$$\left[\frac{\partial}{\partial \bar{t}} + i (\tau_l \bar{v}_{Tj}) \bar{v}_j \bar{k} \right] \tilde{f}_{j,\bar{k}} = 0,$$

$$\left[\frac{\partial}{\partial \bar{t}} + i \left(\frac{\nu_l \bar{q}_j}{\bar{m}_j \bar{v}_{Tj}} \right) \bar{E} \bar{\mu}_j \right] \tilde{f}_{j,\bar{\mu}_j} = 0,$$

where $\tilde{f}_{j,\bar{k}} \equiv \mathcal{F}_{\bar{k}} [\tilde{f}_j]$ and $\tilde{f}_{j,\bar{\mu}_j} \equiv \mathcal{F}_{\bar{\mu}_j} [\tilde{f}_j]$ are the Fourier transform of \tilde{f}_j in position space, with conjugated variable \bar{k} , and in velocity space, with conjugated variable $\bar{\mu}_j$. The solutions for each advection for a time step $\Delta\bar{t}$ are

$$\begin{aligned}\tilde{f}_{j,\bar{k}}(\bar{v}_j, \bar{t} + \Delta\bar{t}) &= \tilde{f}_{j,\bar{k}}(\bar{v}_j, \bar{t}) \exp[-i(\tau_j \bar{v}_{Tj}) \bar{v}_j \bar{k} \Delta\bar{t}], \\ \tilde{f}_{j,\bar{\mu}_j}(\bar{x}, \bar{t} + \Delta\bar{t}) &= \tilde{f}_{j,\bar{\mu}_j}(\bar{x}, \bar{t}) \exp\left[-i\left(\frac{\nu_j \bar{q}_j}{\bar{m}_j \bar{v}_{Tj}}\right) \bar{E} [\tilde{f}_j] \bar{\mu}_j \Delta\bar{t}\right].\end{aligned}$$

Numerical implementation

Fourier transforms are calculated through the FFTW algorithm. Although it is suitable for periodic boundary conditions in position space, its use is not trivial in the velocity space. Dependencies are then forced to be periodic by taking a large enough velocity range, so that the distribution functions are nearly zero at the boundaries $\bar{v}_{j,\max/\min}$. Thus, the periodicity condition

$$\tilde{f}_j(\bar{x}, \bar{v}_{j,\max}, t) = \tilde{f}_j(\bar{x}, \bar{v}_{j,\min}, t),$$

is nearly fulfilled at all times and all positions, and the use of the FFTW algorithm is suitable for the integration over the velocity space.

In regard of the velocity dependency, a plasma may develop filamentation, a process related to the streaming of free particles, observed in the species phase space as filaments whose width in the velocity dependency is reduced as the plasma evolves. In simulations, filamentation limits the maximum instant to advance the plasma as structures whose width is in the order of $\Delta\bar{v}_j$ cannot be solved properly. The development of those lengths in velocity space is damped by the introduction of a

Gaussian-like filter \mathbb{F} [79], given by

$$\mathbb{F}(\bar{\mu}_j) = \exp \left[-36 \left(\frac{\bar{\mu}_j}{\max[\bar{\mu}_j]} \right)^{36} \right] \quad (3.2.8)$$

applied as a convolution to the distribution function of the species j in each velocity advection. If \tilde{f}_j^0 denotes the distribution before any advection is applied and \tilde{f}_j^1 denotes the distribution function after being advected, direct integration yields

$$\begin{aligned} \tilde{f}_j^1 &= \text{IFFT}_{\bar{x}} \left[\text{FFT}_{\bar{k}} \left[\tilde{f}_j^0 \right] \exp \left[-i (\tau_l \bar{v}_{Tj}) \bar{v}_j \bar{k} \Delta \bar{t} \right] \right], \\ \tilde{f}_j^1 &= \text{IFFT}_{\bar{v}_j} \left[\mathbb{F}(\bar{\mu}_j) \text{FFT}_{\bar{\mu}_j} \left[\tilde{f}_j^0 \right] \exp \left[-i \left(\frac{\nu_l \bar{q}_j}{\bar{m}_j \bar{v}_{Tj}} \right) \bar{E} \bar{\mu}_j \Delta \bar{t} \right] \right]. \end{aligned}$$

The values of the coefficients are determined by the specific integrator. In this work, the second order integrator of McLachlan and Atela [80] is used with advection in velocity as the first step, consisting of four advections in the order $\mathbb{V} - \mathbb{T} - \mathbb{V} - \mathbb{T}$, and whose coefficients, in accordance to (3.2.3) are

$$\tau_1 = 0, \quad \nu_1 = \frac{1}{\sqrt{2}}, \quad \tau_2 = \nu_1, \quad \nu_2 = 1 - \nu_1, \quad \tau_3 = \nu_2, \quad \nu_3 = 0.$$

As a closing remark, it is observed that although in this scheme the distribution function, the electric field, and any other related quantity, are fields defined on an Eulerian grid in position space, velocity space and time, the evaluation along trajectories is of Lagrangian nature. Thus, the integration scheme is labeled as semi-Lagrangian.

The previous numerical calculations to required to solve the Vlasov-Poisson sys-

tem are implemented in a Julia (v 1.3.1) code through the library `Vlasova.jl` created by J. A. Gidi, from the Departamento de Física in Universidad de Concepción.

3.3 Resolution of the linear dispersion relation

The roots of the linear dispersion relation are obtained by solving (2.2.10). In order to do this, the plasma dispersion function is calculated through the scaled complement error function, in the form

$$Z(\zeta_j) = i\sqrt{\pi} \operatorname{erfcx}(-i\zeta_j), \quad (3.3.1)$$

where ζ is the resonance parameter $\zeta = \omega/v_T k$, for a given array of k . The library `SpecialFunctions.jl` of Julia language (v 1.3.1). It is numerically calculated through the C `math` standard library [81].

The resolution of (2.2.10) is performed through the Muller algorithm and implemented in a Python code created by R. E. Navarro from the Departamento de Física in Universidad de Concepción. Muller algorithm uses a second order approximation of the derivative used in the Newton-Raphson method [82] to estimate the zeros of the dielectric function (2.2.8). The algorithm is first provided with seeds consisting of points of the ζ -grid which are close to actual zeros of $\varepsilon_{k,\omega}$ for the first wavenumber k_0 . Branches corresponding to modes of the linear dispersion relation are obtained by using each of the roots as a seed for the following wavenumbers. The calculation for the following two wavenumber uses the previous roots as seeds. The roots for the remaining wavenumbers are estimated through a second degree polynomial extrapolation with the three last roots along the same branch.

3.4 Nonlinear curve fit

Curve fittings in this work are made with the Julia (v. 1.3.1) library `LsqFit.jl`, which uses a nonlinear generalization of the least square method called Levenberg-Marquardt method [83].



4 Single wave excitation - Damped perturbations in a Maxwellian electron-ion plasma

Throughout this chapter, when mobile, ions are Maxwellian distributed at the equilibrium configuration, considering a mass ratio $\bar{m}_i = 1836.153$, and being isothermal to electrons, $\bar{T}_i = 1.0$,

$$\tilde{f}_{0,i}(\bar{v}_i) = \frac{1}{\sqrt{2\pi}} \exp\left[-\frac{1}{2}\bar{v}_i^2\right],$$

where the condition of quasi-neutrality, $\bar{n}_i = 1.0$, $\bar{q}_i = 1.0$ is used. The first mode of the electric field is excited, with wavenumber $\bar{k}_1 = 0.4$ and perturbative amplitude ε_e ,

$$\tilde{f}_e(\bar{x}, \bar{v}_e, 0) = [1 + \varepsilon_e \cos(\bar{k}_1 \bar{x})] \tilde{f}_{0,e}(\bar{v}_e), \quad (4.0.1)$$

with $\tilde{f}_{0,e}(\bar{v}_e)$ a Maxwellian distribution of the same form as $\tilde{f}_{0,i}(\bar{v}_i)$. In literature, when considering electron-ion plasmas with both species as kinetic, it is customary to perturb electrons only, while heavy ions are static due to the inertia difference. However, when the system is perturbed by a sudden potential, there is a sudden force acting on all the species.

In order to estimate the perturbation amplitude of the ions distribution, it is assumed that the particle dynamics is nonrelativistic and slightly deviate from their initial position x_0 with impulsive forcing $F(x_0, t) = q_j E_0 \sin(k_1 x_0) \delta(t)$, in accordance with the sudden perturbation. The equations of motion lead to trajectories

$$v(t) = \frac{q_j}{m_j} E_0 \sin(k_1 x_0) + v_0, \quad x(t) = \left[\frac{q_j}{m_j} E_0 \sin(k_1 x_0) + v_0 \right] t + x_0,$$

where v_0 is the initial velocity of the particle, corresponding to the equilibrium configuration. According to this solution, the deviation of the particle from its equilibrium trajectory is proportional to q_j/m_j at a given instant t prior to the plasma evolution. Thus, the perturbation amplitude ratio of both distributions is $\varepsilon_i/\varepsilon_e = \bar{q}_i/(\bar{q}_e \bar{m}_i) = -5.447 \times 10^{-4}$ and the ion initial distribution is given by

$$\tilde{f}_i(\bar{x}, \bar{v}_i, 0) = \left[1 + \frac{\bar{q}_i}{\bar{q}_e \bar{m}_i} \varepsilon_e \cos(\bar{k}_1 \bar{x}) \right] \tilde{f}_{0,i}(\bar{v}_i). \quad (4.0.2)$$

In the following sections, macroscopic quantities and reduced distribution functions are observed for both electrons and ions, considering the mode $\bar{k}_1 = 0.4$ and position space length $\bar{L}_x = 5\pi$. Two amplitudes are tested, one corresponding to the linear regime, $\varepsilon_e = 1.0 \times 10^{-3}$, and one below but close to the critical amplitude $\varepsilon_{e,C}$, $\varepsilon_e = 8.0 \times 10^{-3}$.

4.1 Electric field energy and spectra

The most notorious macroscopic quantity which allows identifying the effects of mobile ions is the amplitude of the excited mode of the electric field $|\bar{E}_1|$. The present

simulations obtain qualitatively the same results as those from Xu *et al.* [27] for the damped regime, as seen in Figs.4.1(a) and (b).

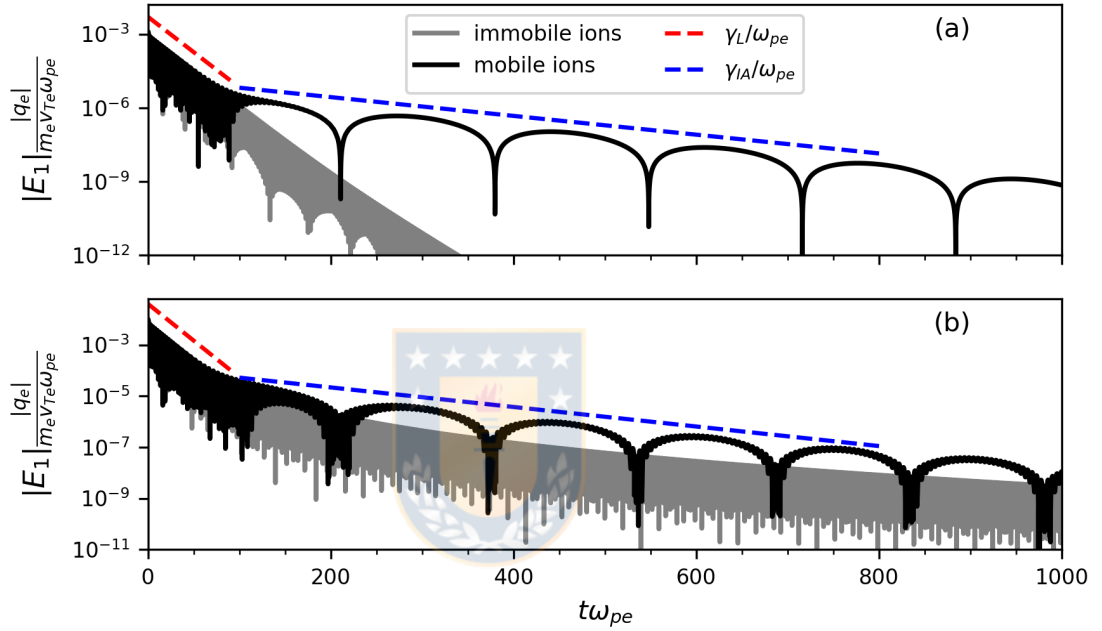


Figure 4.1: Evolution of the amplitude of the first mode of the electric field $|\bar{E}_1|$ for (a) $\varepsilon_e = 1.0 \times 10^{-3}$ and (b) $\varepsilon_e = 8.0 \times 10^{-3}$, with and without mobile ions. The damping rates of the observed modes are shown for the LW (red-dashed line) and the IAW (blue-dashed line).

In the excited mode, it is observed that the effect of the ions dynamics is dominant in both cases, but an increase in ε_e allows fast oscillations to persist with small amplitude. In these cases, two oscillation frequencies are observed in the envelope of $|\bar{E}_1|$, one related to electron dynamics during $t\omega_{pe} < 60$ whose damping rate coincides with that of Langmuir waves for the perturbed wavenumber, $\bar{\gamma}_L = -6.6079 \times 10^{-2}$, and the other one corresponds to low frequency oscillations for $t\omega_{pe} > 100$ with damping rate coinciding with that of IAWs for the excited wavenumber, $\bar{\gamma}_{IA} = -8.7939 \times 10^{-3}$.

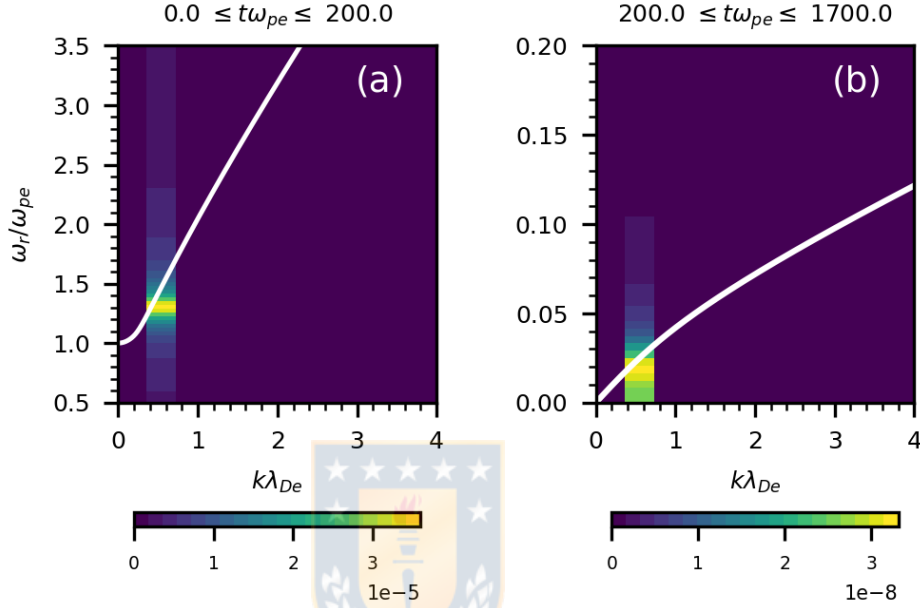


Figure 4.2: Electric field spectra $|\bar{E}_{k,\omega}|$ of $\epsilon_e = 1.0 \times 10^{-3}$ simulations for (a) high frequency early-range and (b) low frequency later-range. Roots of the linear dispersion relation are shown for comparison.

A comparison between the roots of the linear dispersion relation (2.2.10) and the electric field spectra $|\bar{E}_{k,\omega}|$ of both perturbative amplitudes ϵ_e (Figs.4.2 and 4.3, respectively) confirms the excitation Langmuir and IA waves with frequencies $\bar{\omega}_L = 1.2852$ and $\bar{\omega}_{IA} = 1.8265 \times 10^{-2}$, respectively, as interpreted by Xu *et al.*[27]. Both are the least damped modes of the dispersion relation (2.2.10).

For $\epsilon_e = 8.0 \times 10^{-3}$, high frequency LW oscillations are still observable in $|\bar{E}_1|$ [Fig.4.1(b)] and in $|\bar{E}_{k,\omega}|$ [Fig.4.3(b)], but with amplitude one order of magnitude below that of the IAW. These results confirm the modes found by Xu *et al.* for this

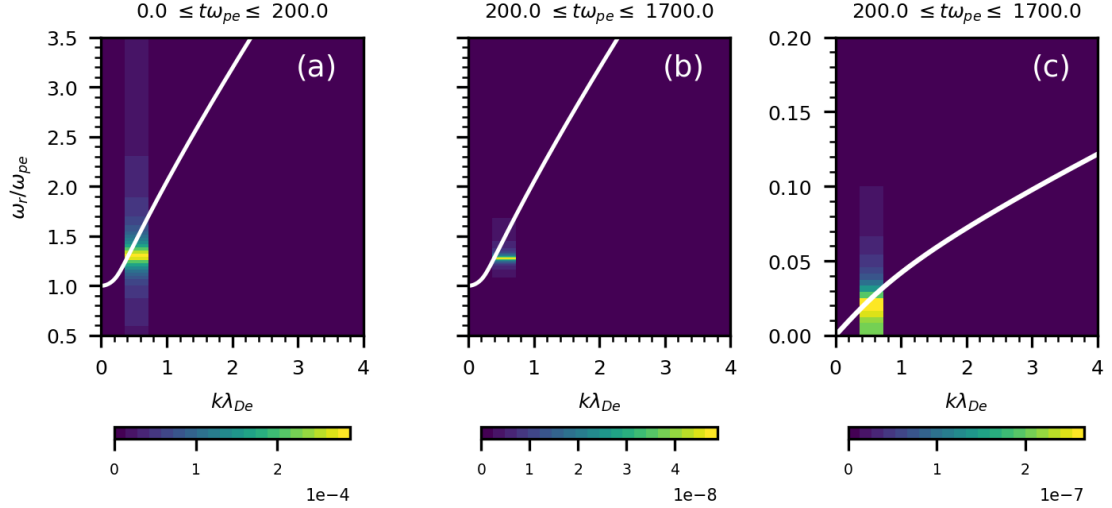


Figure 4.3: Electric field spectra $|\bar{E}_{k,\omega}|$ of $\varepsilon_e = 8.0 \times 10^{-3}$ simulations for (a) high frequency early-range, (b) high frequency later-range and (c) low frequency later-range (right panel). Roots of the linear dispersion relation are shown for comparison.

plasma.

4.2 Behavior in velocity domain

The low amplitudes allow the use of linear theory for the estimation of the overall behavior of the distribution functions (2.2.5). Since the equilibrium distribution of both species is Maxwellian, the charge indicates that the perturbative effects around the phase velocity of the excited IAW, $\bar{v}_{\phi,IA}$ should be opposite on the electrons and heavy ions distribution, and that the amplitude of the variations in the latter should be of lower amplitude.

The position averaged variations of the distribution function $\left\langle \delta \tilde{f}_j \right\rangle_{\bar{x}}(\bar{v})$ is fol-

lowed for both species. This quantity is given by

$$\langle \delta \bar{f}_j \rangle_{\bar{x}}(\bar{v}) = \frac{1}{\bar{L}_x} \int_0^{\bar{L}_x} [\bar{f}_j(\bar{x}, \bar{v}, \bar{t}) - \bar{f}_{0,j}(\bar{v})] d\bar{x},$$

where f_j and v have been normalized with respect to electron quantities. According to the normalization, the relation between \bar{f}_j and \tilde{f}_j , obtained from the simulations, is $\bar{f}_j = \bar{n}_j / \bar{v}_{Tj} \tilde{f}_j$. It is noted that as the system is symmetric in velocity space, the same dynamics occurs at $\bar{v} < 0$ and at $\bar{v} > 0$. Therefore, only one range is shown. Also, the overall behavior with both perturbative amplitudes is qualitative the same except by the level of the amplitudes, so that only one case is shown ($\varepsilon_e = 8.0 \times 10^{-3}$). The resonance zone about the phase speed of the IAW $\bar{v}_{\phi,IA} = \bar{\omega} / \bar{k} = 4.662 \times 10^{-2}$ is followed.

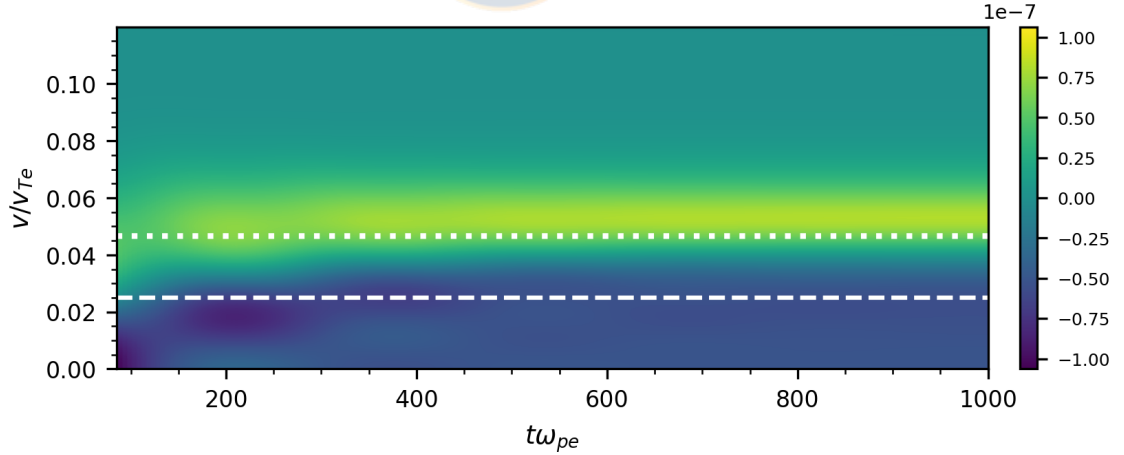


Figure 4.4: Evolution of the variation position-averaged ions distribution function, $\langle \delta \bar{f}_i \rangle_{\bar{x}}$. As references, the phase velocity of the IAW (white dotted line) and the initial resonant velocity (white dashed line) are shown, for $\varepsilon_e = 8.0 \times 10^{-3}$.

In Figs.4.4, 4.5, 4.6 (d) through (f), the particle distribution of the heavy ions,

$\langle \delta \bar{f}_i \rangle_{\bar{x}}$, is shown. The initial perturbation produces a resonance zone about $\bar{v} \simeq 2.5 \times 10^{-2}$ [Fig.4.5(a)]. After $t\omega_{pe} = 100$ the same tendency in velocity domain holds but around $\bar{v} \simeq 4.0 \times 10^{-2}$ [Figs.4.5(b)], with negligible changes at longer times (Fig.4.4).

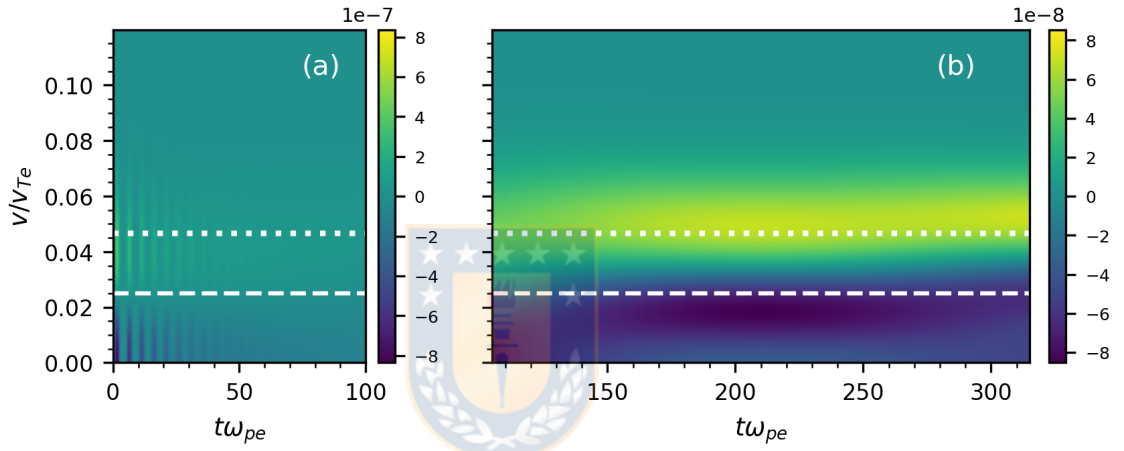


Figure 4.5: Details of (a) the initial stage and (b) transition to long-term range of the variations of the position-averaged ions distribution function, $\langle \delta \bar{f}_i \rangle_{\bar{x}}$, for $\varepsilon_e = 8.0 \times 10^{-3}$. The same velocities are plotted.

The evolution of $\langle \delta \bar{f}_i \rangle_{\bar{x}}$ shows that fast oscillations in the particle distribution take place about $\bar{v} = 2.5 \times 10^{-2}$, as the fast oscillations dominate the dynamics of the plasma [Fig.4.5(a)], with a large reduction in the number of ions slower than $\bar{v} = 2.5 \times 10^{-2}$ [see Fig.4.6(d)] from the initial instant. This component decays in time as observed in Figs.4.4 and 4.5(b). The decay corresponds to a reversal in the initial acceleration that occurs as ions accumulate at the boundaries of the position domain during $0 \leq t\omega_{pe} \leq 100$ (Fig.4.7), indicating the presence of a low frequency positive potential that slows them down [Fig.4.6(d)] and stop the bunching. Afterwards, ions are repelled, reducing the density variations $\delta \bar{n}_i$ ($100 \leq t\omega_{pe} \leq 200$,

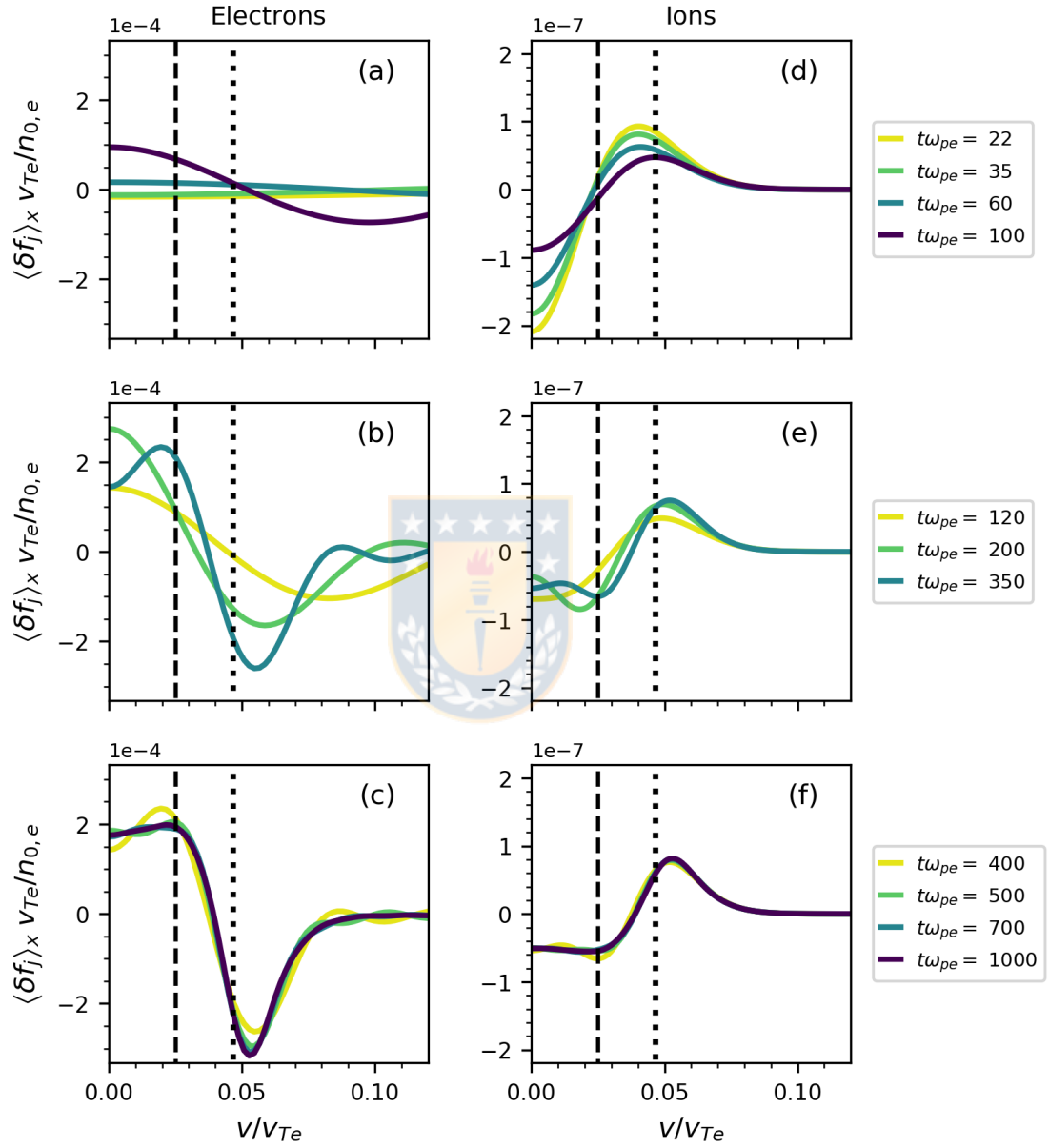


Figure 4.6: Sections of the variations of the position-averaged particle distribution function of electrons, $\langle \delta \bar{f}_e \rangle_x$ [(a), (b) and (c)], and ions, $\langle \delta \bar{f}_i \rangle_x$ [(d), (e) and (f)], for $\varepsilon_e = 8.0 \times 10^{-3}$. The initial resonant velocity (black dashed-line) and $\bar{v}_{\phi,IA}$ (black dotted-line) are shown.

Fig.4.7), and accelerated, producing an accumulation of ions with velocities close to $\bar{v}_{\phi,IA}$ [Fig.4.6(e)] as the oscillations are damped. The damping causes a weak forcing on the particles yielding lower variations in the particle density afterwards ($t\omega_{pe} > 200$, Fig.4.7). Consequently, time variations in $\langle \delta \bar{f}_i \rangle_{\bar{x}}$ become smaller, retaining the same shape at longer times [Figs.4.4 and 4.6(f)].

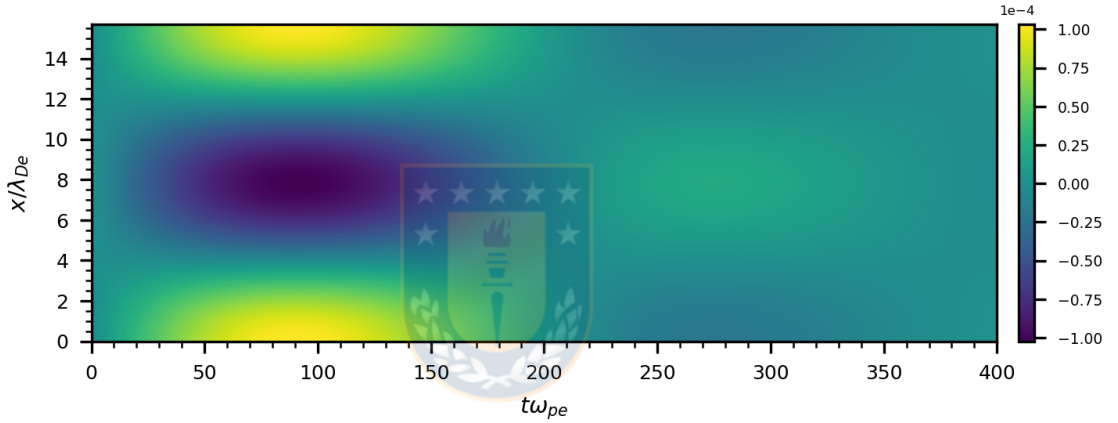


Figure 4.7: Variations of the ions density $\delta \bar{n}_i$ during the initial evolution of the plasma. Perturbative amplitude $\varepsilon_e = 8.0 \times 10^{-3}$.

The variations of the position averaged distribution of electrons $\langle \delta \bar{f}_e \rangle_{\bar{x}}$ are shown in Figs.4.6(a) through (c) and 4.8. It is observed that electrons are resonantly affected by the propagation of the IAWs. The resonant region exhibits the inverse pattern around $\bar{v} \simeq 4.0 \times 10^{-2}$ during most of the evolution in comparison to that of the ions distribution. This means that electrons are slowed down in this velocity range.

Initially, low amplitude fast oscillations are observed without signals of resonant interaction up to $t\omega_{pe} \simeq 100$ [Fig.4.6(a)], when there is a sudden accumulation of

electrons with $\bar{v} < 4.0 \times 10^{-2}$ at the expense of the faster ones, reaching a peak at $t\omega_{pe} = 200$ [Fig.4.6(b)]. It is observed that the depopulation of faster electrons initially takes place in a wide range of velocities and becomes localized at $4.0 \times 10^{-2} \leq \bar{v} \leq 7.5 \times 10^{-2}$ around $t\omega_{pe} = 250$. Simultaneously, electrons with velocities $\bar{v} \simeq 0$ are accelerated and faster electrons continue to be slowed down, accumulating slow electrons at $\bar{v} \simeq 2.5 \times 10^{-2}$, as heavy ions are accelerated from the same velocity, depopulating the center of the distribution and a bounded range of velocities around $\bar{v}_{\phi,IA}$ [Fig.4.6(b)]. At longer times, variations become nearly stationary in the trough, and electrons with velocities around $\bar{v} \simeq 2.5 \times 10^{-2}$ are slowed down, flattening the distribution for $0 \leq \bar{v} < 2.5 \times 10^{-2}$ [Figs.4.8 and 4.6(c)].

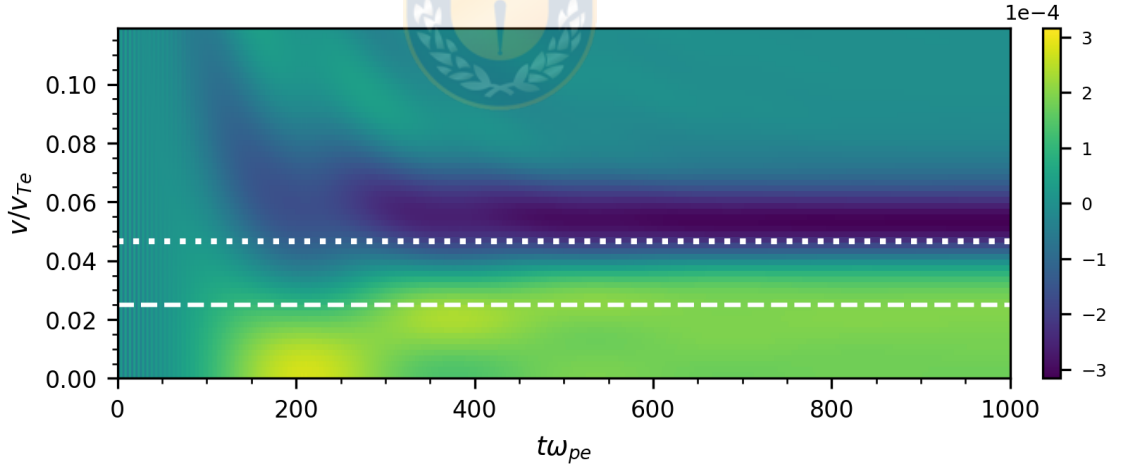


Figure 4.8: Evolution of the variation position-averaged particles distribution function, $\langle \delta f_e \rangle_{\bar{x}}$. As references, the phase velocity of the IAW (white dotted line) and one resonant velocity (white dashed line) are shown, for $\varepsilon_e = 8.0 \times 10^{-3}$.

The observed difference between both species can be attributed to the opposite dynamic effect of the electric field on each species due to the particle charge. As the

ions lead the dynamics of this mode, in the same way electrons do in the LWs, the interaction with the electric field crowds them at velocities slightly faster than $\bar{v}_{\phi,IA}$, by increasing and reducing the velocity of nearby ions, depending on their relative velocity. As electrons have the opposite charge, the electric field slows them down in this velocity range.

4.3 Contribution of each species to the damped oscillations

The evolution of the envelope of the particle densities can be found through the position averaged density variations, $\langle \delta \bar{n}_j^2 \rangle_{\bar{x}}$, defined as

$$\langle \delta \bar{n}_j^2 \rangle_{\bar{x}} = \frac{1}{\bar{L}_x} \int_0^{\bar{L}_x} [n_j - n_{0,j}]^2 d\bar{x}. \quad (4.3.1)$$

This quantity is shown in Fig.4.9 for both species with $\varepsilon_e = 1.0 \times 10^{-3}$ and in Fig.4.10 for $\varepsilon_e = 8.0 \times 10^{-3}$. It is observed that initially, both species evolve at different time scales with ions sustaining a low frequency propagation of the IAWs and electrons sustaining the propagation of both the LWs, up to $t\omega_{pe} = 100$, and of the IAWs. The change in the frequency of $\langle \delta \bar{n}_j^2 \rangle_{\bar{x}}$ occurs when the amplitude of the variations of both species reach the same levels, as shown by Xu *et al.* [27], indicating that the dominant oscillations in the electrons distribution are due to the propagation of the IAW after the LW has decayed, although a high frequency component remains at the larger amplitude case $\varepsilon_e = 8.0 \times 10^{-3}$.

Both resonant zones are eventually affected by the same electric field at all times. In order to determine the extent at which both zones are affected by the propagation of one wave or the other, two approaches are used. A comparison is made for the

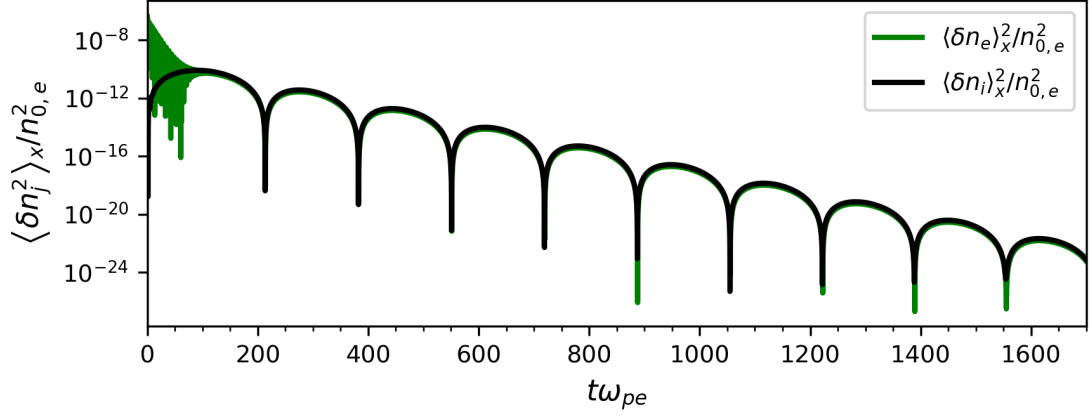


Figure 4.9: Evolution of the position averaged amplitudes $\langle \delta \bar{n}_j^2 \rangle_{\bar{x}}$ of the particle densities for $\varepsilon_e = 1.0 \times 10^{-3}$.

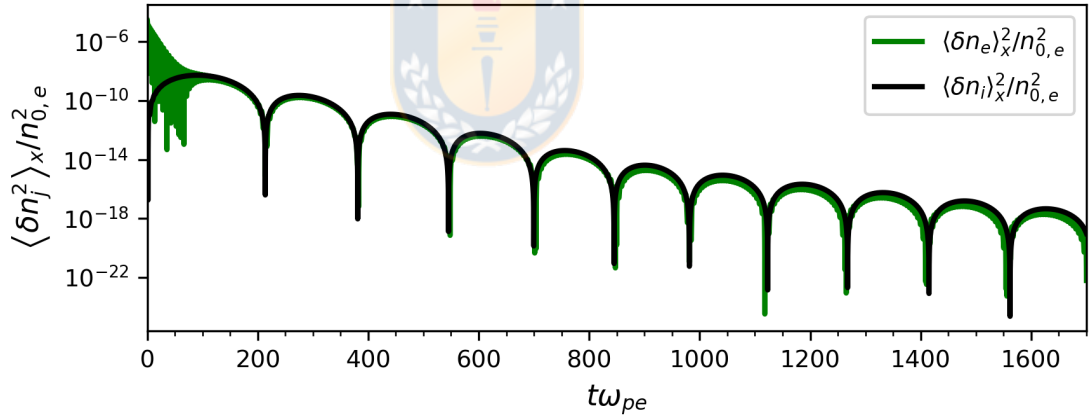


Figure 4.10: Evolution of the position averaged amplitudes $\langle \delta \bar{n}_j^2 \rangle_{\bar{x}}$ of the particle densities for $\varepsilon_e = 8.0 \times 10^{-3}$.

resonant zone of the LW with the case of immobile ions through the correlations

between the distribution $\langle \delta \bar{f}_e \rangle_{\bar{x}}$ from each case, $C [\langle \delta \bar{f}_{e,i} \rangle_{\bar{x}}, \langle \delta \bar{f}_{e,m} \rangle_{\bar{x}}]$, given by

$$C [\langle \delta \bar{f}_{e,i} \rangle_{\bar{x}}, \langle \delta \bar{f}_{e,m} \rangle_{\bar{x}}] (\bar{v}, t) = \frac{[\langle \delta \bar{f}_{e,i} \rangle_{\bar{x}} - \langle \delta \bar{f}_{e,i} \rangle_{\bar{x}, \bar{v}_r}] [\langle \delta \bar{f}_{e,m} \rangle_{\bar{x}} - \langle \delta \bar{f}_{e,m} \rangle_{\bar{x}, \bar{v}_r}]}{\sigma_{i, \bar{v}_r} \sigma_{m, \bar{v}_r}},$$

where $\langle \delta \bar{f}_{e,j} \rangle_{\bar{x}}$ are the position averaged variations of the electrons distribution for ($j = i$) immobile ions and for ($j = m$) mobile ions, the brackets $\langle \cdot \rangle_{\bar{v}_r}$ represent average on velocity space over the range $\bar{v}_r = [\bar{v}_{\min}, \bar{v}_{\max}]$, and σ_{j, \bar{v}_r} is the standard deviation of the distribution of species j over the range \bar{v}_r . If the distributions are the same, they are maximally correlated at all times ($\langle C [\langle \delta \bar{f}_{e,i} \rangle_{\bar{x}}, \langle \delta \bar{f}_{e,m} \rangle_{\bar{x}}] \rangle_{\bar{v}_r} = 1$) but if this region is affected by the IAW, a deviation from the unity should be observed. The second approach, for the ions distribution, is to observe the spectra and to find signatures of LWs activity.

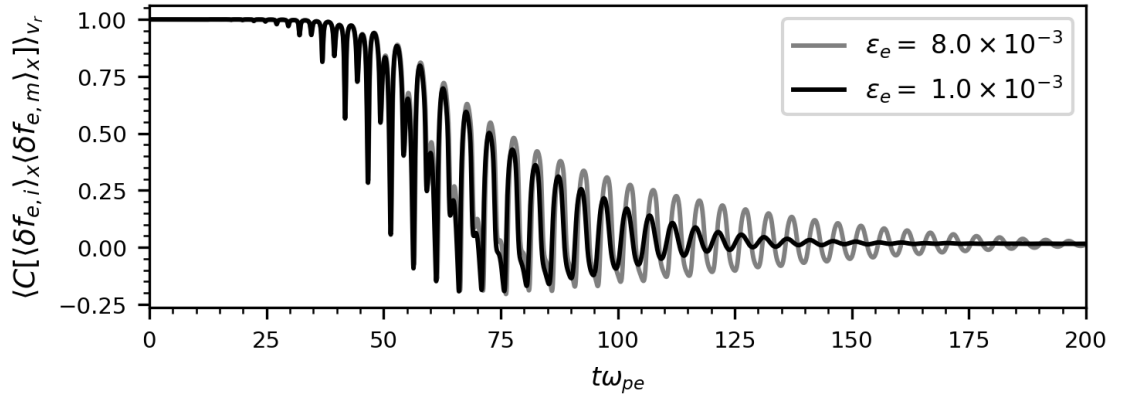


Figure 4.11: Early evolution of the correlations $\langle C [\langle \delta \bar{f}_{e,i} \rangle_{\bar{x}}, \langle \delta \bar{f}_{e,m} \rangle_{\bar{x}}] \rangle_{\bar{v}_r}$ over the range $v_r = [0.0, 1.5]$ for $\epsilon_e = 1.0 \times 10^{-3}$ and 8.0×10^{-3} .

In the velocity range $0 \leq \bar{v} \leq 1.5$ electrons are nonresonantly affected by the LW. They respond to the ions dynamics from $t\omega_{pe} \simeq 25$, as observed in the correlations

in Fig.4.11 with small deviations from the unity. This response is enhanced after $t\omega_{pe} = 40$ when the correlations begin to decay in magnitude, and the dynamics from both cases become uncorrelated.

Since fast electrons are nonresonant with the IAW, it is expected that the predominating electric field weakly affects fast electrons. This fact is observed in Fig.4.12, which shows a reduction of the correlations of the distributions in the range $2.0 \leq \bar{v} \leq 4.0$, with low frequency variations in the order of 10^{-5} , so that there is no significant deviation from the dynamics with immobile ions. Nonetheless, electrons with velocities around $\bar{v}_{\phi,L}$ are affected by the IAWs from the beginning of the evolution. The larger deviation from unity is observed about $t\omega_{pe} = 110$, and it is possible to associate it to the onset of the slow oscillations. As the perturbations decay, electrons resonating with the LW become less affected by the slow dynamics and ultimately remain unaltered, as the correlations tend to the unity.

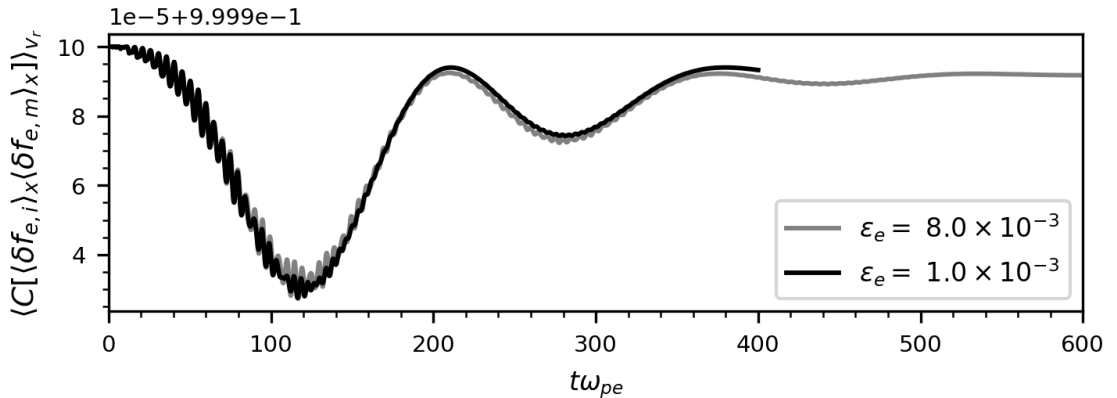


Figure 4.12: Evolution of the correlations $\langle C[\langle \delta \bar{f}_{e,i} \rangle_{\bar{x}} \langle \delta \bar{f}_{e,m} \rangle_{\bar{x}}] \rangle_{\bar{v}_r}$ over the range $v_r = [2.0, 4.0]$ for $\epsilon_e = 1.0 \times 10^{-3}$ and 8.0×10^{-3} .

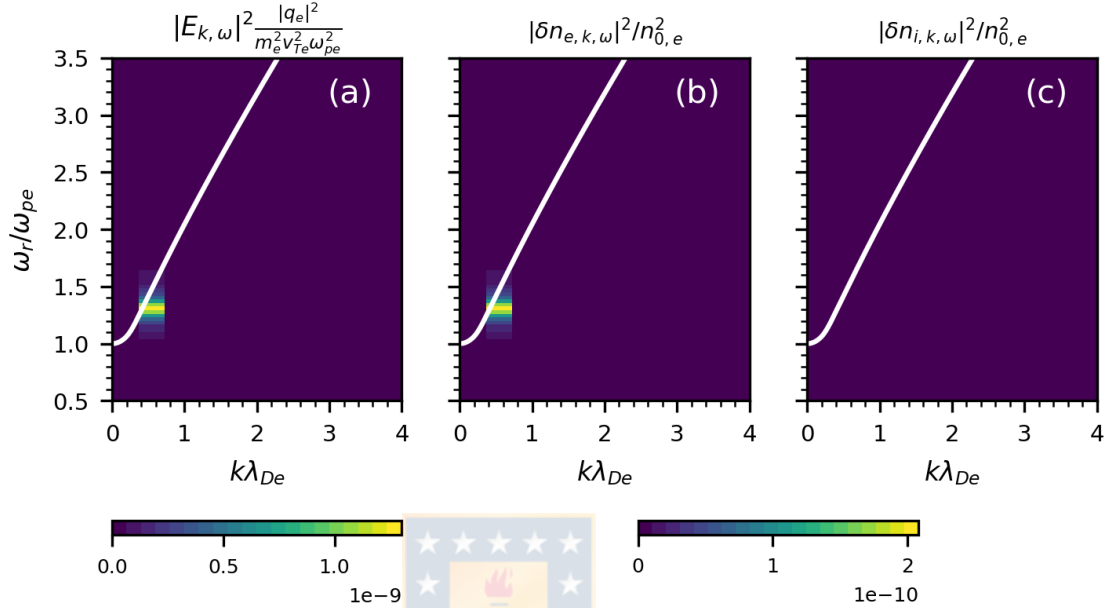


Figure 4.13: Spectra of the (a) electric field, $|\bar{E}_{k,\omega}|$, (b) electrons density, $|\bar{n}_{e,k,\omega}|$, and (c) ions density, $|\bar{n}_{i,k,\omega}|$, from the range $0 \leq t\omega_{pe} \leq 200$ for $\varepsilon_e = 1.0 \times 10^{-3}$.

The effects of the LW on the ions distribution are weaker for both $\varepsilon_e = 1.0 \times 10^{-3}$ and 8.0×10^{-3} . This can be observed in the spectra of Fig.4.13 for $\varepsilon_e = 1.0 \times 10^{-3}$, and Fig.4.15 for $\varepsilon_e = 8.0 \times 10^{-3}$ for the initial stage, $0 \leq t\omega_{pe} \leq 200$, in which the Langmuir mode is dominant, and for the remaining stage, $200 \leq t\omega_{pe} \leq 1700$, in which the IAW is dominant. No appreciable signals around the Langmuir frequency are found in $|\delta\bar{n}_{i,k,\omega}|$ on the first stage [Figs.4.13(c) and 4.15(c)] or in the later stage [Figs.4.14(c) and 4.16(c)], even though there is a low amplitude peak in the electric field [4.16(a)] and the electrons density spectra [4.16(b)].

The case $\varepsilon_e = 1.0 \times 10^{-3}$ differs at longer times (Fig.4.14), as the peak around $\bar{\omega}_L$ is not observed in the electric field or the electrons density, indicating that variations

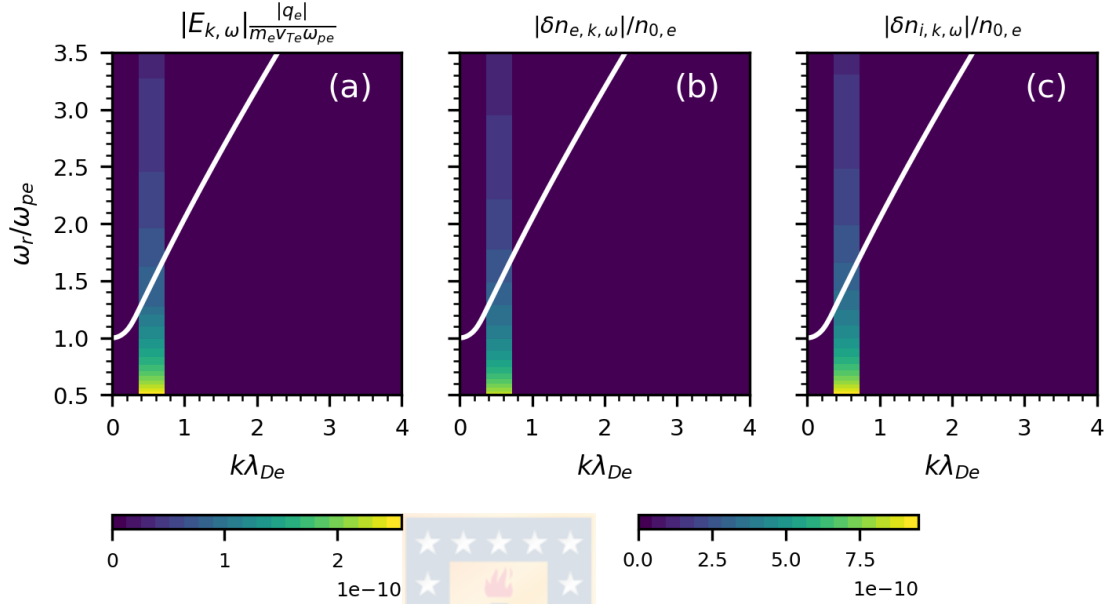


Figure 4.14: Spectra of (a) the electric field, $|\bar{E}_{k,\omega}|$, (b) electrons density, $|\bar{n}_{e,k,\omega}|$, and (c) ions density, $|\bar{n}_{i,k,\omega}|$, from the range $200 \leq t\omega_{pe} \leq 1700$ for $\varepsilon_e = 1.0 \times 10^{-3}$.

due to the propagation of the LW are below those produced by the propagation of the IAW. Considering that the behavior of the resonant zone in $\langle \delta \bar{f}_i \rangle_{\bar{x}}$ is produced right after the initial perturbation is applied and that it remains the same regardless of the initial high frequency component, it is concluded that the LWs do not affect on the resonant zone related to the propagation of the IAW.

4.4 Summary and discussion

This chapter addresses the evolution of an electron-ion plasma with mass ratio $\bar{m}_i = 1836.153$, isothermal species, $\bar{T}_i = 1.0$, both initialized with driftless Maxwellian distributions. Mobile heavy ions allow the development of damped IAWs besides the damped LWs, as found by Xu *et al.* [27]. Due to the difference of inertia, the

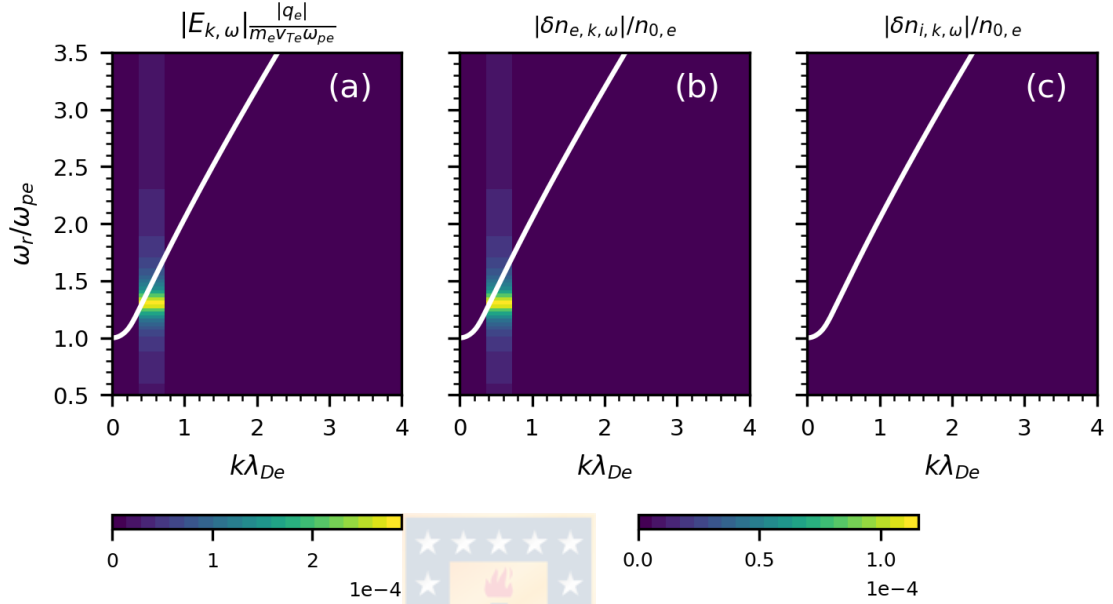


Figure 4.15: Spectra of (a) the electric field, $|\bar{E}_{k,\omega}|$, (b) electrons density, $|\bar{n}_{e,k,\omega}|$, and (c) ions density, $|\bar{n}_{i,k,\omega}|$, from the range $0 \leq t\omega_{pe} \leq 200$ for $\varepsilon_e = 8.0 \times 10^{-3}$.

propagation of these waves yields two different time scales. The LWs, interacting with electrons with velocities $\sim \bar{v}_{\phi,L}$, decay faster than the IAWs, which interact with both electrons and ions with velocities in the order of $\bar{v}_{\phi,IA}$, leading to the domination of low frequency oscillations at longer times. In this process, ions in the resonance zone are accelerated towards $\bar{v}_{\phi,IA}$, whereas slow electrons tend to be slowed down to velocities $0 \leq \bar{v} \leq 2.5 \times 10^{-2}$, depopulating the region around $\bar{v}_{\phi,IA}$ as the forcing of the electric field on each species depends on the sign of their charge.

The observed waves develop with a large degree of independence. The evolution of the correlations of the electrons distribution around the resonant zone of the LW indicates that the development of the IAWs leaves signatures. As the field amplitude undergoes further damping, the correlations tend to unity, indicating that the res-

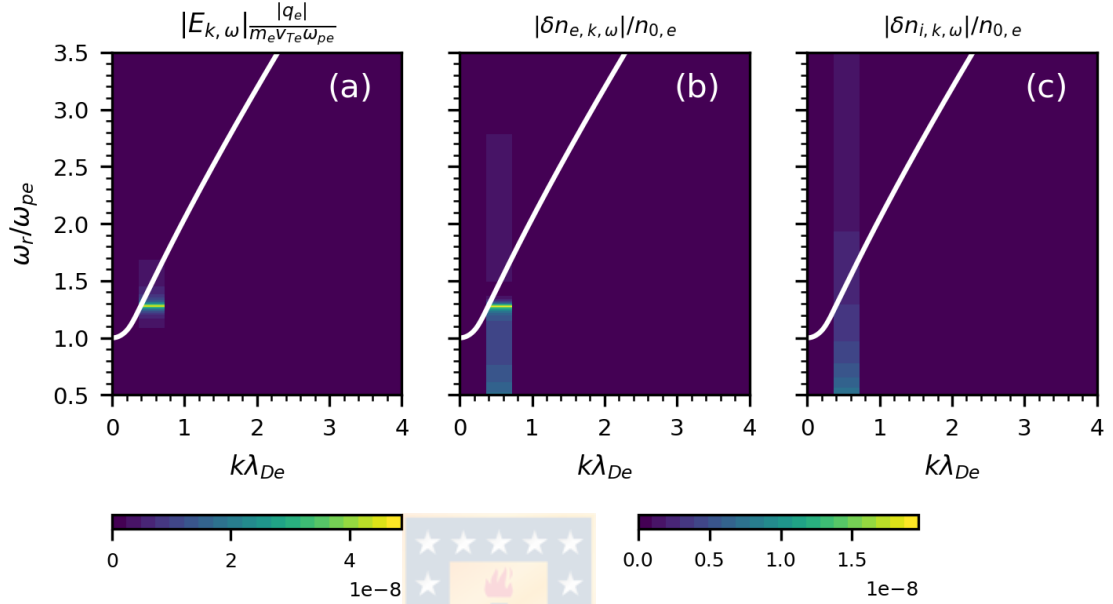


Figure 4.16: Spectra of (a) the electric field, $|\bar{E}_{k,\omega}|$, (b) electrons density, $|\bar{n}_{e,k,\omega}|$, and (c) ions density, $|\bar{n}_{i,k,\omega}|$, from the range $200 \leq t\omega_{pe} \leq 1700$ for $\varepsilon_e = 8.0 \times 10^{-3}$.

onance zone behaves as in the case of immobile ions. However, it is noted that the deviation of the correlations from unity is in the order of 10^{-5} , so that the dynamics of the resonance zone related to the LWs remain mostly unaffected by the IAWs. On the ions distribution, the pattern observed in the resonance zone is excited at the very beginning and is not affected afterward, and it is therefore not related to dynamics of the LW, and although there is a high frequency component in $\langle \delta \bar{f}_i \rangle_{\bar{x}}$ initially, it fades out as the LW damps out, yielding weak or none signals around $\bar{\omega}_L$ in the spectra of $\delta \bar{n}_i$. Hence, the resonance zone related to the IAW is not greatly affected by the fast wave either. As a consequence, the oscillations in the envelope of the electrons density $\langle \delta \bar{n}_e^2 \rangle_{\bar{x}}$ are initially produced by electrons resonating with the LWs, and they are later produced by electrons resonating with the IAWs. The same conclusion follows for the amplitude of the excited mode $|E_1|$.

The dominance of the IAW in the long term can be understood through the inertia of the ions. A time scale larger than that of the electrons is introduced, observed in the magnitudes of the damping rates, $|\bar{\gamma}_L| > |\bar{\gamma}_{IA}|$. Both waves are present from the initial perturbation, with LWs of larger amplitude and fast decay, and the IAWs of lower amplitude but slower decay. Once the oscillations of the LW reach the level of the IAWs, since electrons around $\bar{v}_{\phi,L}$ continue to damp the fast wave, IAWs become dominant and oscillations still occur as they slowly damp out.



5 Single wave excitation - Nonlinear evolution of a Maxwellian electron-ion plasma

This chapter is focused on the study of the nonlinear evolution of the system analyzed in Chapter 4. Ion mass ratio is $m_i/m_e = 1836.153$, driftless Maxwellian distributions and temperature ratio $T_i/T_e = 1.0$, exciting the first mode of the plasma. The perturbative amplitude ε_e is large enough to trigger the nonlinear regime of the fast mode. In addition to the trapping zone associated to the fast mode, nonlinear structures are observed in the low velocity range, near $\bar{v}_{\phi,IA}$ and related to the dynamics of heavy positively charged ions.

In the subsequent sections, it is noted that due to the symmetry of this plasma in velocity space, the spectra are symmetric with respect to \bar{k} and $\bar{\omega}_r$, hence only one quadrant of the $\bar{k} - \bar{\omega}_r$ is shown. Similarly, the distribution functions are shown only for $\bar{v} \geq 0$, since the behavior any structure found in this range is also found in $\bar{v} < 0$ is the same but with the opposite velocity.

5.1 Low frequency dynamics in the case of immobile ions

For comparison purposes, the low frequency dynamics of an electron plasma with immobile ions in the nonlinear regime with amplitude $\varepsilon_e = 4.0 \times 10^{-2}$ is described. This dynamics develops at larger times compared to that of the saturation of the electric field and involves low frequency, low amplitude modes.

5.1.1 Electric field spectra

The spectra of the electric field is shown in Fig.5.1. It is observed that low frequency waves are excited. A region close to $\bar{\omega}_r \sim 0$ is excited around $0.4 < \bar{k} < 2.0$ in Figs.5.1(b) and (c). Later during $1100 \leq t\omega_{pe} \leq 1800$, two regions of waves are excited, one acoustic-like and another with frequencies below $\bar{\omega}_r = 6.0 \times 10^{-2}$ [Fig.5.1(c)]. Their levels, however, remain two orders of magnitude below those of the waves around the nonlinear Langmuir mode. The phase speed of the waves in the acoustic-like region are in the range $4.488 \times 10^{-2} \leq \bar{v}_\phi \leq 8.976 \times 10^{-2}$ with most of the waves verifying $5.236 \times 10^{-2} \leq \bar{v}_\phi \leq 7.854 \times 10^{-2}$. The second region of excitation has waves with phase velocities $8.976 \times 10^{-3} \leq \bar{v}_\phi \leq 2.244 \times 10^{-2}$.

5.1.2 Electrons density and phase space

In order to distinguish the low frequency dynamics in the variations of the electrons particle density, a filter in frequency and wavenumber is applied, obtaining the filtered electrons density $\delta\bar{n}_{e,\text{fl}}(\bar{x}, \bar{t})$,

$$\delta\bar{n}_{e,\text{fl}}(\bar{x}, \bar{t}) = \mathcal{F}_{\bar{x}, \bar{t}}^{-1} \left[\mathcal{F}_{\bar{k}, \bar{\omega}_r} [\delta\bar{n}_e(\bar{x}, \bar{t})] \Omega(\bar{k}, \bar{\omega}_r) \right], \quad (5.1.1)$$

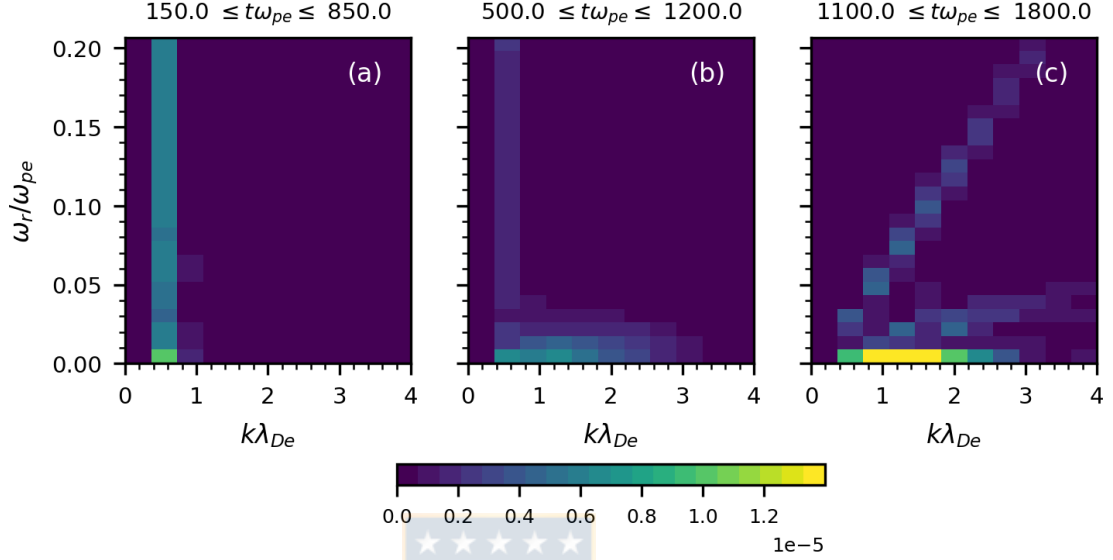


Figure 5.1: Spectra of the electric field $|\bar{E}_{k,\omega}|$ for $\epsilon_e = 4.0 \times 10^{-2}$ for the case of immobile ions. Three time intervals are shown.

where $\Omega(\bar{k}, \bar{\omega}_r)$ is a filter function given by

$$\Omega(\bar{k}, \bar{\omega}_r) = \exp \left[- \left(\frac{\bar{\omega}_r - \bar{\omega}_{\text{shift}}}{\bar{\omega}_{\text{width}}/2} \right)^{36} \right] \mathcal{K}(\bar{k}), \quad (5.1.2)$$

with $\bar{\omega}_{\text{width}}$ the frequency width of the filter, $\bar{\omega}_{\text{shift}}$ the central frequency of the filter and \mathcal{K} a function of \bar{k} . For the case of filtering low frequencies only, $\bar{\omega}_{\text{shift}} = 0$, $\bar{\omega}_{\text{width}} = 1.2$, excluding frequencies related to the fast mode and retaining the most relevant frequencies of the slow modes, and $\mathcal{K}(\bar{k}) = 1$. For the case of one single propagating structure, $\bar{\omega}_{\text{shift}} = \pm 0.3$ with $\mathcal{K}(\pm \bar{k}) = \Theta(\bar{k})$, and $\bar{\omega}_{\text{shift}} = \mp 0.3$ with $\mathcal{K}(\bar{k}) = \Theta(\mp \bar{k})$, both with $\bar{\omega}_{\text{width}} = 0.6$, where the upper signs are for positively propagating structures, the lower signs are for negatively propagating structures and Θ is the Heaviside function.

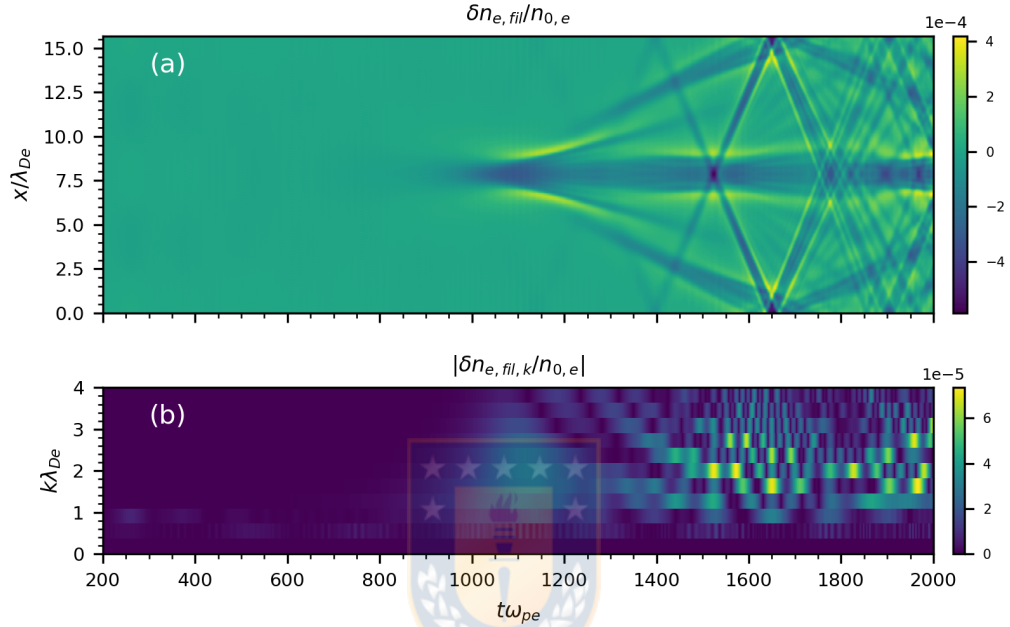


Figure 5.2: Evolution of the variation of (a) electrons density, filtered in frequency, $\delta \bar{n}_{e, fil}$, and its spatial Fourier transform (b) for $\varepsilon_e = 4.0 \times 10^{-2}$, for immobile ions.

Figure 5.2 shows the evolution of the filtered electrons density [(a)] and its representation in wavenumber space [(b)]. It is observed that localized structures, corresponding to electron cavities, are excited around $t\omega_{pe} \simeq 900$ at the center of the position domain that evolve into several counter-propagating narrower electron cavities. In Fig.5.2(b), it corresponds to the development of several large wavenumbers \bar{k} in the same range of the nearly zero frequency region in the electric field spectrum [Fig5.1(c)]. The initial cavities, $1200 \leq t\omega_{pe} \leq 1650$, propagate with speed $|\bar{v}| \simeq 1.5 \times 10^{-2}$. The following cavities appear during $1400 \leq t\omega_{pe} \leq 1650$ and propagate with speed $|\bar{v}| = 6.2831 \times 10^{-2}$ and yield several narrower cavities after they cross with the central cavity at $t\omega_{pe} = 1775$. The speed of these structures are

within the range of the excited waves in the electric field spectrum [Fig5.1(c)].

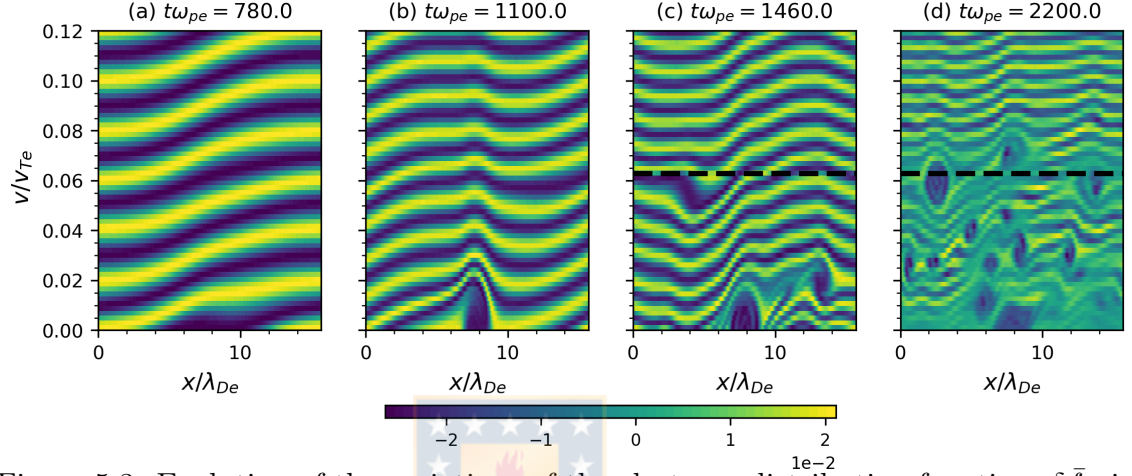


Figure 5.3: Evolution of the variations of the electrons distribution function, $\delta \bar{f}_e$, in the low velocity range with immobile ions for perturbative amplitude $\varepsilon_e = 4.0 \times 10^{-2}$. The velocity of the structures found in Fig.5.2 are shown (black dashed line).

In the electrons phase space of Fig.5.3, a region of electron trapping is developed at $\bar{v} = 0$ [Figs.5.3(a) and (b)] which is still observed at further instants [Fig.5.3(d)]. This structure would account for the initial electron cavity in $\delta \bar{n}_{e,\text{fl}}$ and the for the high intensity waves in Fig.5.1. Other holes are formed at $t\omega_{pe} = 1460$ [Fig.5.3(c)] whose speeds are similar compared to those of the cavities in $\delta \bar{n}_{e,\text{fl}}$ during $1200 \leq t\omega_{pe} \leq 1600$. Several small electron holes are observed at $t\omega_{pe} = 2200$ [Fig.5.3(d)], which would account for the development of narrow cavities in $\delta \bar{n}_{e,\text{fl}}$ after $t\omega_{pe} = 1800$ [Fig.5.2(a)].

5.2 Comparison between mobile ions and immobile ions for the nonlinear regime

As shown by Xu *et al.* [27], low frequency signals in $|E_1|$ for the nonlinear regime are not found. As several modes are excited after the saturation, the electric field energy \bar{E}_E is a more representative quantity to observe. According to Fig.5.4, the field energy behaves in the same way as the case of immobile ions.

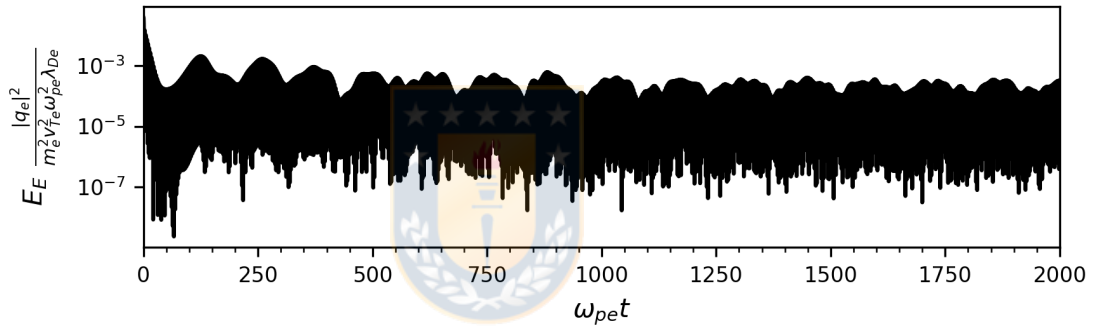


Figure 5.4: Evolution of the electric field energy \bar{E}_E for the nonlinear case, $\varepsilon_e = 4.0 \times 10^{-2}$.

5.2.1 Electric field spectrum

Differences are found with the case of immobile ions by observing the electric field spectrum, the frequency filtered electron density, and the electrons distribution function. The evolution of the electric field spectrum in Fig.5.5 shows a similar structure compared to that in Fig.5.1 for immobile ions, however with larger amplitudes. The waves with nearly zero observed in Fig.5.1 are still observed when ions are allowed to move, but their amplitudes remain nearly one order of magnitude below those found along the acoustic-like branch, the most excited ones in this range of frequencies.

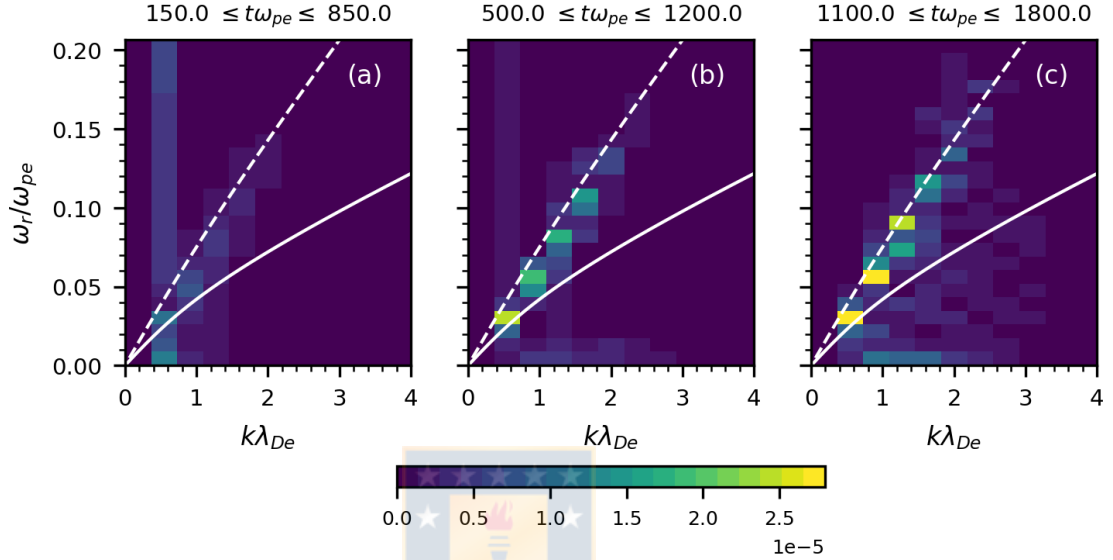


Figure 5.5: Spectra of the electric field $|\vec{E}_{k,\omega}|$ for $\varepsilon_e = 4.0 \times 10^{-2}$ for the case of mobile ions. Three time intervals are shown. Roots of the linear dispersion relation (2.2.10) are shown, corresponding to the IA mode (solid white line) and the least damped higher order mode (dashed white line).

It is observed that the acoustic-like branch lies on a region coinciding with a root of the linear dispersion relation for $T_i/T_e = 1.0$ corresponding to the least damped higher order mode. These waves are excited earlier, during $300 \leq t\omega_{pe} \leq 1000$ [Fig.5.5(a)], whereas in the case of immobile ions, they are first observed during $1000 \leq t\omega_{pe} \leq 1700$ [Fig.5.1(b)].

5.2.2 Frequency filtered electrons density

In the frequency filtered electrons density in Fig.5.6 there are notorious differences with the density obtained with immobile ions of Fig.5.2. Firstly, the amplitude of the low frequency variations is increased to nearly the double both in the density

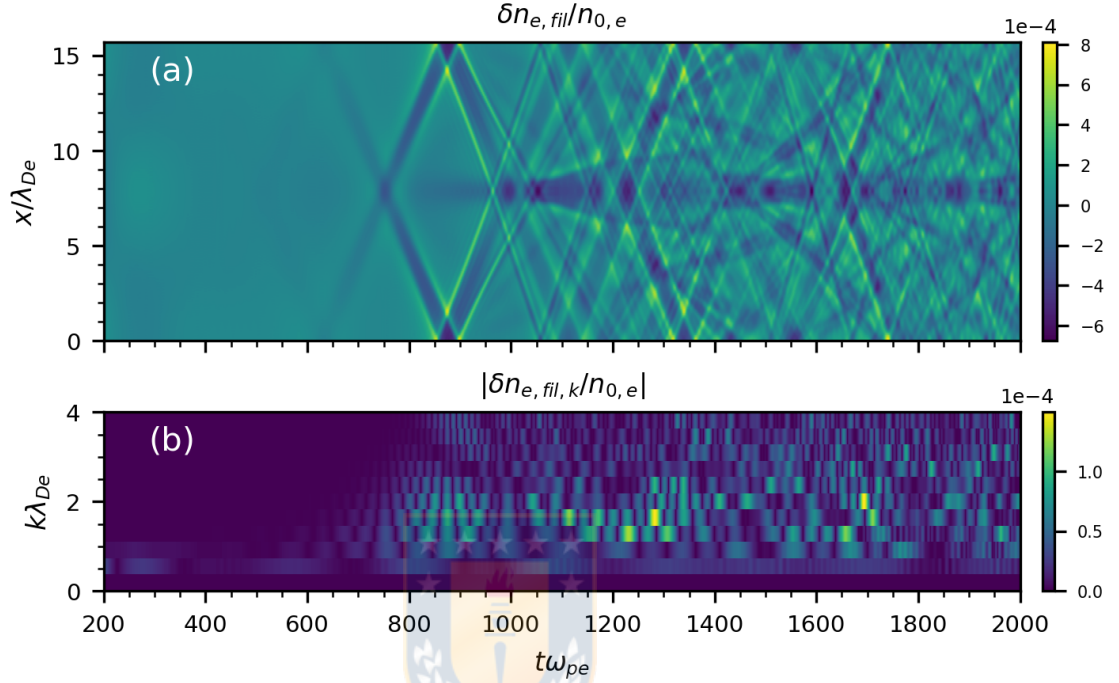


Figure 5.6: Evolution of the variation of (a) electrons density, filtered in frequency, $\delta \bar{n}_{e,fil}$, and its spatial Fourier transform (b) for $\varepsilon_e = 4.0 \times 10^{-2}$, for mobile ions.

[Fig.5.6(a)] and in its position space Fourier transform [Fig.5.6(b)]. Second, the electron cavities fine structure developed in both cases is different: for mobile ions, it develops from $t\omega_{pe} \simeq 500$ as observed in both $\delta \bar{n}_{e,fil}$ and $|\delta \bar{n}_{k,e,fil}|$, with cavities propagating with speed $|\bar{v}_c| = 6.2831 \times 10^{-2}$ being the predominant structure. The central cavity formed with immobile ions [Fig.5.6(a)] is still formed. After $t\omega_{pe} = 1000$, these cavities yield narrower cavities at larger times, developing a structure rich in short wavelengths.

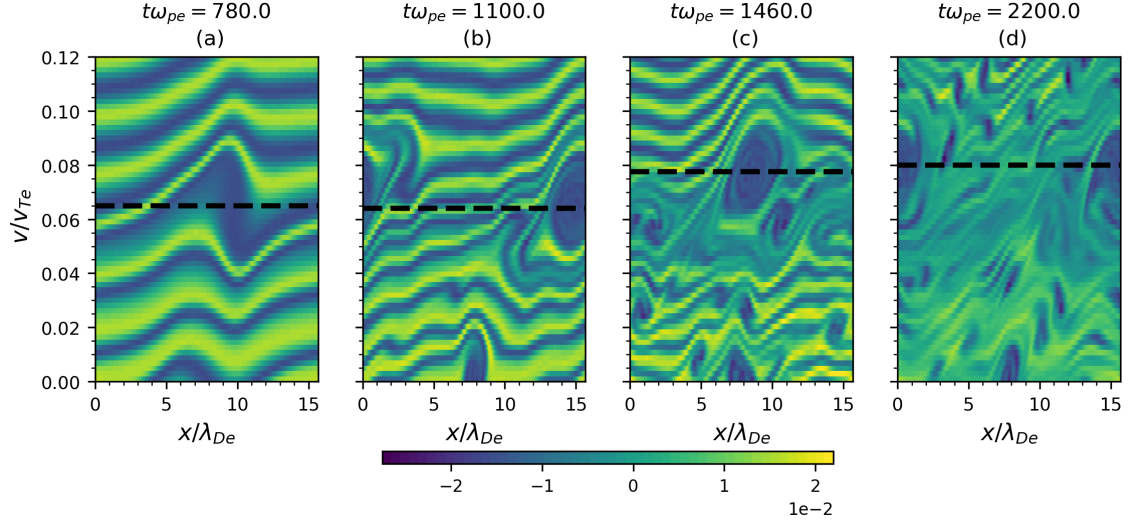


Figure 5.7: Evolution of the variations of the electrons distribution function, $\delta \bar{f}_e$, in the low velocity range with mobile ions for perturbative amplitude $\varepsilon_e = 4.0 \times 10^{-2}$. The velocity of the structures is shown for each instant (black dashed line).

5.2.3 Electrons distribution function

The evolution of the electrons distribution function differs from that observed in the case of immobile ions. Figure 5.7 shows that there is an electron hole being closed at $t\omega_{pe} = 780$ around \bar{v}_c [Fig.5.7(a)], whereas in the case of immobile ions there is no signatures of trapping at that velocity up to $t\omega_{pe} = 1460$ [Fig.5.3(a) and (c)]. This hole is wider in position and in velocity spaces, indicating the presence of a more intense potential than in the case of immobile ions. It is also observed that the hole has accelerated motion [Figs.5.7(b) through (d)].

Similar aspects hold: **(i)** the trapping region at the center of the position domain with zero velocity is still excited, but it is not the predominant structure. This accounts for the low energy in modes with nearly zero frequency in Fig.5.5, and **(ii)**

smaller holes are excited, which may account for the finer structure developed in the electrons density.

5.2.4 Effects on the high velocity range

The introduction of mobile ions also affects the particle distribution at higher velocities. This fact is shown with the velocity averaged correlations between the distributions $\langle \delta \bar{f}_{e,i} \rangle_x$ and $\langle \delta \bar{f}_{e,m} \rangle_x$ in Fig.5.8, evaluated in the velocity range $2.0 \leq \bar{v} \leq 5.0$. Correlations deviate from unity at $t\omega_{pe} = 500$ and exhibit larger deviations after $t\omega_{pe} = 1100$.

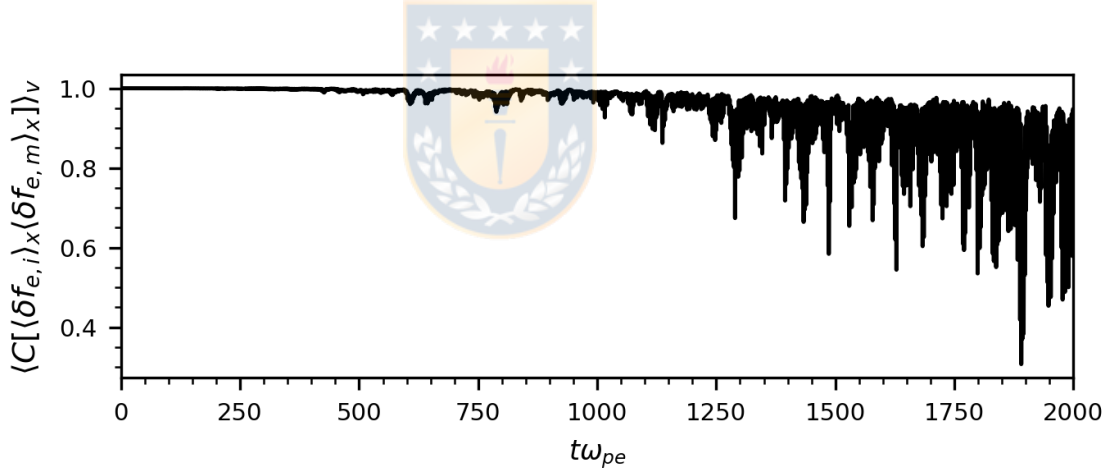


Figure 5.8: Velocity averaged correlations between the position averaged variations in the electrons distributions of the case with mobile ions, $\langle \delta \bar{f}_{e,m} \rangle_x$, and immobile ions, $\langle \delta \bar{f}_{e,i} \rangle_x$, $\langle C[\langle \delta \bar{f}_{e,m} \rangle_x, \langle \delta \bar{f}_{e,i} \rangle_x] \rangle_v$. Correlations are averaged over the velocity range $2.0 \leq \bar{v} \leq 5.0$.

Position averaged correlations of the whole distribution functions at single instants, $\delta \bar{f}_{e,j}$, show that deviations from the case of immobile ions are observed in a wide range of velocities, starting with the trapping region, as observed in Fig.5.9.

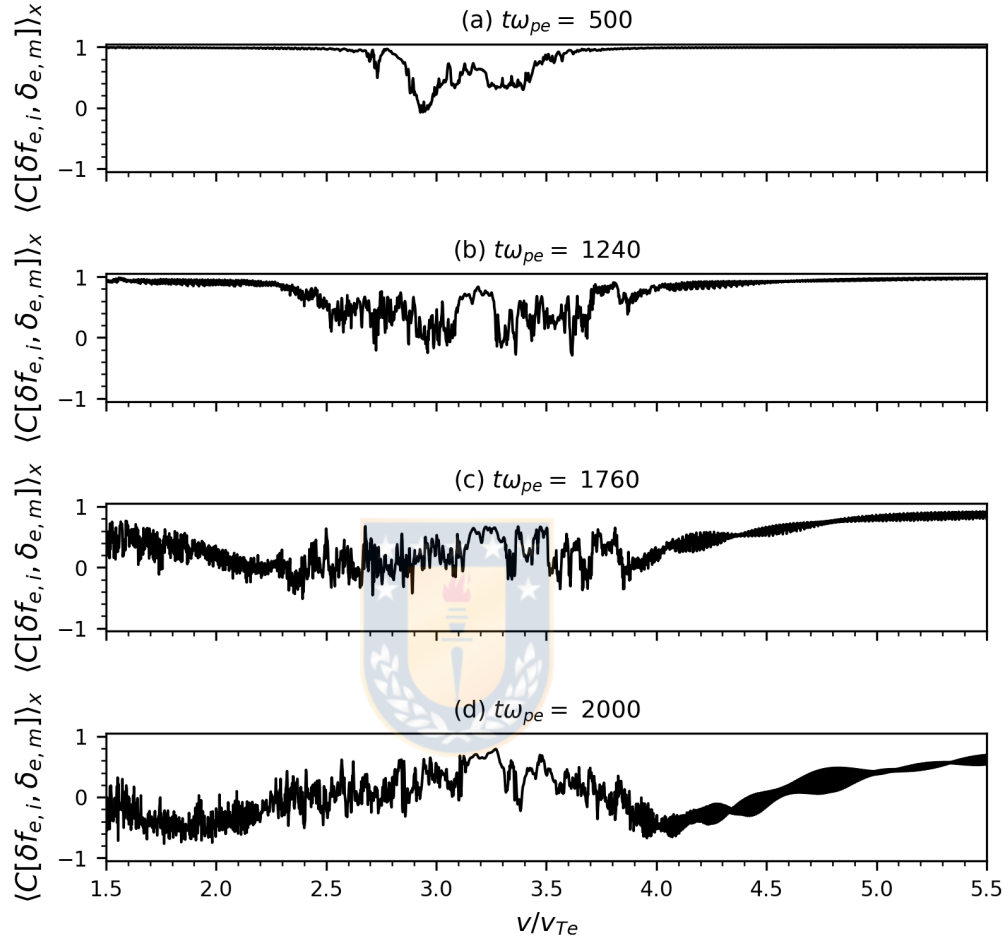


Figure 5.9: Sections of the position averaged correlations between the variations of the electrons distributions of the case with mobile ions, $\delta \bar{f}_{e,m}$, and immobile ions, $\delta \bar{f}_{e,i}$, $\langle C[\delta \bar{f}_{e,i}, \delta \bar{f}_{e,m}] \rangle_x$. Perturbative amplitude is $\varepsilon_e = 4.0 \times 10^{-2}$.

The corresponding phase space of the electrons distribution at the instants in Fig.5.9 is shown. Although there are differences in the position of some of the holes, and specific details in the main trapping region, the overall structure of the phase space remains the same, as observed in Fig.5.10.

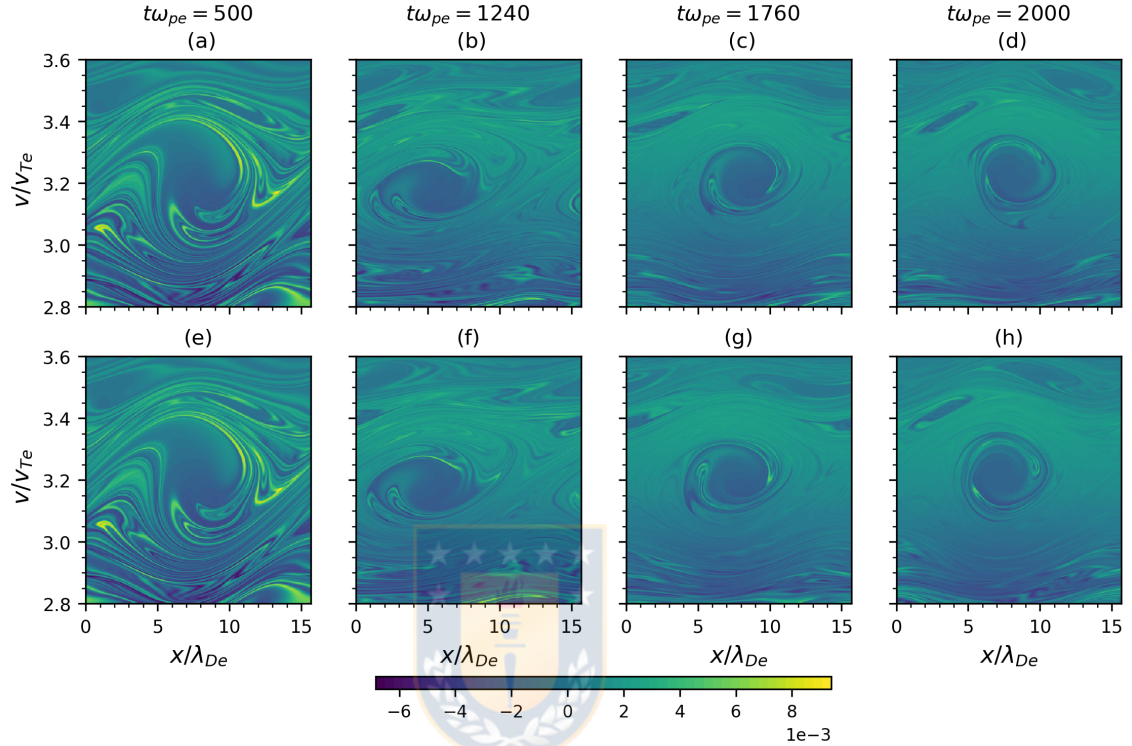


Figure 5.10: Phase space of the variations of the electrons distribution function for the case of immobile ions [(a) through (d)] and mobile ions [(e) through (h)], for the trapping region related to the Langmuir mode. Perturbative amplitude is $\varepsilon_e = 4.0 \times 10^{-2}$.

5.3 Low frequency dynamics due to mobile heavy ions

In this section, the effects of the dynamics of heavy ions in an electron plasma are studied, focusing on the low frequency, slow velocity ranges. Results shown in the previous sections for the electrons distribution are discussed.

5.3.1 Electric field spectrum

The low frequency range spectra of the electric field shown in Fig.5.5 is discussed. As previously noted, the excited modes lie on a region corresponding to the least damped higher order mode predicted by the dispersion relation (2.2.10). Low amplitude waves are found lying on the linear IA branch for $\bar{k} = 0.4$, suggesting minor role in this configuration. The phase speed of the most intense waves are in the range $5.610 \times 10^{-2} \leq \bar{v} \leq 8.976 \times 10^{-2}$ for all three time intervals. The observed waves grow in amplitude and reach shorter wavelengths as the system evolves: initially, the most intense waves are observed with $\bar{k} < 0.8$ [Fig.5.5(a)], then the waves on the linear order higher branch arise with $\bar{k} < 2.4$ with the largest amplitude wave having $\bar{k} = 0.4$ [Fig.5.5(b)]. At last, waves reach $\bar{k} = 3.2$, and there are three large amplitude waves along the same branch with $\bar{k} = 0.4, 0.8$ and 1.2 [Fig.5.5(c)].

5.3.2 Low frequency component of the electrostatic potential

The electrostatic potential is directly related to the electric field and its structure. Therefore, the evolution of the low frequency filtered electrostatic potential, estimated similarly as the filtered electrons density (5.1.1) and considering the filter (5.1.2), is described. This filter retains the component of the potential that interacts with the heavy ions and the slow electrons.

The position dependency of the electrostatic potential for the time interval $150 \leq t\omega_{pe} \leq 700$ is shown in Fig.5.11. The potential mostly exhibits a dependency on one wavenumber ($\bar{k} = 0.4$), up to $t\omega_{pe} = 500$, when a localized positive potential is formed

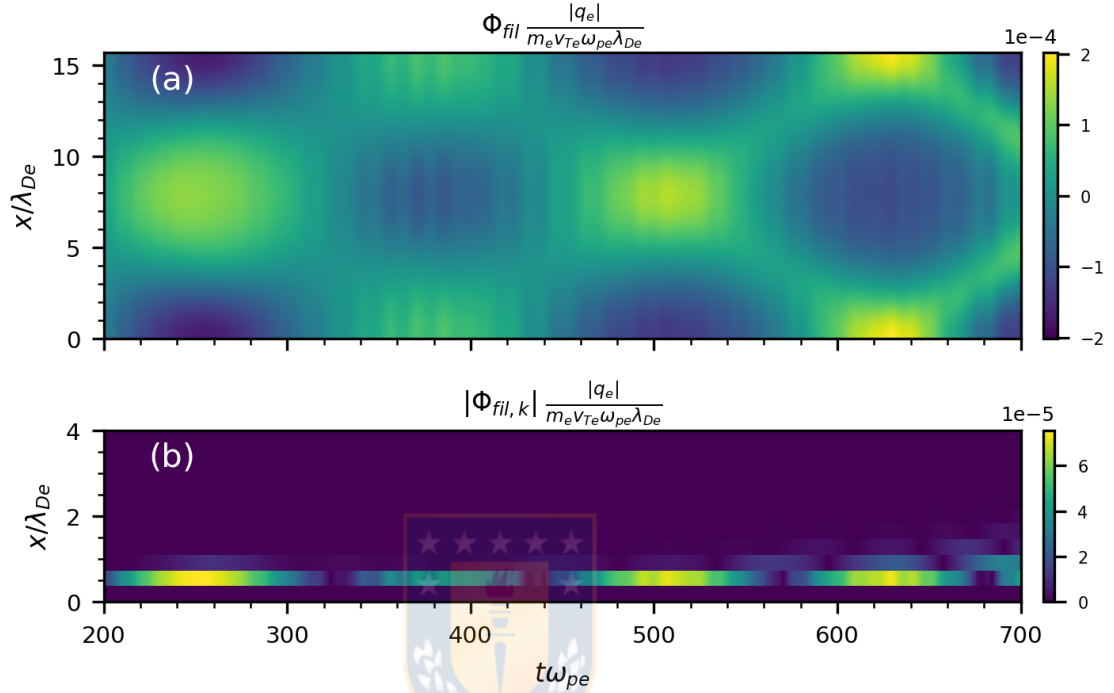


Figure 5.11: Evolution of the variation of (a) the electrostatic potential, filtered in frequency, $\bar{\Phi}_{fil}$, and its spatial Fourier transform (b) for $\varepsilon_e = 4.0 \times 10^{-2}$, for mobile ions. Time interval corresponding to the localization of the solitary structure in the potential.

around the center of the position domain, $\bar{x} = \bar{L}_x/2$ [Fig.5.11(a)], with wavenumbers up to $\bar{k} = 0.8$ [Fig.5.11(b)]. After this instant, variations with $\bar{k} = 1.2$ are excited and the potential becomes localized during $500 \leq t\omega_{pe} \leq 600$, when the cavities in the electrons density are being formed [Fig.5.13(a)].

In Fig.5.12, during $400 \leq t\omega_{pe} \leq 1000$, the potential is observed to become more localized and to grow in amplitude, as the electron cavities are deepened [see Fig.5.6(a)], up to $t\omega_{pe} = 1000$, forming two solitary low frequency counter-propagating waves propagating with speed $|\bar{v}_{s,\Phi}| = 6.283 \times 10^{-2}$, equal to that of

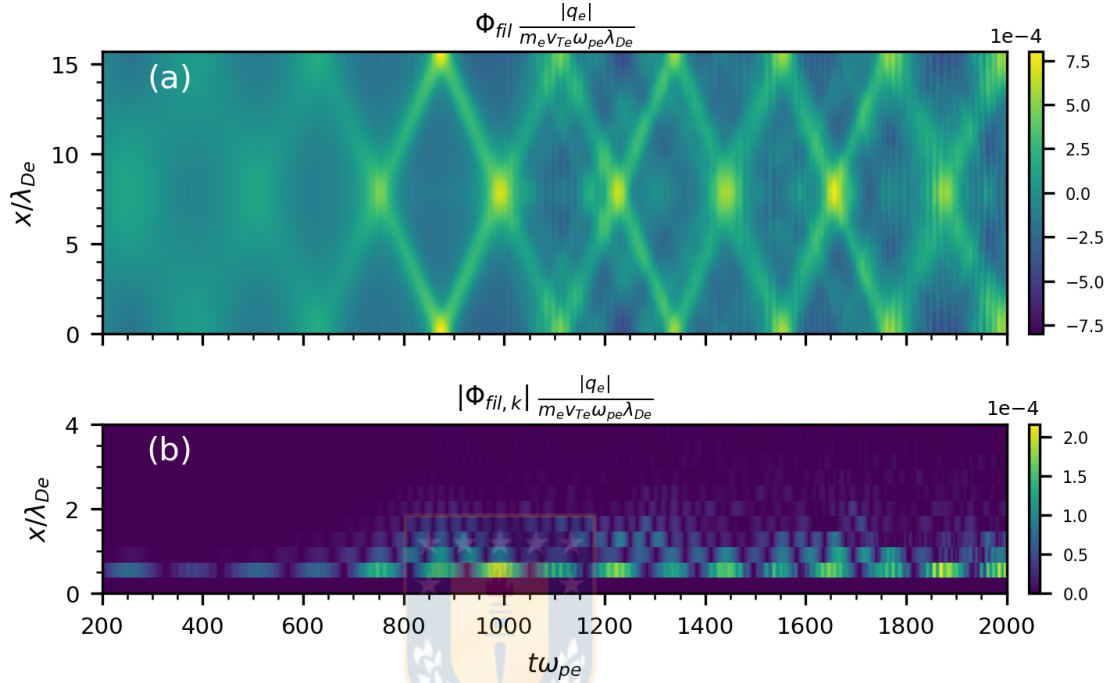


Figure 5.12: Evolution of the variation of (a) the electrostatic potential, filtered in frequency, $\bar{\Phi}_{fil}$, and its spatial Fourier transform (b) for $\varepsilon_e = 4.0 \times 10^{-2}$, for mobile ions. The time interval considers the initial formation of the solitary structures and further propagation.

the structures in $\delta\bar{n}_{e,fil}$. Since the system is periodic, the boundaries of the position domain as well as $\bar{x} = \bar{L}_x/2$ are crossing points at which the potential is locally and instantaneously enhanced. After the crossing at $t\omega_{pe} = 1000$, the solitary structure is dispersed and several wavelengths of low amplitude are then excited [see Fig.5.12(b)]. This coincides with a crossing of the main cavities and a growing cavity at the center of the position domain, and the further generation of narrower cavities in the electrons density. The main structure persists at further instants.

5.3.3 Evolution of the electrons density

In the electrons density in Figs.(5.6), cavities are formed at $t\omega_{pe} \simeq 500$, when the electrostatic potential begins to become localized. Figure 5.13 shows a detail of the frequency filtered electrons density for $200 \leq t\omega_{pe} \leq 700$. Initially, most of the variations occur with the excited wavenumber, $\bar{k} = 0.4$. The charge is homogenized as the polarity of the potential is reversed [$320 \leq t\omega_{pe} \leq 440$, Fig.5.11(a)]. During $400 \leq t\omega_{pe} \leq 500$, a local depletion of electrons is observed around $\bar{x} = \bar{L}_x/2$, reaching the center that position at $t\omega_{pe} = 500$. After this instant, shallow electrons cavities begin to propagate.

The cavities propagate in the position domain, yielding deeper cavities at the crossing points [Fig.5.6(a)]. Cavities are broadened and propagate accompanied by an excess of electrons at their boundaries from $t\omega_{pe} = 800$. At $t\omega_{pe} = 900$, the central cavity is excited. The three cavities cross at $t\omega_{pe} = 1000$, leading to the generation of shorter wavelengths variations [Fig.5.6(b)] and several narrower cavities [Fig.5.6(a)].

The evolution of the spectrum of the electrons density $\delta\bar{n}_e$ is discussed. Figure 5.14 shows that the low frequency structure of the electrons density involves the excitation of several waves in the same region as those found in the electric field (Fig.5.5). The amplitude of these waves increases as the cavity-like regions are formed [Fig.5.14(a) and (b)], exciting mostly waves of short wavelength, $1.2 < \bar{k} < 2.4$. The amplitudes of these waves continue to grow at longer times, exciting shorter wavelengths, $\bar{k} > 2.4$ [Fig.5.14(c)]. Therefore, most of the low frequency dynamics of $\delta\bar{n}_e$ is associated to waves lying on the linear higher order branch, with $\bar{k} = 1.2$

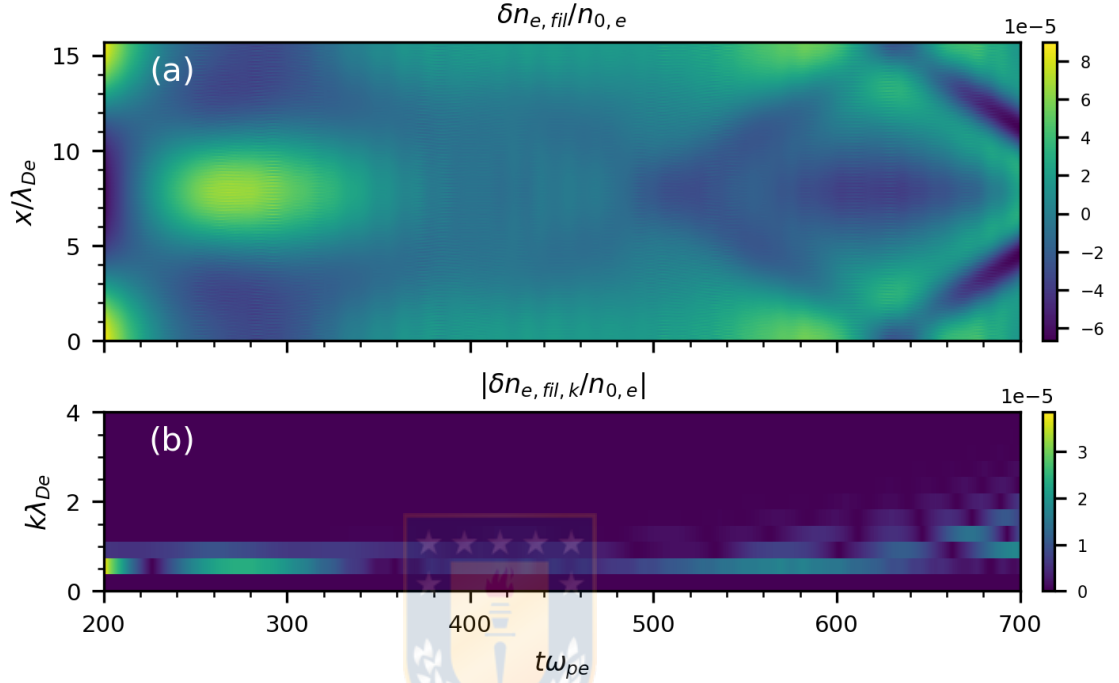


Figure 5.13: Evolution of the variation of (a) the electrons density filtered in frequency, $\delta \bar{n}_{e,fil}$, and its spatial Fourier transform (b) for $\varepsilon_e = 4.0 \times 10^{-2}$, for mobile ions. The time interval considers the initial formation of the electron cavities.

and $\bar{k} = 1.6$. Waves below the linear IA branch are excited [white solid line in Fig.5.14(c)], remaining of low amplitude in comparison to those in the acoustic-like branch.

It is noted that the most intense waves excited in this case propagate with phase speeds nearly in the same range and close to the speed $|\bar{v}_c|$ of the electron cavities of Fig.5.6(a). In the initial time interval, the ranges are $4.488 \times 10^{-2} \leq \bar{v} \leq 8.976 \times 10^{-2}$ and a low speed range, $0.0 \leq \bar{v}_\phi \leq 2.244 \times 10^{-2}$ [Fig.5.14(a)], $6.732 \times 10^{-2} \leq \bar{v}_\phi \leq 8.334 \times 10^{-2}$ [Fig.5.14(b)], $5.984 \times 10^{-2} \leq \bar{v}_\phi \leq 8.228 \times 10^{-2}$ [Fig.5.14(c)]. Also, slower waves are excited [Fig.5.14(b) and (c)], coinciding with the formation of the

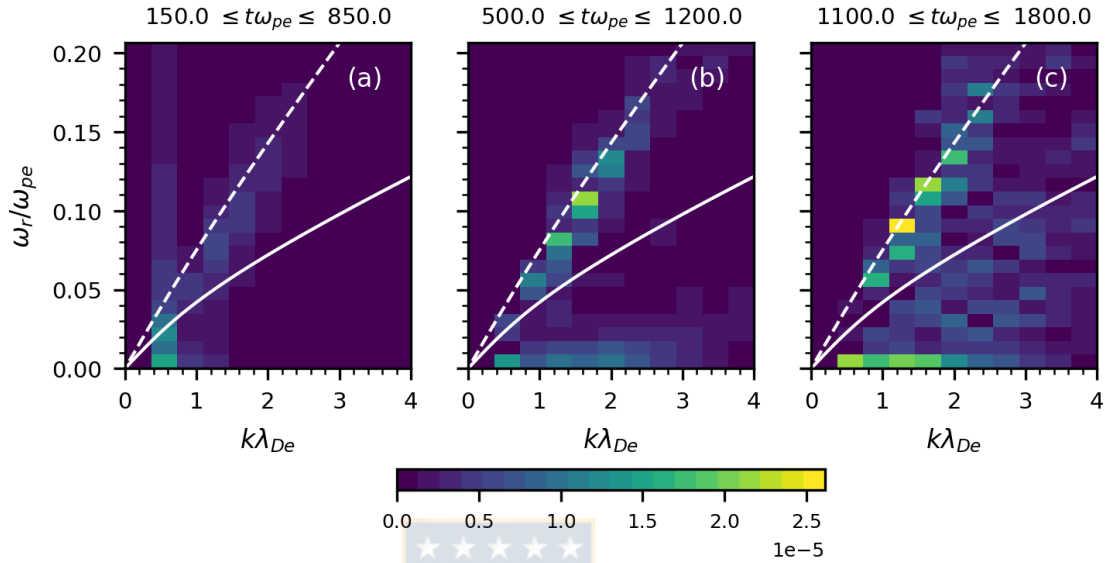


Figure 5.14: Spectra of the electrons density $|\delta\bar{n}_{e,k,\omega}|$ for $\varepsilon_e = 4.0 \times 10^{-2}$ for the case of mobile ions. Three time intervals are shown. Roots of the linear dispersion relation (2.2.10) are shown, corresponding to the IA mode (solid white line) and the least damped higher order mode (dashed white line).

central cavity [Fig.5.6(a)].

5.3.4 Evolution of the heavy ions density

The variations of the ions density, $\delta\bar{n}_i$, are shown in Figs.5.15 and 5.16. Initially, time variations of the ions density occur mostly with $\bar{k} = 0.4$ [Figs.5.15(b) and 5.16(b)] with decreasing amplitude. During $200 \leq t\omega_{pe} \leq 300$, the potential has a maximum which expels ions to the boundaries of the position domain, as observed in $300 \leq t\omega_{pe} \leq 450$ [Fig.5.15(a)]. The potential then increases at those regions and ions are again crowded at $\bar{x} = \bar{L}_x/2$. This charge accumulation is accompanied by the formation of a cavity in the electrons density [Fig.5.13(a)] and yields the localized positive potential observed at $t\omega_{pe} = 500$ [Fig.5.11(a)]. As the potential

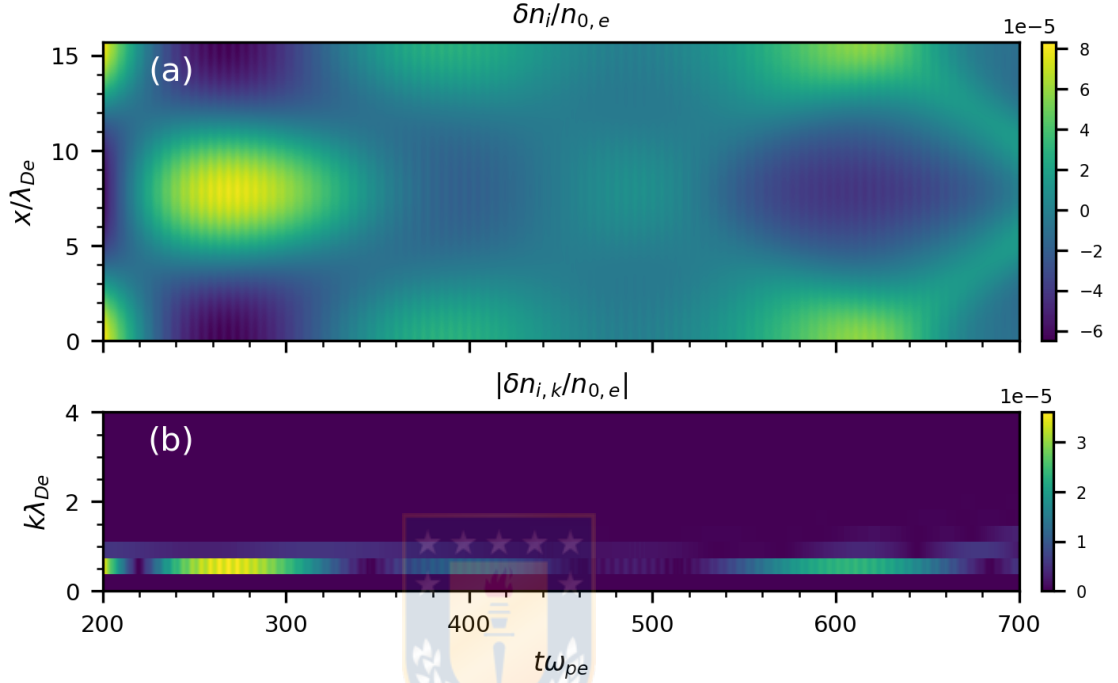


Figure 5.15: Evolution of the variation of (a) ions density, $\delta \bar{n}_i$, and its spatial Fourier transform (b) for $\varepsilon_e = 4.0 \times 10^{-2}$. The time interval considers the localization of compressive pulses.

involves shorter wavelengths, the force on the species is enhanced, accumulating a large amount of ions at the borders at $t\omega_{pe} = 600$ [Fig.5.15(a)].

Figure 5.16 shows the evolution of $\delta \bar{n}_i$ for longer times. After the localization process, two counter-propagating solitary structures, corresponding to compressive pulses, begin to propagate with speeds $|\bar{v}_s| \simeq 6.283 \times 10^{-2}$. Their propagation coincides with that of the electron cavities [Fig.5.6(a)], suggesting that both structures propagate coupled in position space, and account for the solitary potential [Fig.5.12(a)]. The solitary structures lose coherence after $t\omega_{pe} = 1000$ as shorter wavelength are developed ($\bar{k} > 2.1$), even though of low amplitude [see Fig.5.16(b)].

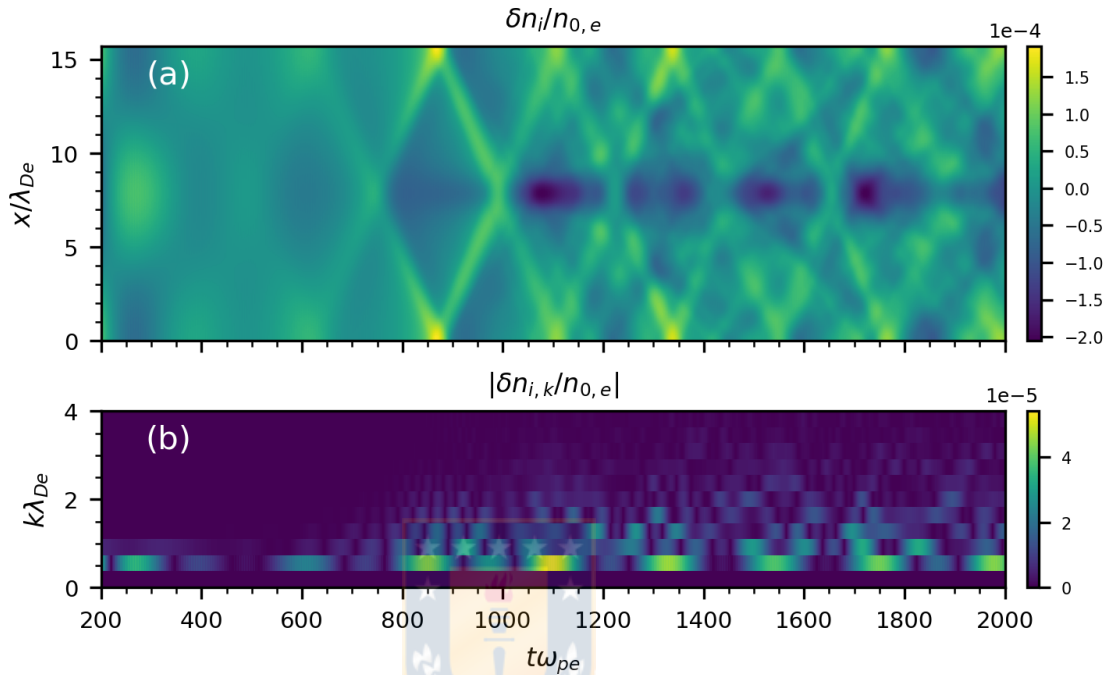


Figure 5.16: Evolution of the variation of (a) ions density, $\delta \bar{n}_i$, and its spatial Fourier transform (b) for $\varepsilon_e = 4.0 \times 10^{-2}$. The time interval considers the formation of the ion compressive pulses and further propagation.

This event coincides with the development of shorter wavelength structures in the electrons density and the dispersion of the electrostatic potential.

The evolution of the low frequency spectrum of the ions density in Fig.5.17 exhibits low amplitude variations with the most intense waves having longer wavelengths, $\bar{k} < 1.2$. Waves along the acoustic-like branch are observed, with the most intense waves having wavenumber $\bar{k} \leq 0.8$. The phase speed of these waves lie within the range $4.488 \times 10^{-2} \leq \bar{v}_\phi \leq 8.976 \times 10^{-2}$, being coincident with the wave structure in $|\bar{E}_{k,\omega}|$ and $|\delta \bar{n}_e|$. Other intense waves are observed with nearly zero frequency for the range $0.4 \leq \bar{k} \leq 1.2$ [Figs.5.17(b) and (c)]. As in the case of the electrons

density, low amplitude waves located below the linear IA branch are present during $1100 \leq t\omega_{pe} \leq 1800$ with smaller wavenumbers, $\bar{k} \leq 2.4$ [Figs.5.17(c)].

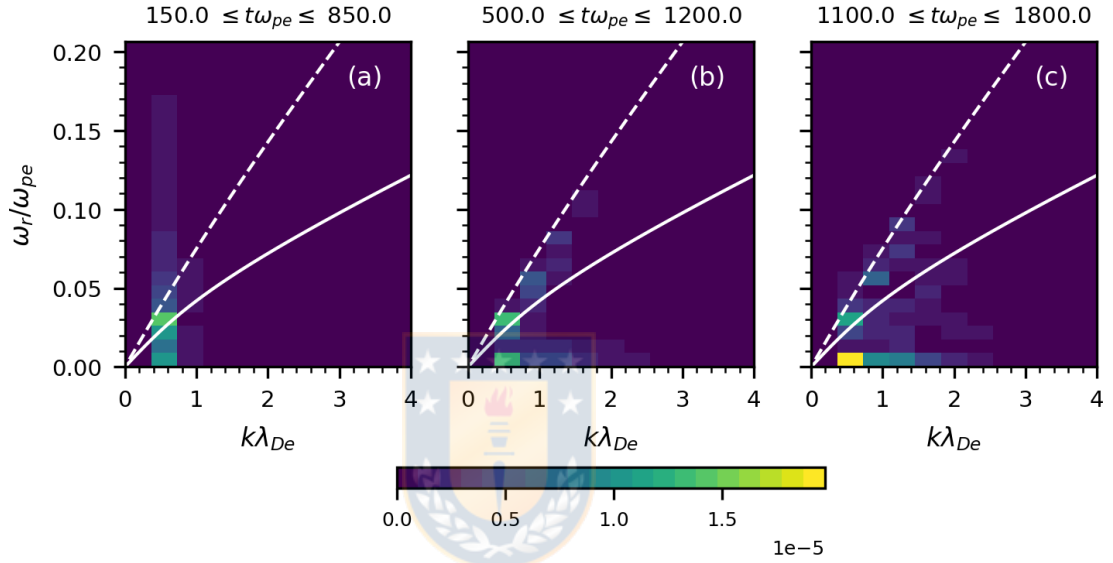


Figure 5.17: Spectra of the ions density $|\delta\bar{n}_{i,k,\omega}|$ for $\varepsilon_e = 4.0 \times 10^{-2}$ for the case of mobile ions. Three time intervals are shown. Roots of the linear dispersion relation (2.2.10) are shown, corresponding to the IA mode (solid white line) and the least damped higher order mode (dashed white line).

5.4 Electron and ion nonlinear structures

The structures observed in the ions density and the low frequency component of the electrons are located at the same positions and propagate with the same velocities, as noted from Figs.5.6(a) and 5.16(a). The instant at which such a coupling would occur, τ_{loc} , and the full distribution functions of each species are discussed.

5.4.1 Local correlations

Since the low frequency structure of the electrons density and the ions density exhibit an opposite tendency, their local correlations, $C[\delta\bar{n}_i, \delta\bar{n}_{e,\text{fil}}]$, estimated as

$$C[\delta\bar{n}_i, \delta\bar{n}_{e,\text{fil}}](\bar{x}, \bar{t}) = \frac{\delta\bar{n}_i(\bar{x}, \bar{t})\delta\bar{n}_{e,\text{fil}}(\bar{x}, \bar{t})}{\sigma_i(\bar{t})\sigma_{e,\text{fil}}(\bar{t})},$$

where $\sigma_j(\bar{t})$ the standard deviation of the particle density of species j in time, should exhibit anti-correlation at the positions where the electron cavities and the compressive pulses are located. The evolution of the local correlations of these densities is shown in Fig.5.18.

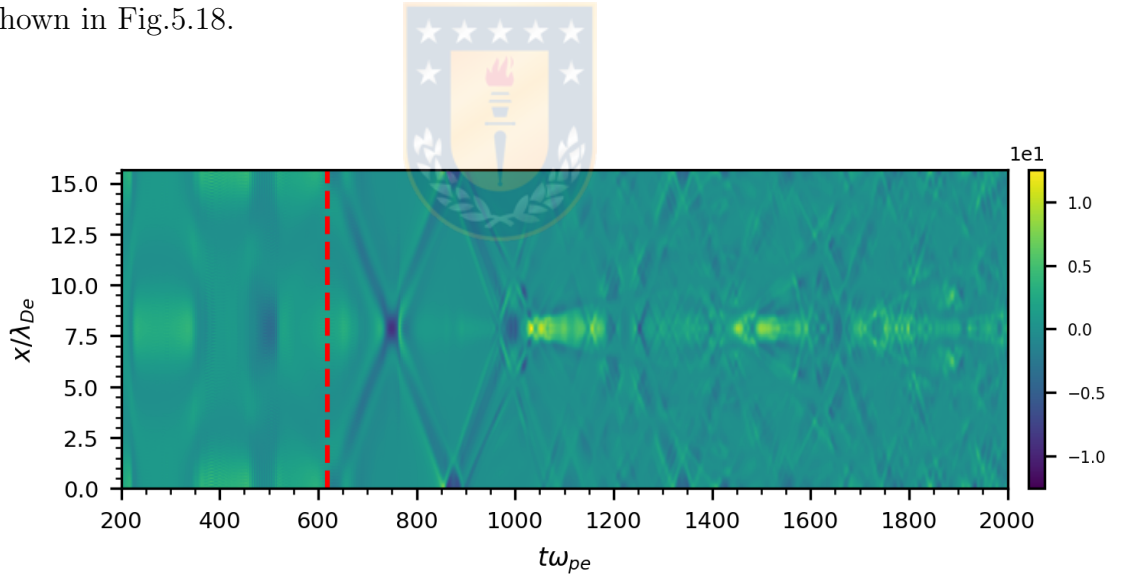


Figure 5.18: Evolution of $C[\delta\bar{n}_i, \delta\bar{n}_{e,\text{fil}}]$ and the transition to the localization of perturbations in position space. The localization time τ_{loc} is indicated (red dashed line) for $\varepsilon_e = 4.0 \times 10^{-2}$.

Local correlations also allow to determine the instant τ_{loc} by finding the instant at which the correlations begin to be negative at the positions of these structures. In this case, $\tau_{\text{loc}} = 618.75$. Before this instant, correlations are mostly positive. After

τ_{loc} , anti-correlation is observed at the location of the structures. At $t\omega_{pe} > 1000$, the anti-correlative behavior is lost at a large extent although at certain regions is intermittently observed (for instance, see Fig.5.18 during $1200 \leq t\omega_{pe} \leq 1400$ and $1700 \leq t\omega_{pe} \leq 1800$). Most of the time both densities are nearly uncorrelated ($C \sim 0$), due to the difference in the range of wavelength developed by each species.

5.4.2 Particle distribution functions

The particle distribution functions are observed during three stages: **(i)** at the onset of the formation of the structures ($t\omega_{pe} < \tau_{loc}$), **(ii)** during the propagation of the structures ($\tau_{loc} \leq t\omega_{pe} \leq 1000$) and **(iii)** at the formation of shorter wavelength structures ($t\omega_{pe} > 1000$).

Onset of the formation of the structures

Figure 5.19 shows the variations of the distribution function of electrons [Figs.5.19(a) through (d)], and of the ions [Figs.5.19(e) through (h)], at four instants prior to the propagation of the low frequency structures in both densities. The variations in the electrons distribution show the formation of a localized region of depletion of electrons right above the phase speed $\bar{v}_{\phi,IA}$ that is further localized as the filamentation progresses [Fig.5.19(d)]. This region is centered about $|\bar{v}| \simeq 6.0 \times 10^{-2}$, close to $|\bar{v}_c|$ and would account for the formation of shallow cavities during $400 \leq t\omega_{pe} \leq 500$ in the electrons density (Fig.5.13).

In the variations of the ions distribution, large amplitude variations occur for velocities in the range $|\bar{v}| \leq \bar{v}_{\phi,IA}$. This distribution exhibits a slow filamentation process. It is noted that as the localized depletion of electrons moves in position

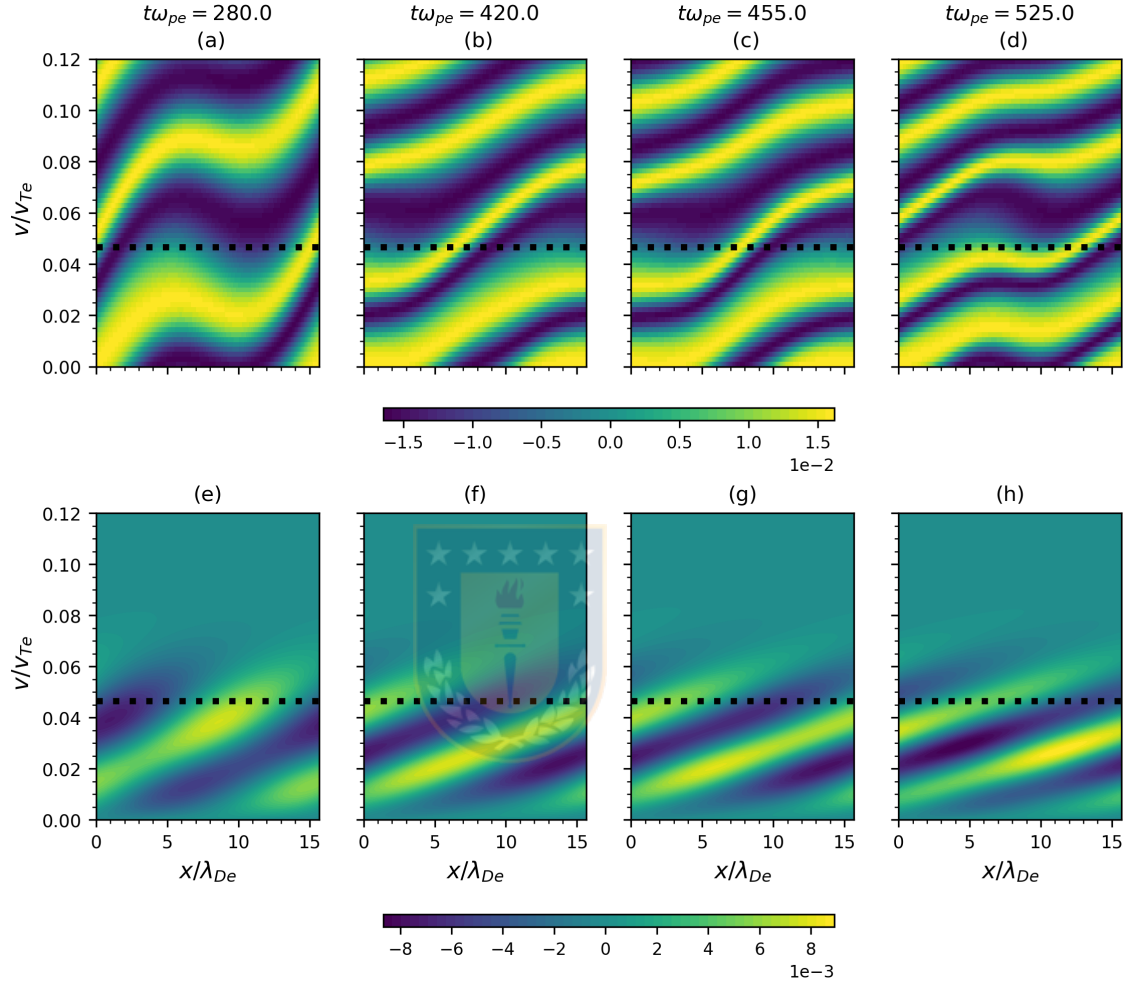


Figure 5.19: Phase space portraits of electrons $\delta \bar{f}_e$ [(a) through (d)] and ions $\delta \bar{f}_i$ [(e) through (h)] for $\varepsilon_e = 4.0 \times 10^{-2}$, before the localization of the structures in both densities. Velocity $\bar{v}_{\phi,IA}$ (black dotted line) is indicated.

space, the density of ions along the filaments exhibits a localized accumulation of particles at the same position, which is observed to be accelerated from $\bar{v} = 2.0 \times 10^{-2}$ [Fig.5.19(g)] towards $\bar{v} = 4.0 \times 10^{-2}$ [Fig.5.19(h)]. This accumulation would account for the formation of compressive pulses in the ions density for $t\omega_{pe} \leq 600$ [Fig.5.15(a)].

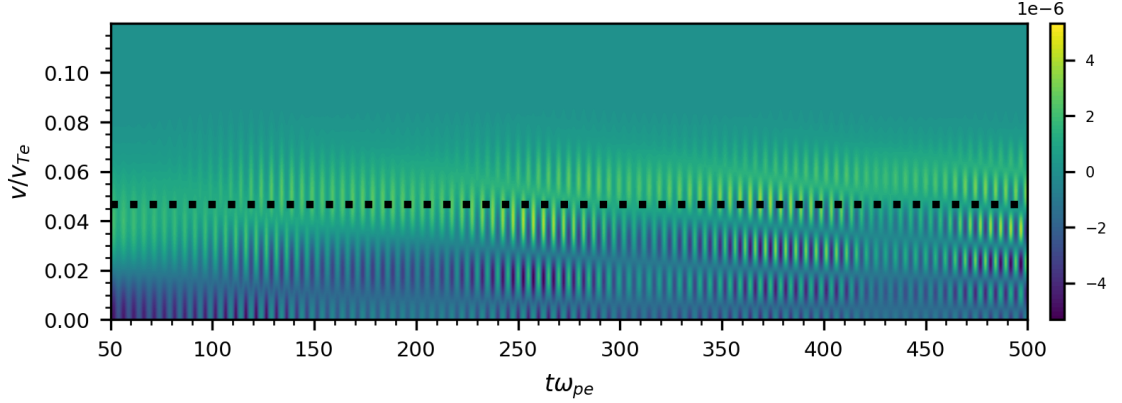


Figure 5.20: Evolution of the variations of the position averaged distribution function of ions, $\langle \delta \bar{f}_i \rangle_{\bar{x}}$, around $\bar{v} = \bar{v}_{\phi, IA}$ for $\varepsilon_e = 4.0 \times 10^{-2}$.

The depopulation of the electrons can be understood by observing the position averaged variations of the distribution function, $\langle \delta \bar{f}_j \rangle_{\bar{x}}$, from each species. Although a high frequency component is observed, it is noted that the behavior of both distributions resembles that of the case of damped perturbations, namely, a population of ions is sped up to the velocities around $\bar{v}_{\phi, IA}$ (Fig.5.20), whereas electrons with velocity slightly above $\bar{v}_{\phi, IA}$ are slowed down (Fig.5.21). As ions naturally interact with waves at that velocity, slow electrons undergo the opposite dynamical effects of the associated electric field. As the filamentation progress, this information is translated into the position dependency, being observed as cavities in the electrons density $\delta \bar{n}_{e, \text{fil}}$. From the present analysis, it is unclear if the electron holes related to the Langmuir wave contribute to this localized depletion.

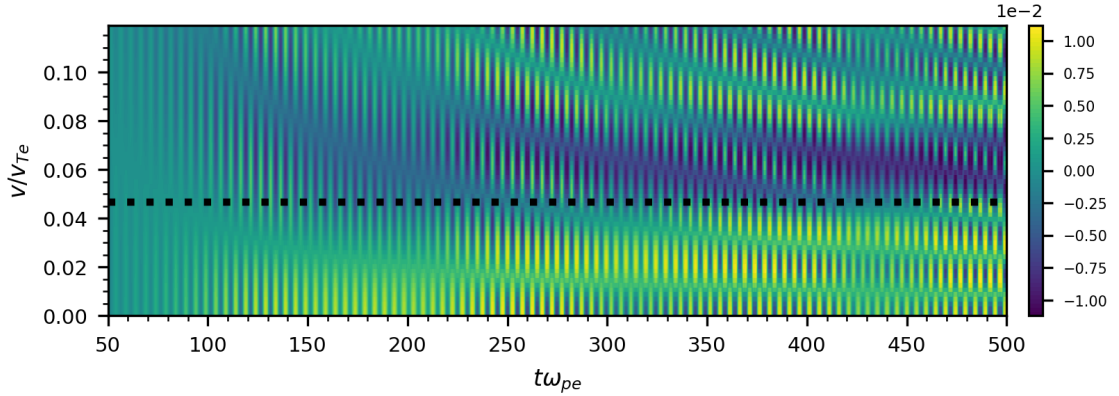


Figure 5.21: Evolution of the variations of the position averaged distribution function of electrons, $\langle \delta \bar{f}_e \rangle_{\bar{x}}$, around $\bar{v} = \bar{v}_{\phi, IA}$ for $\varepsilon_e = 4.0 \times 10^{-2}$.

Propagation of nonlinear structures

Figure 5.22 shows the distribution function of electrons [Figs.5.22(a) through (d)], and of the ions [Figs.5.22(e) through (h)], at four instants corresponding to the propagation of the localized structures. In the electrons distribution it is observed that the localized depopulation evolves into a electron hole which propagates with speed $\bar{v}_H = 6.25 \times 10^{-2}$. This speed is in the range of the phase speed of the waves found in the electric field spectrum [Fig.5.5(a)] and of the electrons density [Fig.5.14(a)]. As it propagates, its width in the velocity range increases, indicating an intensification of the trapping potential associated to it [see Fig.5.12(a)], and the electrons population increases around the hole producing the shielding observed in Ref.[48], which leads to a steep decay of the trapping potential at its boundaries. Such excess of electrons can be observed in Figs.5.23(b) through (d) in $\delta \bar{n}_{e, fl}$.

In the ions distribution [Figs.5.22(e) through (g)], it is observed that the localized accumulation of ions is enhanced, as also observed in the ions density in Fig.5.23,

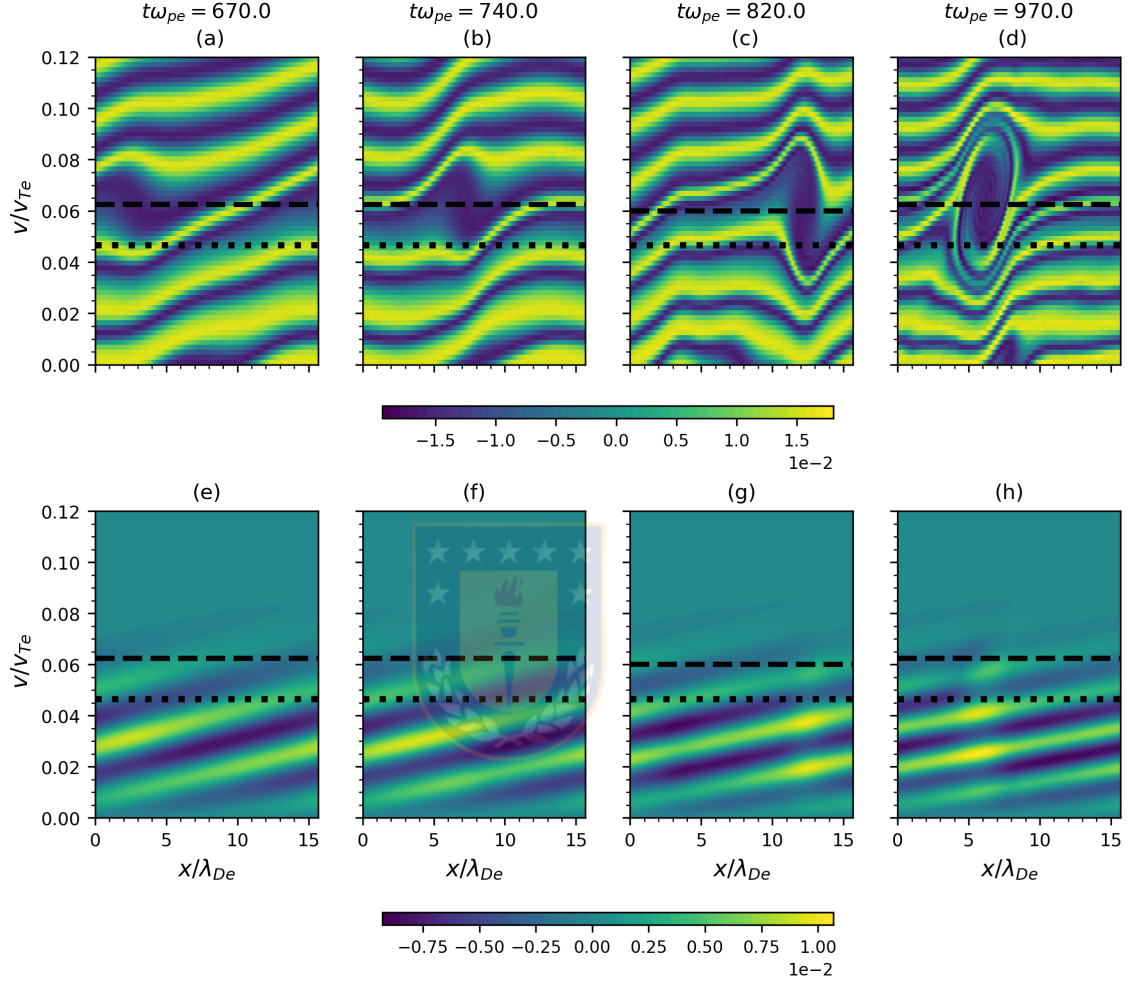


Figure 5.22: Phase space portraits of electrons $\delta \bar{f}_e$ [(a) through (d)] and ions $\delta \bar{f}_i$ [(e) through (h)] for $\varepsilon_e = 4.0 \times 10^{-2}$, during the propagation of the electron cavities and the ion compressive pulses. Velocity $\bar{v}_{\phi,IA}$ (black dotted line) and the electron hole velocity \bar{v}_H (black dashed line) are indicated.

and displaced to $\bar{v}_{\phi,IA}$. This enhancement could be explained by the fact that an increase in the intensity of the moving potential of the electron hole leads to the accumulation of heavy ions within the trapping region [47]: a localized positive potential with growing amplitude slows down incoming ions with an increasing force,

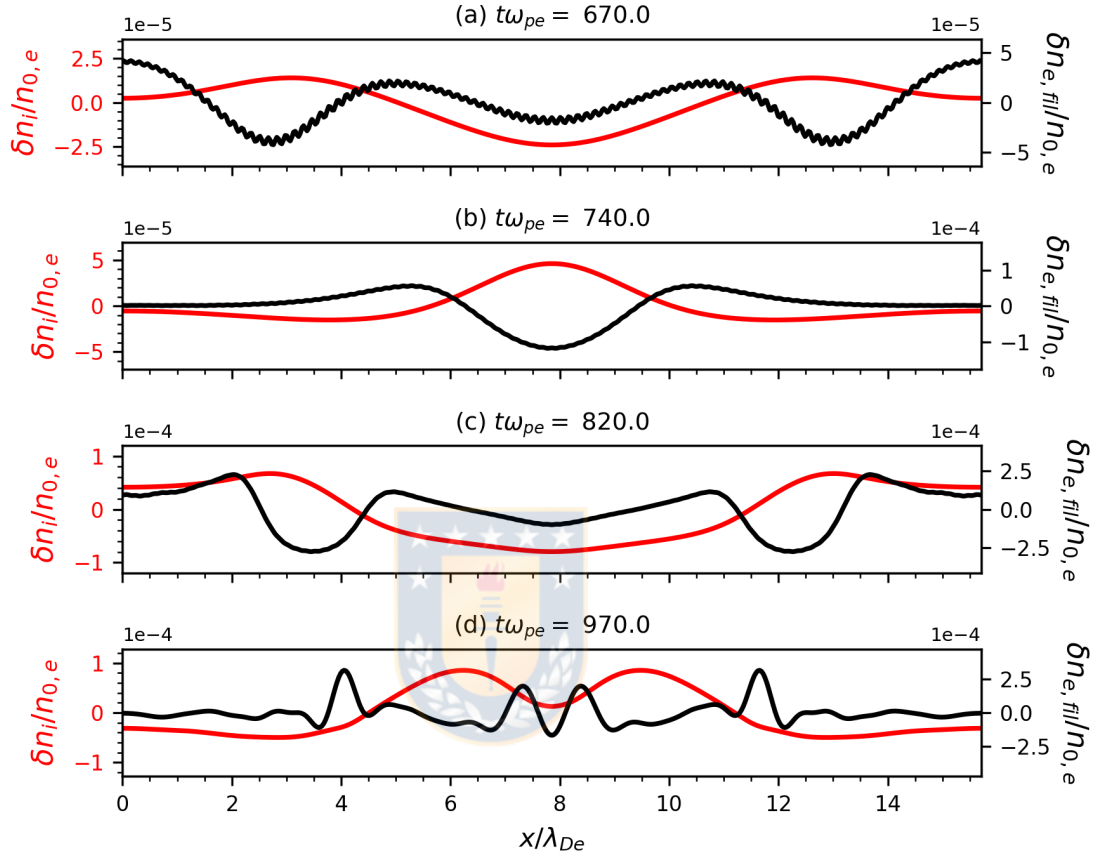


Figure 5.23: Variations of the low frequency component of the electrons density, $\delta\bar{n}_{e,fil}$ (black), and ions density, $\delta\bar{n}_i$ (red), for the instants shown in Fig.5.22, considering positive and negative velocities of the distribution functions.

enlarging their transiting time. Since ions enhance the positive potential, this process self-consistently leads to a growth in the trapping region, the cavity depth in the electrons density, and the amplitude of the compressive pulses in the ions density observed during $600 \leq t\omega_{pe} \leq 1000$ in Figs.5.6(a) and 5.16(a). These structures account for the solitary waves found in the electrostatic potential in Fig.5.12(a).

Once the hole is established [Fig.5.22(c)], ions with different velocities contribute to the formation of the pulse. This is observed in the local accumulation of ions along two filaments close to $\bar{x} = \bar{L}_x$ [Fig.5.22(g)], with lower velocity. Also, as the potential of these structures grows in amplitude, it is capable to limit the transit of faster ions, as noted around \bar{v}_H at $t\omega_{pe} = 970$ [Fig.5.22(h)].

Formation of shorter wavelength structures

Figure 5.24 shows the distribution functions of electrons [Figs.5.24(a) through (d)] and ions [Fig.5.24(e) through (h)], at four instants corresponding to the development of short wavelength structures after $t\omega_{pe} = 1000$ found in Figs.5.6 and 5.16. The density sections plot in Fig.5.25 shows structures with positive velocity of propagation.

The electrons distribution shows the development of smaller electron holes which would account for the propagation of narrower electron cavities in $\delta\bar{n}_{e,\text{fil}}$ [Figs.5.6(a) and 5.25]. At $t\omega_{pe} = 1000$, the electrons distribution exhibit distortions at the boundaries in position space of the primary hole [Fig.5.24(a)] from which secondary holes then grow, one around \bar{v}_H and the other around $\bar{v}_{\phi,IA}$, as observed at $t\omega_{pe} = 1240$ [Fig.5.24(c)]. The process is detailed in Figs.5.26(a) through (d). At further instants, smaller and slower holes are excited below $\bar{v} = \bar{v}_{\phi,IA}$, which is observed in $\delta\bar{n}_{e,\text{fil}}$ as narrower cavities [Fig.5.6(a)]. These holes grow from disturbances in the distribution function below $\bar{v}_{\phi,IA}$ observed at $t\omega_{pe} = 970$ [Fig.5.22(d)] and established once the secondary holes are formed. By comparison with the case of immobile ions, the growth of these holes would be due to structures related to the Langmuir waves.

The ions distribution continues to exhibit local accumulations within the pri-

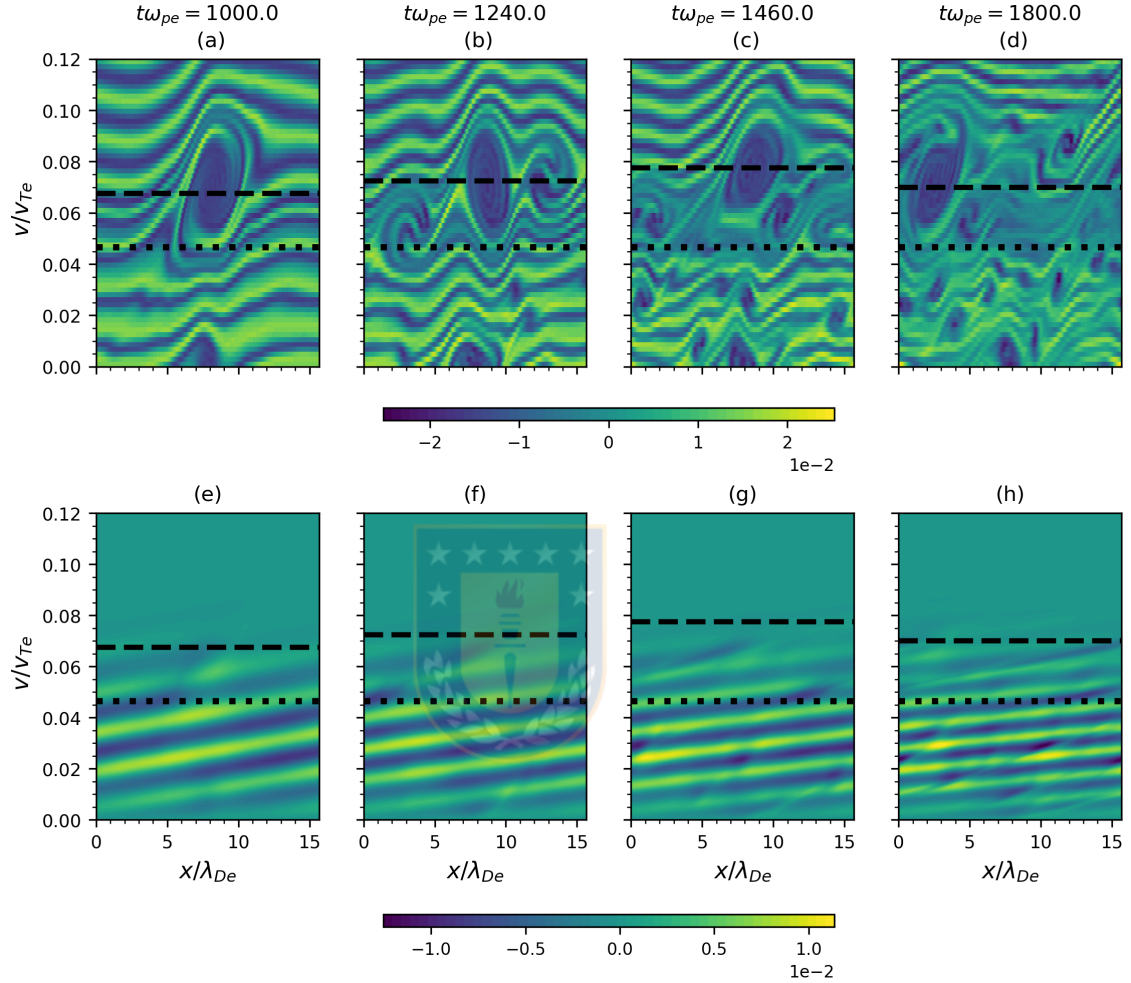


Figure 5.24: Phase space portraits of electrons $\delta \bar{f}_e$ [(a) through (d)] and ions $\delta \bar{f}_i$ [(e) through (h)] for $\varepsilon_e = 4.0 \times 10^{-2}$, during the propagation of the electron cavities and the ion compressive pulses. Velocity $\bar{v}_{\phi, IA}$ (black dotted line) and the electron hole velocity \bar{v}_H (black dashed line) are indicated.

mary region of electron trapping, at $t\omega_{pe} = 1000$ [Fig.5.24(e)]. Once the secondary and smaller holes are developed, the ions distribution has undergone disturbances which lead to the formation of several local accumulation of ions along the filaments [Fig.5.24(f) and more notoriously in Fig.5.24(h)]. In this process, a deformation in the

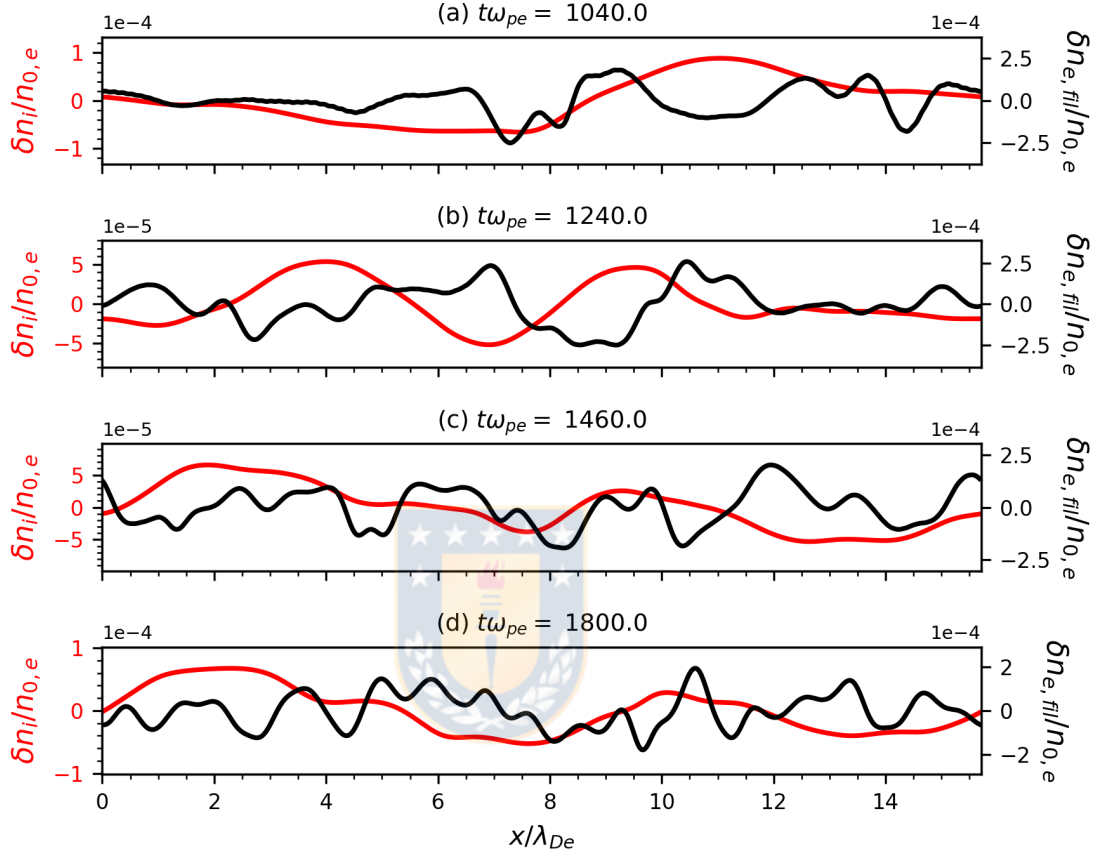


Figure 5.25: Variations of the low frequency component of the electrons density, $\delta\bar{n}_{e,fil}$ (black), and ions density, $\delta\bar{n}_i$ (red), for the instants shown in Fig.5.24, considering only positively propagating structures.

filament in the range $\bar{v}_{\phi,IA} \leq \bar{v} \leq \bar{v}_H$ is observed as the secondary holes are formed [Fig.5.26(e) through (h)]. At further instants, such deformations also occur below $\bar{v}_{\phi,IA}$ when several holes have been developed [Fig.5.24(h)]. This process seems to produce the loss of coherence in both the compressive pulses and the electrostatic potential found from $t\omega_{pe} = 1000$. However, Fig.5.25 suggests that the electron and ion structures remain coupled [Figs.5.25(a) and (b)].

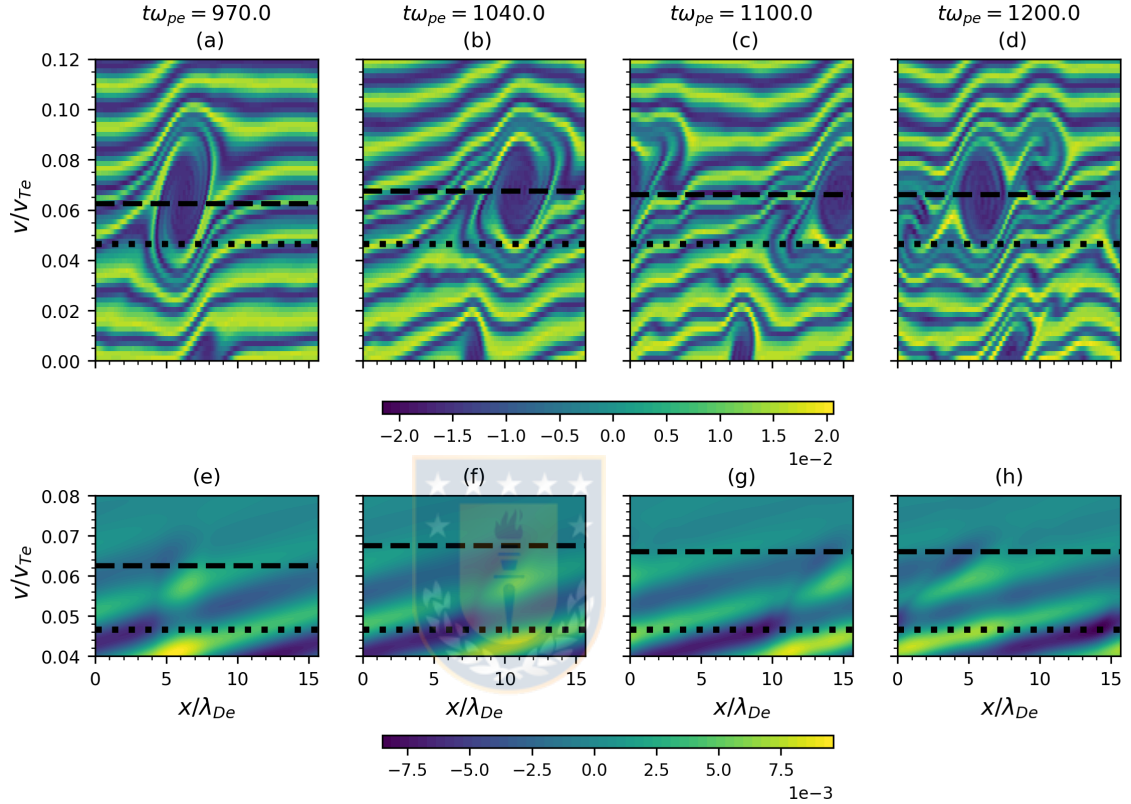


Figure 5.26: Details of the variations of electrons distribution $\delta \bar{f}_e$ [(a) through (d)], and ions distribution $\delta \bar{f}_i$ [(e) through (h)]. Velocity range $\bar{v}_{\phi, IA} \leq \bar{v} \leq \bar{v}_H$ during the process of acceleration of the primary electron hole. Velocity $\bar{v}_{\phi, IA}$ (black dotted line) and the electron hole velocity \bar{v}_H (black dashed line) are indicated.

Figure 5.26 shows the formation of the secondary holes between $t\omega_{pe} = 970$ and $t\omega_{pe} = 1200$, and of the structure in ions distribution around \bar{v}_H . Before the secondary holes are formed, ions locally bunch at the center of the primary hole [Fig.5.26(a) and (e)] around the velocity of the hole \bar{v}_H , sharing boundaries in position space with the electron hole. This region is then stretched with one boundary dragged towards the velocity $\bar{v}_{\phi, IA}$ and the other to \bar{v}_H [Figs.5.24(f) through (h)],

indicating that a portion of these ions has been sped up and another portion has been slowed down with respect to the primary hole. The deformation occurs after the crossing of the three holes at $t\omega_{pe} = 1000$ when the potential is locally enhanced at the crossing point. These deformations are more notorious at larger times [see Fig.5.24(e)], and can be interpreted as compressive ion pulses [45, 84], located at the boundaries of the hole that trap neighbouring electrons [Fig.5.24(c) and (d)]. In the cited references such pulses lead to the disruption of the primary hole into two secondary counter-propagating holes. However, in this case, the primary hole persists. The reason could be that a small population of ions contribute to the pulses, whereas there is still a large number of ions within the primary hole that sustains its trapping potential.

In all the shown instants, the electron holes propagate with larger and increasing speed ($\bar{v}_H = 6.25 \times 10^{-2}$ to 7.75×10^{-2}) compared to those in Fig.5.24. Such acceleration could be related to the generation of secondary holes, as in the initial stages the hole propagates at nearly constant speed [see Figs.5.22(a) through (d)].

5.5 Variation of the amplitude of the initial perturbation ε_e

The previously described dynamics is still observed for lower perturbative amplitudes ε_e . The processes differ mainly in the level of the amplitudes of the involved quantities, the time scales at which they are formed and the velocity of propagation of the structures. In this section, the effects of the variation of ε_e on the instant τ_{loc} are addressed.

5.5.1 Effects on the amplitude of the ions density

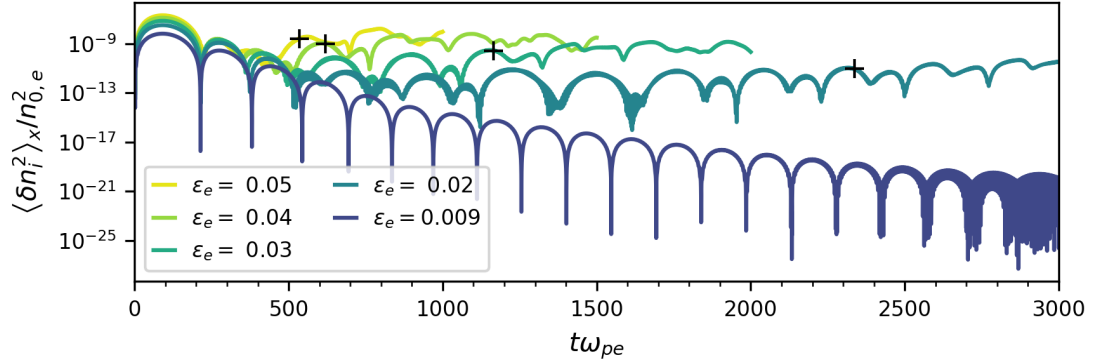


Figure 5.27: Evolution of the position averaged squared amplitude of the ions density, $\langle \delta n_i^2 \rangle_x$, for different ε_e . The time of localization τ_{loc} (black crosses) is indicated.

As ε_e is reduced, the variations in the ions density occur at lower levels. Four processes can be observed in this quantity, as noted in Fig.5.27, resembling the behavior of the electrons density with the Langmuir wave for the same configuration: **(i)** an initial damping, which occurs at nearly the same rate for different ε_e , **(ii)** an arresting of the damping, after which variations in the ions density slowly grow, **(iii)** a coupling with electrons structures, which can be recognized through the correlations $C[\delta \bar{n}_i, \delta \bar{n}_{e,fl}]$, and **(iv)** a saturation.

A reduction in ε_e leads these stages to occur at longer times. If the amplitude ε_e is low enough, the variations can eventually be fully damped, as in the cases addressed in Chapter4, and therefore nonlinear structures are not formed. This suggests the existence of a threshold amplitude to excite this nonlinear dynamics.

5.5.2 Determination of the threshold amplitude ε_e for the localizations in ions density

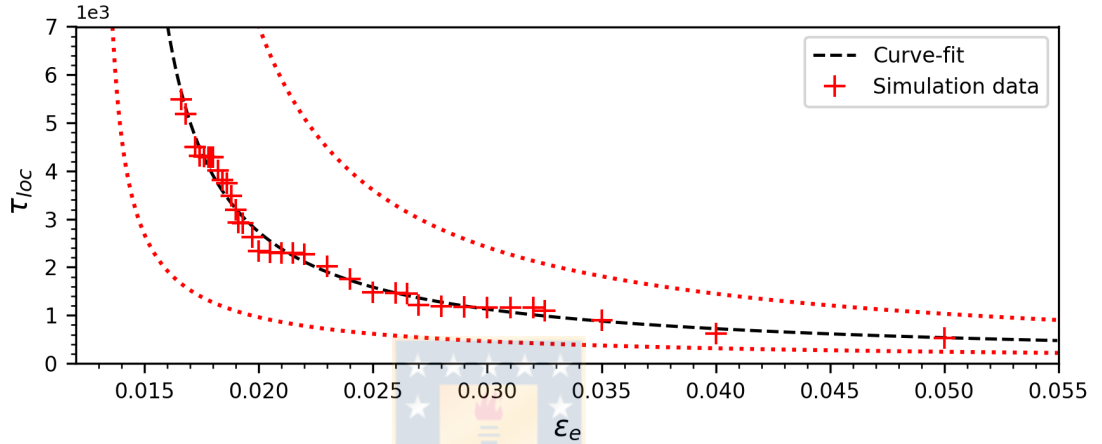


Figure 5.28: Simulation data and curve fit of τ_{loc} for the range $1.66 \times 10^{-2} \leq \varepsilon_e \leq 5.0 \times 10^{-2}$. The red dotted lines correspond to the confidence bands of the curve fit, with a 0.85 confidence for the fit.

The instant τ_{loc} is determined for the range $1.66 \times 10^{-2} \leq \varepsilon_e \leq 5.0 \times 10^{-2}$, by following $C[\delta\bar{n}_i, \delta\bar{n}_{e,fl}]$, $\delta\bar{n}_i$ and $\delta\bar{n}_{e,fl}$. The simulation data in Fig.5.28 suggest that τ_{loc} is ruled by a power law,

$$\tau_{loc} = \alpha [\varepsilon_e - \varepsilon_{e,T}]^{-\beta}, \quad (5.5.1)$$

where α and β are positive coefficients to be estimated, and $\varepsilon_{e,T}$ is the threshold perturbative amplitude, for which $\varepsilon_{e,T} < \varepsilon_e$ triggers the development of the coupled structures. According to the results from the simulations, a curve fitting considering $\varepsilon_e \leq 5.0 \times 10^{-2}$ provides the following parameters with their respective intervals of

confidence.

$$\begin{aligned}\alpha &= 24.7295 \pm 9.0143, \\ \beta &= (9.2714 \pm 0.9723) \times 10^{-1}, \\ \varepsilon_{e,T} &= (1.3743 \pm 0.079) \times 10^{-2},\end{aligned}$$

for 0.85 confidence. The threshold to trigger this nonlinear behavior is higher than that required to trigger the nonlinear Landau damping process for the same wavenumber reported in Ref.[9], implying that the development of these nonlinear structures requires a larger amount of initial energy.

5.6 Summary and discussion

This chapter focuses on the nonlinear evolution of an electron-ion plasma with mass ratio $\bar{m}_i = 1836.153$, initially isothermal species, $\bar{T}_i = 1.0$, both being initialized with driftless Maxwellian distributions. A comparison between the cases of mobile and immobile ions indicate that a low frequency dynamics occurs with waves located in a region corresponding to the least damped higher order mode of the linear dispersion relation, developing trapping regions in the electrons distribution function around $\bar{v}_H = 6.0 \times 10^{-2}$, and being observed as cavities in the electrons density. When ions are endowed with motion, several quantities exhibit larger amplitudes. Specifically, the excited electron holes are larger and exhibit more dynamics in this case. Therefore, heavy ions with $\bar{T}_i = 1.0$ enhance the low frequency dynamics.

At higher velocities, the phase space structures related to the Langmuir wave

are also modified, as shown by the position averaged correlations of the electrons distributions for both cases at fixed instants. However, the overall dynamics remains the same, as observed in the phase space portraits.

The observed low frequency dynamics indicates that the presence of mobile ions excites electrostatic solitary waves related to the formation of slow counter-propagating electron holes of growing amplitude, allowing to accumulate ions within the trapping region, which further enhance the potential of the structure, leading to the formation of solitary compressive pulses in the ions density and of solitary waves in the electrostatic potential without drifting distributions and naturally developed with the initial perturbation, unlike in Refs.[46, 48, 49] in which electrons and ions have a drift or the initial perturbation is an electron hole. Once these structures are established, both structures couple and propagate with the same velocity. This velocity is in the order of the phase speed of the waves on the excited branch, as observed in the electric field spectrum. The density spectra show that electrons mostly contribute to the development of short wavelength structures, whereas ions do with longer wavelengths. It is unclear if the electron holes created due to the nonlinear regime of Langmuir waves contribute to the formation of these holes.

Remarkably, the spectra exhibit low activity around the region of the linear IA branch, the least damped low frequency mode according to the linear dispersion relation, in the propagation of these structures, suggesting a weak role in the dynamics of the plasma. However, information from the distribution functions indicates resonant interaction around the IAW phase speed $\bar{v}_{\phi,IA}$ from early instants in the simulation. Electrons with similar velocities undergo the opposite dynamical effects due to the

charge difference, being mostly slowed down and depopulating a bounded interval in velocity space above $\bar{v}_{\phi,IA}$. As the system evolves, this depopulation is translated into a depopulation in position space, leading to the formation of nonlinear structures.

The compressive pulses in the ions density propagate with speed $\bar{v}_s = 2.6919\bar{c}_s$, where $\bar{c}_s = \sqrt{T_e/\bar{m}_i} = 2.334 \times 10^{-2}$, out of the velocity range predicted by the fluid model for IASs [35]. Also, the waves related to their propagation do not lie on the linear IA branch, as required in the low amplitude analytical solution [36, 85] and as observed in simulations [39, 40]. Therefore, the present results suggest that the excited structures are not IASs.

As the potential grows, the hole grows in extension and interacts with ions of faster velocities. These ions, co-moving with the electron hole can be eventually expelled from within the trapping region if the potential is intense enough. This is observed when the counter-propagating holes and the central hole cross at the center of the position domain. At enhancing the potential, its gradient at the boundaries becomes larger, speeding up or slowing down ions depending on their location. This process introduces low amplitude short wavelength structures in the ions density and accounts for the loss of coherence in the compressive pulses. As ions are forced to the boundaries of the trapping region, they form compressive pulses with positive potential which trap electrons from the boundaries, yielding secondary holes. Unlike other works in which the primary hole is disrupted [45, 84], this hole persists, possibly due to a larger number of heavy ions accumulated within. It remains to study the acceleration of the primary hole, as well as the formation of the central

hole and the smaller narrower holes with speeds below $\bar{v}_{\phi,IA}$. It is hypothesized that these smaller holes should be caused by the development of fine structures in the fast modes at both sides of the distribution whose net effect is a low frequency electric field, as they are also observed in the case of immobile ions.

Finally, this low frequency dynamics still occurs for lower perturbative amplitudes ε_e having longer time scales. Specifically, the ions density shows a decay in the amplitude of its variations and exhibits similar behavior to that observed in the electrons density of the nonlinear Landau damping of Langmuir waves. The instant at which the structures in the electrons and ions distribution are formed and become coupled is also larger. Tests with several amplitudes ε_e allow estimating the threshold amplitude for this dynamics to occur. It is found that this threshold is larger than that required for the nonlinear Landau damping of Langmuir waves; it is a process that requires larger energy to occur.

6 Single wave excitation - Variation of the initial temperature ratio for nonlinear perturbation in a Maxwellian electron-ion plasma

In this chapter the effect of the variation of the temperature ratio \bar{T}_i on the evolution of a driftless Maxwellian electron-ion plasma is analyzed in the nonlinear regime of perturbations. The analysis considers perturbative amplitude $\varepsilon_e = 4.0 \times 10^{-2}$, perturbative wavenumber $\bar{k} = 0.4$ and the plasma is initialized with temperature ratios $\bar{T}_i = 0.025, 0.2, 1.8$ and 5.0 .

6.1 Electric field spectra

The spectra of the electric field are shown in Figs.6.1 for $\bar{T}_i \leq 1.0$ and 6.2 for $\bar{T}_i \geq 1.0$. The case $\bar{T}_i = 1.0$ is shown for comparison. The spectra are compared with the roots of their respective linear dispersion relation for three time intervals considering the formation of nonlinear structures ($500 \leq t\omega_{pe} \leq 1200$), a middle term interval ($1100 \leq t\omega_{pe} \leq 1800$) and a longer term interval ($1700 \leq t\omega_{pe} \leq 2400$).

It is observed that the low frequency activity is more intense for $\bar{T}_i < 1.0$ with waves mostly lying on linear higher order modes. The excited regions in $\bar{\omega}_r - \bar{k}$

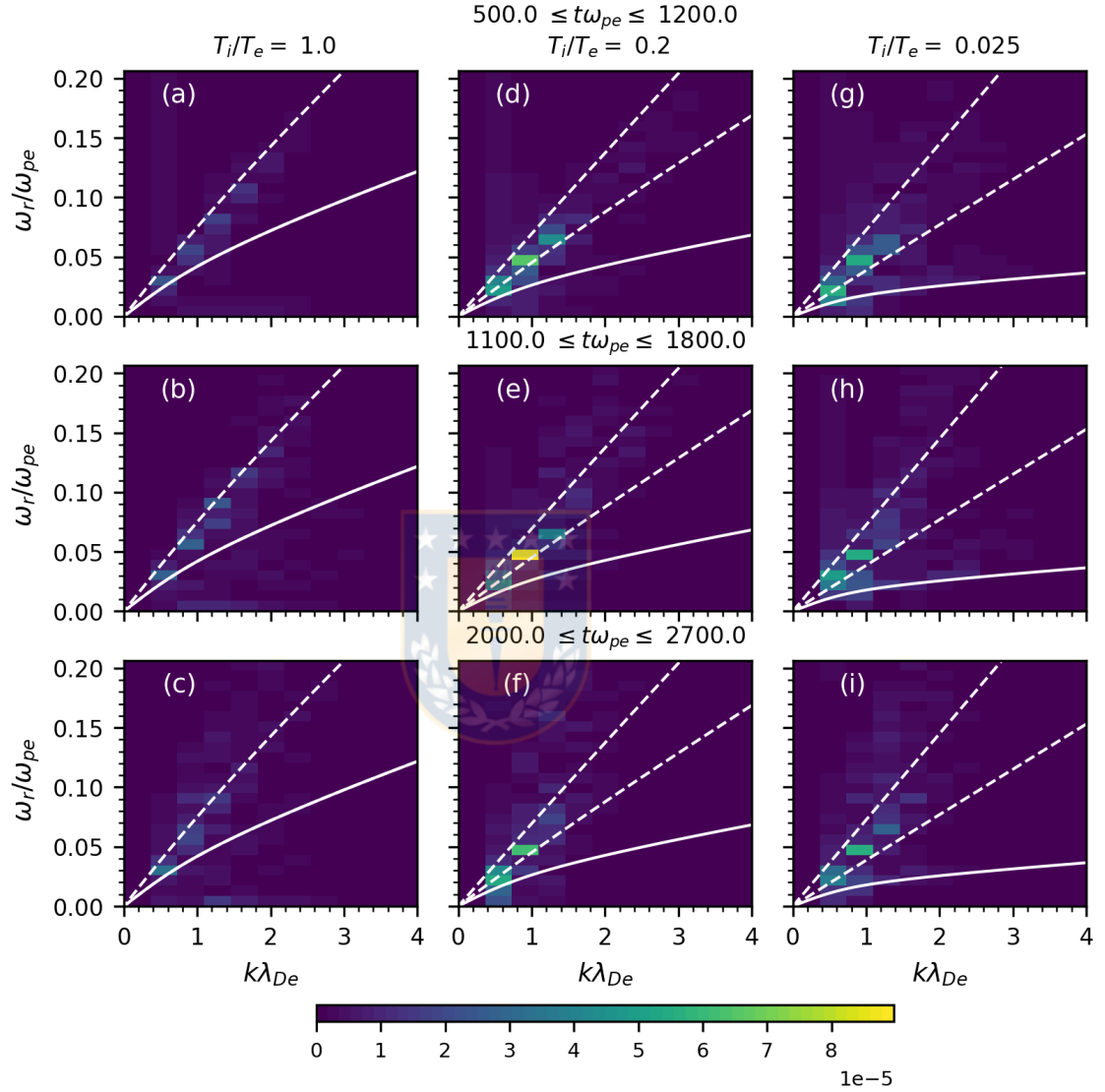


Figure 6.1: Evolution of the electric field spectra, $|\bar{E}_{k,\omega}|$, for $\bar{T}_i = 1.0$ [(a) through (c)], 0.2 [(d) through (f)] and 0.025 [(g) through (i)], for three time intervals (rows). Perturbative amplitude $\varepsilon_e = 4.0 \times 10^{-2}$. The respective IA mode (solid white line) and higher order linear modes (dashed white line) from the linear dispersion relation are shown. For $\bar{T}_i < 1.0$, the higher order modes show the boundaries of the excited region.

space are nearly the same than in case $\bar{T}_i = 1.0$. However, their respective linear dispersion relations predict a larger number of higher order modes for this region rather than just the least damped one, as the number of modes in a region increases with lower \bar{T}_i in linear theory. The most of the excited waves in the plasma have wavenumbers $\bar{k} \leq 1.2$ and frequencies $\bar{\omega}_r \leq 0.1$ [Figs.6.1(d) through (i)], lower in comparison to those found in the isothermal case. The range of phase velocities for these waves is $4.488 \times 10^{-2} \leq \bar{v}_\phi \leq 8.976 \times 10^{-2}$, in the same range as those excited with $\bar{T}_i = 1.0$. Low intensity waves are excited in the region of the linear IA mode for $\bar{T}_i = 0.025$ [Figs.6.1(g) through (i)] with phase velocities in the range $1.122 \times 10^{-2} \leq \bar{v}_\phi \leq 4.488 \times 10^{-2}$.

In comparison, the amplitude of low frequency waves for $\bar{T}_i > 1.0$ is at least one order of magnitude lower than with $\bar{T}_i < 1.0$, having the case $\bar{T}_i = 5.0$ the lower amplitudes [Figs.6.2(a) through (c)] for all three time intervals. Furthermore, the dispersion structure of this case found from the simulations is similar to that found in the case of an electron-ion plasma with immobile ions, as shown in Fig.6.3, except by waves with frequencies $\bar{\omega}_r \leq 0.05$ during $1100 \leq t\omega_{pe} \leq 1800$ [Figs.6.3(c) and (d)], and along the acoustic-like branch during $2000 \leq t\omega_{pe} \leq 2700$ [Figs.6.3(e) and (f)]. Further differences are found in the long term, as observed in Fig.6.4. The middle case $\bar{T}_i = 1.8$ [Figs.6.2(d) through (f)] shows a structure similar to that of the isothermal case but with lower amplitudes.

The excited regions in the cases $\bar{T}_i > 1.0$ are not necessarily coincident with regions of linear higher order branches, as in the case of $\bar{T}_i = 1.8$ during $1100 \leq t\omega_{pe} \leq 1800$ [Fig.6.2(e)] and $\bar{T}_i = 5.0$ during $2000 \leq t\omega_{pe} \leq 2700$ [Fig.6.2(c)]. With

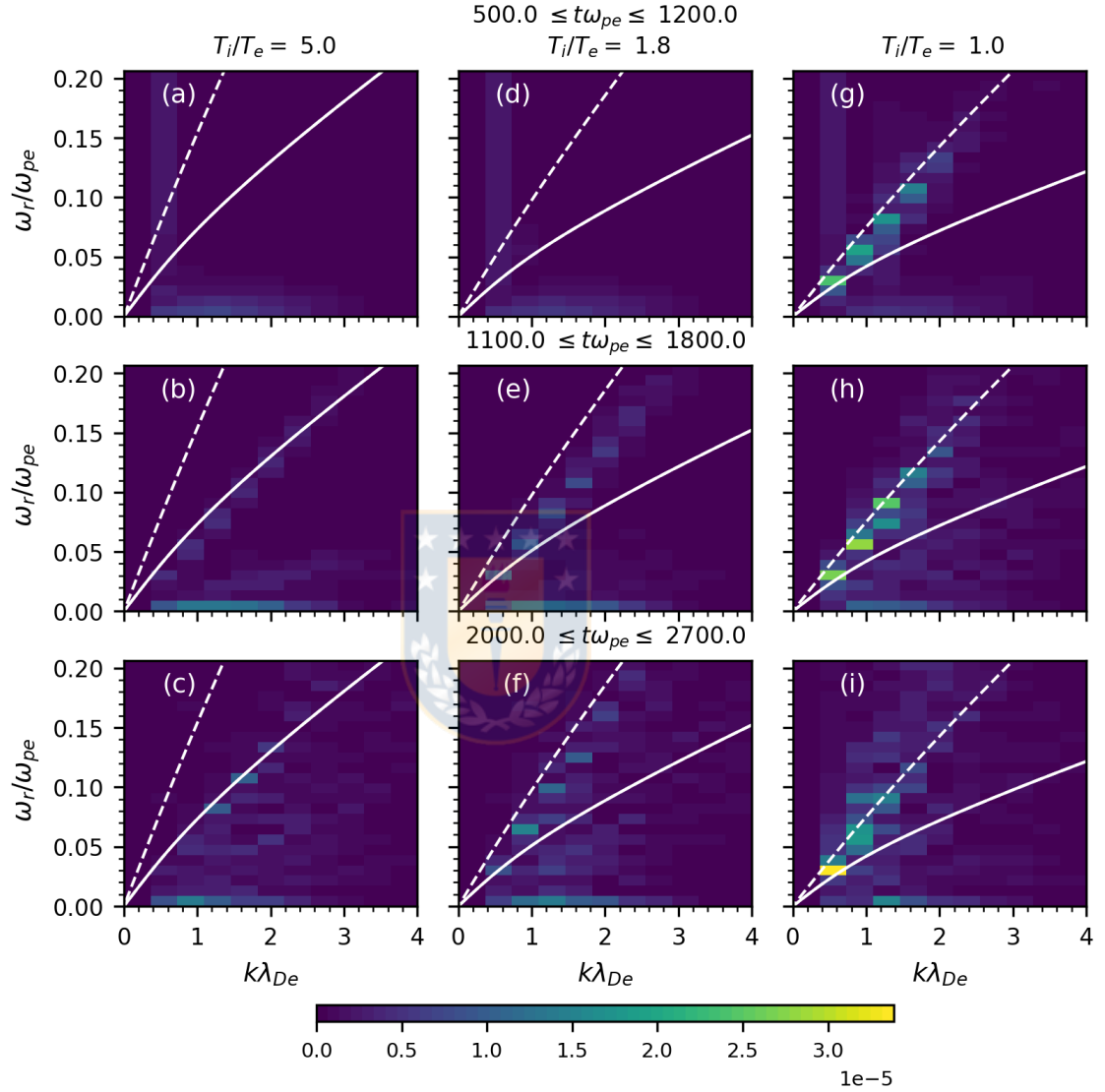


Figure 6.2: Evolution of the electric field spectra, $|\bar{E}_{k,\omega}|$, for temperature ratios $\bar{T}_i = 5.0$ [(a) through (c)], 1.8 [(d) through (f)] and 1.0 [(g) through (i)]. The respective IA mode (solid white line) and the least damped higher order linear modes (dashed white line) from the linear dispersion relation are shown. Perturbative amplitude $\varepsilon_e = 4.0 \times 10^{-2}$.

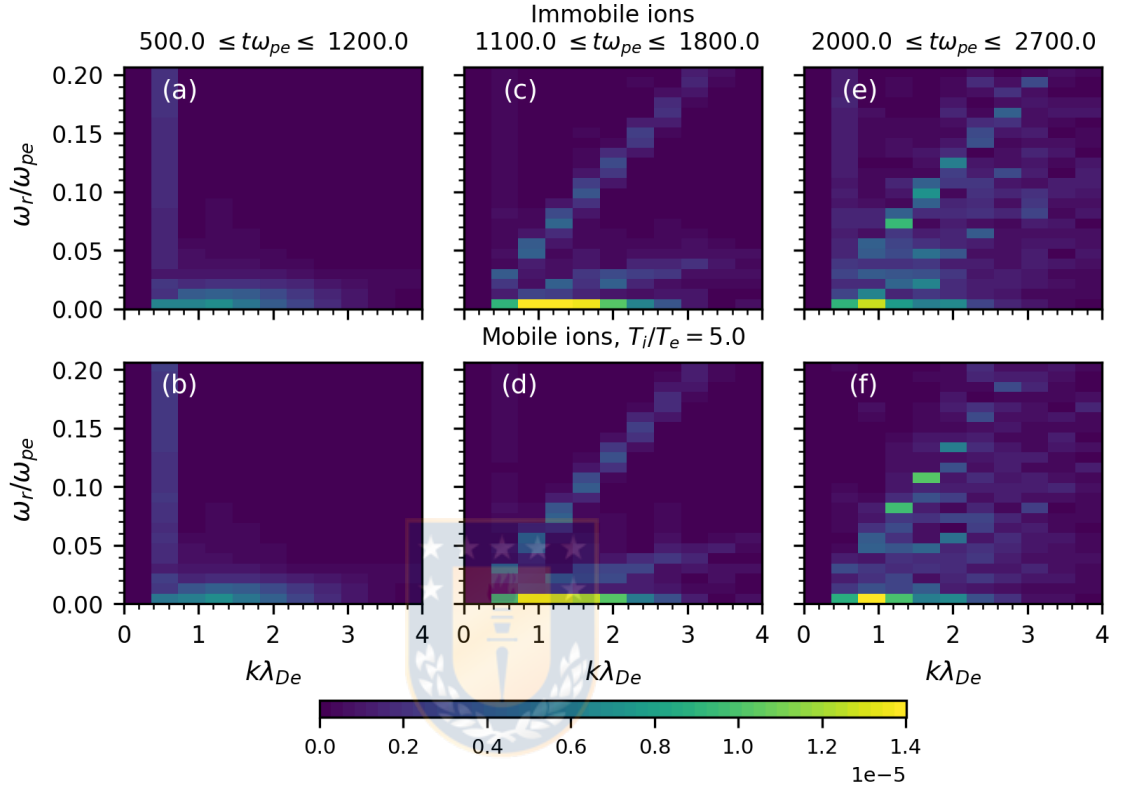


Figure 6.3: Comparison of the electric field spectra, $|\bar{E}_{k,\omega}|$, between the case of immobile ions [(a), (c) and (e)] and the case of mobile ions with initial temperature ratio $\bar{T}_i = 5.0$ [(b), (d) and (f)]. Perturbative amplitude $\varepsilon_e = 4.0 \times 10^{-2}$.

$\bar{T}_i = 5.0$ the most excited waves lie on its corresponding IA branch. However, at longer times the excited waves reach the least damped linear higher order mode for $\bar{T}_i = 1.8$ [Fig.6.2(f)]. This is not the case of $\bar{T}_i = 5.0$, in which the most excited waves remain on the region of the linear IA branch at longer times [Fig.6.4(b), (d) and (f)].

A remarkable feature is the difference in the amplitudes in each case, increasing for lower \bar{T}_i , however being larger with $\bar{T}_i = 0.2$ than with $\bar{T}_i = 0.025$. Also, the

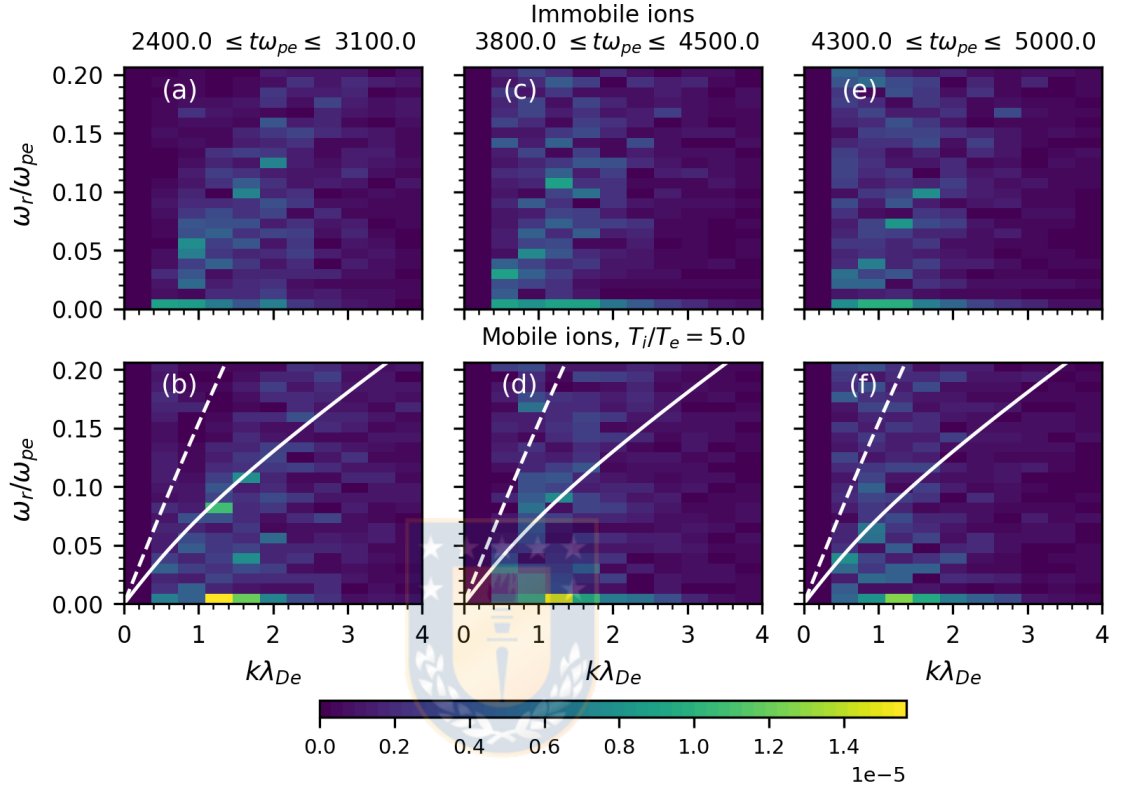


Figure 6.4: Comparison of the electric field spectra, $|\bar{E}_{k,\omega}|$, between the case of immobile ions [(a), (c) and (e)] and the case of mobile ions with initial temperature ratio $\bar{T}_i = 5.0$ [(b), (d) and (f)]. Three long term time intervals are considered. The respective IA mode (solid white line) and the least damped higher order linear mode (dashed white line) from the linear dispersion relation are shown. Perturbative amplitude $\varepsilon_e = 4.0 \times 10^{-2}$.

excited waves involve nearly the same region in $\bar{\omega}_r - \bar{k}$ space. As the linear dispersion relation predicts different modes in that region, from IA mode with $\bar{T}_i = 5.0$ to a series of higher order modes with $\bar{T}_i = 0.025$, it is suggested that the excited waves cannot be associated to any branch of the linear dispersion relation.

6.2 Nonlinear structures propagating in position space

The frequency filtered electrostatic potential $\bar{\Phi}_{\text{fil}}$ and variations in the electrons density $\delta\bar{n}_{e,\text{fil}}$, and the variations in the ions density $\delta\bar{n}_i$ are followed for all the tested temperature ratios in order to describe how the nonlinear structures found in the isothermal case are modified.

6.2.1 Frequency filtered electrostatic potential

The evolution of the frequency filtered electrostatic potential is shown in Figs.6.5 for $\bar{T}_i \leq 1.0$ and in Fig.6.6 for $\bar{T}_i \geq 1.0$. The frequency filter applied to the electrostatic potential is given by eq.(5.1.2).

It is noted that in both temperature ranges the structure of the waves found in the electric field spectra is related to the propagation of electrostatic solitary structures. The structures differ in the following aspects: **(i)** Although the amplitudes and size in position space of the solitary potential are similar in cases $\bar{T}_i = 0.2$ and $\bar{T}_i = 0.025$, these features are smaller for larger \bar{T}_i [Fig.6.6(a), for $\bar{T}_i = 5.0$]. Therefore, the solitary potential is more intense and large with $\bar{T}_i = 0.2$ and $\bar{T}_i = 0.025$ [Figs.6.5(a) and (b)] than with the isothermal case. **(ii)** The instant at which the solitary potential is generated is earlier with lower \bar{T}_i . This fact might be related to the level of the potential in each case. **(iii)** The speed of propagation of the structures is slower with lower \bar{T}_i , being in the range $4.833 \times 10^{-2} \leq \bar{v}_\Phi \leq 5.236 \times 10^{-2}$ for $\bar{T}_i = 0.025$ and increasing to $5.818 \times 10^{-2} \leq \bar{v}_\Phi \leq 6.981 \times 10^{-2}$ for the isothermal case, and then to $6.981 \times 10^{-2} \leq \bar{v}_\Phi \leq 7.854 \times 10^{-2}$ for $\bar{T}_i = 1.8$. In the case of $\bar{T}_i = 5.0$, however, the speed is slower, ranging in $6.283 \times 10^{-2} \leq \bar{v}_\Phi \leq 6.684 \times 10^{-2}$.

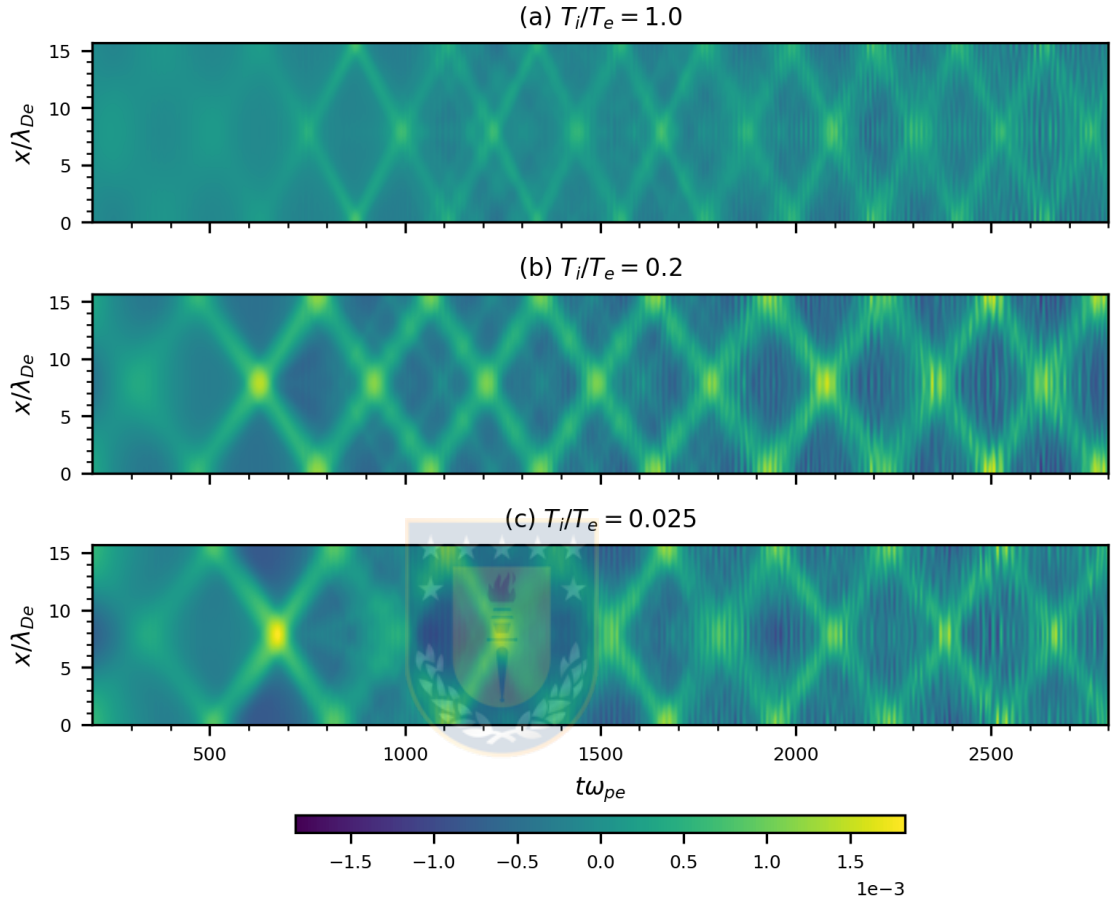


Figure 6.5: Evolution of the frequency filtered electrostatic potential, $\bar{\Phi}_{\text{fil}}$, for temperature ratios (a) $\bar{T}_i = 1.0$, (b) 0.2 and (c) 0.025 . Perturbative amplitude $\varepsilon_e = 4.0 \times 10^{-2}$.

6.2.2 Particle densities

The evolution of the ions density, $\delta\bar{n}_i$ (shown in Figs.6.7 and 6.11 for $\bar{T}_i \leq 1.0$, and in Figs.6.8 and 6.13 for $\bar{T}_i \geq 1.0$), and the frequency filtered electrons density, $\delta\bar{n}_{e,\text{fil}}$ (in Figs.6.12 and 6.9 for $\bar{T}_i \leq 1.0$, and Figs.6.14 and 6.10 for $\bar{T}_i \geq 1.0$) are followed.

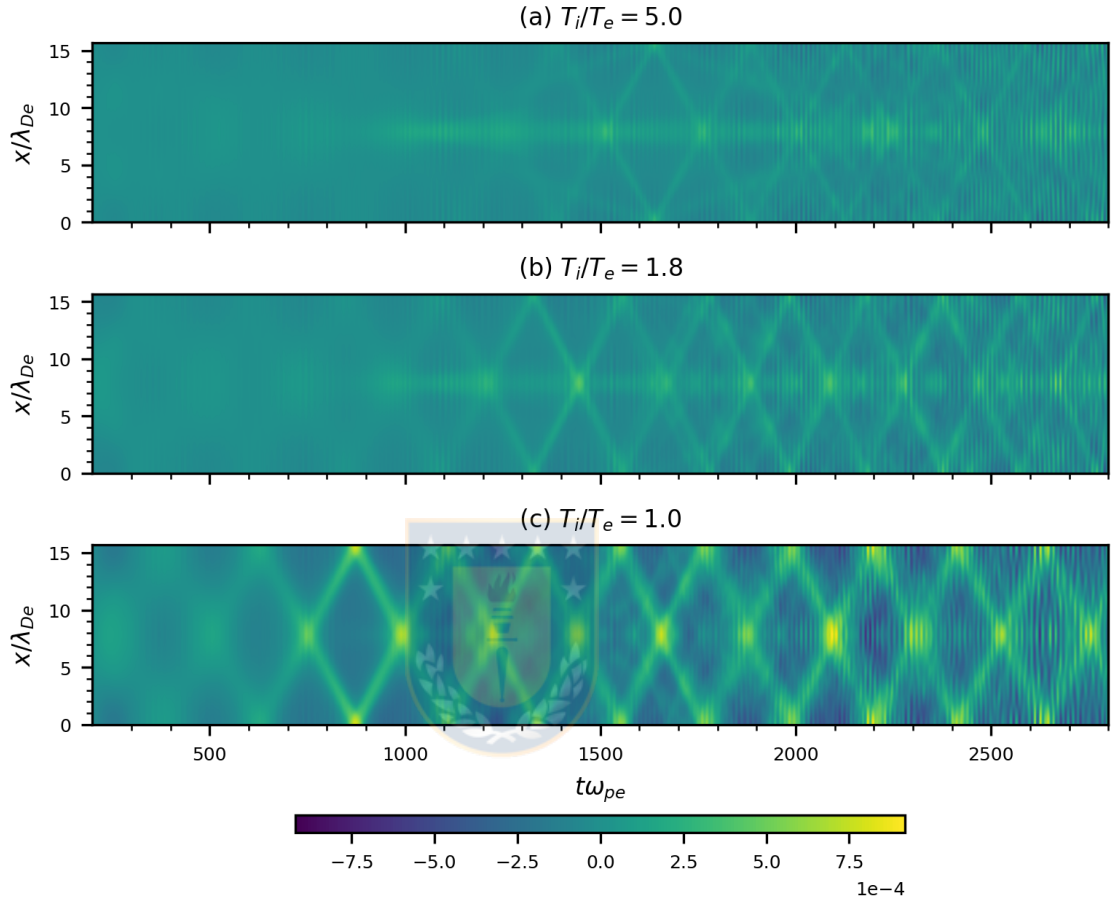


Figure 6.6: Evolution of the frequency filtered electrostatic potential, $\bar{\Phi}_{\text{fil}}$, for temperature ratios (a) $\bar{T}_i = 5.0$, (b) 1.8 and (c) 1.0. Perturbative amplitude $\varepsilon_e = 4.0 \times 10^{-2}$.

For the cases $0.1 \leq \bar{T}_i \leq 1.8$, the structures found in both species correspond to the same structures found in the isothermal case, namely, counter-propagating compressive pulses in $\delta\bar{n}_i$ and density cavities in $\delta\bar{n}_{e,\text{fil}}$. These structures coincide in position space at all times and propagate with the same velocity as the solitary structures in $\bar{\Phi}_{\text{fil}}$ do. Both the deficit of electrons and the accumulation of positive ions account for the low frequency electrostatic potential in Figs.6.5 and (6.6).

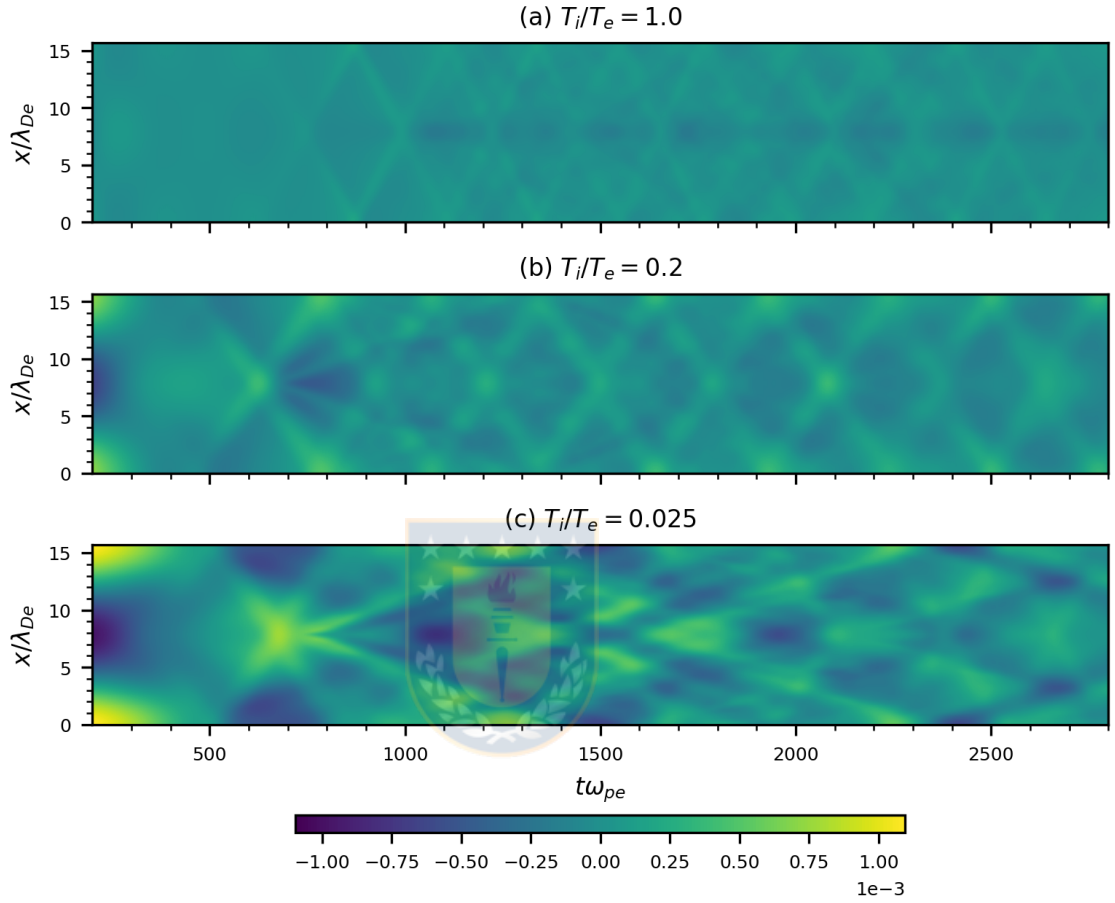


Figure 6.7: Evolution of variations of the ions density, $\delta\bar{n}_i$, for temperature ratios (a) $\bar{T}_i = 1.0$, (b) 0.1 and (c) 0.025. Perturbative amplitude $\varepsilon_e = 4.0 \times 10^{-2}$.

The structures of both species mainly differ in the following aspects: **(i)** Their width in position space is larger for lower \bar{T}_i , in accordance to the same tendency of $\bar{\Phi}_{\text{fil}}$. Additionally, the amplitudes of the compressive pulses in $\delta\bar{n}_i$ are larger at lower temperature ratios. The depth of the electrons cavities is not greatly affected. **(ii)** The instant at which the structures are formed is earlier for lower \bar{T}_i , varying from

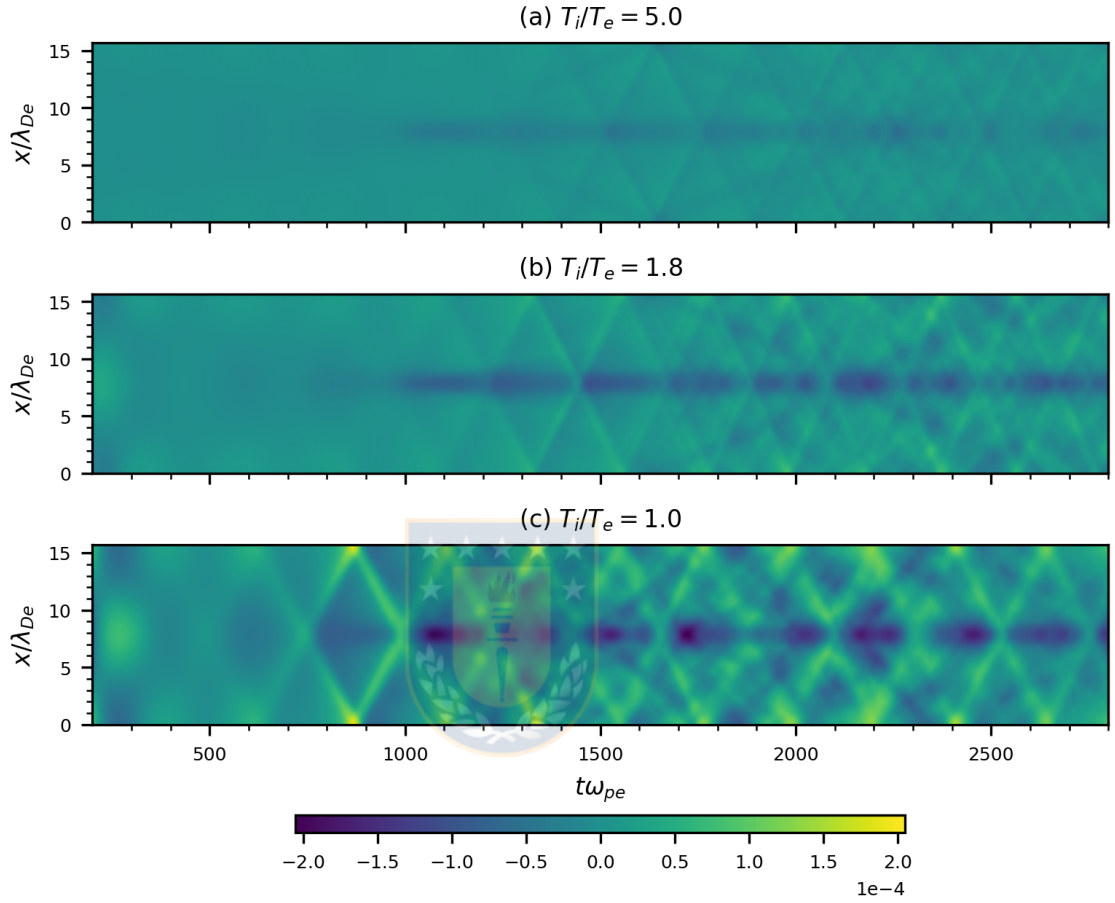


Figure 6.8: Evolution of variations of the ions density, $\delta\bar{n}_i$, for temperature ratios (a) $\bar{T}_i = 5.0$, (b) 1.8 and (c) 1.0. Perturbative amplitude $\varepsilon_e = 4.0 \times 10^{-2}$.

$t\omega_{pe} \simeq 1000$ with $\bar{T}_i = 1.8$ [Figs.6.8 and 6.10, both in frame (b)], to $t\omega_{pe} \simeq 500$ with $\bar{T}_i = 0.2$ [Figs.6.7 and 6.9, both in frame (b)]. **(iii)** The structures propagate with slower velocity for lower \bar{T}_i , in the same way as $\bar{\Phi}_{\text{fil}}$.

In case of the lowest temperature ratio ($\bar{T}_i = 0.025$), a different structure is found from $t\omega_{pe} = 500$, which leads to an intense compressive pulse at the center of the

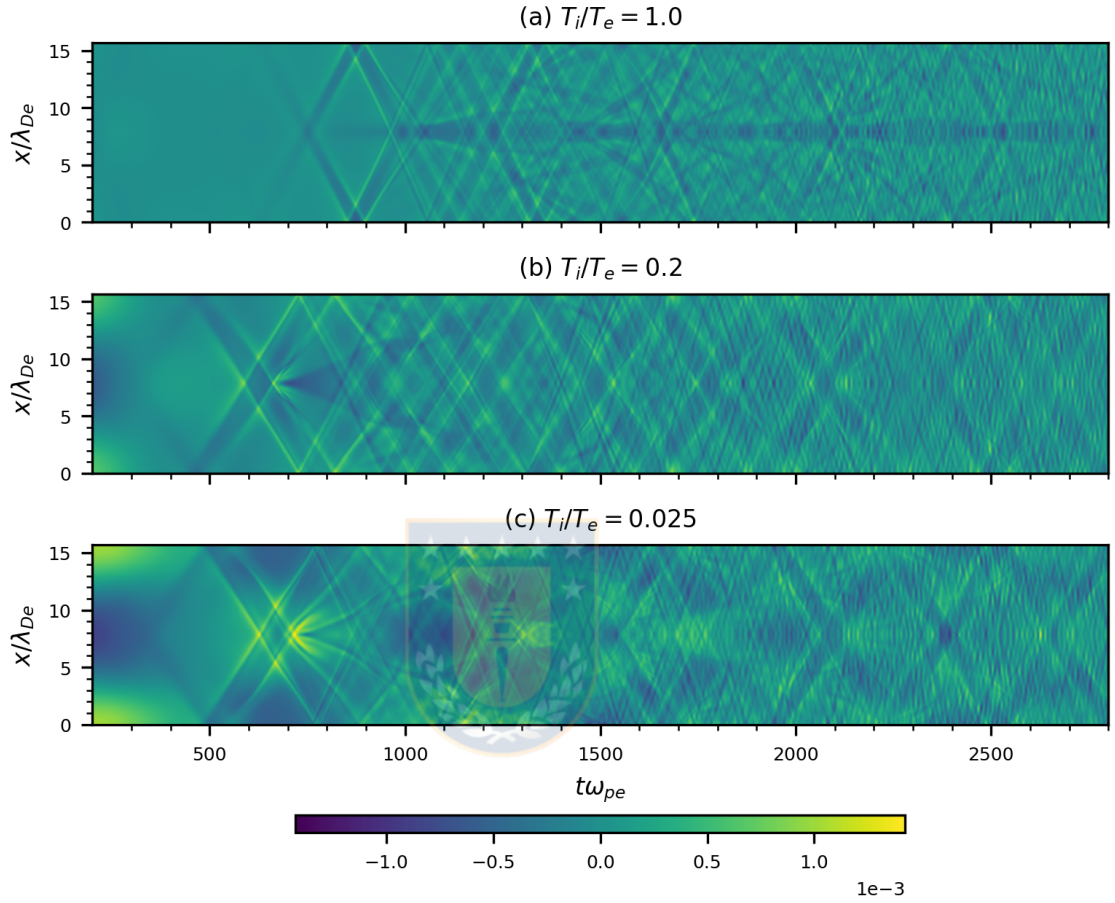


Figure 6.9: Evolution of variations of the electrons density filtered in frequency, $\delta\bar{n}_{e,fl}$, for temperature ratios (a) $\bar{T}_i = 1.0$, (b) 0.1 and (c) 0.025. Perturbative amplitude $\varepsilon_e = 4.0 \times 10^{-2}$.

position domain at $t\omega_{pe} \simeq 670$ [Fig.6.9(c)]. This pulse bifurcates and generates a structure propagating with velocities $3.415 \times 10^{-2} \leq \bar{v} \leq 5.236 \times 10^{-2}$, generating afterwards counter-propagating structures with velocities $\bar{v} = 1.707 \times 10^{-2}$ in accordance with the low frequency structures in the electric field spectra [Figs.6.1 (g) through (i)]. This structure is also formed with $\bar{T}_i = 0.2$ at $t\omega_{pe} = 500$, but is rapidly surpassed by the compressive ion pulses at $t\omega_{pe} = 800$. In the electrons density, this is

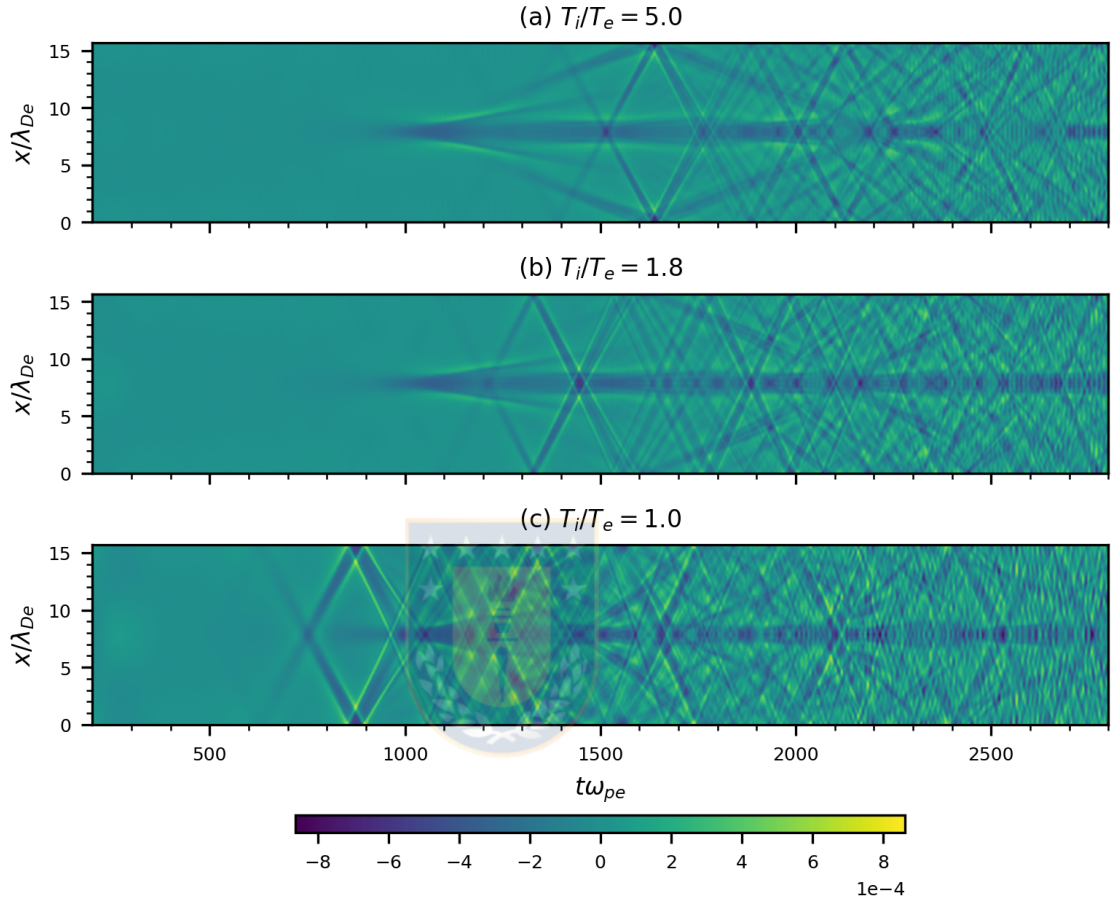


Figure 6.10: Evolution of variations of the electrons density filtered in frequency, $\delta\bar{n}_{e,\text{fil}}$, for temperature ratios (a) $\bar{T}_i = 5.0$, (b) 1.8 and (c) 1.0. Perturbative amplitude $\varepsilon_e = 4.0 \times 10^{-2}$.

observed as a low coherence structure formed during $700 \leq t\omega_{pe} \leq 1500$. In the long term, the structures are the same as those found in the previous cases: in $\delta\bar{n}_i$ correspond to low coherence compressive ion pulses (Fig.6.11). In the electrons density, low frequency cavities continue to propagate (Fig.6.12).

With the highest temperature ratio ($\bar{T}_i = 5.0$), the ions density develops cavi-

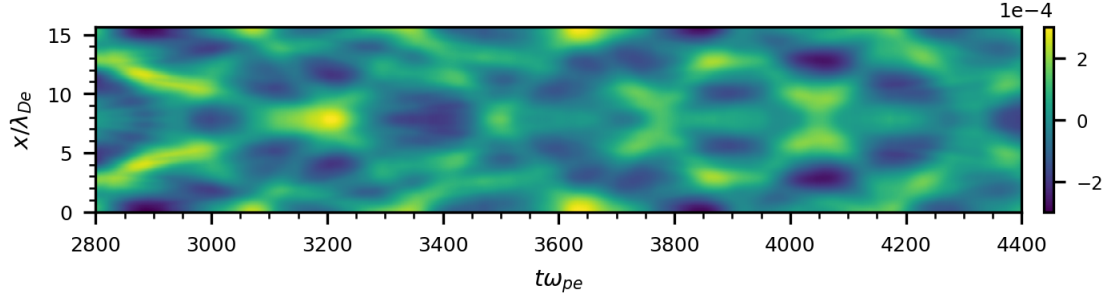


Figure 6.11: Evolution of variations of the ions density, $\delta\bar{n}_i$, for temperature ratio $\bar{T}_i = 0.025$. Perturbative amplitude $\varepsilon_e = 4.0 \times 10^{-2}$. Long term time interval.

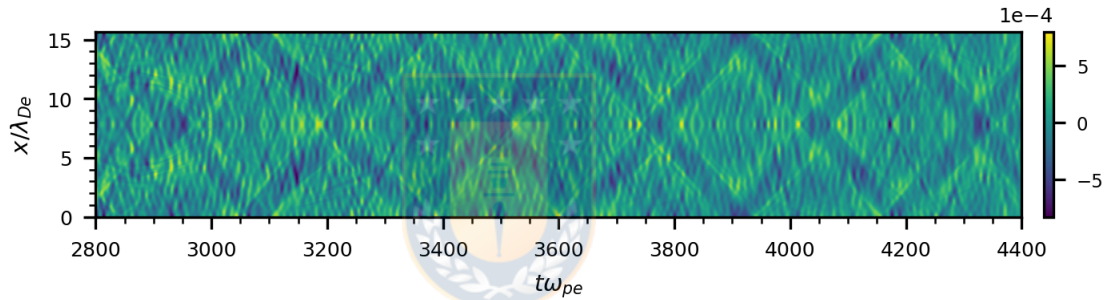


Figure 6.12: Evolution of variations of the electrons density filtered in frequency, $\delta\bar{n}_{e,fl}$, for temperature ratio $\bar{T}_i = 0.025$. Perturbative amplitude $\varepsilon_e = 4.0 \times 10^{-2}$. Long term time interval.

ties instead of compressive pulses. These structures are formed about $t\omega_{pe} = 1400$ [Figs.6.10 (a)] up to $t\omega_{pe} \simeq 3000$. Afterwards, a low coherence structure is developed (Fig.6.13). In the $\delta\bar{n}_{e,fl}$, the cavity structure resembles the case of immobile ions, in which cavities are formed about the same instant. Accordingly, ions would behave as a mobile neutralizing background, and the formation of cavities in $\delta\bar{n}_i$ would be a response to sustain quasi-neutrality. At longer times (Fig.6.14) $\delta\bar{n}_{e,fl}$ exhibits a low coherence structure, as in $\delta\bar{n}_i$, in which the primary cavities from earlier instants are not traceable.

The cavity structure in $\delta\bar{n}_{e,\text{fil}}$ with $\bar{T}_i = 1.8$ [Fig.6.10(b)] is similar to that in $\bar{T}_i = 5.0$. However, it is formed earlier ($t\omega_{pe} \simeq 1000$) and ion compressive pulses are still formed [Fig.6.8(b)]. Therefore, in the transition from $\bar{T}_i = 1.8$ to 5.0, the presence of mobile ions becomes less relevant in the low frequency dynamics of the plasma.

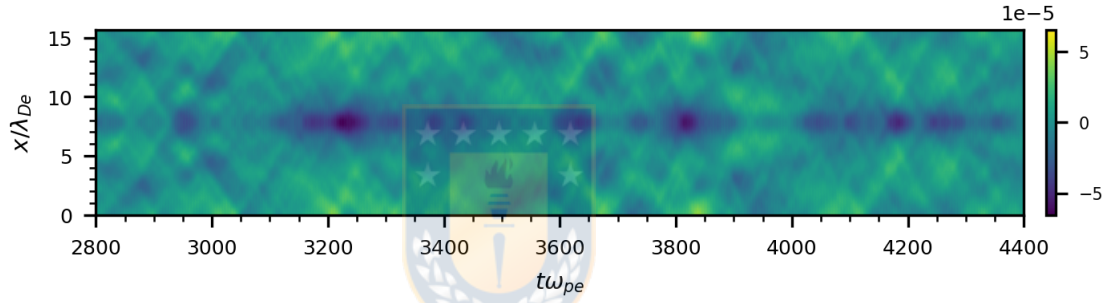


Figure 6.13: Evolution of variations of the ions density, $\delta\bar{n}_i$, for temperature ratio $\bar{T}_i = 5.0$. Perturbative amplitude $\varepsilon_e = 4.0 \times 10^{-2}$. Long term time interval.

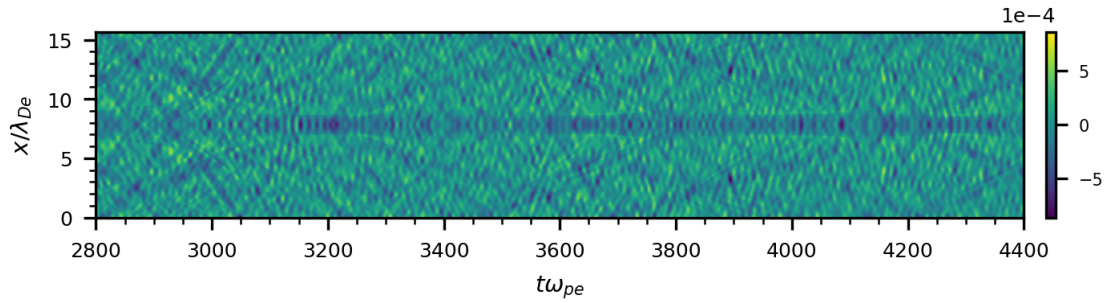


Figure 6.14: Evolution of variations of the electrons density filtered in frequency, $\delta\bar{n}_{e,\text{fil}}$, for temperature ratio $\bar{T}_i = 5.0$. Perturbative amplitude $\varepsilon_e = 4.0 \times 10^{-2}$. Long term time interval.

The position averaged square variations of the ions density, $\langle\delta\bar{n}_i^2\rangle_{\bar{x}}$, estimated

through eq.(4.3.1), is shown in Fig.6.15 for different temperature ratios. This quantity describes the envelope of $\delta\bar{n}_i$. Two important characteristics are noted: **(i)** the first maximum reached by the variations of the ions density, corresponding to an initial accumulation of ions at the boundaries of the position domain (see Fig.6.16), is lower for higher \bar{T}_i , and **(ii)** a damping process that is observed right after the first maximum is reached. The damping in $\langle\delta\bar{n}_i^2\rangle_{\bar{x}}$ is larger for higher \bar{T}_i , reaching lower amplitudes in $\delta\bar{n}_i$. Figure 6.15 suggests that the initial damping sets the level of variations at further instants.

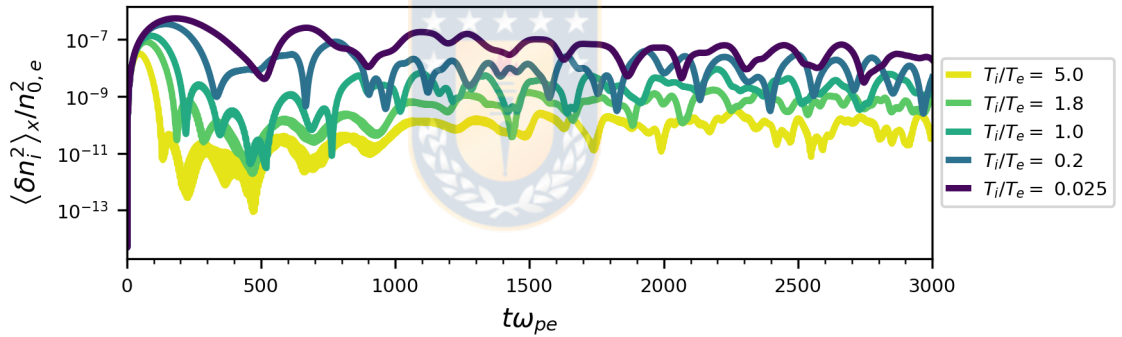


Figure 6.15: Evolution of the amplitude of the position averaged squared variations of the ions density $\langle\delta\bar{n}_i^2\rangle_{\bar{x}}$ for temperature ratios from $\bar{T}_i = 0.025$ to $\bar{T}_i = 5.0$. Perturbative amplitude $\varepsilon_e = 4.0 \times 10^{-2}$.

As the low frequency dynamics in an electron plasma is eased by the presence of heavy ions, features of their distribution, such as \bar{T}_i , have effects on the electrons distribution. This is observed through $\delta\bar{n}_i$ and $\delta\bar{n}_{e,\text{fil}}$, in which the nonlinear structures formed in the low frequency range depends directly on \bar{T}_i . A higher \bar{T}_i would lead electrons to behave as in the case of immobile ions. This could be understood from the damping in the envelope of $\delta\bar{n}_i$. Larger damping would set the level of the variations in lower amplitudes, which in turn would produce a weaker effect on the

electrons distribution. On the opposite case damping is nearly absent, producing large variations $\delta\bar{n}_i$ and a characteristic structure of cavities in $\delta\bar{n}_{e,\text{fil}}$ from earlier instants.

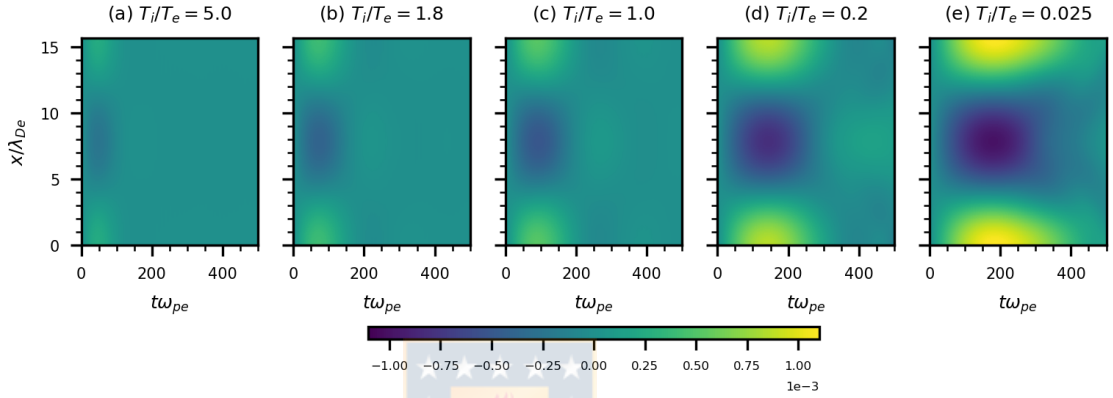


Figure 6.16: Initial evolution of the variations of the ions density $\delta\bar{n}_i$ for all the tested temperature ratios. Perturbative amplitude $\varepsilon_e = 4.0 \times 10^{-2}$.

6.3 Phase space structures

The phase space described by the electrons and ions distributions are followed through the variations of the distribution functions $\delta\bar{f}_j$ for all the tested temperature ratios. The phase speed of the respective IAW for $\bar{k} = 0.4$ is used as a reference.

6.3.1 Electrons distribution

The variations of the electrons distribution function are shown in Figs.6.17 and 6.18 for $\bar{T}_i \leq 1.0$, and in Fig.6.19 for $\bar{T}_i \geq 1.0$.

In all the cases an electron hole, referred to as primary, is formed. In the cases $0.025 \leq \bar{T}_i \leq 1.8$, the primary hole has a lower bound in velocity space close to $\bar{v}_{\phi,IA}$

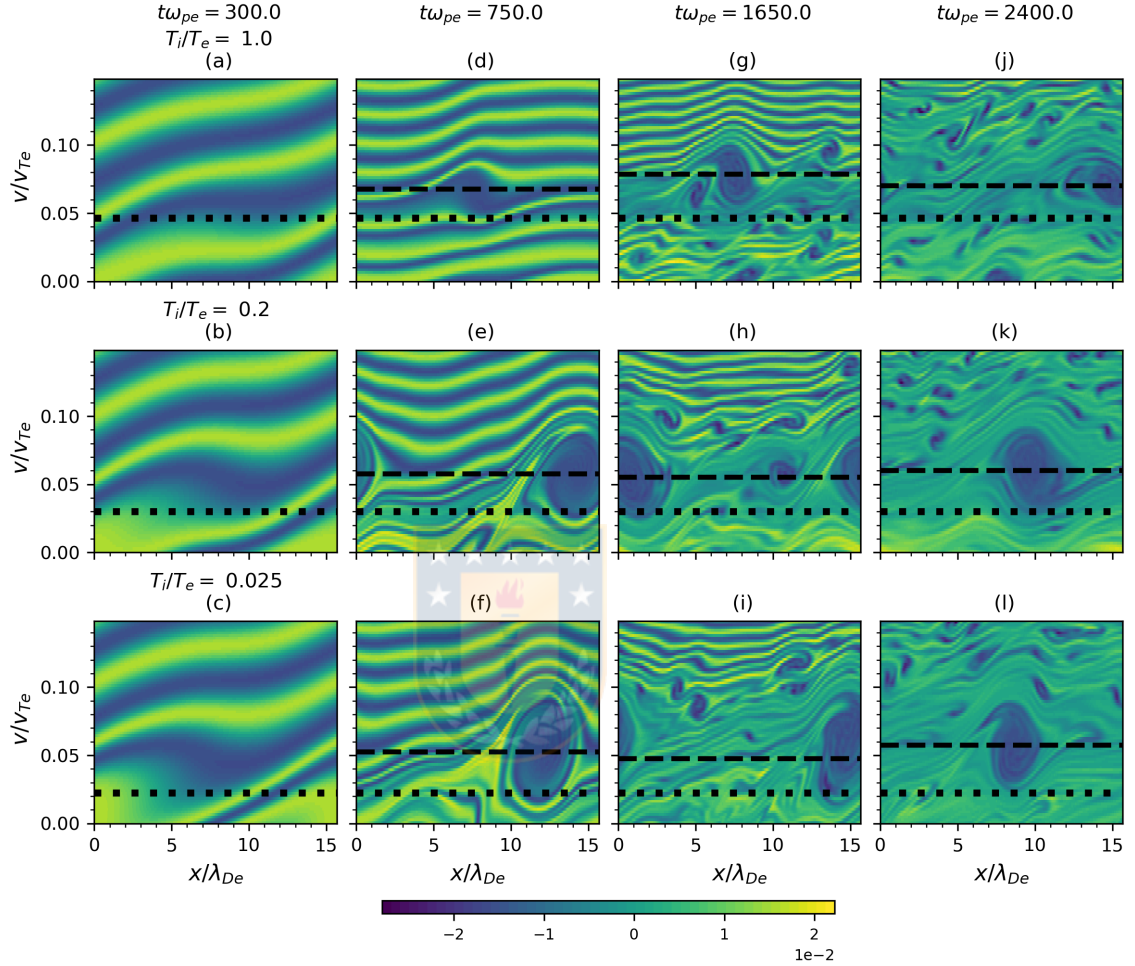


Figure 6.17: Evolution of variations of the electrons distribution function, $\delta \bar{f}_e$, for temperature ratios $\bar{T}_i = 1.0$ [(a), (d), (g) and (j)], $\bar{T}_i = 0.2$ [(b), (e), (h) and (k)] and $\bar{T}_i = 0.025$ [(c), (f), (i) and (l)], at four instants. The respective IA speed (black dotted line) and the speed of the trapping region (black dashed line) are shown. Perturbative amplitude $\varepsilon_e = 4.0 \times 10^{-2}$.

for each \bar{T}_i (shown as a black dotted line). The primary hole has a larger size in position space as well as in velocity space, for lower \bar{T}_i , in accordance with a more intense electrostatic potential $\bar{\Phi}_{\text{fil}}$ and with wider cavities in $\delta \bar{n}_{e,\text{fil}}$. Thus, the for-

mation of nonlinear structures, their size and the intensity of the potential $\bar{\Phi}_{\text{fil}}$ are directly associated to the formation of a trapping zone.

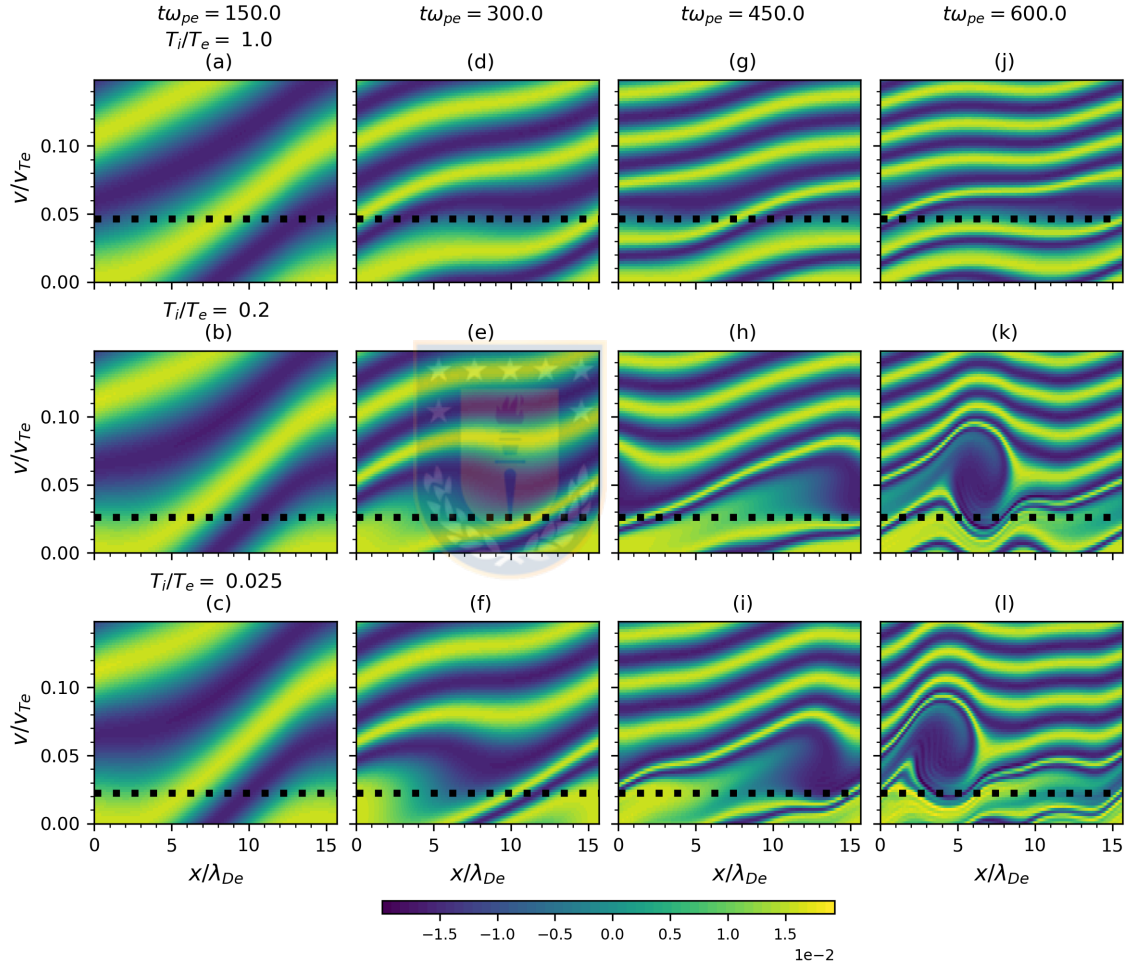


Figure 6.18: Early instants of the evolution of variations of the electrons distribution function, $\delta \bar{f}_e$, for temperature ratios $\bar{T}_i = 1.0$ [(a), (d), (g) and (j)], $\bar{T}_i = 0.2$ [(b), (e), (h) and (k)] and $\bar{T}_i = 0.025$ [(c), (f), (i) and (l)], at four instants. The respective IA speed (black dotted line) is shown. Perturbative amplitude $\varepsilon_e = 4.0 \times 10^{-2}$.

Before the formation of the primary hole, it can be observed that at $t\omega_{pe} = 300$,

the distribution function exhibits a depopulation in a bounded range of velocities right above $\bar{v}_{\phi,IA}$ [Figs.6.17(a) through (c)] for lower \bar{T}_i which evolves into an electron hole [Figs.6.17(d) through (f) and Fig.6.18]. These disturbances take place later for larger \bar{T}_i (Fig.6.19 for $\bar{T}_i \leq 1.8$).

In the extreme case $\bar{T}_i = 5.0$, [Fig.6.19(a), (d), (g) and (j)], signatures of early disturbance are not found, although a primary region of trapping is still formed and followed by smaller electron holes at longer times, accounting for the structure in $\delta\bar{n}_{e,\text{fil}}$. A direct comparison with the case of immobile ions [Figs.6.20(a) through (c)] shows similarities in the distribution function in the low velocity range [Figs.6.20(e) through (g)]. The evolution of the holes differ at further instants, as observed at $t\omega_{pe} = 2550$ [Figs.6.20(d) and (h)], although it still consists of small electron holes within the same range of velocities. In addition to the evolution of $\delta\bar{n}_{e,\text{fil}}$ and $|\bar{E}_{k\omega}|^2$, the phase space portraits indicate a weak effect of mobile ions in the electrons distribution at higher \bar{T}_i , and suggesting that initially the electron holes observed in this range are solely due to the faster electron modes.

The speed $\bar{v}_{\phi,IA}$ seems to play an important role in the evolution of the primary electron hole [Fig.6.18 and Fig.6.17]. It is noted that there is an early depletion of electrons as the filamentation develops [Fig.6.18(a) through (c)] right above $\bar{v}_{\phi,IA}$, allowing for a positive potential that eventually trap electrons. Once these structures are formed, they retain a lower bound at $\bar{v}_{\phi,IA}$ in velocity space. This is also observed at $\bar{T}_i = 1.8$ with a smaller primary hole [Figs.6.19(b), (e), (h) and (k)].

Additionally, the speed of the primary hole is reduced with lower \bar{T}_i . Such fact

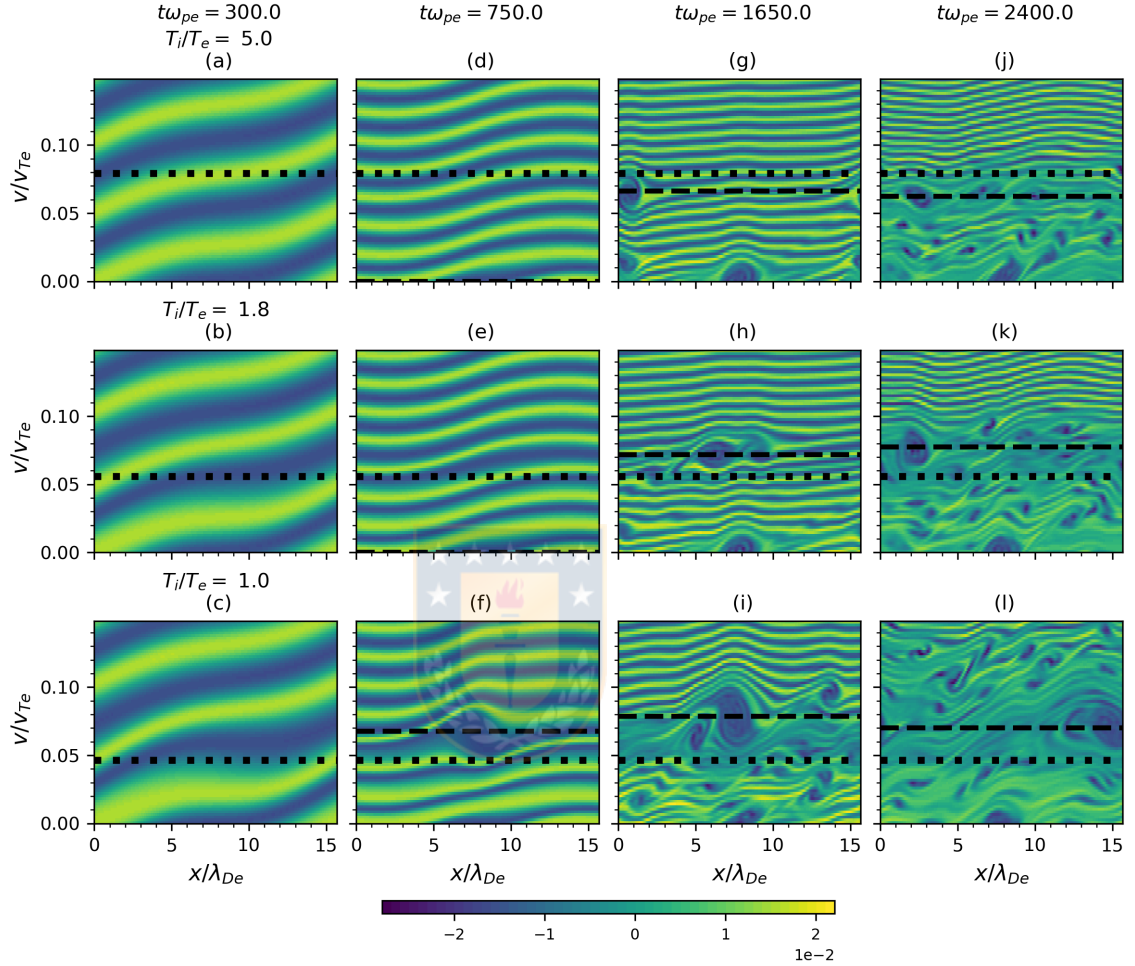


Figure 6.19: Evolution of variations of the electrons distribution function, $\delta \bar{f}_e$, for temperature ratios $\bar{T}_i = 5.0$ [(a), (d), (g) and (j)], $\bar{T}_i = 1.8$ [(b), (e), (h) and (k)] and $\bar{T}_i = 1.0$ [(c), (f), (i) and (l)], at four instants. The respective IA speed (black dotted line) and the speed of the trapping region (black dashed line) are shown. Perturbative amplitude $\varepsilon_e = 4.0 \times 10^{-2}$.

can be understood by considering that the processes that trigger the formation of the hole are related to the speed $\bar{v}_{\phi, IA}$ which also decreases with \bar{T}_i . The upper bound of the hole in velocity space is determined by the intensity of the potential $\bar{\Phi}_{\text{fil}}$: a

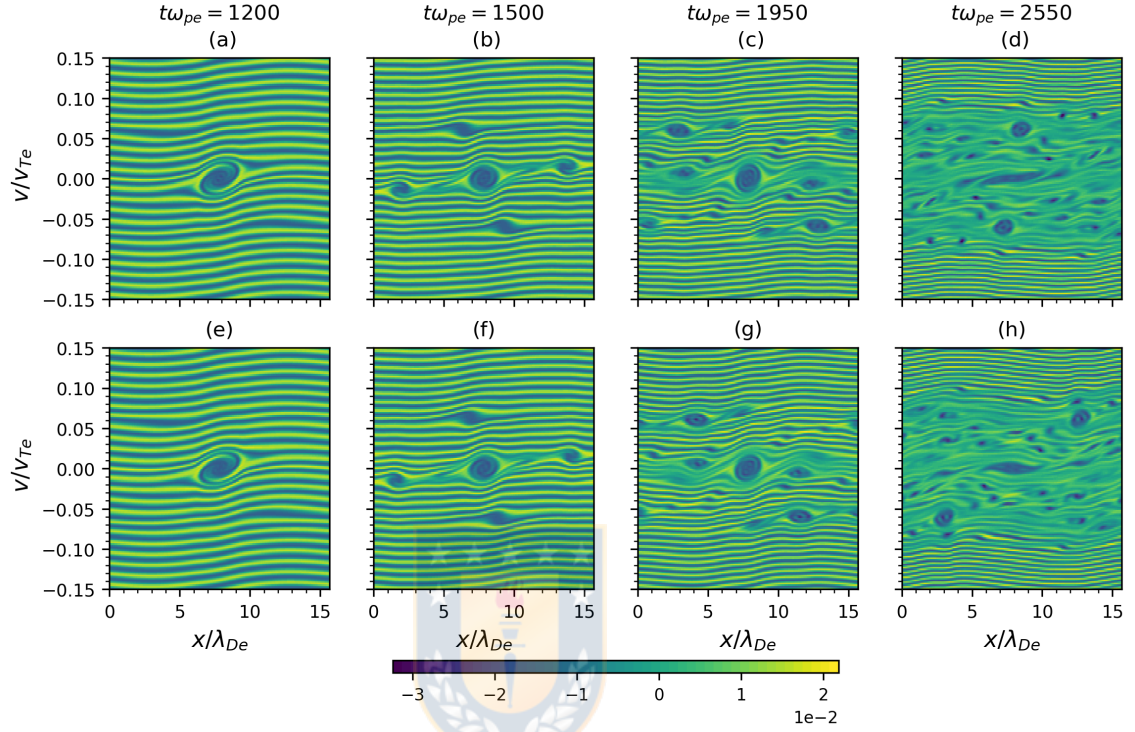


Figure 6.20: Comparison of the variations of the electrons distribution function, $\delta \bar{f}_e$, between the cases of immobile ions [(a) through (d)] and temperature ratio $\bar{T}_i = 5.0$ [(e) through (h)]. Perturbative amplitude $\varepsilon_e = 4.0 \times 10^{-2}$.

stronger potential yields a larger upper boundary and in the cases with $\bar{T}_i < 1.8$ such boundary is in the order of $\bar{v} = 0.1$. Therefore, the net effect is that hole is centered at a lower speed for lower \bar{T}_i .

6.3.2 Ions distribution

The ions distribution function in the equilibrium state, $\bar{f}_{0,i}$ given by a one dimensional Maxwellian distribution,

$$\bar{f}_{0,i} = \frac{\bar{n}_{0,i}}{\sqrt{2\pi} \bar{v}_{T_i}} \exp \left[-\frac{\bar{v}^2}{2\bar{v}_{T_i}^2} \right], \quad (6.3.1)$$

is shown in Fig.6.21 for each tested \bar{T}_i . The variations of the distribution function, $\delta \bar{f}_i$, are shown in Fig.6.27 for $\bar{T}_i \leq 1.0$, and in Fig.6.30 for $\bar{T}_i \geq 1.0$.

The equilibrium distribution function

Figure 6.21 shows that a reduction of the temperature ratio in $\bar{f}_{0,i}$ implies a reduction in the mobility of the heavy ions as a large fraction of them will have velocities closer to the mean velocity of the distribution, restricting the dynamics of the species to narrower ranges of velocity.

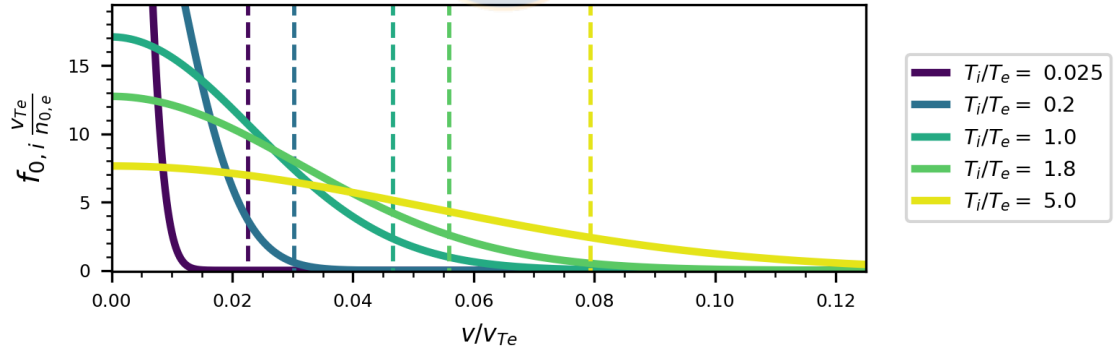


Figure 6.21: Half of the equilibrium distribution function of the ions distribution, $\bar{f}_{0,i}$, for different temperature ratios \bar{T}_i . The respective speed $\bar{v}_{\phi,IA}$ is shown (dashed line of the respective color).

As noted in Chapter 2, the phase speed of the corresponding IAW also decreases with \bar{T}_i for fixed \bar{k} . If the temperature is too low, the speed $\bar{v}_{\phi,IA}$ falls far from the bulk of the distribution (see $\bar{T}_i = 0.025$ in Fig.6.21). In the case $\bar{T}_i = 0.025$, it is

verified that $\bar{v}_{\phi,IA} = 6.139\bar{v}_{Ti}$, and any activity related to this speed is nonresonant with the ions distribution. On the other hand, for high temperatures $\bar{v}_{\phi,IA} = 1.787\bar{v}_{Ti}$ ($\bar{T}_i = 1.8$) and $1.52\bar{v}_{Ti}$ ($\bar{T}_i = 5.0$), meaning that any activity in this range is well into the bulk of the ions distribution and resonant interactions associated to $\bar{v}_{\phi,IA}$ exist.

The resonance zone in the ions distribution

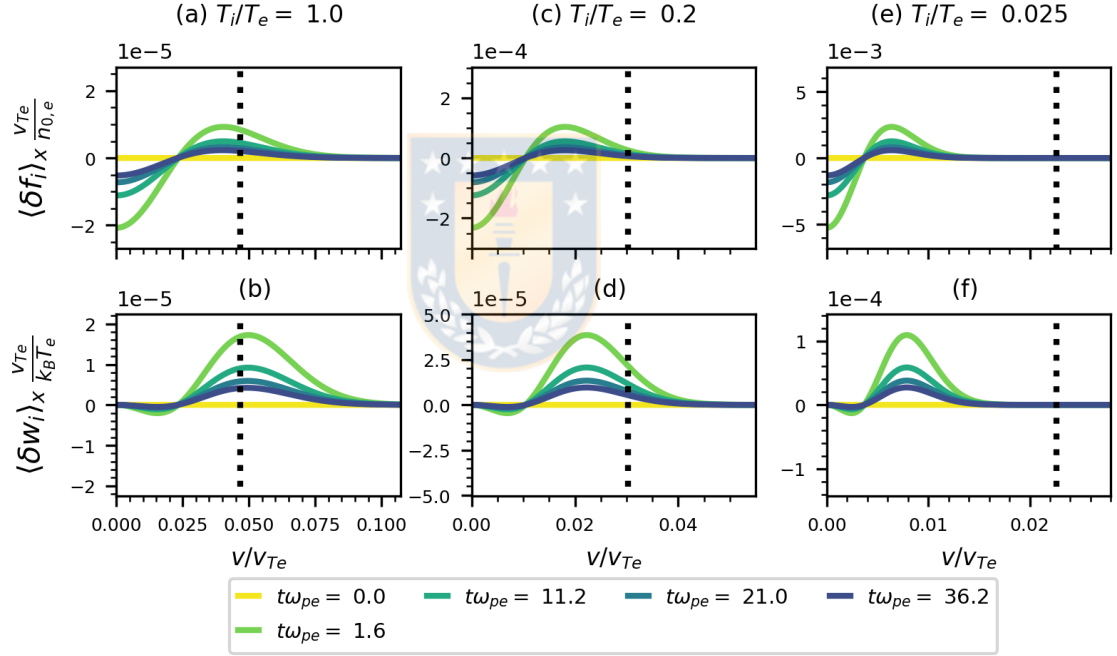


Figure 6.22: Sections of the position averaged variations of the ions distribution function $\langle \delta \bar{f}_i \rangle_{\bar{x}}$ (upper row) and of the ions kinetic energy distribution $\langle \delta \bar{w}_i \rangle_{\bar{x}}$ (lower row) for temperature ratios $\bar{T}_i = 1.0$ [(a) and (b)], 0.2 [(c) and (d)] and 0.025 [(e) and (f)], during the beginning of the simulation. The respective IA speeds are shown. Perturbative amplitude $\varepsilon_e = 4.0 \times 10^{-2}$.

The position averaged variations of the ions distribution function $\langle \delta \bar{f}_i \rangle_{\bar{x}}$ and of the kinetic energy distribution $\langle \delta \bar{w}_i \rangle_{\bar{x}}$, where $\delta \bar{w}_i = \bar{m}_i \bar{v}^2 \delta \bar{f}_i / 2$, are followed to clarify

the behavior of ions around $\bar{v}_{\phi,IA}$. These quantities are shown in Figs.6.22 and 6.24 for $\bar{T}_i \leq 1.0$, and in Figs.6.23 and 6.25 for $\bar{T}_i \geq 1.0$ for the initial and the damping stages found in Fig.6.15. Generally, it is observed that the level of the variations $\langle \delta \bar{f}_i \rangle_{\bar{x}}$ and $\langle \delta \bar{w}_i \rangle_{\bar{x}}$ decrease with larger temperature ratio, as in the previously described quantities in position space.

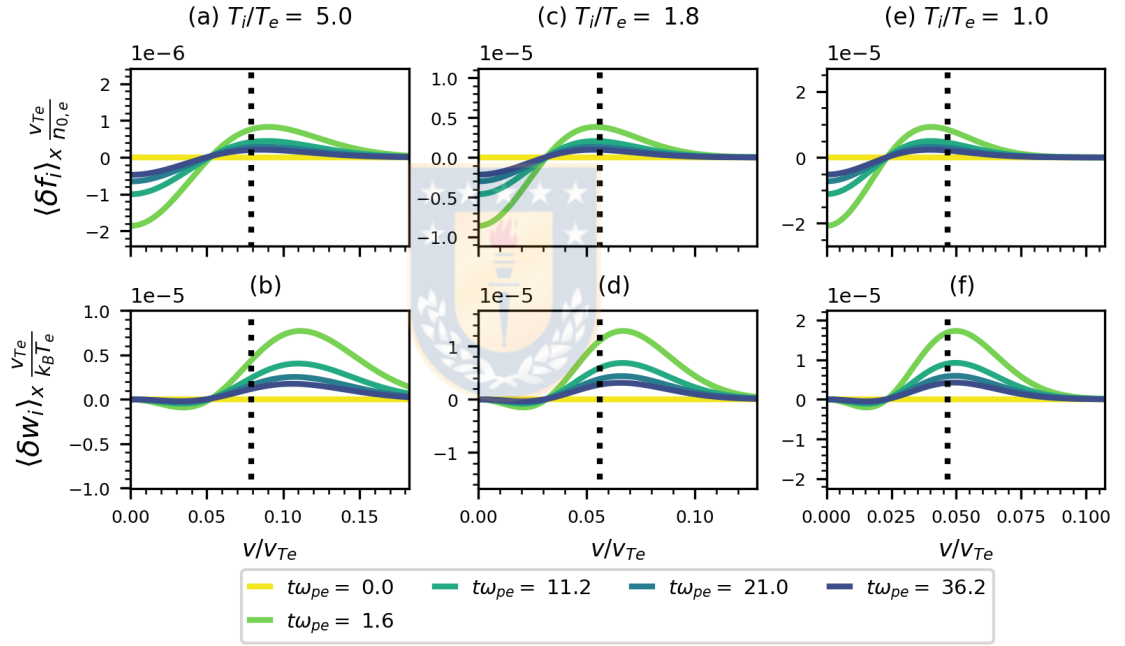
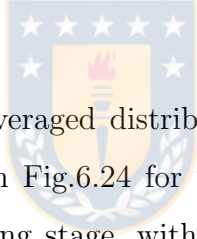


Figure 6.23: Sections of the position averaged variations of the ions distribution function $\langle \delta \bar{f}_i \rangle_{\bar{x}}$ (upper row) and of the ions kinetic energy distribution $\langle \delta \bar{w}_i \rangle_{\bar{x}}$ (lower row) for temperature ratios $\bar{T}_i = 5.0$ [(a) and (b)], 1.8 [(c) and (d)] and 1.0 [(e) and (f)]. The respective IA speeds (black dotted line) are shown. Perturbative amplitude $\varepsilon_e = 4.0 \times 10^{-2}$.

In all cases with $1.0 \leq \bar{T}_i \leq 5.0$ (Fig.6.23) it is observed that there is an initial accumulation of ions in a velocity range around the velocity $\bar{v}_{\phi,IA}$ whose extension is larger for higher \bar{T}_i , that is rapidly formed after the plasma is perturbed, along with

an increase in the kinetic energy ($t\omega_{pe} = 1.6$). Due to the decrease in the population of slower ions and the increment in $\langle\delta\bar{w}_i\rangle_{\bar{x}}$ over the observed velocity ranges, the net effect is an acceleration towards faster velocities. Afterwards, the acceleration is rapidly reversed, reducing the level of the variations $\langle\delta\bar{f}_i\rangle_{\bar{x}}$ and $\langle\delta\bar{w}_i\rangle_{\bar{x}}$ in all the observed cases. In the nonresonant cases $\bar{T}_i \leq 0.1$ [Figs.6.22(c) through (f)] the same accumulation is observed at velocities slower than $\bar{v}_{\phi,IA}$, without variations about $\bar{v}_{\phi,IA}$. In all the studied cases of \bar{T}_i the reversion occurs as the envelope of $\delta\bar{n}_i$ approaches to the first maximum (Fig.6.15). As the ions accumulate at certain regions in position space, the self-consistent potential locally increases and slows down a fraction of the ions.



Sections of the position averaged distribution function and kinetic energy distribution of ions are shown in Fig.6.24 for $\bar{T}_i \leq 1.0$ and in Fig.6.25 for $\bar{T}_i \geq 1.0$ during their respective damping stage, with the first instant corresponding to the first maximum in the envelope of $\delta\bar{n}_i$.

In the cases $\bar{T}_i \geq 1.0$, from the first to the second instant the variations in $\langle\delta\bar{f}_i\rangle_{\bar{x}}$ occur into two adjacent velocity intervals corresponding to an increase in the faster range and a decrease in the slower range, indicating a resonant interaction. The net effect is a large increase in kinetic energy $\langle\delta\bar{w}_i\rangle_{\bar{x}}$ in the faster range and a slight decrease in the slower range. The extension of these ranges is shorter and the location of the velocity $\bar{v}_{\phi,IA}$ is more weighted to the faster range, both for lower \bar{T}_i . Such variations are produced by the self-consistent potential $\bar{\Phi}_{fl}$ created by the local accumulation of ions in position space in the first instant. The associated electric field is strong enough to expel ions from those zones, redistributing them, and damping

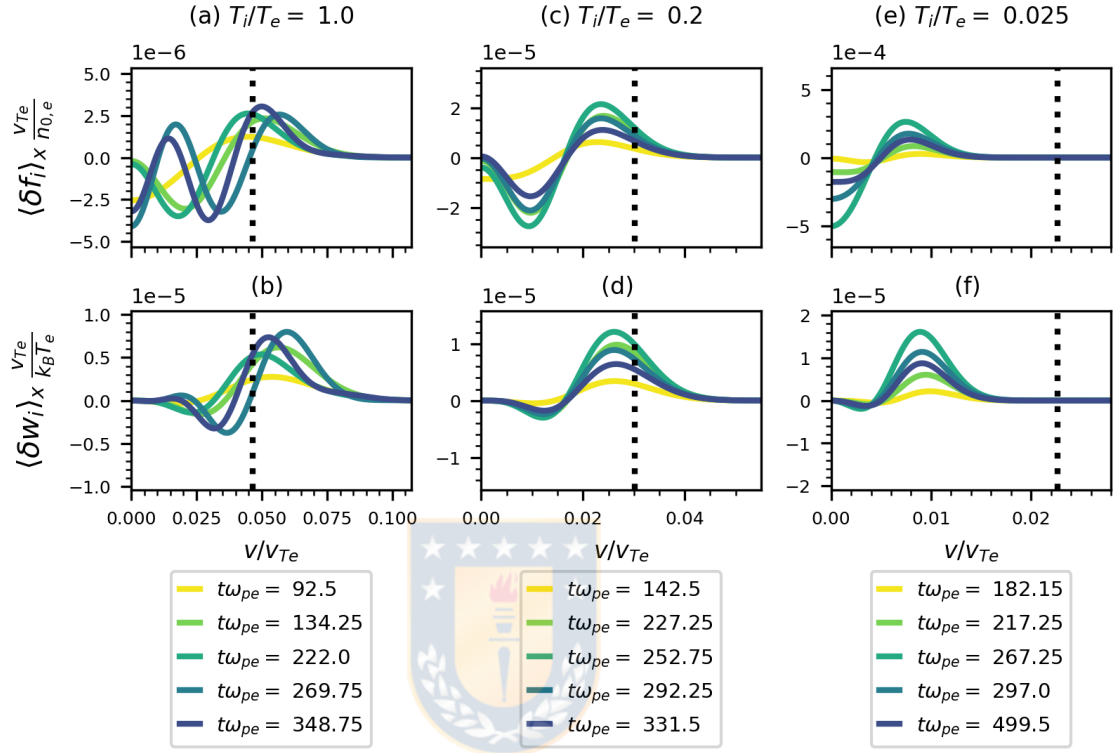


Figure 6.24: Sections of the position averaged variations of the ions distribution function $\langle \delta \bar{f}_i \rangle_{\bar{x}}$ (upper row) and of the ions kinetic energy distribution $\langle \delta \bar{w}_i \rangle_{\bar{x}}$ (lower row) for temperature ratios $\bar{T}_i = 1.0$ [(a) and (b)], 0.2 [(c) and (d)] and 0.025 [(e) and (f)]. The respective IA speeds are shown. Perturbative amplitude $\varepsilon_e = 4.0 \times 10^{-2}$.

the variations $\delta \bar{n}_i$. At the following instants, both quantities exhibit oscillations in the velocity dependency, maintaining most of the variations close to $\bar{v}_{\phi, IA}$.

In the nearly undamped cases $\bar{T}_i < 1.0$ [Figs.6.24(c) through (f)], a similar behavior is observed between the first and second instants in both quantities but at velocities slower than $\bar{v}_{\phi, IA}$. In the next instants the acceleration to faster velocities is reversed as ions are slowly redistributed in position space [Figs.6.7(b) and (c)].

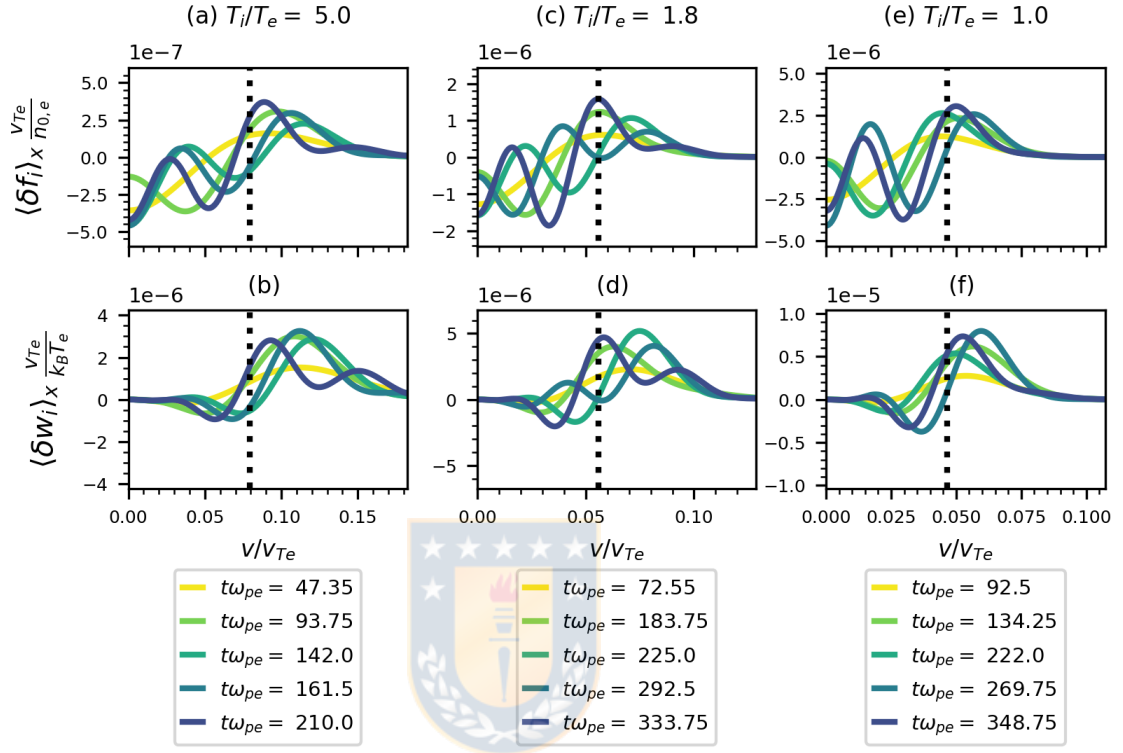


Figure 6.25: Sections of the position averaged variations of the ions distribution function $\langle \delta \bar{f}_i \rangle_{\bar{x}}$ (upper row) and of the ions kinetic energy distribution $\langle \delta \bar{w}_i \rangle_{\bar{x}}$ (lower row) for temperature ratios $\bar{T}_i = 1.0$ [(a) and (b)], 0.2 [(c) and (d)] and 0.025 [(e) and (f)]. The respective IA speeds are shown. Perturbative amplitude $\varepsilon_e = 4.0 \times 10^{-2}$.

These results indicate that during the initial damping of $\delta \bar{n}_i$ there is activity around $\bar{v}_{\phi, IA}$ of resonant nature in the ions distribution for $\bar{T}_i \geq 1.0$. If there are nearly zero ions at that velocity, as in colder distributions, the damping is nearly absent. For cases $\bar{T}_i \geq 1.0$, there is an increase in both the number of ions and the ion kinetic energy at velocities in the order of or larger than $\bar{v}_{\phi, IA}$. As the electric field driving this dynamics has the opposite effect on the electrons distribution, that is, depopulating this region, it is suggested that this process generates the initial depopulation that evolves into the primary trapping region for $1.0 \leq \bar{T}_i \leq 1.8$

[Fig.6.19 for $\bar{T}_i = 1.0$ and 1.8].

Variations of the distribution function

The variations of the ions distribution function, $\delta\bar{f}_i$, are presented in Figs.6.27 and 6.28 for $\bar{T}_i \leq 1.0$, and in Fig.6.30 for $\bar{T}_i \geq 1.0$.

In the temperature ratio range $\bar{T}_i \geq 0.2$ [Figs.6.27(b), (e), (h) and (k) for $\bar{T}_i = 0.2$, and Fig.6.30 for $\bar{T}_i \geq 1.0$] the evolution of $\delta\bar{f}_i$ mainly exhibits filamentation. The speed at which the filamentation progresses differs with \bar{T}_i , being faster in distributions with higher temperature ratios, as there is a large amount of faster ions available to transport perturbations in phase space. The dominance of this process also depends on \bar{T}_i , being dominant in $\bar{T}_i = 5.0$ and is greatly reduced towards $\bar{T}_i = 0.2$. The extreme case $\bar{T}_i = 0.025$ does not exhibit filamentation at all.

As in all the previously discussed quantities, the level of the variations $\delta\bar{f}_i$ increase for lower \bar{T}_i . In comparison with $\delta\bar{f}_e$, in the isothermal case variations in the ions distribution are of the same order of magnitude, whereas in $\bar{T}_i = 0.025$ the levels exceeds those of electrons distribution by one order of magnitude, at least.

The difference of such variations could be due to the initial development of filamentation, the presence of faster ions and a larger extension in velocity range of ions that are affected by the perturbations depending on \bar{T}_i . In their motion, fast ions can rapidly compensate density variations generated by slower ions. As a consequence, the resulting potential will be weaker with higher \bar{T}_i , generating self-consistent variations of smaller amplitude at further times. This is observed in Fig.6.26, which

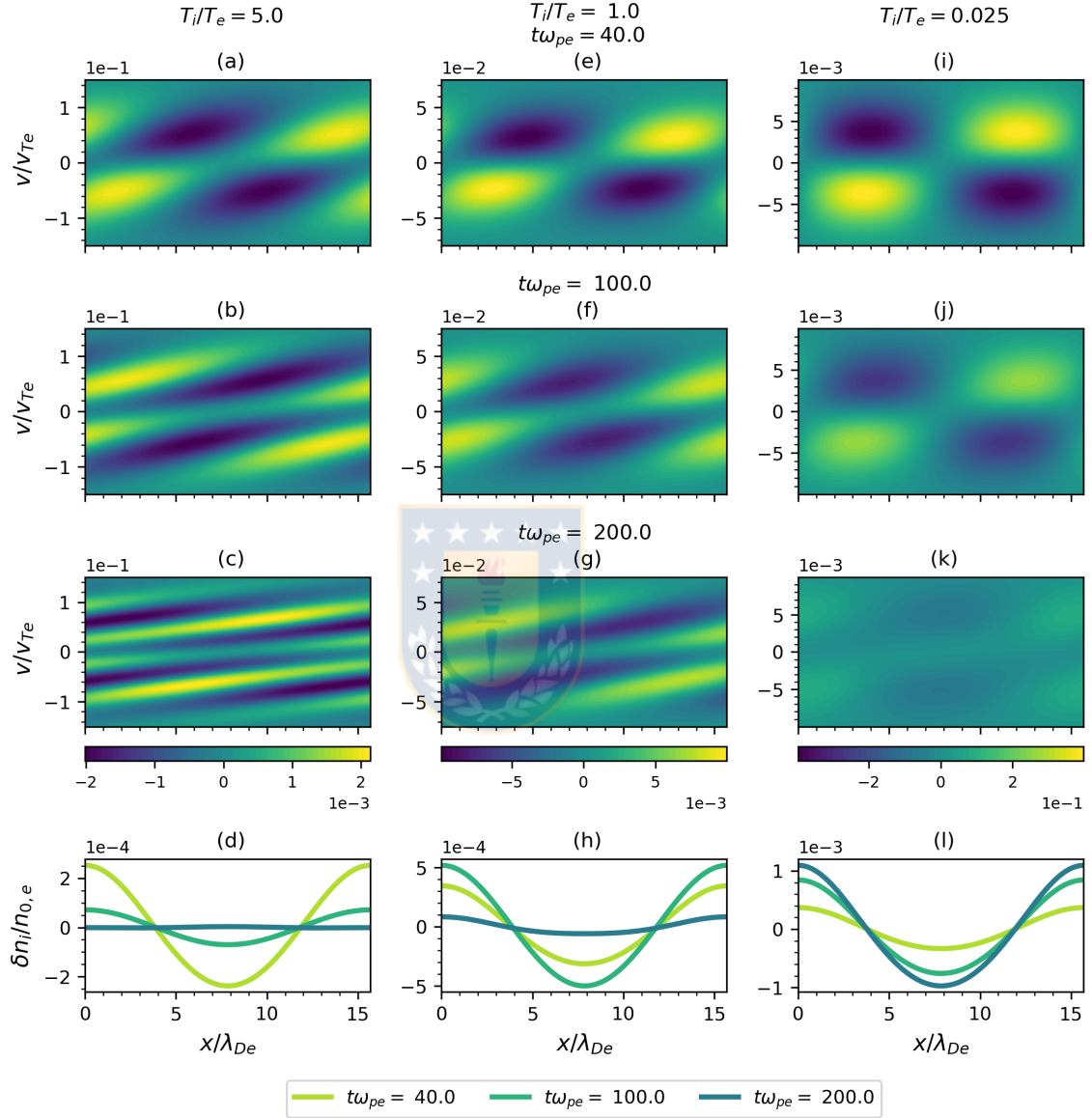


Figure 6.26: Phase space plots of the variations of the ions distribution, $\delta \bar{f}_i$ and their corresponding variations in particle density, $\delta \bar{n}_i$, for $\bar{T}_i = 5.0$ [(a) through (d)], 1.0 [(e) through (h)] and 0.025 [(i) through (l)], for three instants during the damping of $\delta \bar{n}_i$ with $\bar{T}_i = 5.0$. Perturbative amplitude $\varepsilon_e = 4.0 \times 10^{-2}$. Mass ratio is $\bar{m}_i = 1836.153$.

shows the phase space plots for three instants during the damping of $\delta\bar{n}_i$ for $\bar{T}_i = 5.0$ and their respective particle density, for temperature ratios $\bar{T}_i = 5.0$ [Figs.6.26(a) through (d)], 1.0 [Figs.6.26(e) through (h)] and 0.025 [Figs.6.26(i) through (l)].

To estimate the variations $\delta\bar{n}_i$ both sides of the distribution in velocity space are considered. The width in velocity space in which ions are affected is relevant in the following way: as the plasma evolves, ions transport the initial perturbation in phase space. If the range of velocities is too short, as in $\bar{T}_i = 0.025$, it will be transported nearly unaltered [Figs.6.26(i) through (k)] remaining localized in position space. Structures at both sides of the velocity domain yield large amplitudes in $\delta\bar{n}_i$ when they are in or close to be in phase [Fig.6.26(k)] and low amplitudes when they are in or close to be in anti-phase [for instance, in Fig.6.26(i) and (j)], whose variations contribute to the low frequency potential $\bar{\Phi}_{\text{fl}}$. If the velocity range is wider, as with $\bar{T}_i \geq 1.0$, the structure will be transported at different velocities and will cover a large region in position space [Fig.6.26(c)], compensating density variations due to slower ions. The contribution of the whole velocity domain is therefore more likely to yield a very small contribution in density variations and therefore in $\bar{\Phi}_{\text{fl}}$. This process can be interpreted as a screening due to fast ions. The screening would be faster and more effective if there is a large number of ions with larger velocities.

This process would also account for the damping in the envelope of $\delta\bar{n}_i$. A colder distribution does not exhibit screening and therefore variations will remain nearly undamped, whereas a hotter distribution exhibits a more effective screening and variations will be more rapidly damped. As a consequence, the variations $\delta\bar{f}_i$ and $\delta\bar{n}_i$ remain lower, with a low frequency potential $\bar{\Phi}_{\text{fl}}$ incapable of disturbing the

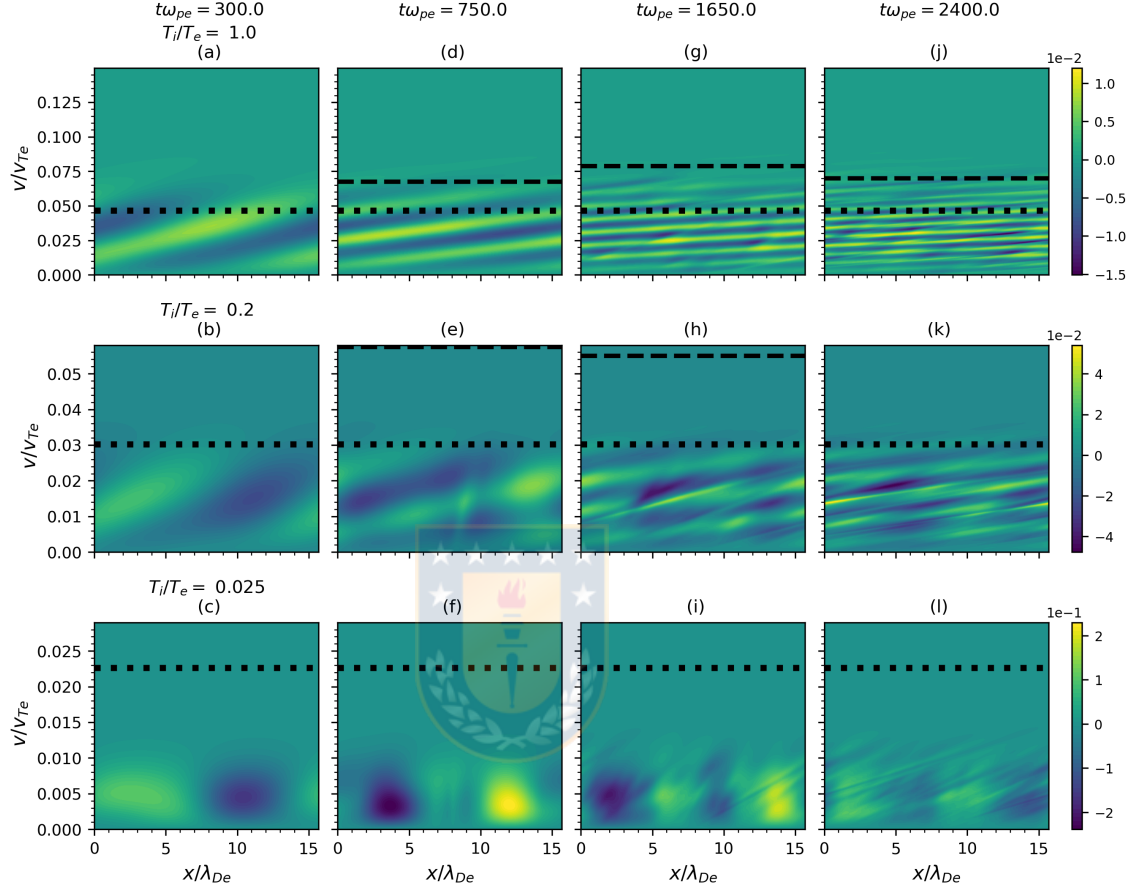


Figure 6.27: Evolution of variations of the ions distribution function, $\delta \bar{f}_i$, for temperature ratios $\bar{T}_i = 1.0$ [(a), (d), (g) and (j)], $\bar{T}_i = 0.2$ [(b), (e), (h) and (k)] and $\bar{T}_i = 0.025$ [(c), (f), (i) and (l)], at four instants. The respective IA speed (black dotted line) and the speed of the trapping region (black dashed line) are shown. Perturbative amplitude $\varepsilon_e = 4.0 \times 10^{-2}$. Mass ratio is $\bar{m}_i = 1836.153$.

electrons distribution at low velocities and the ions distribution itself with higher \bar{T}_i , and the plasma tends to behave as if ions were immobile. On the other hand, with lower \bar{T}_i , ions have a larger initial contribution to $\bar{\Phi}_{fl}$ self-consistently sustaining their dynamics and disturbing the electrons distribution at low velocities, rapidly leading them to trapping.

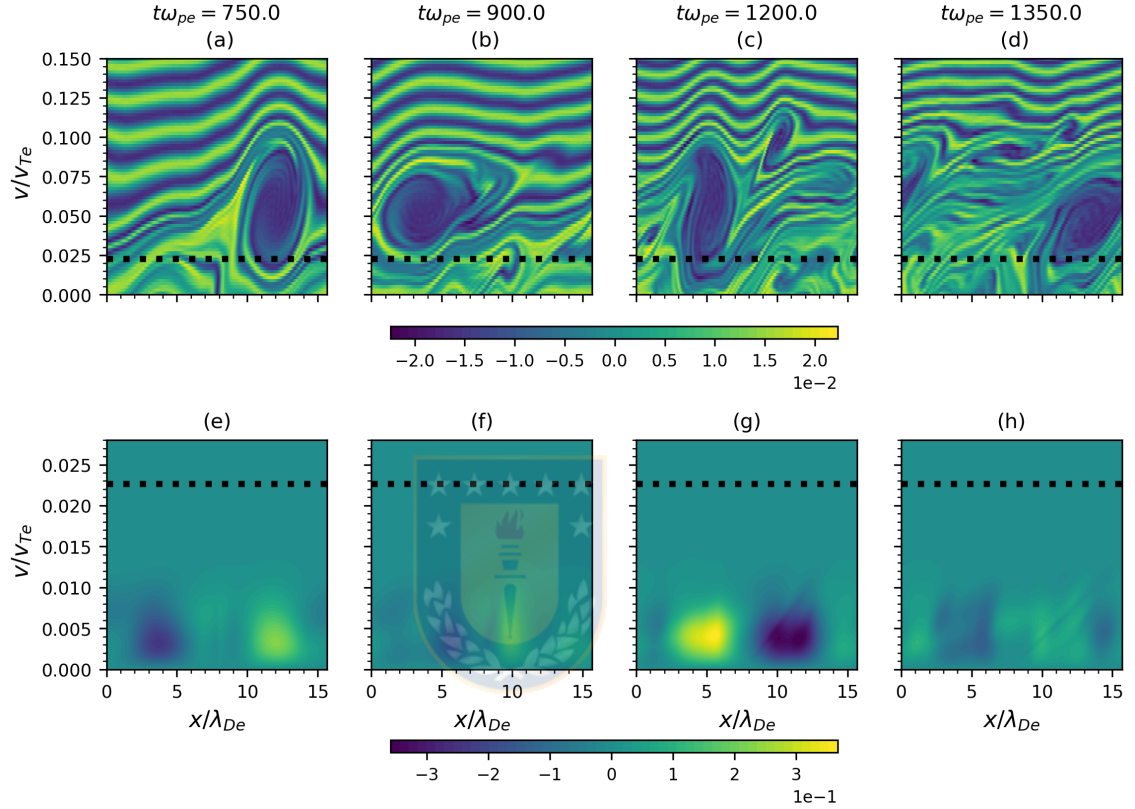


Figure 6.28: Evolution of variations of the ions distribution function, $\delta \bar{f}_i$, and of the electrons distribution function, $\delta \bar{f}_e$, for temperature ratio $\bar{T}_i = 0.025$ during the formation of secondary holes from the primary hole. The respective IA speed (black dotted line) is shown. Perturbative amplitude $\varepsilon_e = 4.0 \times 10^{-2}$. Mass ratio is $\bar{m}_i = 1836.153$.

For the following instants, the phase space plots show a local accumulation of ions within the region of trapping once the primary electron hole has been formed, due to the deepening of the potential of the hole [47]. In the cases in which the speed of the primary electron hole is close to the bulk of the ions distribution, co-moving ions are directly affected. As observed in the isothermal case, the positive potential would

expel ions from the center of the hole, forming compressive pulses at its boundaries [45, 84] and producing secondary holes [Figs.6.27(g) for $\bar{T}_i = 1.0$, and Fig.6.30(h) for $\bar{T}_i = 1.8$]. With the formation of further narrower holes, more compressive ion pulses are formed around them [see Figs.6.27 (g) and (j) for $\bar{T}_i = 1.0$, and Figs.6.30(h) and (k) for $\bar{T}_i = 1.8$].

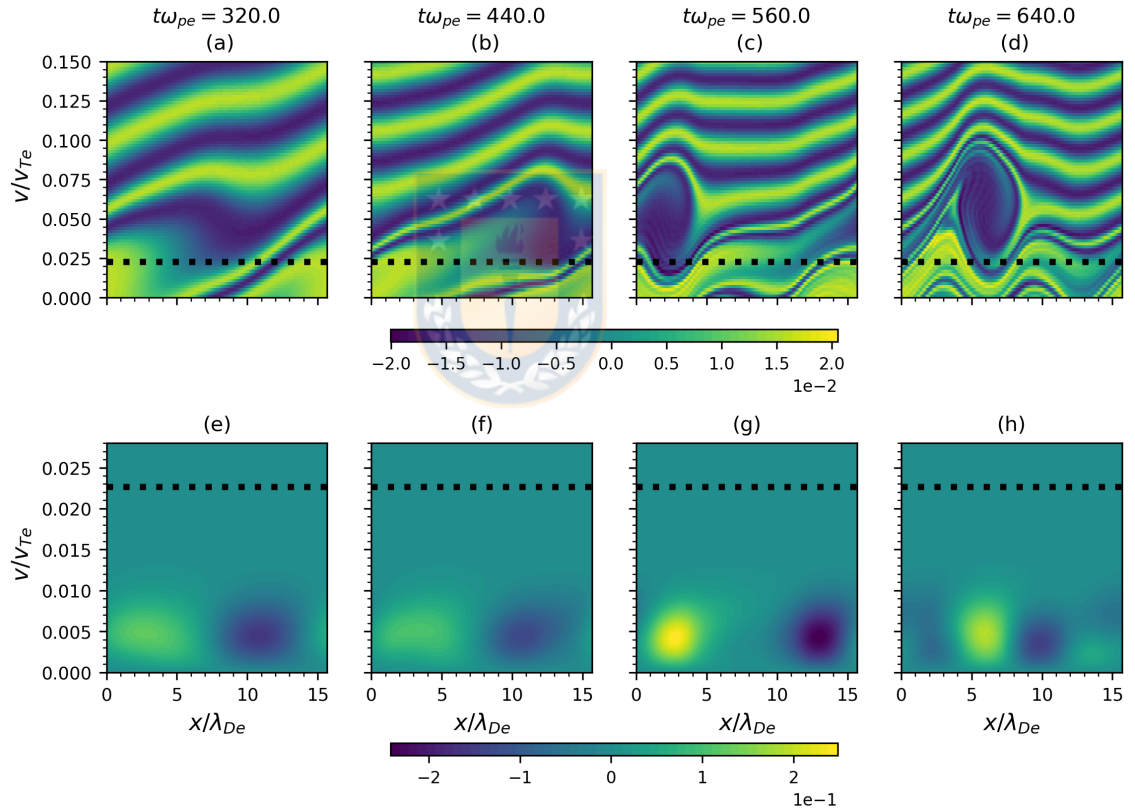


Figure 6.29: Evolution of variations of the ions distribution function, $\delta \bar{f}_i$, and of the electrons distribution function, $\delta \bar{f}_e$, for temperature ratio $\bar{T}_i = 0.025$ during the formation of the primary electron hole. The respective IA speed (black dotted line) is shown. Perturbative amplitude $\varepsilon_e = 4.0 \times 10^{-2}$. Mass ratio is $\bar{m}_i = 1836.153$.

In the case $\bar{T}_i = 0.025$ [Figs.6.27(c), (f), (i) and (l), Figs.6.28(e) through (h) and

Figs.6.29(e) through (h)], no variations occur about $\bar{v}_{\phi,IA}$, yet trapping occurs by a depopulation of electrons at this velocity. Phase space plots [Figs.6.18(c), (f), (i) and (l) and Figs.6.29(a) and (b)] indicate that there is a localized depletion of electrons at the center of the position domain in the velocity range of the ions distribution and is transported to larger velocities and is amplified above $\bar{v}_{\phi,IA}$. This process would account for the cases where $\bar{v}_{\phi,IA}$ is nonresonant with the ions distribution.

As the primary hole propagates, the ions distribution is distorted in the same manner as the cases of higher temperature, being ions repelled from the hole [Figs.6.27(i) and (l), and Figs.6.28(f) through (h)] and although no ions are co-moving with the primary hole, the electrons distribution is distorted and yields secondary holes [Figs.6.28(a) through (d)]. The same occurs for $\bar{T}_i = 0.2$ (not shown), which also has no ions co-moving with the primary electron hole.

With $\bar{T}_i = 5.0$, the ions distribution also exhibits localized accumulation but filamentation is the dominant process [Figs.6.30(a), (d) and (g)], indicating that these ions mostly free stream in the plasma. At larger times, however, compressive pulses are observed when further smaller electron holes are formed [Fig.6.19(j)], contributing to the formation of a low coherence structure found in $\delta\bar{n}_i$ (Fig.6.13), which might be responsible for the slight differences between this case and the case of immobile ions.

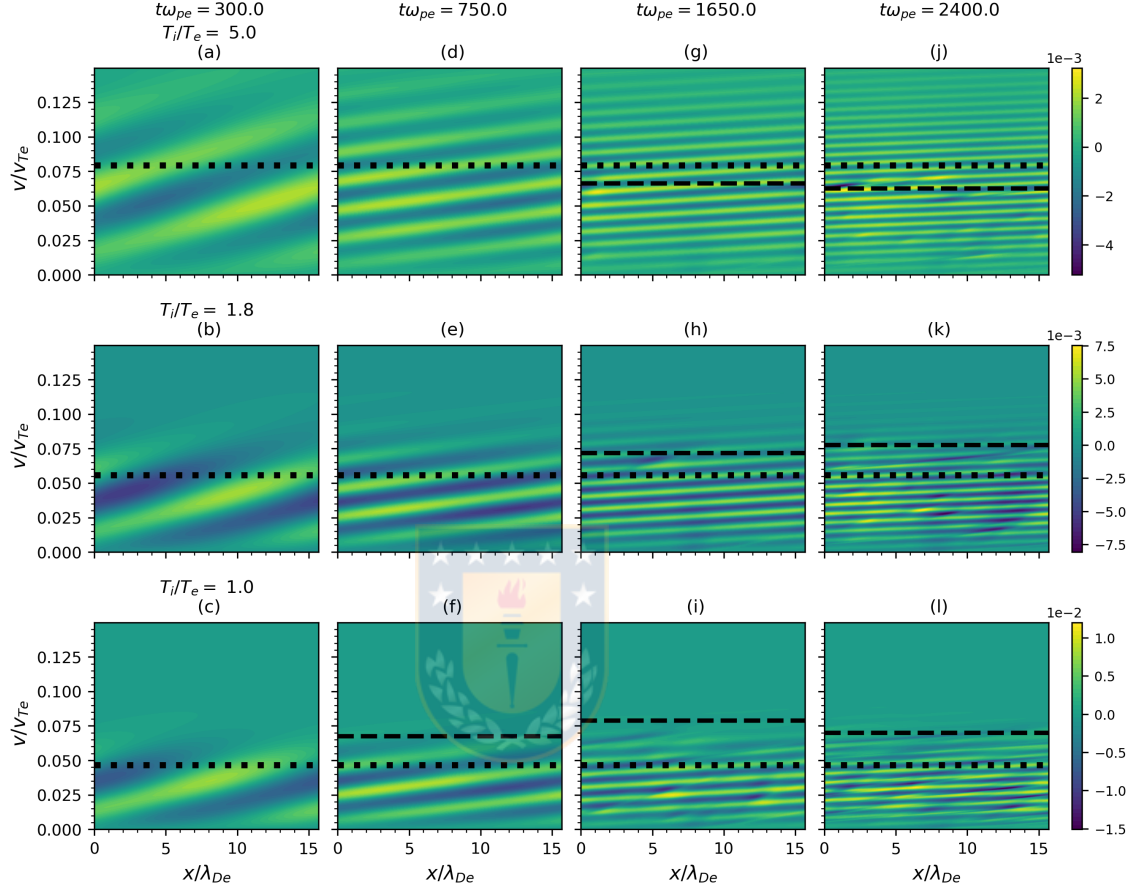


Figure 6.30: Evolution of variations of the ions distribution function, $\delta \bar{f}_i$, for temperature ratios $\bar{T}_i = 5.0$ [(a), (d), (g) and (j)], $\bar{T}_i = 1.8$ [(b), (e), (h) and (k)] and $\bar{T}_i = 1.0$ [(c), (f), (i) and (l)], at four instants. The respective IA speed (black dotted line) and the speed of the trapping region (black dashed line) are shown. Perturbative amplitude $\varepsilon_e = 4.0 \times 10^{-2}$.

6.4 Summary and discussion

This chapter studies the nonlinear dynamics of a driftless electron-ion Maxwellian plasma with mass ratio $\bar{m}_i = 1836.153$ with perturbative amplitude $\varepsilon_e = 4.0 \times 10^{-2}$ for different temperature ratios \bar{T}_i , making a comparison with the case $\bar{T}_i = 1.0$ and

describing the observed dynamics. The evolution of the electric field spectra for the tested \bar{T}_i shows that the most excited waves lie in nearly the same region in $\bar{\omega}_r - \bar{k}$ space. As the linear dispersion relation varies with \bar{T}_i , different linear branches coincide with the excited region, from the IA branch with $\bar{T}_i = 5.0$ to several higher order modes with $\bar{T}_i = 0.025$, suggesting that the excited waves do not correspond to a branch in the linear dispersion relation, in opposition to the conclusion in Chapter 5, and reinforcing the conclusion that the observed dynamics is not due to IAWs.

The electric field spectra show that the amplitudes of the signals in the electric field spectra are decreasing for higher \bar{T}_i . Also, weak or negligible activity around the linear IAW branch is found in all the studied cases, even in $\bar{T}_i = 5.0$. Similarly, the signals found along this branch decrease with higher \bar{T}_i . This behavior is in agreement with that found in IAWs whether linear [51] or nonlinear [54], in which they are favored by lower temperature ratios \bar{T}_i , suggesting that not only IAWs undergo this tendency but also other nonlinear waves related to heavy ions.

The nonlinear counter-propagating structures found in the isothermal case, namely, solitary compressive pulses in $\delta\bar{n}_i$, cavities in $\delta\bar{n}_{e,\text{fil}}$ and solitary structures in the potential $\bar{\Phi}_{\text{fil}}$ are still generated in the range $\bar{T}_i \leq 1.8$. The differences are the instant at which they are formed, their width in position space, and their amplitudes. The maximum width and amplitude and the earlier times occur with $\bar{T}_i < 1.0$, closer to $\bar{T}_i = 0$. The cases $\bar{T}_i > 1.0$ have lower amplitudes and longer times. If \bar{T}_i is too high (in the range $\bar{T}_i > 1.8$), these structures are not formed. In the case $\bar{T}_i = 5.0$, the evolution of the electrons distribution resembles the case of immobile ions, whereas ions behave mostly as a neutralizing mobile background. These results suggest that

a hotter distribution of ions has a lower contribution to the dynamics of the plasma, a similar tendency found by Zhou and Hutchinson [43] between electron holes and IASs. Unlike their work, in the plasma studied here at the highest \bar{T}_i there is no transition between coupled and decoupled electron holes.

It is also observed that the envelope of $\delta\bar{n}_i$ exhibits initial damping that increases with \bar{T}_i , being nearly zero for temperature ratios close to zero. This damping seems to determine the level of variations at further instants and exhibits the same tendency of the damping rate of the IAWs with \bar{T}_i [51]. As mobile ions ease the generation of a low frequency dynamics, if ion density variations are too damped, as with $\bar{T}_i = 5.0$, there will be a weak perturbation in the electrons distribution and the ions distribution itself, and they will behave as if ions were motionless, in accordance with the quantities observed in position space.

The distribution function of ions has a degree of mobility that depends on \bar{T}_i in the sense that the same number of ions is distributed over a range of velocities of different extensions. This width increases with higher \bar{T}_i . The resulting response if \bar{T}_i is too low is that perturbations are slowly transported and their structure remains unaltered and may remain localized for larger times, generating localized potentials of large amplitude capable of producing trapping in the electrons density. Fast ions can transport the perturbations far from their initial positions. If the density of faster ions increases (higher \bar{T}_i) they may compensate density variations produced by slower ions, and therefore, screen the self-consistent potential. Hence, amplitudes in several quantities, including the energy in the electric field spectra at low frequencies decrease with larger \bar{T}_i , but are still capable of driving the electrons distribution

to develop a region of trapping. The screening occurs at the rate of motion of the whole distribution which is faster in hotter distributions. In the case of $\bar{T}_i = 5.0$, the large range of velocities allows screening the perturbation in a large region in position space, leading to a fast decay of the amplitudes to low levels in a short time scale. As the level of variations in the ions distribution strongly depends on the amplitude of their self-consistent potential, $\delta\bar{n}_i$ will remain low at further times. It is suggested that this process yields the initial damping in the envelope of $\delta\bar{n}_i$.

As the filamentation progresses, the primary electron hole is formed right above the velocity $\bar{v}_{\phi,IA}$ due to an initial depopulation of electrons. In the case where ions are resonant with this velocity ($\bar{T}_i = 1.0$ and 1.8), there is a net increase in ions density and ion kinetic energy around it, along with a depletion of ions at slower velocities. Due to the opposite dynamical effects of the electric field depending on the charge, electrons in this region would be slowed down with respect to this velocity, generating the initial depletion. When $\bar{v}_{\phi,IA}$ is nonresonant with the ions distribution, there is an initial depletion of electrons at velocities close zero that is afterward transported towards larger velocities, however, the mechanism through which the depopulation occurs is not clear. Once the primary hole is formed, it grows in depth and rapidly accumulates ions, incrementing the amplitude of the localized potential, until compressive ion pulses are formed. It is noted that compressive ion pulses are formed at the boundaries of the hole in position space that yields secondary holes even when there are no ions co-moving with the primary hole ($\bar{T}_i = 0.2$ and 0.025). According to these observations, the velocity $\bar{v}_{\phi,IA}$ is still relevant in the response of the plasma although the spectra indicate that there is weak or negligible activity in the region corresponding to this linear mode.

It is noted that although certain temperature ratios are tested, the transition of the observed phenomena with different \bar{T}_i suggests that there is a continuous transition between the tested temperature ratios. In fact, there is a continuous transition in the location of $\bar{v}_{\phi,IA}$ with respect to the bulk of the distribution. Therefore, there is still resonant interaction with the ions distribution at this velocity in the range $0.2 < \bar{T}_i < 1.0$, and the net acceleration of ions around $\bar{v}_{\phi,IA}$ during the initial damping should contribute to the generation of the initial depopulation that leads to trapping in the electrons distribution. On the other hand, a continuous transition should also be found within the range $1.8 \leq \bar{T}_i \leq 5.0$ in which the dynamics of heavy ions is rapidly damped and the low frequency dynamics remains the same than in the case of immobile ions. A threshold temperature ratio \bar{T}_c is expected to be found in this range.

7 Conclusions

Throughout this work collisionless, unmagnetized, driftless Maxwellian electron-ion plasmas with mass ratio $\bar{m}_i = 1836.153$ and charge ratio $q_i/|q_e| = 1.0$ have been studied by exciting a single wavenumber, $\bar{k} = 0.4$, with perturbative amplitudes ε_e below the critical amplitude for nonlinear Landau damping of Langmuir waves, $\varepsilon_{e,C}$, yielding damped oscillations, and above $\varepsilon_{e,C}$ yielding nonlinear oscillations, both for initially isothermal species, $\bar{T}_i = 1.0$. In the nonlinear case, the initial temperature ratio \bar{T}_i has been varied to explore the effects in the dynamics of the plasma.

In the case of damped oscillations two kind waves propagate in the plasma, the LWs led by the dynamics of the electrons, and the IAWs led by the heavy ions dynamics as found by Xu *et al.* [27], identified by comparison between the electric field spectra and the frequencies and damping rates predicted by the kinetic linear dispersion relation. As $\bar{T}_i = 1.0$, the differences between the frequencies and the damping rates are due to the difference of inertia, yielding weak damping and smaller frequency for the IAWs, than for the LWs. The electrons distribution participates in the propagation of both waves.

A resonance zone is found in the distribution of both species involving the phase

velocity of the IAW, $\bar{v}_{\phi,IA}$ in which ions resonantly lead the dynamics and electrons with velocities in the order of $\bar{v}_{\phi,IA}$ undergo the opposite dynamical effects due to the charge difference, as expected from the linear theory estimation of the distribution function. It is also found that both kinds of waves propagate relatively independently one from the other as the resonance zone related to each one of them, or the whole species, are not largely affected by the propagation of the other wave, suggesting that the overall dynamics corresponds to a superposition of both kinds of waves. Therefore, initially, the large amplitude Langmuir wave predominates in the plasma sustained by electrons with velocities close to $\bar{v}_{\phi,L}$. Since its damping rate is larger, Langmuir oscillations rapidly decay below the levels of the IAWs, sustained by particles with velocities close to $\bar{v}_{\phi,IA}$, and the dynamics is then governed by these waves.

In the case of nonlinear oscillations, the case of immobile ions is found to exhibit a low frequency dynamics several electron plasma cycles after the formation of the trapping zone of nonlinear Landau damping of Langmuir waves. The variations of the electrons distribution show the development of an electron hole with velocity $\bar{v} = 0$ followed by counter-propagating holes propagating with velocities $|\bar{v}| \simeq 6.0 \times 10^{-2}$, with acoustic-like signatures in the electric field spectrum $|\bar{E}_{\omega,k}|$. Afterwards, the electrons distribution becomes densely populated by small electron holes within the range $|\bar{v}| \leq 0.1$. It is shown that the introduction of mobile initially isothermal ions enhance the low frequency dynamics by allowing the propagation of electron holes with velocities $|\bar{v}| = 6.283^{-2}$ of large extension in position and velocity spaces, at earlier times than in the case of immobile ions. Further comparison of the variations of the averaged distribution function and the distribution function indicate that the phase space structure is modified even in the electron hole related to Langmuir waves.

The spectrum $|\bar{E}_{k,\omega}|$ shows the excitation of waves in the same region as with mobile ions, but the acoustic-like branch involves waves of larger amplitude. Although low frequency activity is detected the IAWs are not the most excited wave in this system, unlike the case of damped oscillations, and are rather on a branch corresponding to the least damped higher order mode in the low frequency range predicted by the linear dispersion relation.

By focusing on the low frequency dynamics, it is observed that the low-frequency-filtered electrostatic potential exhibits solitary counter-propagating structures that last for long times with nearly constant velocities, $|\bar{v}_{s,\Phi}| = 6.283 \times 10^{-2}$, which can be identified as solitary electrostatic waves. The frequency filtered variations of the electrons density and the variations of the total ions density exhibit complementary structures that propagate with the same velocity, corresponding to cavities in the electrons density and compressive pulses in the ions density. It is remarkable that these structures are excited without a relative drift between electrons and ions and naturally develop from the initial perturbation without requiring an initial seed for the electron hole or the ion soliton [46, 48, 49]. The spectrum of each quantity indicates that the electrons contribute to the development of short wavelength structures whereas heavy ions sustain longer wavelengths. Both account for the generation of the localized positive low frequency potential $\bar{\Phi}_{\text{fil}}$. These structures also account for the dispersion structure found in $|\bar{E}_{\omega,k}|$.

The phase space portraits indicate that the cavity structure in the electrons density is due to the development of the electron holes. Particularly, holes initially moving with velocity $|\bar{v}| = 6.283 \times 10^{-2}$, labeled as primary, are related to the ions

dynamics as they are originated by depletion of electrons with velocities slightly above $\bar{v}_{\phi,IA}$ in a bounded range of velocities. The averaged distributions from each species suggest that this depletion is caused by the opposite dynamical effects of the electric field on both species around $\bar{v}_{\phi,IA}$ due to charge difference. As the associated potential grows in time, ions are bunched within the primary holes. This process accounts for the formation of compressive ion pulses in the ions density, enhancing the local potential. As the waves related to these structures do not lie on the linear IAW branch, as identified in works related to IASs [39, 40], and their velocity of propagation is out of the range analytically predicted for IASs [35], these structures cannot be associated to IASs.

Ions co-moving with the primary hole are particularly affected by the trapping yielding two compressive pulses at the boundaries of the primary hole in position space and leading to the formation of secondary electron holes. Unlike other works in which the primary hole is disrupted into two secondary holes [45, 84], this primary hole continues to propagate, possibly due to the comparatively large population of ions that still remain accumulated within the primary hole in comparison to those producing the secondary ones.

This nonlinear behavior is found even for lower perturbative amplitudes ε_e , however higher than $\varepsilon_{e,C}$. For lower ε_e the formation of the nonlinear structures is delayed and their amplitudes reduced. By following the instant τ_{loc} at which the structures in the electrons and ions density become coupled, identified as the instant at which the local correlations start to exhibit anti-correlative behavior in the localized structures, it is noted that τ_{loc} diverges close to a certain perturbative amplitude. Through a

curve fit, it is found that the coupling instant obeys a power law from which it is deduced that the threshold amplitude to excite this low frequency dynamics is larger than that required to excite the nonlinear Landau damping of Langmuir waves.

The nonlinear dynamics of the plasma is modified by changing the initial temperature ratio between the electrons and heavy ions. Except for $\bar{T}_i = 5.0$, the same nonlinear structures are developed in nearly all the tested cases differing in the level of the variations of particle densities, distribution functions and frequency filtered potential, being larger for lower \bar{T}_i , the instant at which the structures are formed, being earlier for lower \bar{T}_i , and the velocity of propagation of the structures, being slower for lower \bar{T}_i . The low frequency dispersion structure found in the electric field spectrum indicates that the region of waves in $\bar{\omega}_r - \bar{k}$ space is nearly the same, being more weighted to lower frequency and wavenumber waves with lower \bar{T}_i . A comparison with the roots of the respective kinetic linear dispersion relations suggests that the excited branches cannot be associated to linear modes, in opposition to the conclusion from the isothermal case.

The levels of every quantity from each case decrease with higher \bar{T}_i , suggesting that the excited structures follow the same tendency as those related to IAWs [51, 54], in which the propagation of these waves is favored by lower \bar{T}_i . The amplitudes seem to be settled by an initial damping found in the variations of the ions density. Variations are largely damped at higher \bar{T}_i , as in the case of IAWs [51]. Furthermore, if \bar{T}_i is high enough ($\bar{T}_i = 5.0$), the dynamics is similar to that found in the case of immobile ions, evidencing their weak influence in the evolution of the plasma. In this case, ions behave as a mobile neutralizing background. This behavior is similar

to that found by Zhou and Hutchinson [43] for the coupling between slow electron holes and IASs. The presence of mobile, positively charged, heavy ions enhance the low frequency dynamics. Therefore, the level of the perturbations in $\delta\bar{n}_i$ has a direct effect on the electrons distribution at velocities in the order of $\bar{v}_{\phi,IA}$. As a consequence, if the variations in the ions density undergo heavy damping, as occurs for $\bar{T}_i = 5.0$, there are lower variations and the dynamics of the electrons is not greatly affected, behaving as if ions were immobile. These results suggest that this tendency is not unique to IAWs but rather to perturbations related to the dynamics of heavy ions.

The mobility of the ions distribution, determined by \bar{T}_i for each case, seems to be responsible for the initial damping, screening the initial perturbation and yielding weak perturbations on the electrons distribution and on the ions distribution itself. Accordingly, a distribution in which there is a large number of fast ions, density variations are rapidly homogenized and damped. This is not the case of temperature ratios below $\bar{T}_i = 1.0$ and close to zero, specifically in the cases where $\bar{v}_{\phi,IA}$ is far from the core of the distribution, in which the effects of the initial perturbation persist for longer times.

The initial depopulation in the electrons density from which the primary electron holes are formed occurs right above the velocity $\bar{v}_{\phi,IA}$ for each \bar{T}_i , reasserting the relevance of the phase velocity of the IAWs for the excited wavenumber in the development of the low frequency dynamics of the plasma. In the cases in which there are ions co-mobile with the primary holes ($\bar{T}_i = 1.8$ and 1.0), it is suggested that the opposite dynamical effects of the IAW sustained by resonant interaction

with the mobile ions would account for the initial depopulation. In the cases in which $\bar{v}_{\phi,IA}$ is nonresonant with the ions distribution, phase space portraits indicate that there is a local depletion of electrons close to the core of the distribution which is transported to larger velocities. It is noted that in the cases in which there are no ions co-moving with the primary electron hole, compressive ion pulses are still formed and the primary hole still yields secondary holes, as in the case $\bar{T}_i = 0.025$.

In order to complete the picture of the low frequency dynamics of the plasma, it is still necessary to study any possible effect of the predominant structures in the plasma, namely, the electron holes related to the nonlinear Langmuir waves, which although involving large frequencies ($\bar{\omega}_r \gtrsim 0.1$) and larger velocities ($\bar{v} \sim \bar{v}_{\phi,L}$), it is still possible for them to couple and yield low frequency structures which might influence the development of low frequency structures in the presence of mobile ions. It is also of interest to study the behavior of the electrons distribution function at other velocity ranges, as the position averaged correlations of the electrons distribution function between the cases of immobile ions and mobile ions with $\bar{T}_i = 1.0$ become uncorrelated at a large extent of the velocity domain, indicating the presence of further nonlinear structures which has also excluded from the present analysis.

7 Conclusiones

A lo largo de este trabajo se han estudiado plasmas no colisionales, no magnetizados, sin deriva relativa compuestos por electrones y iones Maxwellianos con razón de masa $\bar{m}_i = 1836.153$ y razón de carga $q_i/|q_e| = 1.0$, excitando sólo un número de onda, $\bar{k} = 0.4$, con amplitudes de perturbación ε_e bajo la amplitud crítica $\varepsilon_{e,C}$ necesaria para excitar el amortiguamiento no lineal de Landau de ondas de Langmuir, obteniéndose oscilaciones amortiguadas, y por sobre $\varepsilon_{e,C}$, produciendo oscilaciones no lineales, ambas para el caso de especies inicialmente isotérmicas, $\bar{T}_i = 1.0$. En el caso no lineal, se ha variado la razón inicial de temperaturas \bar{T}_i para explorar los efectos en la dinámica del plasma.

En el caso de oscilaciones amortiguadas, dos tipos de ondas se propagan en el plasma, las LWs, conducidas por la dinámica de los electrones, y las IAWs, conducidas por la dinámica de los iones pesados, como fue concluido por Xu *et al.* [27], identificados por la comparación entre los espectros del campo eléctrico y las frecuencias y tasas de amortiguamiento predichas por la relación de dispersión lineal cinética. Como $\bar{T}_i = 1.0$, la diferencia entre las frecuencias y tasas de amortiguamiento se deben a la diferencia de inercia, produciendo un amortiguamiento débil y frecuencias más bajas en las IAWs que en las LAWs. La distribución de los electrones

participa en la propagación de ambas ondas.

Se encuentra una zona de resonancia en las distribuciones de ambas especies, involucrando la velocidad de fase de la IAW, $\bar{v}_{\phi,IA}$, en la que los iones dominan la dinámica y electrones con velocidades en el orden de $\bar{v}_{\phi,IA}$ experimentan los efectos dinámicos opuestos debido a la diferencia de carga, como se esperaba de la estimación de la función de distribución de la teoría lineal. También se encuentra que ambos tipos de ondas se propagan de forma relativamente independiente una de la otra, ya que la zona de resonancia relacionada con una de ellas, o toda la especie, no son afectados de forma importante por la propagación de la otra onda, sugiriendo que toda la dinámica corresponde a una superposición de ambos tipos de ondas. Por lo tanto, inicialmente, predominan las LWs de gran amplitud, sostenida por electrones con velocidades cercanas a $\bar{v}_{\phi,L}$. Dado que la tasa de amortiguamiento es mayor, las oscilaciones de Langmuir decaen rápidamente por debajo de los niveles de las IAWs, sostenidas por partículas con velocidades cercanas a $\bar{v}_{\phi,IA}$, y la dinámica es gobernada por estas ondas.

En el caso de oscilaciones no lineales, se encuentra que el caso de iones inmóviles exhibe una dinámica de baja frecuencia varios ciclos de oscilaciones de plasma de electrones después de la formación de la zona de atrapamiento del amortiguamiento no lineal de Landau de ondas de LWs. Las variaciones en la distribución de los electrones muestran el desarrollo de un *electron hole* con velocidad $\bar{v} = 0$ seguido por holes contra-propagantes con velocidades $|\bar{v}| \simeq 6.0 \times 10^{-2}$, con señales tipo-acústicas en el espectro del campo eléctrico $|\bar{E}_{\omega,k}|$. Posteriormente, la distribución de los electrones se pobla densamente por *electron holes* pequeños dentro del rango $|\bar{v}| \leq 0.1$.

Se muestra que la introducción de iones móviles inicialmente isotérmicos potencia la dinámica de baja frecuencia, permitiendo la propagación de *electron holes* con velocidades $|\bar{v}| = 6.283^{-2}$ de gran extensión en los espacios de posición y velocidad, en instantes anteriores a los del caso de iones inmóviles. Una comparación en más detalle de las variaciones de la función de distribución promediada en posiciones y la función de distribución en ambos casos indica que hay una modificación en la estructura del espacio de fase, incluso en el *electron hole* relacionado a las LWs. El espectro $|\bar{E}_{k,\omega}|$ muestra la excitación de ondas en la misma región que en el caso de iones móviles, pero la rama tipo-acústica involucra ondas de mayor amplitud. Aunque se detecta actividad de baja frecuencia, las IAWs no son las más excitadas en el sistema, al contrario del caso de oscilaciones amortiguadas, y se encuentra más bien sobre una rama correspondiente al modo de orden superior de baja frecuencia menos amortiguado predicha por la relación de dispersión lineal.

Al enfocarse en la dinámica de baja frecuencia, se observa que el potencial electrostático filtrado en frecuencias exhibe estructuras solitarias contra-propagantes que persisten por largos tiempos con velocidades aproximadamente constantes, $|\bar{v}_{s,\phi}| = 6.283 \times 10^{-2}$, las que pueden identificarse como ondas solitarias electrostáticas. Las variaciones filtradas en frecuencias de la densidad de electrones y las variaciones de la densidad de iones exhiben estructuras complementarias que se propagan con la misma velocidad, correspondientes a cavidades en la densidad de electrones y pulsos compresivos en la densidad de iones. Es destacable que estas estructuras se excitan sin haber una deriva relativa entre ambas especies, y que se desarrollan naturalmente desde la perturbación inicial sin requerir una semilla inicial para el *electron hole* o el solitón de iones [46, 48, 49]. El espectro de cada cantidad indica que los electrones

contribuyen al desarrollo de estructuras de onda corta mientras que los iones pesados sostienen las de longitud de onda larga. Ambas dan cuenta de la generación de un potencial electrostático positivo localizado de baja frecuencia $\bar{\Phi}_{\text{fil}}$. Estas estructuras también dan cuenta de la estructura de dispersión encontrada en $|\bar{E}_{\omega,k}|$.

Secciones del espacio de fase indican que la estructura de cavidades en la densidad de electrones se debe al desarrollo de *electron holes*. Particularmente, los *holes* que inicialmente se mueven con velocidad $|\bar{v}| = 6.283 \times 10^{-2}$, aquí denominados como primarios, están relacionados con la dinámica de los iones, ya que se originan por un despoblamiento de electrones con velocidades ligeramente superiores a $\bar{v}_{\phi,IA}$ en un rango acotado de velocidades. Las funciones de distribución promediadas de ambas especies sugieren que este despoblamiento se debe a los efectos dinámicos opuestos del campo eléctrico en ambas especies alrededor $\bar{v}_{\phi,IA}$ debido a una diferencia de carga. A medida que el potencial asociado crece en el tiempo, los iones se acumulan en el interior de los *holes* primarios. Este proceso da cuenta de la formación de pulsos compresivos en la densidad de iones, potenciando el potencial local. Debido a que las ondas relacionadas a estas estructuras no yacen sobre la rama IAW lineal, como sí se ha observado en trabajos relacionados a IASs [39, 40], y su velocidad de propagación está fuera del rango predicho analíticamente para IASs [35], estas estructuras no pueden relacionarse a IASs.

Los iones que se mueven junto con el *hole* primario son particularmente afectados por el atrapamiento, produciendo dos pulsos compresivos en los bordes del *hole* primario en el espacio de posiciones y llevan a la formación de *electron holes* secundarios. A diferencia de otros trabajos en los que el *hole* primario se rompe

en dos *holes* secundarios [45, 84], este hole primario continúa propagándose, posiblemente por la comparativamente mayor población de iones que aún se encuentran acumulados en el *hole* primario en comparación con la de aquellos que producen los secundarios.

Este comportamiento no lineal se encuentra incluso para amplitudes de perturbación ε_e , mientras sean mayores que $\varepsilon_{e,C}$. Para amplitudes ε_e más bajas, la formación de estructuras no lineales se retrasa y sus amplitudes se reducen. Siguiendo el instante τ_{loc} en el que las estructuras en las densidades de iones y electrones se acoplan, identificado como el instante en que las correlaciones locales comienzan a exhibir comportamiento anti-correlativo en las estructuras localizadas, se puede notar que τ_{loc} diverge cerca de una cierta amplitud de perturbación. Por medio de un ajuste de curva, se encuentra que el instante de acoplamiento obedece una ley de potencia de a que se deduce que amplitud umbral para excitar esta dinámica de baja frecuencia es mayor que la requerida para excitar el amortiguamiento no lineal de LWs.

La dinámica no lineal del plasma se modifica al cambiar la razón inicial de temperatura entre los electrones y los iones pesados. Excepto por $\bar{T}_i = 5.0$, se desarrollan las mismas estructuras no lineales en casi todos los casos, difiriendo en el nivel de las variaciones de las densidades de partículas, funciones de distribución y potencial filtrado en frecuencias, siendo mayor para \bar{T}_i inferiores, el instante en que las estructuras se forman, siendo más corto para \bar{T}_i inferiores, y la velocidad de propagación de las estructuras, siendo menor para \bar{T}_i inferiores. La estructura de dispersión de baja frecuencia encontrada en el espectro del campo eléctrico indica que la región

de ondas en el plano $\bar{\omega}_r - \bar{k}$ es aproximadamente la misma, estando más cargada a frecuencias y números de onda más bajos para \bar{T}_i más pequeños. Una comparación con las raíces de las respectivas relaciones de dispersión lineales cinéticas sugiere que las ramas excitadas no pueden asociarse a modos lineales, en oposición con la conclusión deducida en el caso isotérmico.

Los niveles de todas las cantidades para cada caso decrecen con mayores \bar{T}_i , sugiriendo que las estructuras excitadas siguen la misma tendencia que la de las IAWs [51, 54], en las que la propagación de estas ondas se ve favorecida con \bar{T}_i inferiores. Las amplitudes parecen fijadas por un amortiguamiento inicial encontrado en las variaciones de la densidad de los iones. Las variaciones son fuertemente amortiguadas con \bar{T}_i altos, como en el caso las IAWs [51]. Más aún, si \bar{T}_i es lo suficientemente alto ($\bar{T}_i = 5.0$), la dinámica es similar a la encontrada en el caso de iones inmóviles, evidenciando su débil influencia en la evolución del plasma. En este caso, los iones se comportan como un fondo neutralizante móvil. Este comportamiento es similar al encontrado por Zhou y Hutchinson [43] para el acoplamiento entre *electron holes* lentos y IASs. La presencia de iones pesados móviles con carga positiva potencia la dinámica de baja frecuencia. Por lo tanto, el nivel de las perturbaciones en $\delta\bar{n}_i$ tiene un efecto directo en la distribución de los electrones en velocidades del orden de $\bar{v}_{\phi,IA}$. Como consecuencia, si las variaciones en la densidad de los iones experimentan un amortiguamiento fuerte, como ocurre para $\bar{T}_i = 5.0$, hay variaciones más bajas y la dinámica de los electrones no es mayormente afectada, comportándose como si los iones fueran inmóviles. Estos resultados sugieren que esta tendencia no es única de las IAWs, sino que de perturbaciones asociadas a la dinámica de iones pesados.

La movilidad de la distribución de los iones, determinada por \bar{T}_i para cada caso, parece ser responsable del amortiguamiento inicial, apantallando la perturbación inicial y produciendo perturbaciones débiles en la distribución de los electrones y de los iones mismos. En consecuencia, la distribución en la que hay un mayor número de iones rápidos, las variaciones en la densidad son rápidamente homogeneizadas y amortiguadas. Este no es el caso de razones de temperaturas menores que $\bar{T}_i = 1.0$ y cercanas a cero, donde $\bar{v}_{\phi,IA}$ está lejos del centro de la función de distribución, en la que los efectos de la perturbación inicial persisten por tiempos más largos.

El despoblamiento inicial en la densidad de los electrones, a partir de la que se forman los *electron holes* primarios, ocurre justo por sobre la velocidad $\bar{v}_{\phi,IA}$ para cada \bar{T}_i , reafirmando la relevancia de la velocidad de fase de las IAWs para el número de onda excitado en el desarrollo de la dinámica de baja frecuencia del plasma. En los casos en que hay iones co-móviles con los *holes* primarios ($\bar{T}_i = 1.8$ and 1.0), se sugiere que los efectos dinámicos opuestos de la IAW sostenidos por interacción resonante con los iones móviles daría cuenta del despoblamiento inicial. En los casos en que $\bar{v}_{\phi,IA}$ es no resonante con la distribución de iones, secciones del espacio de fase indican que hay un despoblamiento localizado de electrones cerca del centro de la distribución que es transportado a velocidades mayores. Se debe notar que en los casos en que no hay iones co-móviles con los *holes* primarios, aún se forman pulsos compresivos y que los *holes* primarios aún producen *holes* secundarios, como en el caso de $\bar{T}_i = 0.025$.

Con el fin de completar la imagen de la dinámica de baja frecuencia del plasma, aún es necesario estudiar cualquier posible efecto de las estructuras predominantes en

el plasma, a saber, *electron holes* relacionados con LWs no lineales, las que aunque involucran frecuencias altas ($\bar{\omega}_r \gtrsim 1$) y velocidades altas ($\bar{v} \sim \bar{v}_{\phi,L}$), aún es posible que estas estructuras se acoplen y produzcan estructuras de baja frecuencia que podrían afectar el desarrollo de las estructuras producidas en presencia de iones móviles. Es también de interés estudiar el comportamiento de la función de distribución de los electrones en otros rangos de velocidades, ya que las correlaciones promediadas en posiciones de las funciones de distribución de electrones de los casos de iones inmóviles y móviles con $\bar{T}_i = 1.0$ se tornan no correlacionadas en una gran extensión del dominio de velocidades, indicando la presencia de más estructuras no lineales que también fueron excluidas del presente análisis.



Appendices



A Linear dispersion relation calculation

A.1 Linear dispersion relation from (2.2.6) to (2.2.8)

By considering the unperturbed trajectories, the exponential is given by

$$\exp [i (\mathbf{k} \cdot [\mathbf{r}'(t') - \mathbf{r}] - \omega [t' - t])] = \exp [i ([\mathbf{k} \cdot \mathbf{v} - \omega] t' + \omega t)].$$

Direct integration of (2.2.6) and use of the electric potential in Fourier space yields

$$\begin{aligned} \int_{-\infty}^t \exp [i (\mathbf{k} \cdot [\mathbf{r}'(t') - \mathbf{r}] - \omega [t' - t])] \times \\ \mathbf{E}_{1,\mathbf{k},\omega} \cdot \nabla_v f_{0,j} dt' &= i \frac{\mathbf{E}_{1,\mathbf{k},\omega} \cdot \nabla_v f_{0,j}}{\omega - \mathbf{k} \cdot \mathbf{v}} \\ &= \Phi_{1,\mathbf{k},\omega} \frac{\mathbf{k} \cdot \nabla_v f_{0,j}}{\omega - \mathbf{k} \cdot \mathbf{v}}. \end{aligned}$$

The Laplace-Fourier transform of the perturbed distribution function then is given by

$$f_{1,j,\mathbf{k},\omega} = -\Phi_{1,\mathbf{k},\omega} \frac{q_j}{m_j} \frac{\mathbf{k} \cdot \nabla_v f_{0,j}}{\omega - \mathbf{k} \cdot \mathbf{v}}.$$

Introduction of this result and electric potential into Gauss law, and use of Fourier transform in space yield

$$i\mathbf{k} \cdot \mathbf{E}_{1,\mathbf{k},\omega} = \frac{\rho_{1,\mathbf{k},\omega}}{\epsilon_0}$$

$$k^2 \Phi_{1,\mathbf{k},\omega} = -\Phi_{1,\mathbf{k},\omega} \sum_j \frac{q_j^2}{\epsilon_0 m_j} \int \frac{\mathbf{k} \cdot \nabla_{\mathbf{v}} f_{j0}}{\omega - \mathbf{k} \cdot \mathbf{v}} d^3v,$$

from which it is obtained the equation

$$\left[1 + \sum_j \frac{q_j^2}{\epsilon_0 m_j k^2} \int \frac{\mathbf{k} \cdot \nabla_{\mathbf{v}} f_{j0}}{\omega - \mathbf{k} \cdot \mathbf{v}} d^3v \right] \Phi_{1,\mathbf{k},\omega} = 0,$$

which is stated in the form $\epsilon_{\mathbf{k},\omega} \Phi_{1,\mathbf{k},\omega} = 0$, where $\epsilon_{\mathbf{k},\omega}$ is identified as the term in square brackets, corresponding to the dispersion function in (2.2.8).

A.2 Linear dispersion relation from (2.2.8) to (2.2.10)

For the following calculations, the equilibrium distribution functions for all species are Maxwellian distributions without drift.

$$f_{0,j}(\mathbf{v}) = \frac{n_{0,j}}{[\sqrt{2\pi}v_{Tj}]^3} \exp \left[-\frac{v^2}{2v_{Tj}^2} \right].$$

Its gradient is given by

$$\nabla_{\mathbf{v}} f_{0,j} = -\frac{\mathbf{v}}{v_{Tj}^2} \frac{n_{0,j}}{[\sqrt{2\pi}v_{Tj}]^3} \exp \left[-\frac{v^2}{2v_{Tj}^2} \right].$$

By introducing this result into $\varepsilon_{\mathbf{k},\omega}$, and the plasma frequency definition, $\omega_{pj}^2 \equiv q_j^2 n_j / \epsilon_0 m_j$, the dispersion function is given by

$$\varepsilon_{\mathbf{k},\omega} = 1 - \frac{1}{[\sqrt{2\pi}]^3 v_{Tj}^5} \sum_j \frac{\omega_{pj}^2}{k^2} \int \frac{\mathbf{k} \cdot \mathbf{v}}{\omega - \mathbf{k} \cdot \mathbf{v}} \exp\left[\frac{-v^2}{2v_{Tj}^2}\right] d^3v.$$

To solve the integral, the velocity axes are aligned with respect to \mathbf{k} , thus

$$\mathbf{v} = v_{\parallel} \mathbf{e}_{\parallel} + v_{\perp} \mathbf{e}_{\perp},$$

where \mathbf{e}_{\parallel} and \mathbf{e}_{\perp} are unitary vectors parallel and perpendicular to \mathbf{k} , respectively, so that $\mathbf{k} \cdot \mathbf{v} = kv_{\parallel}$ and $\mathbf{k} \cdot \mathbf{V}_j = kV_{j\parallel} = V_j \cos \theta$, being θ_j the angle between \mathbf{k} and \mathbf{V}_j . The integral is then solved.

$$\begin{aligned} \int \frac{\mathbf{k} \cdot \mathbf{v}}{\omega - \mathbf{k} \cdot \mathbf{v}} \exp\left[-\frac{v^2}{2v_{Tj}^2}\right] d^3v &= \int \frac{kv_{\parallel}}{\omega - kv_{\parallel}} \exp\left[-\frac{v_{\parallel}^2}{2v_{Tj}^2}\right] \exp\left[-\frac{\mathbf{v}_{\perp}^2}{2v_{Tj}^2}\right] d^3v \\ &= k \int \exp\left[-\frac{v_{\perp}^2}{2v_{Tj}^2}\right] d^2v_{\perp} \int_{-\infty}^{\infty} \frac{v_{\parallel}}{\omega - kv_{\parallel}} \exp\left[-\frac{v_{\parallel}^2}{2v_{Tj}^2}\right] dv_{\parallel}. \end{aligned}$$

The integral on \mathbf{v}_{\perp} consists of two integrals of Maxwellian functions, one for each perpendicular direction.

$$\begin{aligned} \int \exp\left[-\frac{v^2}{2v_{Tj}^2}\right] d^2v_{\perp} &= \int_{-\infty}^{\infty} \exp\left[-\frac{v_{\perp,1}^2}{2v_{Tj}^2}\right] dv_{\perp,1} \int_{-\infty}^{\infty} \exp\left[-\frac{v_{\perp,2}^2}{2v_{Tj}^2}\right] dv_{\perp,2} \\ &= 2\pi v_{Tj}^2. \end{aligned} \tag{A.2.1}$$

For the integral on v_{\parallel} , it is considered that

$$\frac{kv_{\parallel}}{\omega - kv_{\parallel}} = -1 + \frac{\omega}{\omega - kv_{\parallel}},$$

thus,

$$k \int_{-\infty}^{\infty} \frac{v_{\parallel}}{\omega - kv_{\parallel}} \exp \left[-\frac{v_{\parallel}^2}{2v_{Tj}^2} \right] dv_{\parallel} = -\sqrt{2\pi}v_{Tj} + \int_{-\infty}^{\infty} \frac{\omega}{\omega - kv_{\parallel}} \exp \left[-\frac{v_{\parallel}^2}{2v_{Tj}^2} \right] dv_{\parallel},$$

where the first term on the right hand side has been obtained in the same way as (A.2.1). The integral in the second term on the right hand side is solved by introducing a change of variables, $\xi = v_{\parallel}/\sqrt{2}v_{Tj}$ and $\zeta_j = \omega/\sqrt{2}kv_{Tj}$, yielding

$$k \int_{-\infty}^{\infty} \frac{v_{\parallel}}{\omega - kv_{\parallel}} \exp \left[-\frac{v_{\parallel}^2}{2v_{Tj}^2} \right] dv_{\parallel} = -\sqrt{2\pi}v_{Tj} \left[1 + \frac{\zeta_j}{\sqrt{\pi}} \int_{-\infty}^{\infty} \frac{\exp[-\xi^2]}{\xi - \zeta_j} d\xi \right].$$

The integral in the right side does not have analytical expression and has been thoroughly studied by mathematicians. It depends on the variable ζ_j , which is known as the resonance factor [51] and indicates the location of the resonance zone in the distribution function with respect to the initial thermal velocity. This function is called plasma dispersion function [61], defined as

$$Z(\zeta_j) \equiv \frac{1}{\sqrt{\pi}} \int_{-\infty}^{\infty} \frac{\exp[-\xi^2]}{\xi - \zeta_j} d\xi.$$

Therefore,

$$k \int_{-\infty}^{\infty} \frac{v_{\parallel}}{\omega - kv_{\parallel}} \exp \left[-\frac{v_{\parallel}^2}{2v_{Tj}^2} \right] dv_{\parallel} = -\sqrt{2\pi}kv_{Tj} [1 + \zeta_j Z(\zeta_j)]. \quad (\text{A.2.2})$$

Finally, by gathering results from (A.2.1) and (A.2.2), the dispersion function is

$$\begin{aligned}\varepsilon_{\mathbf{k},\omega} &= 1 + \sum_j \frac{q_j^2}{\epsilon_0 m_j k^2} \int \frac{\mathbf{k} \cdot \nabla_{\mathbf{v}} f_{j0}}{\omega - \mathbf{k} \cdot \mathbf{v}} d^3v \\ &= 1 + \sum_j \frac{\omega_{pj}^2}{v_{Tj}^2 k^2} [1 + \zeta_j Z(\zeta_j)].\end{aligned}$$



B Dictionary

B.1 Abbreviations

- **BGK** : Bernstein-Greene-Kruskal (referred to BGK states).
- **LW/s** : Langmuir wave/s.
- **IA** : Ion acoustic.
- **IAS/s** : Ion acoustic soliton/s.
- **IAW/s** : Ion acoustic wave/s.



Bibliography

- [1] L. D. Landau. “On the vibrations of the electronic plasma”. In: *Zh. Eksp. Teor. Fiz.* 16,574 10 (1946), pp. 25–34 (cit. on pp. 3, 22).
- [2] Thomas O’neil. “Collisionless damping of nonlinear plasma oscillations”. In: *The Physics of Fluids* 8.12 (1965), pp. 2255–2262 (cit. on pp. 3, 22, 51).
- [3] Tsutomu Imamura, Ryo Sugihara, and Tosiya Taniuti. “An asymptotic method for the Vlasov equation”. In: *Journal of the Physical Society of Japan* 27.6 (1969), pp. 1623–1630 (cit. on pp. 3, 22).
- [4] R Sugihara et al. “Initial damping of large amplitude waves”. In: *The Physics of Fluids* 24.3 (1981), pp. 434–441 (cit. on pp. 3, 22, 51).
- [5] Ryo Sugihara and Kaoru Yamanaka. “Enhancement of damping of a large amplitude wave”. In: *The Physics of Fluids* 18.1 (1975), pp. 114–116 (cit. on pp. 3, 22).
- [6] Ryo Sugihara and Jun-ichi Sakai. “Correction Term of Landau Damping Due to Trapped Particles”. In: *Journal of the Physical Society of Japan* 29.2 (1970), pp. 447–449 (cit. on pp. 3, 22).
- [7] G Brodin. “Nonlinear landau damping”. In: *Physical Review Letters* 78.7 (1997), p. 1263 (cit. on pp. 3, 22).

- [8] JR Danielson, F Anderegg, and CF Driscoll. “Measurement of Landau damping and the evolution to a BGK equilibrium”. In: *Physical Review Letters* 92.24 (2004), p. 245003 (cit. on pp. 3, 22, 51).
- [9] A. V. Ivanov, Iver H. Cairns, and P. A. Robinson. “Wave damping as a critical phenomenon”. In: *Physics of Plasmas* (2004). ISSN: 1070664X. DOI: 10.1063/1.1785789 (cit. on pp. 3, 22, 125).
- [10] AV Ivanov and Iver H Cairns. “Nontrapping arrest of Langmuir wave damping near the threshold amplitude”. In: *Physical Review Letters* 96.17 (2006), p. 175001 (cit. on pp. 3, 22).
- [11] Ira B. Bernstein, John M. Greene, and Martin D. Kruskal. “Exact nonlinear plasma oscillations”. In: *Physical Review* 108.3 (1957), pp. 546–550. ISSN: 0031899X. DOI: 10.1103/PhysRev.108.546 (cit. on pp. 3, 22, 52, 53).
- [12] IH Hutchinson. “Electron holes in phase space: What they are and why they matter”. In: *Physics of Plasmas* 24.5 (2017), p. 055601 (cit. on pp. 3, 7, 22, 27, 53).
- [13] Abid Ali Abid et al. “Effects of electron trapping on nonlinear electron-acoustic waves excited by an electron beam via particle-in-cell simulations”. In: *Plasma Science and Technology* (2019) (cit. on pp. 3, 22).
- [14] John D Lindl et al. “The physics basis for ignition using indirect-drive targets on the National Ignition Facility”. In: *Physics of Plasmas* 11.2 (2004), pp. 339–491 (cit. on pp. 3, 23).
- [15] HC Bandulet et al. “Thomson-scattering study of the subharmonic decay of ion-acoustic waves driven by the brillouin instability”. In: *Physical Review Letters* 93.3 (2004), p. 035002 (cit. on pp. 3, 23).

- [16] Hoanh X Vu, DF DuBois, and B Bezzerides. “Transient enhancement and de-tuning of laser-driven parametric instabilities by particle trapping”. In: *Physical Review Letters* 86.19 (2001), p. 4306 (cit. on pp. 4, 23).
- [17] CJ Pawley, HE Huey, and NC Luhmann Jr. “Observation of the growth and saturation of ion waves generated by optical mixing”. In: *Physical Review Letters* 49.12 (1982), p. 877 (cit. on pp. 4, 23).
- [18] QS Feng et al. “Excitation of nonlinear ion acoustic waves in CH plasmas”. In: *Physics of Plasmas* 23.8 (2016), p. 082106 (cit. on pp. 4, 23).
- [19] Paul Neumayer et al. “Suppression of stimulated Brillouin scattering by increased Landau damping in multiple-ion-species hohlraum plasmas”. In: *Physical Review Letters* 100.10 (2008), p. 105001 (cit. on pp. 4, 23).
- [20] C Riconda et al. “Electron and ion kinetic effects in the saturation of a driven ion acoustic wave”. In: *Physics of Plasmas* 12.11 (2005), p. 112308 (cit. on pp. 4, 23).
- [21] J Bonnell et al. “Modulated langmuir waves: observations from freja and SCIFER”. In: *Journal of Geophysical Research: Space Physics* 102.A8 (1997), pp. 17233–17240 (cit. on pp. 4, 23).
- [22] R Pottelette et al. “Modulated electron-acoustic waves in auroral density cavities: FAST observations”. In: *Geophysical Research Letters* 26.16 (1999), pp. 2629–2632 (cit. on pp. 4, 23).
- [23] Hamish Andrew Sinclair Reid and Heather Ratcliffe. “A review of solar type III radio bursts”. In: *Research in Astronomy and Astrophysics* 14.7 (2014), p. 773 (cit. on pp. 4, 11, 24, 31).

- [24] George Blair Hospodarsky and Donald A Gurnett. “Beat-type Langmuir wave emissions associated with a type III solar radio burst: Evidence of parametric decay”. In: *Geophysical Research Letters* 22.10 (1995), pp. 1161–1164 (cit. on pp. 5, 24).
- [25] Iver H Cairns. “Role of collective effects in dominance of scattering off thermal ions over Langmuir wave decay: Analysis, simulations, and space applications”. In: *Physics of Plasmas* 7.12 (2000), pp. 4901–4915 (cit. on pp. 5, 24).
- [26] B Layden, Iver H Cairns, and PA Robinson. “Exact evaluation of the rates of electrostatic decay and scattering off thermal ions for an unmagnetized Maxwellian plasma”. In: *Physics of Plasmas* 20.8 (2013), p. 082310 (cit. on pp. 5, 24).
- [27] Hui Xu et al. “Effects of ion motion on linear Landau damping”. In: *Physics of Plasmas* 24.2 (2017), p. 022101 (cit. on pp. 5–7, 13, 15, 26, 33, 35, 47, 73, 74, 81, 86, 95, 169, 176).
- [28] Hans Schamel. “Electron holes, ion holes and double layers: Electrostatic phase space structures in theory and experiment”. In: *Physics Reports* 140.3 (1986), pp. 161–191 (cit. on pp. 7, 27, 53).
- [29] Bengt Eliasson and Padma K Shukla. “Formation and dynamics of coherent structures involving phase-space vortices in plasmas”. In: *Physics Reports* 422.6 (2006), pp. 225–290 (cit. on pp. 8, 27).
- [30] JP McFadden et al. “FAST observations of ion solitary waves”. In: *Journal of Geophysical Research: Space Physics* 108.A4 (2003) (cit. on pp. 8, 27).

- [31] Maxime Lesur, PH Diamond, and Yusuke Kosuga. “Nonlinear current-driven ion-acoustic instability driven by phase-space structures”. In: *Plasma Physics and Controlled Fusion* 56.7 (2014), p. 075005 (cit. on pp. 8, 10, 27, 30).
- [32] B Eliasson and PK Shukla. “The dynamics of electron and ion holes in a collisionless plasma”. In: (2005) (cit. on pp. 8, 27).
- [33] P Guio et al. “Phase space vortices in collisionless plasmas”. In: *Nonlinear Processes in Geophysics* 10.1/2 (2003), pp. 75–86 (cit. on pp. 8, 27).
- [34] TE Sheridan, S Yi, and KE Lonngren. “On the origin of the ion acoustic soliton”. In: *Physics of Plasmas* 5.9 (1998), pp. 3165–3170 (cit. on pp. 8, 27).
- [35] N.A. Krall and A.W. Trivelpiece. *Principles of plasma physics*. International series in pure and applied physics v. 0-911351. McGraw-Hill, 1973. ISBN: 9780070353466. URL: <https://books.google.cl/books?id=b0BRAAAAMAAJ> (cit. on pp. 8, 28, 43, 44, 57, 127, 172, 179).
- [36] Haruichi Washimi and Tosiya Taniuti. “Propagation of ion-acoustic solitary waves of small amplitude”. In: *Physical Review Letters* 17.19 (1966), p. 996 (cit. on pp. 8, 28, 56, 127).
- [37] MQ Tran. “Ion acoustic solitons in a plasma: a review of their experimental properties and related theories”. In: *Physica Scripta* 20.3-4 (1979), p. 317 (cit. on pp. 8, 28).
- [38] TE Sheridan. “Evolution of unstable ion acoustic solitons”. In: *IEEE Transactions on Plasma Science* 27.1 (1999), pp. 140–141 (cit. on pp. 8, 28).

- [39] Sarveshwar Sharma, Sudip Sengupta, and Abhijit Sen. “Particle-in-cell simulation of large amplitude ion-acoustic solitons”. In: *Physics of Plasmas* 22.2 (2015), p. 022115 (cit. on pp. 8, 28, 127, 172, 179).
- [40] Bharati Kakad, Amar Kakad, and Yoshiharu Omura. “Nonlinear evolution of ion acoustic solitary waves in space plasmas: Fluid and particle-in-cell simulations”. In: *Journal of Geophysical Research: Space Physics* 119.7 (2014), pp. 5589–5599 (cit. on pp. 9, 28, 127, 172, 179).
- [41] SM Hosseini Jenab and F Spanier. “Study of trapping effect on ion-acoustic solitary waves based on a fully kinetic simulation approach”. In: *Physics of Plasmas* 23.10 (2016), p. 102306 (cit. on pp. 9, 28, 57).
- [42] SM Hosseini Jenab and F Spanier. “Simulation study of overtaking of ion-acoustic solitons in the fully kinetic regime”. In: *Physics of Plasmas* 24.3 (2017), p. 032305 (cit. on pp. 9, 28, 57).
- [43] Chuteng Zhou and Ian H Hutchinson. “Dynamics of a slow electron hole coupled to an ion-acoustic soliton”. In: *Physics of Plasmas* 25.8 (2018), p. 082303 (cit. on pp. 9, 12, 28, 31, 56, 57, 166, 174, 181).
- [44] Koichi Saeki and J Juul Rasmussen. “Stationary solution of coupled electron hole and ion soliton in a collisionless plasma”. In: *Journal of the Physical Society of Japan* 60.3 (1991), pp. 735–738 (cit. on pp. 9, 28, 29, 57).
- [45] Koichi Saeki and Hitoshi Genma. “Electron-hole disruption due to ion motion and formation of coupled electron hole and ion-acoustic soliton in a plasma”. In: *Physical Review Letters* 80.6 (1998), p. 1224 (cit. on pp. 9, 28, 29, 57, 122, 127, 162, 172, 180).

- [46] Hans Schamel, Debraj Mandal, and Devendra Sharma. “On the nonlinear trapping nature of undamped, coherent structures in collisionless plasmas and its impact on stability”. In: *Physics of Plasmas* 24.3 (2017), p. 032109 (cit. on pp. 9, 28, 29, 52, 126, 171, 178).
- [47] Ian Horner Hutchinson and Chuteng Zhou. “Plasma electron hole kinematics. I. Momentum conservation”. In: *Physics of Plasmas* 23.8 (2016), p. 082101 (cit. on pp. 9, 10, 28, 29, 55, 56, 116, 161).
- [48] C Zhou and IH Hutchinson. “Plasma electron hole kinematics. II. Hole tracking Particle-In-Cell simulation”. In: *Physics of Plasmas* 23.8 (2016), p. 082102 (cit. on pp. 9, 28, 29, 54, 55, 115, 126, 171, 178).
- [49] Debraj Mandal, Devendra Sharma, and Hans Schamel. “Electron hole instability as a primordial step towards sustained intermittent turbulence in linearly subcritical plasmas”. In: *New Journal of Physics* 20.7 (2018), p. 073004 (cit. on pp. 9, 10, 29, 126, 171, 178).
- [50] Bengt Eliasson and PK Shukla. “Dynamics of electron holes in an electron–oxygen-ion plasma”. In: *Physical Review Letters* 93.4 (2004), p. 045001 (cit. on pp. 10, 30).
- [51] S. Peter Gary. *Theory of Space Plasma Microinstabilities*. Cambridge Atmospheric and Space Science Series. Cambridge University Press, 1993. DOI: 10.1017/CB09780511551512 (cit. on pp. 11, 30, 165, 166, 173, 181, 188).
- [52] Cecilia Norgren et al. “Slow electron holes in multicomponent plasmas”. In: *Geophysical Research Letters* 42.18 (2015), pp. 7264–7272 (cit. on pp. 11, 31).

- [53] Yu V Khotyaintsev et al. “Observations of slow electron holes at a magnetic reconnection site”. In: *Physical Review Letters* 105.16 (2010), p. 165002 (cit. on pp. 11, 31).
- [54] DA Gurnett et al. “Ion acoustic waves and related plasma observations in the solar wind”. In: *Journal of Geophysical Research: Space Physics* 84.A5 (1979), pp. 2029–2038 (cit. on pp. 11, 31, 165, 173, 181).
- [55] Y Omura et al. “Electron beam instabilities as generation mechanism of electrostatic solitary waves in the magnetotail”. In: *Journal of Geophysical Research: Space Physics* 101.A2 (1996), pp. 2685–2697 (cit. on pp. 12, 32).
- [56] Constantin F Rupp, Rodrigo A Lopez, and Jaime A Aranedo. “Critical density for Landau damping in a two-electron-component plasma”. In: *Physics of Plasmas* 22.10 (2015), p. 102306 (cit. on p. 33).
- [57] Gérard Belmont et al. *Collisionless plasmas in astrophysics*. John Wiley & Sons, 2013 (cit. on pp. 42–44).
- [58] A. A. Vlasov. “The vibrational properties of an electron gas”. In: *Soviet Physics Uspekhi* (1968). ISSN: 0038-5670. DOI: 10.1070/PU1968v010n06ABEH003709 (cit. on p. 43).
- [59] D Gary Swanson. *Plasma Waves*. 2nd Edition Institute of Physics Publishing. Series in Plasma Physics Plasma Waves, 2003. ISBN: 0 7503 0927 X (cit. on pp. 44, 45, 57).
- [60] R. C. Davidson. *Kinetic Waves and Instabilities in a Uniform Plasma*. MIT Plasma Science and Fusion Center, 1981 (cit. on pp. 44, 45).

- [61] B.D. Fried and S.D. Conte. *The Plasma Dispersion Function: The Hilbert Transform of the Gaussian*. Academic Press, 1961. ISBN: 9781483261737. URL: <https://www.elsevier.com/books/the-plasma-dispersion-function/fried/978-1-4832-2929-4> (cit. on pp. 47, 188).
- [62] Francesco Valentini, Thomas M O’Neil, and Daniel HE Dubin. “Excitation of nonlinear electron acoustic waves”. In: *Physics of Plasmas* 13.5 (2006), p. 052303 (cit. on p. 49).
- [63] David Campbell Montgomery. *Theory of the unmagnetized plasma*. CRC Press, 1971 (cit. on p. 49).
- [64] Burton D Fried and Roy W Gould. “Longitudinal ion oscillations in a hot plasma”. In: *The Physics of Fluids* 4.1 (1961), pp. 139–147 (cit. on p. 49).
- [65] Hans Schamel. “Analytic BGK modes and their modulational instability”. In: *Journal of Plasma Physics* 13.1 (1975), pp. 139–145 (cit. on pp. 52, 53).
- [66] Hans Schamel. “Stationary solitary, snoidal and sinusoidal ion acoustic waves”. In: *Plasma Physics* 14.10 (1972), p. 905 (cit. on p. 52).
- [67] Chuteng Zhou and Ian H Hutchinson. “Plasma electron hole oscillatory velocity instability”. In: *Journal of Plasma Physics* 83.5 (2017) (cit. on p. 54).
- [68] TJ Stuchi. “Symplectic integrators revisited”. In: *Brazilian Journal of Physics* 32.4 (2002), pp. 958–979 (cit. on p. 62).
- [69] Herbert Goldstein, Charles Poole, and John Safko. *Classical mechanics*. 2002 (cit. on p. 62).
- [70] Haruo Yoshida. “Construction of higher order symplectic integrators”. In: *Physics letters A* 150.5-7 (1990), pp. 262–268 (cit. on p. 62).

- [71] Vladimir Igorevich Arnol'd. *Mathematical methods of classical mechanics*. Vol. 60. Springer Science & Business Media, 2013 (cit. on p. 62).
- [72] Jesus M Sanz-Serna. “Symplectic integrators for Hamiltonian problems: an overview”. In: *Acta numerica* 1 (1992), pp. 243–286 (cit. on p. 62).
- [73] Haruo Yoshida. “Recent progress in the theory and application of symplectic integrators”. In: *Qualitative and Quantitative Behaviour of Planetary Systems*. Springer, 1993, pp. 27–43 (cit. on p. 63).
- [74] IP Omelyan, IM Mryglod, and R Folk. “Symplectic analytically integrable decomposition algorithms: classification, derivation, and application to molecular dynamics, quantum and celestial mechanics simulations”. In: *Computer Physics Communications* 151.3 (2003), pp. 272–314 (cit. on pp. 63–65).
- [75] Brett Gladman, Martin Duncan, and Jeff Candy. “Symplectic integrators for long-term integrations in celestial mechanics”. In: *Celestial Mechanics and Dynamical Astronomy* 52.3 (1991), pp. 221–240 (cit. on p. 63).
- [76] Masuo Suzuki. “Fractal decomposition of exponential operators with applications to many-body theories and Monte Carlo simulations”. In: *Physics Letters A* 146.6 (1990), pp. 319–323 (cit. on p. 64).
- [77] Siu A. Chin. “Symplectic integrators from composite operator factorizations”. In: *Physics Letters, Section A: General, Atomic and Solid State Physics* 226.6 (1997), pp. 344–348. ISSN: 03759601. DOI: 10.1016/S0375-9601(97)00003-0 (cit. on p. 65).
- [78] Gilbert Strang. “On the construction and comparison of difference schemes”. In: *SIAM journal on numerical analysis* 5.3 (1968), pp. 506–517 (cit. on p. 65).

- [79] Chio-Zong Cheng and Georg Knorr. “The integration of the Vlasov equation in configuration space”. In: *Journal of Computational Physics* 22.3 (1976), pp. 330–351 (cit. on p. 68).
- [80] Robert I McLachlan and Pau Atela. “The accuracy of symplectic integrators”. In: *Nonlinearity* 5.2 (1992), p. 541 (cit. on p. 68).
- [81] *Julia Language SpecialFunctions, Functions*. URL: https://juliamath.github.io/SpecialFunctions.jl/dev/functions_list/ (cit. on p. 69).
- [82] Kendall E Atkinson. *An introduction to numerical analysis*. John wiley & sons, 2008 (cit. on p. 69).
- [83] *Julia Language, LsqFit.jl*. URL: <https://julianlsolvers.github.io/LsqFit.jl/latest/> (cit. on p. 70).
- [84] SM Hosseini Jenab, F Spanier, and Gert Brodin. “A study of the stability properties of Sagdeev solutions in the ion-acoustic regime using kinetic simulations”. In: *Physics of Plasmas* 25.7 (2018), p. 072304 (cit. on pp. 122, 127, 162, 172, 180).
- [85] Hans L Pécseli. “Solitons and weakly nonlinear waves in plasmas”. In: *IEEE Transactions on Plasma Science* 13.2 (1985), pp. 53–86 (cit. on p. 127).